micromachines

Micro/Nano-Chip Electrokinetics

Edited by
Xiangchun Xuan and Shizhi Qian

Printed Edition of the Special Issue Published in *Micromachines*

www.mdpi.com/journal/micromachines

MDPI

Micro/Nano-Chip Electrokinetics

Special Issue Editor
Xiangchun Xuan
Shizhi Qian

MDPI • Basel • Beijing • Wuhan • Barcelona • Belgrade

Special Issue Editor
Xiangchun Xuan
Clemson University
USA

Shizhi Qian
Old Dominion University
USA

Editorial Office
MDPI AG
St. Alban-Anlage 66
Basel, Switzerland

This edition is a reprint of the Special Issue published online in the open access journal *Micromachines* (ISSN 2072-666X) from 2016–2017 (available at: http://www.mdpi.com/journal/micromachines/special_issues/micro_nano_chip_electrokinetics).

For citation purposes, cite each article independently as indicated on the article page online and as indicated below:

Author 1; Author 2. Article title. *Journal Name* **Year**, *Article number*, page range.

First Edition 2017

ISBN 978-3-03842-452-9 (Pbk)
ISBN 978-3-03842-453-6 (PDF)

Table of Contents

About the Special Issue Editors

Xiangchun Xuan is currently an Associate Professor of Mechanical Engineering at Clemson University. He received his PhD degree from the Department of Mechanical and Industrial Engineering at the University of Toronto in 2006 and Bachelor of Engineering degree from the University of Science and Technology of China in 1995. Dr. Xuan was a recipient of the NSF CAREER award in 2012. His research interests cover micro/nanofluidics fundamentals and lab-on-a-chip applications with particular focus on electrofluidics, magnetofluidics and elastofluidics. He has published over 100 articles in leading international journals.

Shizhi Qian received his B.S. and first Ph.D. from Huazhong University of Science and Technology, China in 1994 and 1998, respectively. He worked afterwards as a senior engineer in industry for two years. From February 2001 to August 2002 he worked as a Postdoctoral Researcher in Mechanical Engineering and Applied Mechanics (MEAM), University of Pennsylvania (PENN). From September 2002 to December 2004, he pursued another Ph.D in MEAM at PENN. He was then promoted to Research Associate, and worked at PENN until he became Assistant Professor in the Department of Mechanical Engineering at the University of Nevada Las Vegas (UNLV) in August 2005. He joined the Department of Aerospace Engineering at the Old Dominion University as an Assistant Professor in July 2008 and was promoted to tenured associate professor in July 2011. He was a WCU (World Class University) Fellow in Korea during the period from 2009 to 2014. Since 2002, he has published 150+ peer-reviewed SCI journal articles.

micromachines

MDPI

Editorial

Editorial for the Special Issue on Micro/Nano-Chip Electrokinetics

Xiangchun Xuan [1,*] and Shizhi Qian [2]

[1] Department of Mechanical Engineering, Clemson University, Clemson, SC 29634, USA
[2] Department of Mechanical and Aerospace Engineering, Old Dominion University, Norfolk, VA 23529, USA; SQian@odu.edu
* Correspondence: xcxuan@clemson.edu

Academic Editor: Nam-Trung Nguyen
Received: 2 May 2017; Accepted: 2 May 2017; Published: 4 May 2017

Micro/nanofluidics-based lab-on-a-chip devices have found extensive applications in the analysis of chemical and biological samples over the past two decades. Electrokinetics is the method of choice in these micro/nano-chips for transporting, manipulating and sensing various analyte species (e.g., ions, molecules, fluids and particles, etc.) [1,2]. This Special Issue in *Micromachines* is aimed to provide the recent development in the field of Micro/Nano-Chip Electrokinetics. It consists of 15 papers, which cover both fundamentals and applications, original research and reviews. These papers can be classified into four groups as summarized below.

(1) Fundamentals of electrokinetics. Yuan et al. [3] demonstrated a tunable particle focusing in a straight rectangular microchannel with symmetric semicircle obstacle arrays by the use of electrophoretic slip-induced Saffman lift force. Zhou et al. [4] investigated the aggregation of TiO_2 submicron particles in deionized water under ultra-violet light irradiation and reported a neutralization effect on the particle zeta potential. Bashirzadeh et al. [5] proposed the use of graphite pencil-leads as low cost, disposable electrodes for the study of various electrokinetic phenomena in straight cylindrical microchannels.

(2) Applications of electrokinetics to (bio)particle manipulations. Natu and Martinez-Duarte [6] used numerical simulation to investigate the effects of device geometry and experimental variables on the continuous sorting of neural stem/progenitor cells via streaming dielectrophoresis (DEP). Zhou et al. [7] proposed a microfluidic device with a contraction channel and tested it numerically for the deformability-based particle separation by DC DEP. Zhu et al. [8] demonstrated the use of multiple parallel microchannels in a two-layer stacked microfluidic device for a significantly enhanced throughput in particle and cell manipulation via reservoir-based DEP (rDEP). Li et al. [9] presented a rapid fabrication of high-aspect-ratio 3D hydrogel microstructures using optically induced electrokinetics (OEK).

(3) Applications of electrokinetics to ionic species manipulation. Zhou et al. [10] proposed an electroosmotic flow-based micromixer with an asymmetrical lateral structure for enhanced fluid streams folding and stretching. Mavrogiannis et al. [11] reported a novel microfluidic method for electrokinetic mixing of laminar fluids and controlling of on-chip concentrations using fluidic DEP. Li et al. [12] demonstrated paper-based sample concentration using ion concentration polarization and sample detection with a smart phone. Zhao et al. [13] presented an overview of the various analyte concentration techniques in microfluidic devices with focus on both the physical mechanism and the representative applications.

(4) Other electric field-based applications. Wang et al. [14] investigated the frequency-dependent electroformation of giant unilamellar vesicles in between 3D and 2D microelectrode systems. Liu et al. [15] presented a new method for analyzing the deformability of fused cells under

electrical stresses in a microfluidic array device. Tsai et al. [16] studied the effects of system parameters on the power generation by reverse electrodialysis in a microfluidic device with a Nafion ion-selective membrane. Wang et al. [17] developed a microfluidic device for classification of microalgae cells based on the simultaneous detection and analysis of the signals of fluorescence, scattering, and resistance pulse sensing.

We would like to thank all the contributors for submitting their papers to this Special Issue. We also thank all the reviewers for dedicating their time to help improve the quality of the submitted papers.

Conflicts of Interest: The authors declare no conflict of interest.

References

1. Li, D. *Electrokinetics in Microfluidics*; Elsevier Academic Press: Burlington, MA, USA, 2004.
2. Chang, H.C.; Yeo, L.Y. *Electrokinetically Driven Microfluidics and Nanofluidics*; Cambridge University Press: New York, NY, USA, 2010.
3. Yuan, D.; Pan, C.; Zhang, J.; Yan, S.; Zhao, Q.; Alici, G.; Li, W. Tunable Particle Focusing in a Straight Channel with Symmetric Semicircle Obstacle Arrays Using Electrophoresis-Modified Inertial Effects. *Micromachines* **2016**, *7*, 195. [CrossRef]
4. Zhou, C.; Bashirzadeh, Y.; Bernadowski, T.A.; Zhang, X. UV Light–Induced Aggregation of Titania Submicron Particles. *Micromachines* **2016**, *7*, 203. [CrossRef]
5. Bashirzadeh, Y.; Maruthamuthu, V.; Qian, S. Electrokinetic Phenomena in Pencil Lead-Based Microfluidics. *Micromachines* **2016**, *7*, 235. [CrossRef]
6. Natu, R.; Martinez-Duarte, R. Numerical Model of Streaming DEP for Stem Cell Sorting. *Micromachines* **2016**, *7*, 217. [CrossRef]
7. Zhou, T.; Yeh, L.; Li, F.; Mauroy, B.; Joo, S.W. Deformability-Based Electrokinetic Particle Separation. *Micromachines* **2016**, *7*, 170. [CrossRef]
8. Zhu, L.; Patel, S.H.; Johnson, M.; Kale, A.; Raval, Y.; Tzeng, T.; Xuan, X. Enhanced Throughput for Electrokinetic Manipulation of Particles and Cells in a Stacked Microfluidic Device. *Micromachines* **2016**, *7*, 156. [CrossRef]
9. Li, Y.; Lai, S.H.S.; Liu, N.; Zhang, G.; Liu, L.; Lee, G.; Li, W. Fabrication of High-Aspect-Ratio 3D Hydrogel Microstructures Using Optically Induced Electrokinetics. *Micromachines* **2016**, *7*, 65. [CrossRef]
10. Zhou, T.; Wang, H.; Shi, L.; Liu, Z.; Joo, S.W. An Enhanced Electroosmotic Micromixer with an Efficient Asymmetric Lateral Structure. *Micromachines* **2016**, *7*, 218. [CrossRef]
11. Mavrogiannis, N.; Desmond, M.; Ling, K.; Fu, X.; Gagnon, Z. Microfluidic Mixing and Analog On-Chip Concentration Control Using Fluidic Dielectrophoresis. *Micromachines* **2016**, *7*, 214. [CrossRef]
12. Li, X.; Niu, Y.; Chen, Y.; Wu, D.; Yi, L.; Qiu, X. Microfluidic Paper-Based Sample Concentration Using Ion Concentration Polarization with Smartphone Detection. *Micromachines* **2016**, *7*, 199. [CrossRef]
13. Zhao, C.; Ge, Z.; Yang, C. Microfluidic Techniques for Analytes Concentration. *Micromachines* **2017**, *8*, 28. [CrossRef]
14. Wang, Q.; Zhang, X.; Fan, T.; Yang, Z.; Chen, X.; Wang, Z.; Xu, J.; Li, Y.; Hu, N.; Yang, J. Frequency-Dependent Electroformation of Giant Unilamellar Vesicles in 3D and 2D Microelectrode Systems. *Micromachines* **2017**, *8*, 24. [CrossRef]
15. Liu, Y.; Zhang, X.; Chen, M.; Yin, D.; Yang, Z.; Chen, X.; Wang, Z.; Xu, J.; Li, Y.; Qiu, J.; et al. Electro-Deformation of Fused Cells in a Microfluidic Array Device. *Micromachines* **2016**, *7*, 204. [CrossRef]
16. Tsai, T.; Liu, C.; Yang, R.J. Power Generation by Reverse Electrodialysis in a Microfluidic Device with a Nafion Ion-Selective Membrane. *Micromachines* **2016**, *7*, 205. [CrossRef]
17. Wang, J.; Zhao, J.; Wang, Y.; Wang, W.; Gao, Y.; Xu, R.; Zhao, W. A New Microfluidic Device for Classification of Microalgae Cells Based on Simultaneous Analysis of Chlorophyll Fluorescence, Side Light Scattering, Resistance Pulse Sensing. *Micromachines* **2016**, *7*, 198. [CrossRef]

micromachines

MDPI

Article

Microfluidic Techniques for Analytes Concentration

Cunlu Zhao [1,*,†], Zhengwei Ge [2,†] and Chun Yang [2,*]

1 Key Laboratory of Thermo-Fluid Science and Engineering of MOE, School of Energy and Power Engineering, Xi'an Jiaotong University, Xi'an 710049, China
2 School of Mechanical and Aerospace Engineering, Nanyang Technological University, 50 Nanyang Avenue, Singapore 639798, Singapore; GEZH0001@e.ntu.edu.sg
* Correspondence: mclzhao@mail.xjtu.edu.cn (C.Z.); mcyang@ntu.edu.sg (C.Y.); Tel.: +86-29-8266-3222 (C.Z.); +65-6790-4883 (C.Y.)
† These authors contributed equally to this work.

Academic Editors: Xiangchun Xuan and Shizhi Qian
Received: 6 November 2016; Accepted: 16 January 2017; Published: 22 January 2017

Abstract: Microfluidics has been undergoing fast development in the past two decades due to its promising applications in biotechnology, medicine, and chemistry. Towards these applications, enhancing concentration sensitivity and detection resolution are indispensable to meet the detection limits because of the dilute sample concentrations, ultra-small sample volumes and short detection lengths in microfluidic devices. A variety of microfluidic techniques for concentrating analytes have been developed. This article presents an overview of analyte concentration techniques in microfluidics. We focus on discussing the physical mechanism of each concentration technique with its representative advancements and applications. Finally, the article is concluded by highlighting and discussing advantages and disadvantages of the reviewed techniques.

Keywords: microfluidics; sample preconcentration; stacking; field gradient focusing; electrokinetic trapping; immunocapture based trapping

1. Introduction

Microfluidics is a set of technologies that are capable of accurately manipulating a small amount of fluids and analytes with their volume ranging from microliters to picoliters. Particularly, microfluidics is the core technique for micro total analysis systems (μTAS) or so-called "lab on a chip" (LOC) systems which, during the past two decades, have had a revolutionary impact on biotechnology, medicine, optics and chemistry etc. [1–3]. These microfluidics-based analytical systems show great advantages compared to traditional analytical systems/devices: they consume extremely small amount of sample material and reagents; they can be inexpensive and disposable; the analysis time with microfluidic analytical systems tends to be very short; more prominently one single microfluidic analytical system usually can perform multiple sample manipulation functions, such as sample concentration, separation, detection, pumping, mixing, and chemical reactions etc.

One of the major challenges faced by microfluidics is the difficulty in detecting very dilute concentration of analytes (e.g., pathogen in saliva) with ultrasmall volumes of samples in microchannels. The poor detection sensitivity results from the extremely small quantities of dilute analytes and the very short (10–100 μm) optical detection path lengths [4]. In chemical or biochemical analyses such as the detection of drug molecules in biological fluids, the drug and its metabolites are usually at much lower concentration than those prepared in laboratory [5]. The miniaturized medical/biomedical analysis systems, serving as promising tools for fast clinical and forensic diagnostics, also demand the development of detection and sensing techniques to meet the requirements of sensitivity, resolution and reliability [6]. In the field of portable water analysis

and environmental analysis of nonsaline and saline waters, the analysis equipment is not sensitive enough to detect the low concentrations of organic and inorganic substances present in the samples. For instance, the concentration of organomercury or organolead compounds is less than 1 ng/L in seawater, and the concentration of polyaromatic hydrocarbons is less than 1 nM in waste water [7].

There have been well-developed techniques for analyte concentration for large-volume liquid samples in environment analyses. For example, the extraction method is the most widely used in concentrating environmental samples. The idea of this technique is that it uses a material phase or extraction agent that has strong affinity (either physical or chemical) to a specific component in the sample to increase the concentration of that specific component. After many years' development, it has numerous variations, such as liquid-liquid extraction (LLE), solid phase extraction (SPE), solid phase microextraction (SPME), magnetic solid phase extraction (MSPE), microwave-assisted extraction (MAE), supercritical fluid extraction (SFE) etc. These techniques have been successfully used in concentrating inorganic (largely heavy metal ions) and organic pollutants in large volumes of water sample. The state-of-the-art of the extraction methods has been well documented in Refs. [8–11]. Yet, concentration of analyte in ultra-small volume of sample (usually nanoliter), which is typically required in microfluidic applications, is still in the initial stage of development and facing various challenges. For example, capillary electrophoresis (CE) is a widely-used microfluidic separation technique in chemical, biological and medical analyses. During its development in more than 20 years, enhancing its selectivity and sensitivity for detection/separation is constantly an important topic. CE has two types of detection limit: the concentration detection limit and the mass detection limit. The concentration detection limit is defined as the minimum concentration which can be detected by a given detection technique: typical values for ultraviolet (UV) detection, electrochemical/fluorescence detection and optimized laser-induced fluorescence (LIF) detection are 10^{-6} M, 10^{-8} M and 10^{-10} M, respectively. The mass detection limit is the absolute mass subjected to the analytical separation. In capillary electrophoresis, absolute mass is in a quite small range from pico- to atto-mole. This is because in CE system, the total volumes handled are less than 10 microliters and injection volumes are in the range of several nanoliters or even picoliters [12]. Although some methods of detection, such as LIF and mass spectroscopy can potentially offer improved detection sensitivity, they are not widely applicable and also rather expensive. A more practical method of improving the sensitivity of CE is to increase the concentration of analytes for the analysis. Sample preconcentration methods, usually on-capillary, are used to concentrate dilute samples for increasing the CE sensitivity [13].

Hence, miniaturization of analytical devices involving micro/nanoliter samples call for the demand for efficient preconcentration or focusing of dilute samples prior to detection or further analyses. In microfluidics, numerous techniques have been developed to concentrate analytes for subsequent detection and manipulations. In this review, we provide an overview of microfluidic techniques for analyte concentration. According to the difference in physical mechanisms, this review categorize the concentration techniques into three major groups: the first group of concentration techniques termed as the stacking methods includes the sweeping method, the field amplified sample stacking (FASS) method and the isotachophoresis (ITP); the second group of analyte concentration methods is termed as the equilibrium field gradient focusing methods, including the isoelectric focusing (IEF) by creating a pH gradient, electric field gradient focusing (EFGF) by imposing an electric field gradient, and temperature gradient focusing (TGF) by using a temperature gradient; the third group includes some other concentration techniques based on various trapping mechanisms, including electrokinetic trapping (EKT), dielectrophoretic trapping (DEPT), immunocapture based trapping (ICBT), magnetic beads assisted trapping (MBAT), thermophoretic trapping (TPT) and some other emerging methods. The above three groups are reviewed in a sequential order; for each group the review begins with the discussion of its underlying concentration mechanism and application background, and subsequently presents some of its typical application examples. Finally, the review is concluded by summarizing advantages and disadvantages of the reviewed techniques.

2. Stacking Methods

The main principle of stacking methods is based on the mass conservation in electrophoresis with manipulation of net migration velocities of analytes. Figure 1 shows a schematic view of the stacking mechanism. The stacking zone and the analyte zone are separated by their common boundary. The analyte net velocities in the analyte zone and the stacking zone are denoted by $V_{a,a}$ and $V_{a,s}$, respectively. The velocity of the common boundary is V_b. By manipulation of the magnitude of these three velocities, three cases can be distinguished [14], including boundary stacking when $(V_{a,s} - V_b)/(V_{a,a} - V_b) < 0$, proportional stacking when $0 < (V_{a,s} - V_b)/(V_{a,a} - V_b) < 1$, and no stacking when $(V_{a,s} - V_b)/(V_{a,a} - V_b) > 1$. Clearly, proportional stacking and boundary stacking are two basic modes of stacking. In the proportional stacking, the analytes migrate into a stacking zone with decreasing migration velocity. In the boundary stacking, the analyte is focused at a sharp moving boundary, since the analytes in front of the boundary move slower than the sharp boundary and the analytes behind the boundary move faster than the sharp boundary.

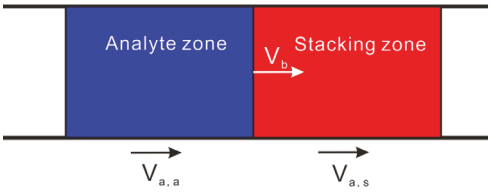

Figure 1. Schematics of the stacking mechanism via manipulation of the net velocities of analytes. The analyte in the analyte (stacking) zone moves with a velocity of $V_{a,a}$ ($V_{a,s}$), and the boundary between analyte zone and stacking zone moves with a velocity of V_b.

2.1. Sweeping

Sweeping was initially developed for concentrating neutral hydrophobic analytes through picking and accumulation of analyte molecules in their pseudo-stationary phase (PSP) that penetrates the sample zone. It was first described in electrokinetic chromatography using a charged pseudo-stationary phase (i.e., micelle) [15]. In combination with stacking by ion selective injection, sweeping has also been applied to charged hydrophobic analytes [16,17]. To elucidate the sweep mechanism, an example of neutral analytes with a negatively charged PSP is shown in Figure 2. Micelles are chosen as the PSP and are suspended in the background solution (BGS). The conductivities of liquids are similar, and thus a homogenous electric field is expected in the capillary. Electroosmotic flow is neglected here, and neutral analytes have to be incorporated into charged micelles for transportation. Under such circumstances, neutral analytes are transported to the detector by micelle electrophoresis.

In Figure 2a, the analytes (S, the light shade area) containing no micelles are injected into a capillary filled with the BGS containing micelles. The analyte zone has the same conductivity as the BGS zone, which ensures a homogenous electric field along the capillary. In Figure 2b, as soon as a voltage is applied across the capillary (with both ends immersed in micellar BGS), the negatively charged micelles enter the capillary from the cathodic end due to electrophoresis. The moving micelles pick up the analytes in the S zone, and then the analytes accumulate into a narrow zone. The accumulation zone denoted by the dark shade area has a higher analyte concentration than the original analyte zone (light shade area). At the interface (dashed line) between the S and BGS zones, a micelle vacancy zone develops simultaneously. In Figure 2c, the micelles completely sweep all analytes into a much narrower zone. The analyte concentration after sweeping is predicted to be enhanced with a factor $1 + k$, where k is the retention factor. Sweeping is capable of achieving a very high degree of sample concentration up to 5000-fold. The technique is useful only for small hydrophobic analytes with a high affinity to a mobile micellar phase [16,18].

The applications of sweeping to the preconcentration of various analytes have been achieved, such as phenols and pesticides in food samples and water, illicit drugs in urine samples, active ingredients of pharmaceutical samples, and even alkaloids in Chinese herbal medicines. The reviews [17,19] provide a good summary of diverse analytes that have been concentrated with the sweeping method. The sweeping method is also combined with other concentration techniques, such as dynamic pH junction and field amplified sample injection, to produce an improved concentration enhancement [17,18]. The combination of sweeping and field amplified sample injection produces a 10,000,000-fold increase in detection sensitivity for capillary electrophoresis separation, which is an unprecedentedly high value [20].

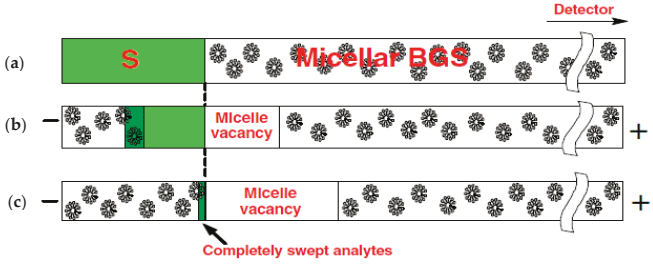

Figure 2. Principle of the sweeping in a homogenous electric field. (**a**) At beginning, the capillary is filled with analyte solution (S) and micellar background solution (BGS), and the two portions have a similar conductivity. (**b**) Application of a voltage electrophoretically drives the pseudo-stationary phase (PSP) into the S zone, and at the same time the moving PSP sweeps analyte molecules to compress the S zone. (**c**) As PSP completely fills the S zone, the analytes are completed swept to form a concentrated band. Reprint from Ref. [17].

2.2. Field Amplified Sample Stacking (FASS)

Field-amplified sample stacking (FASS) is a commonly used method for preconcentrating analytes prior to capillary electrophoresis separation [21]. In FASS, the sample is prepared in the solution with a lower conductivity than the running buffer solution. One portion of capillary is filled with the sample solution of low-conductivity, while the remaining portion of capillary is filled with the running buffer of high-conductivity. Thus, the contact of high and low conductivity solutions inside a capillary creates a boundary. The electric field strength, as well as the electrophoretic velocities of the analytes in the low-conductivity zone is higher than that in the high-conductivity zone due to the difference in solution conductivities between the two zones. The velocity of analytes decreases when the analytes are transported from the low-conductivity zone to the high-conductivity zone. Hence, the analytes accumulate into a narrow concentrated band in the high-conductivity zone. The sample is concentrated due to the velocity change when it passes through the boundary between low- and high-conductivity zones. FASS can achieve fairly high concentration factors of about 100 to 1000 folds, but it requires multiple buffers [22].

Zhang and Thormann [23] demonstrated a head-column FASS for analysis of positively charged, hydrophobic compounds in capillary electrophoresis. To ensure the success of this technique: a water plug with length larger than 1 mm was introduced at the capillary inlet prior to injection of solutes; a modestly high voltage (<20 kV) was applied for less than 60 s during sample introduction; sample solutions with low-conductivity were employed. As a demonstration of the effectiveness of technique, the sensitivity in analyzing amiodarone and desethylamiodarone was enhanced over 1000-fold, as compared to that achieved by hydrodynamic injection without sample stacking. However, head-column FASS suffers from some disadvantages: biological samples have to contain no salts; the devices should be carefully designed to enable the easy application of voltage and pressure/vacuum during any cycle of the run.

How to setup a high conductivity gradient boundary is challenging in a practical FASS. To resolve this issue, Jung et al. [24] developed a novel FASS-capillary electrophoresis chip which uses a photo-initiated porous polymer structure to suppress the flow, but allows electromigration of sample analytes. This can make the sample injection and flow control for high-gradient FASS much easier. The technique yielded an 1100-fold increase of signal intensity in separation of fluorescein and Bodipy.

In order to investigate the dynamics at an interface between high- and low-conductivity zones in FASS, Bharadwaj and Santiago [25] theoretically modeled the FASS process as a combination of electromigration, diffusion, and advection of the multi-sample species and background electrolyte ions. Electric field, background electrolyte concentration, and sample-ion distribution were numerically simulated to predict the time evolution of the FASS process. The model was validated by on-chip FASS experiments. Sustarich et al. [26] studied the FASS in nanofluidic channels with electric double layer effects. Results showed that the concentration enhancement is better in nanochannels than in microchannels, but the inherent signals are relatively low due to the smaller amount of analytes handled in nanoscale level.

For simultaneous concentration of multiple analytes, FASS needs to be combined with other concentration methods. One example is the FASS-sweeping combined technique [27,28]. Figure 3 shows the concentration enhancement of three analytes, namely positively charged, negatively charged and neutral, by a FASS-sweeping combined mechanism. Initially, the sample is loaded into the capillary (Figure 3a). The left portion of capillary is occupied by sample matrix (SM) which holds the sample and the rest is filled with back ground electrolyte (BGE) which contains anionic micelles. The application of a high voltage causes the stacking of charged analytes on the zone boundaries between BGE and SM (Figure 3b). At the same time, background electrolyte mixed with micelles, enters the capillary because of electroosmotic flow (EOF), and sweeps the sample zone analytes (Figure 3c). Thus, charged analytes are subject to both stacking and sweeping, while neutral analytes are only subject to sweeping. Finally, all analytes are completely swept (Figure 3d).

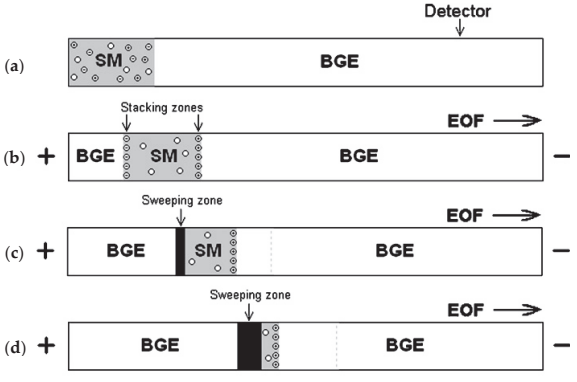

Figure 3. A FASS–sweeping combined mechanism for sample concentration. (**a**) Sample is loaded into the low conductivity sample matrix (SM) which has a lower pH value than the background electrolyte (BGE) that contains anionic micelles. (**b**) Under the effect of an applied voltage, charged analytes are stacked to the two boundaries between SM and BGE, and BGE with micelles enters the anodic end of the capillary by electroosmotic flow (EOF). (**c**) Movement of the micelles into the SM sweep sample compounds. (**d**) All sample compounds are completely swept. ⊖—Anionic analyte, ⊕—cationic analyte, ○—neutral analyte. Reprint from Ref. [28].

FASS is the simplest sample concentration technique used in capillary electrophoresis, and therefore has been employed in diverse fields, such as biology, environmental monitoring, food and pharmaceutical analyses. The readers can have more details from the recent review [19].

2.3. Isotachophoresis (ITP)

Isotachophoresis (ITP) is a technique using variable ion mobility zones for sample focusing and separation [29]. Three electrolytes are used in ITP: a leading electrolyte (LE), a trailing electrolyte (TE) and a sample analytes sandwiched between the two. As to the composition of LE and TE, ITP requires that LE and TE usually have a common counterion, but different coions. Coions (counterions) have an electric polarity same as (opposite to) the charged analytes. The ionic mobility of analytes should be higher than that of coions of the TE, but lower than that of coions of the LE. As an electric potential is applied across the entire zone, a low (high) electrical field in LE (TE) is generated. Analyte ions in the TE migrate faster than the coions of TE, while analytes in the LE migrate slower. Such analyte velocity difference in LE and TE results in the focusing of analytes at the LE/TE interface.

Being a sensitive analytical technique, the analytical capillary ITP has its advantages in concentrating and separating samples with large ratios of macrocomponents to microcomponents. Such samples can be analyzed with pretreatment by applying ITP alone or even better in combination with capillary zone electrophoresis or another separation method [30]. Ma et al. [31] performed an ITP preconcentration followed by capillary zone electrophoresis separation on a quartz microchip with UV detection. Compared to the sole capillary zone electrophoresis mode, the analysis sensitivity is increased 32-fold. Jung et al. [32] conducted a systematic experimental investigation of the initial sample ion concentration, leading ion concentration, and trailing ion concentration effects on ITP stacking. The single-column ITP was greatly improved with high leading ion concentration and electroosmotic flow suppression to achieve a million-fold concentration enhancement. Additionally, the single-column ITP can be readily integrated with capillary electrophoresis separation. Jung et al. [33] subsequently presented another highly sensitive capillary electrophoresis setup with combination of transient, single-interface on-chip ITP and a laser-induced confocal fluorescence detection. Effects of microscope objective specifications and intensity of excitation laser were studied experimentally to optimize the performance of setup. The new setup was demonstrated to separate and detect 100 aM fluorophores from the samples, which is the highest sensitivity ever reported for electrophoretic separation at that time.

Khurana and Santiago [34] developed a theoretical model to analyze the concentration enhancement with ITP peak mode. The model was optimized to achieve the maximum values of preconcentration ratio and peak analyte concentration by perfect suppression of electroosmotic flow. Bottenus et al. [35,36] concentrated the cardiac biomarker, cardiac troponin I (cTnI), using cationic ITP in a 3.9 cm long PMMA microfluidic channel. An increase in concentration by over a factor of more than 10,000 was observed due to the combination of ITP stacking and the reduction in cross-sectional area. Then, a 3-D numerical simulation of ITP was performed by the same group to predict the concentration enhancement of proteins in an ITP experiment, and this could be the first example of an ITP simulation in three dimensions [37]. Although ITP is a very powerful technique to concentrate and separate solutes, one apparent drawback is that it requires some priori knowledge of electrophoretic mobilities of sample ions.

3. Gradient Focusing Methods

The central idea of gradient focusing methods is explained in Figure 4. The analyte inside the two analyte zones moves with a velocity of $V_{a,a}$ towards the focusing zone which is stationary, and gradually the analyte concentration inside the focusing zone is enhanced. To create a variation of analyte velocity in Figure 4 is critical for the success of analyte focusing, and usually various field gradients (such as pH gradient, electric field gradient and temperature gradient) are utilized for such purpose. Gradient focusing is different from stacking, although they both achieve an increase in analyte concentration by varying analyte axial velocity. The main difference between the two is the ways in which analytes are transported to the concentration region [38]. In the stacking, analytes are concentrated at a boundary because of reducing the magnitude of the analyte velocity across the boundary but no change of analyte velocity direction. Therefore, the extent of concentration

enhancement is limited by such velocity reduction. However, for the focusing techniques, analytes are concentrated at a focusing point since analytes migrate to this point from both directions due to a change in direction of the analyte velocity. As a result, the concentration process continues at the focusing point provided that the focusing field is present or until the sample analyte is completely exhausted. The concentration enhancement in focusing techniques is determined by the velocity at which analytes migrate to the focusing zone and the duration for applying the focusing field.

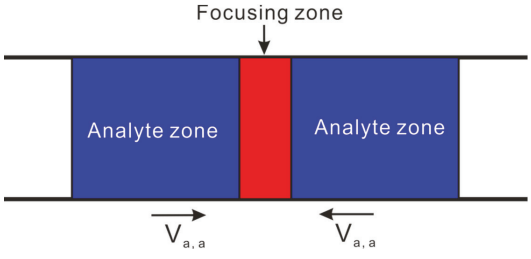

Figure 4. Schematic illustration showing of the gradient focusing mechanism. The analyte accumulates with a velocity of $V_{a,a}$ towards the stationary focusing zone from two analyte zones.

3.1. Isoelectric Focusing (IEF)

Isoelectric focusing (IEF), also known as electrofocusing, is commonly used for concentrating and separating proteins at their respective isoelectric points in the presence of a pH gradient [39,40]. When protein molecules are subject to a pH gradient, they acquire different electric charge. At a specific value of pH (so called isoelectric point), the proteins are unchanged, while the proteins below and above such specific pH value are oppositely charged. Under the effect of an electric field, proteins move electrophoretically towards the isoelectric point and eventually stop at this point. Gradually, protein molecules become more concentrated at the isoelectric point. Successful implementation of IEF relies on the generation of stable pH gradients [41]. However, from an application viewpoint, IEF is limited due to the restriction of sample analytes with an accessible isoelectric point along a pH gradient [42]. In addition, the low solubility of most proteins at their isoelectric points highly degrade concentration enhancement by IEF [43].

Dynamic isoelectric focusing (DIEF) [44] is an improved capillary isoelectric focusing technique which is capable of controlling the shape of the electric field inside the capillary by additional high-voltage power supplies. DIEF is similar to capillary isoelectric focusing (cIEF), because proteins in both methods are focused at their isoelectric point by generating a pH gradient. The difference between cIEF and DIEF is that in cIEF the pH gradient and the electric field are constant, giving each focused protein in the sample a fixed position, while in DIEF, the pH gradient can be adjusted by manipulation of the electric field, making the control of position and width of each focused protein band available. By changing electric fields in DIEF, the protein band can be relocated to a desired location for collection and further analysis without the loss of focusing. The high peak capacity as well as the flexibility to control the focusing band width and location demonstrates that DIEF can be potentially a first dimension in a multidimensional separation system. The highest peak capacity in DIEF can be over 1000, as is evidenced by both mass spectrometry and direct imaging.

Mosher and Thormann [45] performed a high-resolution computer simulation of the dynamics of IEF to search for more realistic input parameters for carrier ampholytes. The simulated cationic migrations were compared well with the experimental data. It was found that the cathodic migration makes the acidic portion of the gradient flat and the basic part steep, which is an additional argument disproving the notion that the focused zones of carrier ampholytes have no electrophoretic flux. Yang et al. [46] developed a free-flow IEF microfluidic device with glass coating by sol-gel methods

to improve the bonding strength, chemical resistance and durability for reuse, as well as to supply a stable pH gradient.

3.2. Electric Field Gradient Focusing (EFGF)

In electric field gradient focusing (EFGF), electric field gradient and an bulk flow are used to enable the net analyte velocity at the focusing point to zero [47]. At the focusing point, the electrophoretic force acting on charged analytes is exactly counteracted by the hydrodynamic force due to bulk fluid flow, while on two sides of focusing point, the imbalance between electrophoretic force and hydrodynamic force causes the analytes to move towards the stationary focusing point. Normally, the bulk flow is constant, and thus a gradient in electrophoretic velocity is required to induce the imbalance between electrophoretic and hydrodynamic forces at two sides of focusing point. In EFGF, electrophoretic velocity gradient is specifically produced by electric field gradient. In comparison with IEF, EFGF can be relatively simple to implement and offers a number of advantages including the use of a single continuous buffer and no limit to analytes with an accessible isoelectric point [48].

Ivory's group did numerous studies on EFGF focusing of proteins. They created the first-generation apparatus to demonstrate that EFGF has the ability of concentrating and separating proteins [49]. Then, they improved their device to separate and focus charged proteins using the EFGF method by setting a constant electroosmotic flow velocity against step-changing electrophoretic velocity [50]. The device could manipulate electrophoretic and electroosmotic velocities independently. The essential difference between this device and other devices for EFGF was the injection of electric current at discrete intersections in the channel, rather than continuously along the length of a membrane-bound separation channel.

EFGF has been both theoretically and experimentally investigated by Lee's group. Tolley et al. [51] did a theoretical simulation of EFGF. Their results showed that high peak capacity (over 10,000) is theoretically possible. Humble et al. [52] demonstrated the use of an ionically conductive polymer to produce the required electric field gradient inside the separation channel, which retains large analytes (e.g., proteins), but permits the transport of small buffer ions. This method was shown to be able to concentrate proteins ~10,000 fold within 40 min. A major drawback of this system is that it is difficult to find the optimal operating conditions for the electric field against the hydrodynamic flow due to the lack of field homogeneity. The system also suffers a problem of mass dispersion, leading to the degradation of resolution and sensitivity.

Liu et al. [53] used a novel fabrication method to integrate a conductive membrane into an EFGF device. They found that membrane properties such as conductivity and ion transport could change the electric field gradient produced in the separation channel, which greatly affects the behavior of the EFGF device. A green fluorescent protein was concentrated up to 4000-fold using this EFGF device. Using phase changing sacrificial layers, Kelly et al. [54] also developed an approach to integrate ionically conductive membranes into microfluidic EFGF device. The membrane-based microchips were demonstrated to be able to concentrate fluorescently labelled peptides more than 150-fold and protein samples more than 10,000-fold.

Sun et al. [55] used a bilinear electric field gradient instead of a linear electric field gradient for EFGF to improve the peak capacity. The EFGF induced by a linear electric field gradient could only achieve 20 static peak capacity in a 4 cm long channel, while the bilinear electric field gradient could improve it to a dynamic peak capacity of 150. In addition, they also used a phosphate buffer containing a salt with high mobility ions instead of Tris-HCl buffer to improve the stability of current and reproducibility [56]. A bilinear electric field gradient produced much narrower focusing bands, with a concentration enhancement of 14,000-fold for protein samples. Ansell et al. [57] reported an on-column detection of native, uncolored proteins by fluorescence quenching with EFGF. However, the technique of visualization is only applicable to proteins that absorb at a specific wavelength of 254 nm.

3.3. Temperature Gradient Focusing (TGF)

Temperature gradient focusing (TGF) was invented by Ross and Locascio [58] to concentrate and separate charged analytes by balancing the electrophoretic motion of analytes against the bulk flow of solution. The electrophoretic velocity gradient is established by a temperature gradient along the channel with an appropriate buffer. The analytes can then be focused at a stagnant point where the sum of their electrophoretic and bulk velocities is zero. The technique was demonstrated for a variety of analytes, including fluorescent dyes, amino acids, DNA, proteins, and particles (polystyrene) with a concentration enhancement of more than 1000-fold.

Balss et al. [59] developed a two-step DNA hybridization assay with TGF (Figure 5). In the first step, ssDNA targets were spatially focused by TGF within a capillary, then peptide nucleic acid (PNA) was transported to the focused DNA by the bulk flow and react with the focused DNA. In the second assay, the PNA/DNA duplexes was first focused with TGF at the cold side of temperature gradient, then as the focused band moved to higher temperature by the flow, the duplexes thermally denatured, and the melting point was identified by a decrease in the intensity of band. The TGF for microfluidic DNA assays has three significant advantages: firstly, targets can be preconcentrated before an assay; secondly, targets can be focused at a stationary point, which facilitates the reaction of targets with probes; thirdly, the target-probe binding partners can be concentrated and spatially separated for sensitive detection. Then the same group [60] further combined micellar electrokinetic chromatography (MEKC) with TGF to concentrate and separate neutral and ionic hydrophobic analytes. This method, which is called micellar affinity gradient focusing (MAGF), is based on a combination of the analytes' electrophoretic mobility and affinity for their partitioning into an ionic micelle phase. A concentration enrichment of 27-fold for anthracene was achieved within 30 s of performing MAGF. After that, they also demonstrated concentration and separation of chiral compounds by TGF [61]. Different enantiomers of an analyte were focused by TGF at different positions along a microchannel or capillary. Such chirality-induced separations are due to the addition of a chiral selector to the buffer. The chiral selector interacts preferentially with one enantiomer, which shifts its focusing location so that it is separated from the other enantiomer. More than 1000-fold concentration enhancement was reported with the use of chiral TGF. In comparison with capillary electrophoresis, this chiral TGF can achieve a high-resolution separation in much shorter microchannels, and thus is more inherently suitable to be integrated into microfluidic devices for chiral analyses of drugs. However, further efforts should be made to identify low-pH TGF buffers because chiral separation of many drug compounds (such as basic pharmaceuticals) is only feasible at low pH.

One drawback of TGF is the limited peak capacity, and only few analyte peaks (~2–3) can be focused and separated at one time. To circumvent such drawback, Hoebel et al. [62] reported a modified version of the TGF in which the bulk flow rate changes over time. This strategy allows a large number of analytes to be focused, transported to a fixed detection point and washed to the waste in a sequential order. The authors termed this technique the scanning TGF, which enables a more controllable analysis since the scanning time and scanning rate can be actively controlled. More significantly, scanning TGF can be done in simple, short, straight microchannels with no injection structures, which can easily reduce the size of microfluidic device.

Munson et al. [63] proposed another type of TGF to improve concentration performance. They implemented the TGF with a low conductivity sample buffer and a (relatively) high conductivity separation buffer, field-amplified sample stacking (FASS) also plays roles in sample enrichment in addition to the normal TGF mechanism. This leads to an improvement of normal TGF concentration. The concentration factor for Oregon Green 488 with the modified method was 36-fold higher than the normal TGF. Munson et al. [64] also found that the counterflow necessary for TGF can be used to exclude lower mobility ions, such as serum proteins, when concentrating the higher mobility ions, such as small molecular weight fluorophores. They then further used the counterflow TGF combined with field-amplified sample injection to do the aptamer-based protein assays [65].

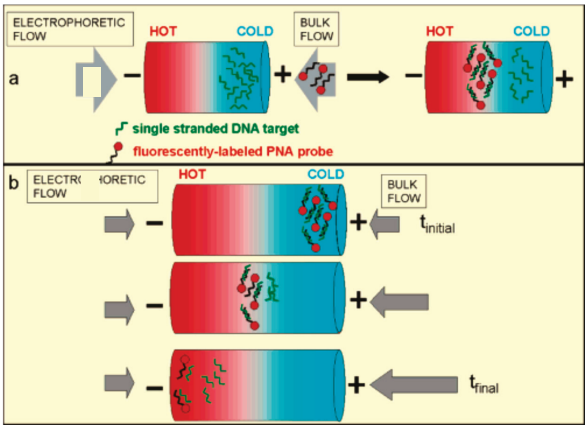

Figure 5. Principle of the two-step temperature gradient focusing (TGF) assays. (**a**) The first-step assay is stationary, and the ssDNA targets are first focused with TGF and then the PNA probe is introduced to the focused DNA with the bulk flow. (**b**) The second-step assay is dynamic. The DNA/PNA hybrid is first focused with TGF to the cold side and then the bulk flow is adjusted to move the analyte against the temperature gradient so that its melting temperature can be determined by observation of the change of fluorescent intensity with temperature. Reprint from Ref. [59].

Normally, the analyte concentration is much lower than buffer ion concentrations. However, when the analyte is concentrated to a significantly high concentration or a low-concentration buffer is used, the analyte concentration cannot be neglected. The nonlinear interactions between analytes and buffer ions can lead to peak shifting and distortion, thereby compromising the detectability and resolution. Lin et al. [66] examined the finite sample effect to elucidate the nonlinear sample-buffer interactions in TGF with theory, simulation and experiment. They derived a generalized Kohlrausch regulating function (KRF) for systems in which electrophoretic mobilities are varying spatially. This generalized KRF greatly simplifies the analysis to a single equation which describes the sample concentration evolution. The peak distortion phenomenon can be predicted by the modified equation, which is consistent with their simulations and experiments.

Dispersion is detrimental to resolution in most focusing techniques, and a clear understanding of dispersion in TGF helps to optimize the technique. Huber and Santiago [67] developed an 1-D model for dispersion in TGF with experimental verification. Their 1-D convection-diffusion equation includes an effective dispersion coefficient for TGF. Dispersion phenomenon can be well explained at low Peclet numbers and relatively low applied electric fields. However, at higher electric field strengths, Joule heating becomes significant and causes spanwise temperature gradients. In this situation, Taylor dispersion analysis fails and ballistic dispersion dominates. Huber and Santiago [68] modified the dispersion model to take into account both molecular diffusion and advective dispersion across all dispersion regimes, from pure diffusion to Taylor dispersion to pure advection. The model was validated by the initial decrease and subsequent increase in peak widths with the increment of electric field strength during the TGF experiments.

Becker et al. [69] applied the TGF to free-flow electrophoresis in microfluidic devices to achieve additional focusing, but only a focusing factor of two fold was obtained for proteins. However, the temperature gradient here is perpendicular to the flow direction which is different from previous reported TGF.

TGF is also a technique for concentration and separation of a mixture of analytes simultaneously. However, one major drawback prevents it from being integrated to portable microfluidic devices. In most studies using TGF, the required temperature gradient is induced by external heating/cooling

units, such as electric heating/cooling or water bath. Furthermore, materials with high thermal conductivity (copper blocks) are normally required to be fixed to the capillary device for setting up the temperature gradient. These heating/cooling units as well as copper blocks are usually quite bulky, which makes the device very bulky and thus unsuitable for portable applications. In addition, the use of external heating and cooling equipment requires a significant amount of energy.

Joule heating describes the conversion of electric energy into heat when applying an electric field across finitely conductive media such as electrolyte solutions. In capillary electrophoresis, the presence of such heat will increase the buffer temperature and lead to temperature gradients along both radial and axial directions in the buffer solution, and eventually dissipate into surroundings through the capillary walls. The temperature-dependent buffer and solute properties, including dielectric permittivity, viscosity and diffusivity, would change because of the increasing buffer temperature and the induced temperature gradient. Eventually, the change in these properties would affect the electrophoretic transport of solutes and electroosmosis of buffer solution. In capillary electrophoretic separation, Joule heating usually causes negative effects, such as sample band dispersion or peak broadening, thereby dreading the separation efficiency and analysis resolution. In addition, substantial temperature increment may result in the decomposition of thermally labile samples and even the formation of vapor bubbles. However, Joule heating can be positively used under some circumstances, such as to control the thermal environments in microfluidic devices. Enhancement of heat transfer by Joule heating induced thermal convection was analytically examined using idealized thermal boundary conditions [70–72]. A normalized source term is introduced to represent the ratio of Joule heating to surface heat flux by Horiuchi et al. [73,74], in their thermal analysis of pure electroosmotic flows and mixed electroosmosis/pressure-driven flows. Studies of Joule heating effects were further extended to electroosmotic flow and mass species transport under steady-state and spatiotemporal conditions [75–77].

One constructive proposal is using Joule heating to induce temperature gradient required for TGF, in lieu of the conventional use of external heating/cooling equipment. The advantages include less power consumption, simple and compact design, and more portable device without need of bulky external heating units. Such idea was first demonstrated by Kim et al. [78] experimentally. The temperature gradient for TGF in their experiments is established by Joule heating effects coupled with the variable channel width. Much less power and energy per analysis is consumed for the Joule heating (0.08 W) compared to the external heating/cooling (6.4 W) to produce the similar temperature gradient focusing. A mixture of two sample analytes was concentrated and separated within 10 min. A quasi-1D numerical model was proposed by Sommer et al. [79] to describe the resulting temperature, velocity, and concentration profiles in the microchannel for Joule heating induced TGF. Their numerical results showed good agreement with the experimental data presented in their previous work [78]. The effects of varying channel geometries and adjusting the temperature of substrate on focusing performance were studied with the numerical model.

Tang and Yang [80] developed a 3D numerical model for describing the Joule heating induced TGF. The numerical model consists of a set of governing equations to describe the temperature gradient and concentration profiles. The thermophysical and electrical properties including the liquid dielectric constant, viscosity, electric conductivity and mobility are all temperature-dependent. The numerical simulations showed good agreement with the experimental results presented by Ross and Locascio [58]. Later, Yang's group invested tremendous effect in experiments to use TGF for analyte concentration. A microchannel with a sudden expansion was designed to produce temperature gradient for the TGF focusing of sample solute [81], and a systematic study showed that higher applied voltage, higher buffer concentration or larger channel width ratio can improve the TGF concentration. The technique was further improved with the use of AC/DC combined electric fields [82,83], see Figure 6. The proposed AC/DC combined field technique led to more than 2500-fold concentration enhancement of Fluorescein–Na solute, which is unprecedentedly high for the Joule heating induced TGF technique. Recently, the group also applied the AC/DC combined field driven

TGF to concentrate DNA, and a rapid concentration enhancement of DNA was achieved with 480 folds in 40 s [84].

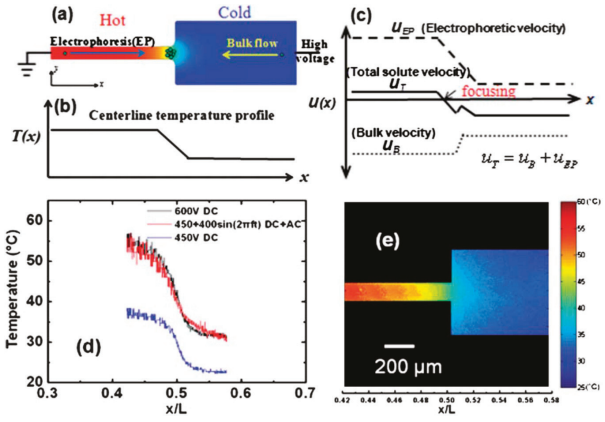

Figure 6. Principle of Joule heating induced TGF in a microfluidic sudden expansion under a combined AC/DC electric field. (**a**) Joule heating in the microfluidic expansion produces a temperature gradient around the junction region connecting narrow and wide channels; (**b**) temperature distribution along the centerline of microchannel (axial direction); (**c**) velocity profiles of sample solute along the centerline of microchannel due to pure electrophoresis (dashed line), pure bulk flow (dotted line), a combination of electrophoresis and bulk flow (solid line); (**d**) temperature distributions along the centerline of a 10 mm long polydimethylsiloxane (PDMS) microchannel for three different applied voltages: 450 V DC, 450 V DC + 400 sin(2*πft*) V AC and 600 V DC, measured with the rhodamine B thermometry; (**e**) temperature contour in the microfluidic expansion for an applied voltage of 450 V DC + 400 sin(2*pft*) V AC, measured in 180 mM Tris–borate buffer solution. Reprint from Ref. [82].

4. Other Microfluidic Concentration Methods

4.1. Electrokinetic Trapping (EKT)

Electrokinetic trapping (EKT) is a result of ion concentration polarization which is a universal phenomenon near ion selective membranes or microchannel-nanochannel junctions. Figure 7 illustrates a typical EKT sample concentration system by ion concentration polarization. The system consists of two microchannels that are connected by an ion selective membrane or nanochannel array. During operation, two ends of the lower channel are electrically grounded (GND), and two ends of the higher channel are provided with voltages, V_H and V_L, and V_H is maintained to be larger than V_L. Then, the electric fields inside the upper microchannel and the membrane, E_T and E_N, are induced, as is shown in the figure. Under the effect of E_N, only ions with polarity that is opposite to the polarity of membrane surface charge can penetrate through the membrane (In most cases, the membrane has negative surface charges, so only cations can pass through the membrane). Such selective transport of ions through membrane at equilibrium leads to the formation of an ion enrichment zone inside the lower microchannel while an ion depletion zone in the higher microchannel. This is characteristic of ion concentration polarization [85,86]. Since ion depletion zone allows no existence of charged species, the left boundary of ion depletion zone must prevent the passage of any charged species from the analyte zone to ion depletion zone. Therefore, the charged analyte from analyte zone would be trapped near the left boundary of the ion depletion zone (the unshaded zone inside the higher microchannel), and gradually the concentration of charged analyte is enhanced [85,87]. The stability of EKT is dependent on various factors such as pore size, charge density of the nanopores membrane, and counteracting flow which one has to take into account for fabricating a viable concentration device.

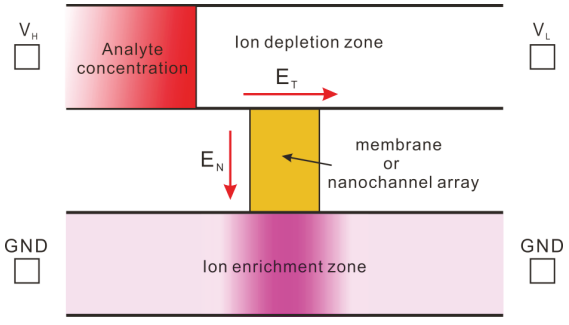

Figure 7. Schematic illustration of a typical electrokinetic trapping (EKT) concentration device. The device consists of two microchannels that are connected by a nanopore membrane or nanochannel array. Under the effect of applied voltages, ion concentration polarization is developed at the membrane-microchannel interfaces, giving rise to the development of an ion enrichment zone inside the lower channel and an ion depletion zone inside the higher channel. The ion depletion zone does not allow the passage of any charged species, thereby leading to the accumulation of charged analytes in front of the ion depletion zone.

EKT method was first reported by Dai et al. [88] who obtained a concentration enhancement of DNA more than 100 fold using an ion-selective membrane. Hahn et al. [89] developed a field-amplified EKT by using poly(ethylene terephthalate) (PET) membranes. The technique was shown to be able to concentrate DNA molecules from a very large volume. Their findings suggest that the field-amplified EKT performs much better than conventional EKT, and also the increasing pore size of membrane has a negative impact on analyte concentration.

Wang et al. [90] improved the EKT technique to achieve a million-fold concentration enhancement of proteins and peptides within several hours with a nanofluidic filter. The nanofluidic filter functions as an ion-selective membrane to generate an ion-depletion region, which was used to trap and concentrate biomolecules. The nanofluidic filter in the device is one single nanochannel with well-defined dimensions (40 nm in depth), which was fabricated with standard soft lithography and deep reactive ion etching on silicon wafers. Unlike membranes, nanofluidic channels do not swell or shrink in response to the change of ionic strength, temperature, or other environmental conditions. This makes the device more controllable than the use of ion-selective membrane. Nevertheless, nanochannels require the use of sophisticated clean room fabrication techniques, and thus are more expensive than commercially-available membranes. Wang and Han [91] utilized the nanochannel-based EKT as a preconcentration technique to enhance immunoassay detection sensitivity and binding kinetics. Their EKT devices have multiple well-defined nanochannels to induced ion depletion zone. With 30 min preconcentration, more than 500-fold enhancement of immunoassay sensitivity was obtained.

For a more systematic review of the EKT technique, we recommend the works [85,87,92]. Here we would only review the most recent development of the technique. Instead of using the conventional two-channel design, Ko et al. [93] simplified the device design of EKT to a single channel. The robustness of EKT was demonstrated with various material combinations such as polydimethylsiloxane (PDMS) channel-glass substrate and silicon channel-PDMS substrate. Because of excellent biocompatibility of PDMS, there are increasing uses of PDMS as channel materials for EKT concentration of biomolecules [93–98]. Recently, paper-based channels were also used in the EKT concentration device [99,100]. Paper-based materials would make the device more disposable and cheaper. Apart from the channel material, the membrane material is also important for EKT device, since it determines the ion concentration polarization that is essential for concentrating analytes. Recent development focuses on the use of Nafion membrane [93–100]. Such a trend is mainly due to

two reasons: the fabrication process of Nafion membrane EKT device is simple and easy; the surface charge density of Nafion membrane is significantly higher than that of bare silicon nanochannels or other membranes, and much higher concentration factors could be achieved. Further improvement in fabrication of EKT device was reported by Phan et al. [101] who developed a robust method using an off-the-shelf Nafion membrane. It was demonstrated that EKT device fabricated with the off-the-shelf Nafion membrane led to a stronger ion-concentration-polarization repulsion force than that fabricated with Nafion resin for the same channel dimension and input parameters. The new device thus could greatly enhance the separation efficiency. In addition, EKT device with the off-the-shelf Nafion membrane has better mechanical stability and thus a longer lifetime compared to the existing method.

4.2. Dielectrophoretic Trapping (DEPT)

When electrically polarizable particles/macromolecules are subject to in a nonuniform electric field, the particles experience dielectrophoretic (DEP) force [102], which can be used to trap the particles. Asbury and van den Engh [103] showed the concentration of DNA in nonuniform AC electric fields by the DEP force. Their design consists of an array of coplanar electrodes which are energized with AC electric field. The electric field is extremely condensed near the edges of electrodes, and hence DNA molecules tend to move to the edges of electrodes because of positive DEP force. More DNA molecules are trapped over the edges of electrodes, leading to the enhancement of DNA concentration. The dielectrophoretic trapping (DEPT) mechanism in this case is graphically illustrated in Figure 8. Application of a voltage between two coplanar electrodes generates an electric field which is most condensed near the edges of electrodes. Particles experiencing positive DEP force move from the region of low electric field strength to the region of high electric field strength. Similar electrode design was also used to concentrate listeria cells [104]. To make DEPT more affordable and commonplace, Park et al. [105] directly used the interdigitated electrodes on a printed circuit board (PCB) for DEPT of HeLa cells and polystyrene particles. Their method does not requires use of sophisticated microfabrication processes, and greatly reduces the cost of device fabrication. More significantly, well-established processing methods in PCB industry allow mass production of their DEPT device. DEPT uses the dielectrophoretic force to collect particles on electrodes. However, the dielectrophoretic force is only present in the very proximity of electrodes. Therefore, DEPT is only able to capture particles that are very close to electrodes, and the concentration enhancement of particles is limited. To overcome such limitation, various micromixer configurations, including the slanted groove, staggered herringbone, and herringbone mixers were proposed to circulate the sample, increasing the probability for the particles to reach the electrodes for trapping [106,107].

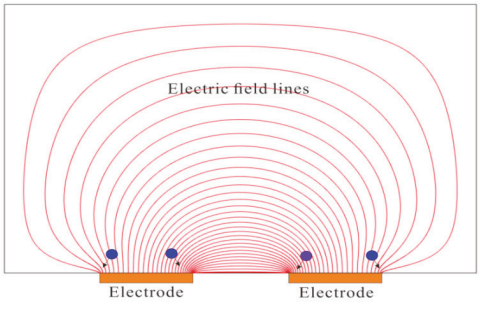

Figure 8. Schematics of dielectrophoretic (DEP) trapping of particles over edges of coplanar electrodes. The density of electric field lines determines the electric field strength, and it is clear that the electric field strength is the highest over the edges of electrodes. Under the effect of positive DEP force, particles would move from the region of low electric field strength (center of electrode) to the region of high electric field strength (edges of electrode).

Du et al. [108] designed a quadrupole electrode platform to induce DNA molecules focusing with the collaborative effects of long-range AC electroosmotic flow and short-range DEP force. The AC electroosmotic flow convects DNA molecules to the regions near electrodes, and then DEP force further traps these molecules towards electrodes. Several tens of enhancement for pico-molarity DNA solutions were achieved without any continuous sample supply. They further proposed a double half-quadrupole electrode system to induce a head-on AC electroosmotic streaming for focusing and trapping DNA molecules. The observed phenomenon is a combined result of the formation of two prefocused DNA jets by AC electroosmotic streaming, dipole-induced attraction between focused DNA molecules, and dielectrophoretic trap near electrodes [109]. In addition to DNA molecules, they also employed the same design for submicrometer particles. The results showed that the trapping of particles is strongly dependent on the AC frequency and particle size. For large particles (e.g., 0.92 μm) and high frequency (20 MHz), DEP plays a significant role, while for small particles (e.g., 0.1 μm) and low frequency (1 kHz), AC electroosmosis plays a more important role than DEP.

With numerical modelling, Loucaides et al. [110] investigated the effect of initial particle concentration on the DEP trapping in an array of coplanar parallel electrodes. The initial concentration was found to have significant impact on the initial rate and steady state of particle collection and the study also showed that AC electroosmosis enhances both of them. They further modelled the trapping of DNA in a same electrode design with consideration of steric effects in the suspension motion [111]. The results from the steric model are more realistic than those from the non-steric model.

The creation of nonuniform electric fields is essential for DEPT. Most studies in the literature, such as those reviewed above, create nonuniform electric fields by specific arrangement of electrodes. Such method is most widely used, but usually requires complicated electrode design and also faces the problem of electrode fouling and degradation. An alternative way of producing nonuniform electric fields is by embedded obstacles such as a specifically arranged array of insulators. Insulators suffer much less from fouling and degradation. In addition, insulators made of polymer-based materials can be mass produced with standard microfabrication processes, giving rise to cheap and large-volume devices. Such concept of insulator-based DEPT was first presented by Cummings and Singh [112] who fabricated a microfluidic device with an array of insulating pillars in a microchannel. One electrode in the microchannel inlet reservoir and the other electrode in the microchannel outlet reservoir are supplied with a DC voltage to set up an electric field along the microchannel. Then nonuniform electric field strength is induced due to the geometric confinement between insulating pillars. The DEPT of 200 nm fluorescent polystyrene particles were successfully demonstrated, as is shown in Figure 9. Chou et al. [113] demonstrated insulator-based DEPT of DNA molecules using AC electric fields. Lapizco-Encinas et al. [114] investigated the selective DEPT of polystyrene particles, live *E. coli*, and dead *E. coli* in an array of insulating micropillars under DC electric fields. The same group reported the selective DEPT of four different types of live bacterial cells, including the Gram-negative Escherichia coli and the Gram-positive Bacillus subtilis, Bacillus cereus and Bacillus megaterium [115]. Mela et al. [116] elaborated the effect of zeta potential of device material on insulator-based DEPT, and found that Zeonor 1060R substrates require lower trapping voltage thresholds as compared to glass substrates. This is due to the fact that the Zeonor substrate has a zeta potential that is lower than the glass substrate under a same physicochemical condition.

In addition to using arrays of insulating pillars, other types of configurations were also proposed to induce nonuniform electric fields required for insulator-based DEPT. Chen et al. [117] reported a rapid concentration of nanoparticles with DEPT induced by DC electric fields. The nonuniform electric field was produced by a series of PDMS microchannels with a tree-like arrangement. Lewpiriyawong et al. [118] utilized a microfluidic constriction to generate nonuniform electric fields for insulator-based DEPT of particles and cells. Zhao et al. [119] recently proposed a novel design of using asymmetric orifices on opposite channel walls to generate nonuniform electric fields. Such design was shown to greatly reduce the magnitude of voltages required for insulator-based DEPT.

Hawkins and Kirby [120] theoretically investigated the electrothermal flow in polymeric, insulator-based DEPT systems with DC-offset, AC electric fields at finite thermal Peclet number. It was shown that electrothermal effects always enhance dielectrophoretic trapping of particles. Sridharan et al. [121] presented the first experimental study of electrothermal effects on insulator-based DEPT, and the results are found in line with the previous theoretical predictions.

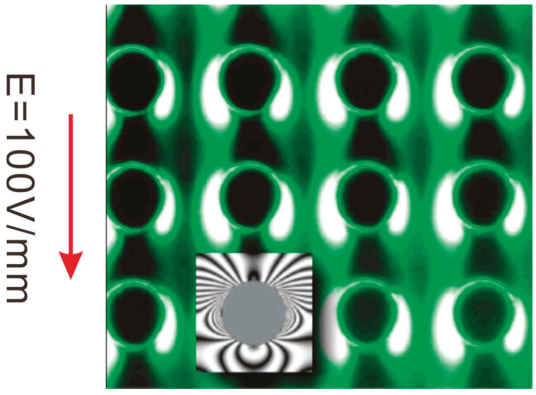

Figure 9. Dielectrophoretic trapping (DEPT) of fluorescent particles by an array of insulating pillars. The pillars are 33 μm in diameter and with a center-to-center separation of 63 μm. The inset picture shows the isopotential lines around one pillar from numerical simulation. Dielectrophoretic traps are defined by regions with isopotential lines bending back onto a pillar surface. Reprint from [112].

4.3. Immunocapture Based Trapping (ICBT)

Immunocapture is a technique for increasing the concentration of biological cells. It is analogous to affinity chromatography in principle. The central idea of immunocapture is that cells are captured by a specific interaction between cell surface and substrate [122]. Take immunecapture of a circulating tumor cell (CTC) as an example (Figure 10), one type of cell surface marker (e.g., protein or receptor) extrudes from the cell membrane. An antibody or aptamer, which is chemically linked to substrate surface by the so-called immunochemistry, specifically interacts *only* with that type of cell surface marker. This process leads to immobilization of cells on the substrate, and thus the concentration enhancement of CTCs.

Immunocapture-based trapping (ICBT) can collect CTCs directly from whole blood samples. This means that blood sample does not need any pretreatment, thereby simplifying the procedure greatly. ICBT has two modes of operation: affinity-based or depletion-based cell concentration. Affinity-based concentration accumulates CTCs from the whole blood sample [123–125], while depletion-based concentration [126–128] removes undesired components of blood, and only CTCs are left behind. Generally, ICBT is an efficient method of CTC isolation, on condition that cancer cells have a specific type of surface marker, and there is also an antibody/aptamer which only binds with that type of surface marker. In addition to concentrating CTCs, ICBT was also used for preconcentration of proteins and HIV subtypes in biological samples to facilitate subsequent detection [129,130].

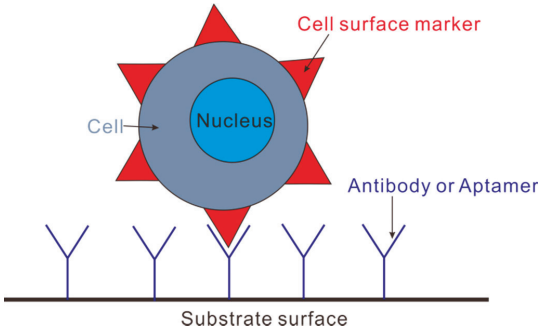

Figure 10. Schematic principle of immunocapture of a circulation tumor cell (CTC). An antibody or aptamer chemically immobilized on the substrate surface can be specifically linked with cell surface markers extruding from the cell membrane.

In practical implementation, ICBT concentration has several typical device designs: micropillar arrays [123,125,131], micro-/nanostructured surfaces [132–134], micromixers [135,136], and microbeads [137–141]. Micropillar arrays use geometric obstacles to increase the surface area to volume ratio, thereby enhancing the frequency of CTC-antibody interaction and then the resultant cell capture. Micro-/Nanostructured surfaces use micro/nano fabrication technology to create roughness on flat substrates; this equivalently increases the surface area to volume ratio and thus the probability of cell-antibody collision and the corresponding cell capture. Micromixers use microfabricated ridges to create flow circulations in the device. CTCs in the circulating flow interact with the walls of the device which are the coated with a CTC-specific antibody or aptamer for cell capturing. Microbeads are usually magnetic and coated with an antibody which tends to bind with a specific cell surface marker. When placed into blood samples, microbeads bind specifically with CTCs to result in cell capture. Finally, the application of a magnetic field across microbeads releases CTCs for later analysis. Among these four device designs, microbeads are the most promising for clinical use because the only ICBT device approved by Food and Drug Administration (FDA) at present (the Veridex CellSearch) uses microbeads [142–144].

The ICBT technique has two major drawbacks [122]: (i) A good immunocapture device requires a cell surface marker which has a uniform expression for all CTCs and an antibody or aptamer which is 100% specific to the CTC, namely without any non-specific cell binding. However, the cell surface marker expression in practice varies from CTC to CTC, and the target antibody can be too specific (losing the chance of binding with altered markers), or not specific enough (producing more non-specific binding). (ii) For effective immunocapture, one has to know a priori the cell surface markers expressed by CTCs. Yet, this is rarely the case in practice. For example, a pan-cancer CTC cell surface marker has been shown to be downregulated by some cancer cells in order to elude detection by the immune system, and to enhance their mobility in the body. The risk of missing entire populations of CTCs that do not express the target cell surface marker is problematic when attempting to identify the most dangerous CTCs.

Some recent efforts have been made to improve the performance of classic immunocapture. In conjunction with dielectrophoresis, immunocapture was shown to be able to maximize the capture of target rare cells, while minimizing the capture of contaminating cells [104,145,146]. Another important development by Kirby and his colleagues is the so-called geometrically enhanced differential immunocapture (GEDI) microfluidic devices that capture rare cells from blood or cell suspensions [125,131,147,148]. Figure 11 decribes the principle of the GEDI capture in detail. GEDI combines the cancer-specific antibody immunocapture with micropillar array to enhance the probability of the collision of larger cells (e.g., CTCs) with the substrate, while minimize the probability

of the collision of smaller contaminating cells (e.g., leukocytes) with the substrate. The GEDI platform has been successfully used by the authors for concentrating pancreatic cancer cells [131], prostate cancer cells [148,149], breast and gastric cancer cells [150]. Very recently, Sarioglu et al. [151] developed a microfluidic device (the cluster-chip) to capture CTC clusters instead of single CTCs from unpretreated blood without the need of tumor-specific markers. CTC clusters were physically captured by geometric obstructions with low-shear liquid flow. For 30 to 40 percent of patients with metastatic breast or prostate cancer or with melanoma, the device was able to identify CTC clusters. The ability to capture CTC clusters is much needed for subsequent characterization of their biological properties and roles in metastasis.

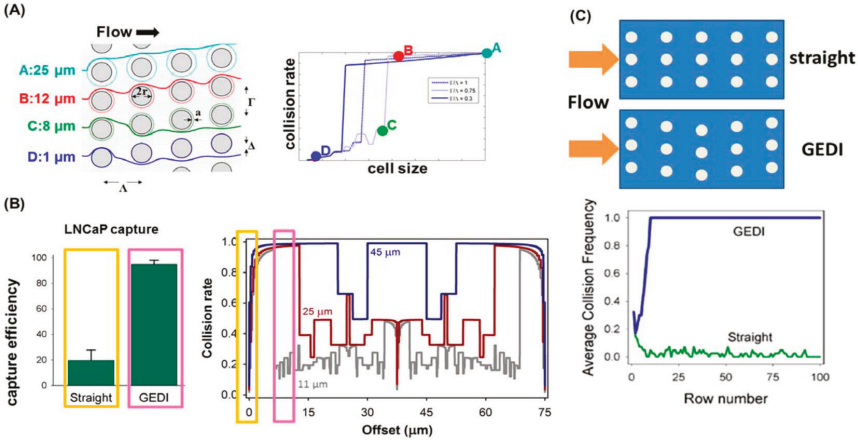

Figure 11. A typical geometrically enhanced differential immunocapture (GEDI) microfluidic device for cell capture. (**A**) Left: Top view of micropillar array. Δ is pillar offset; Λ is pillar separation in the direction of bulk flow; Γ is the pillar separation in the direction perpendicular to bulk flow; 2*r* is the pillar diameter. Light gray lines represent the fluid flow streamlines. Color lines denote trajectories of cells of various sizes. Right: The cell-wall collision rate varies with the cell size and the offset parameter of the array; GEDI prefers size-dependent collision rates introduced by a nonzero offset parameter. The solid lines are the results predicted for the flow geometry at left; four colored dots are corresponding results of four specific cell sizes. The dotted and dashed lines are results predicted for other two offset parameters; (**B**) the comparison of measured LNCaP capture efficiency on J591-functionalized devices for GEDI (7-mm offset) and straight (no offset) geometries (both geometries have the same surface-area-to-volume ratio). Right figure shows the simulated collision rates in these geometries. Straight arrays or arrays with small offsets (yellow boxes) induce low capture efficiency (left) and size independence (right). In contrast, arrays with large offsets (magenta boxes) induce high capture efficiency (left) and size dependence (right); (**C**) the collision frequency in straight (GEDI) array decreases (increases) as the sample flows through the device. Reprint from Ref. [148].

4.4. Magnetic Beads Assisted Trapping (MBAT)

The magnetic beads assisted trapping (MBAT) relies on the magnetic force to trap cells. Figure 12 illustrates two classical systems of MBAT. In the column-based system, cells labeled with superparamagnetic nanobeads (in the order of 100 nm) are retained in the column because of magnetic trapping force, and unlabeled cells are eluted. The removal of external magnetic field would release the labeled cells [152]. Such system has been commercialized for sorting cells (such as Manual MACS by Miltenyi Biotec) with high magnetic field gradient in a column. However, the throughput as well as efficiency of isolating rare cells using such commercial system is usually low because of manual operation and limited magnetic field strength [153]. In the MagSweeper system, magnetic rods covered

with plastics are used to magnetically attract target cells conjugated with magnetic nanobeads, and later trapped cells are released under the effect of external magnetic field [154]. Such system is new and only reported recently, and it can use multiple rods to perform parallel analyses, while the trapping efficiency could be compromised by the reduction of magnetic field strength due to plastic covers. In both MBAT systems, preparation of cell sample is similar. There are typically three steps required to labelling cells with nanobeads which are usually superparamagnetic and biotinylated [152]. The cells are firstly labelled with biotinylated antibody, and secondly dyed with a fluorescent avidin conjugate, e.g., fluorescein-steptavidin. Finally, the biotinylated superparamagnetic nanobeads bind with the avidin on the cell surface. Thus, antibody binding cells finally have a fluorescent and a magnetic label. The choice of nanobeads for cell labeling is critical for MBAT, and there has been a wealth of information regarding their preparation, characterization, functionalization and current development, as are reviewed in Refs. [155,156].

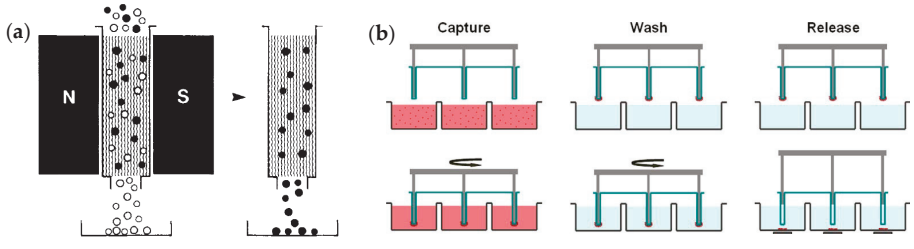

Figure 12. Two typical systems of magnetic beads assisted trapping and releasing of cells. (**a**) Column-based system. Left: Under the effect of external magnetic field, cells labeled with superparamagnetic nanobeads (black dots) are trapped on the matrix of column, while unlabeled cells (white dots) can go through the column. Right: The trapped cells can be released as soon as the magnetic field is removed. "N" and "S" denotes the north pole and south pole of the magnet, respectively; (**b**) MagSweeper system. Blood samples in the capture wells are labeled with magnetic nanobeads. The magnetic rods covered with a thin layer of plastics sweep through the wells in concentric circular loops to magnetically attract target cells labelled with nanobeads. Loosely attracted unwanted cells are washed off from the magnetic rods with them moving in circular loops. Finally, the magnetic rods are immersed into a new buffer solution and disengage from the plastic covers. Cells labeled with magnetic nanobeads are released under the effect of magnetic fields setup by magnets located under the wells. Figure (**a**) is reprinted from [152], Figure (**b**) is reprinted from [154].

MBAT has been advancing quite fast in recent years and playing important roles in the study of CTCs. However, the traditional MBAT devices are incapable of meeting the requirements for sophisticated molecular studies. Additionally, the traditional MBAT devices are quite bulky and thus unsuitable for point-of-care applications, and also prone to cross contamination. With the rapid development of micro- and nanofabrication techniques, microfluidics-based MBAT emerges as a new technology to provide more precise and flexible control of the magnetic and hydrodynamic forces experienced by the target cells to improve cell enrichment. Similar to the traditional MBAT system, a microfluidics-based system uses an external magnetic field to capture target cells which are labelled with magnetic nanobeads. Depending on the way in which the target cells are enriched, microfluidics-based MBAT has two working modes [153]: an retaining mode which magnetically traps CTCs on the substrate [157], and a deflecting mode which magnetically drives CTCs to form discretized concentrated streams [158,159].

There have been continuous efforts to improve MBAT. Luo et al. [160] developed a new microfluidic system with integrated micromixers and micropumps to achieve "negative selection and enrichment" of CTCs. Under an external magnetic field, leukocytes labelled with anti-human CD45 antibodies-coated magnetic beads were removed, and target cells left behind were effectively enriched.

Wang et al. [161] reported the use of a herringbone microstructure in a microfluidic MBAT chip. The introduction of a herringbone microstructure produces two favorable effects: (i) the herringbone microstructure induces vortices which bring CTCs close to herringbone grooves. This increases the possibility of trapping CTCs into herringbone grooves by the magnetic force; (ii) Magnetically trapped CTCs in the herringbone grooves experience significantly smaller shear stress compared to that in the microchannel. This would prevent damaging of CTCs.

4.5. Thermophoretic Trapping (TPT)

Thermophoresis describes the movement of molecules or particles in response to a temperature gradient. This phenomenon can be used to achieve the enhancement of analyte concentration. Braun and Libchaber [162] developed the thermophoretic trapping (TPT) technique which utilizes a synergistic effect of thermophoretic depletion and thermal convection to concentrate DNA. The mechanism behind this technique is depicted in Figure 13 which shows the concentration of DNA with laser-induced heating inside a chamber with thickness of 50 μm. At beginning, the dominant thermophoretic force quickly induces a depletion of DNA from the heating spot (Figure 13b), and then thermal convection counteracting the depletion brings DNA molecules towards the heating spot and causes the concentration of DNA (Figure 13c). The concentration of DNA around the hot spot is a result of the interplay between thermophoresis and thermal convection, as sketched in Figure 13d. These combined effects create a stagnant zone on the lower surface of the chamber near the laser heating spot (the gray area in Figure 13d), where accumulation of DNA occurs. More than 1000-fold enhancement of DNA concentration was achieved within 180 s. The measured temperature distribution around the hot spot is shown in Figure 13e, and the ring-shaped concentration zone can be explained by the ring-shaped temperature gradient which triggers the TPT process.

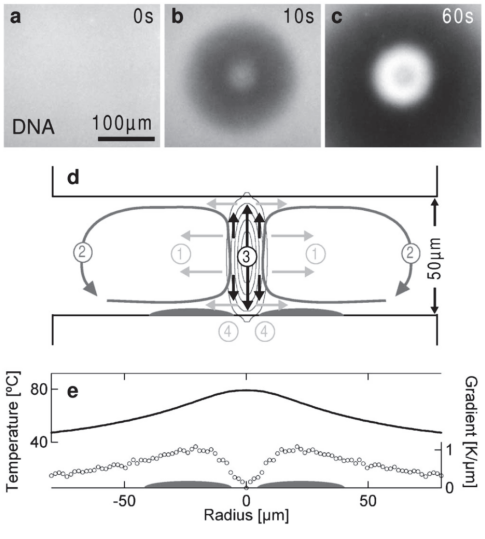

Figure 13. Mechanism of the thermophoretic trapping (TPT) technique for concentrating DNA. (**a**) Initial DNA distribution without any heating; (**b**) fast DNA depletion due to thermophoresis; (**c**) DNA concentration due to the combined effect of thermophoresis and thermal convection; (**d**) the TPT is a synergistic effect of lateral thermophoresis (1)/(4), axial thermophoresis (3) and convection (2); (**e**) the measured lateral temperature distribution around the heating spot. Reprint from Ref. [162].

The same group later showed that thermophoretic characteristics can be adjusted by controlling the background temperature. It was shown that the DNA has a thermophoretic concentration at 3 °C, but a thermophoretic depletion at room temperature [163]. They also utilized the TPT to greatly enhance the efficiency of polymerase chain reaction (PCR) process for DNA replication [164].

The development of TPT induces some variations of the technique. Instead of using the concurrent thermally-induced convection flow, Duhr and Braun [165] applied an external pressured driven flow to counteract thermophoresis. The technique achieves an efficient concentration enhancement (800-fold) of DNA molecules. In comparison with the original TPT technique, this modified TPT has a well-controlled microfluidic condition. Other than the conventionally-used laser induced heating, Serey et al. explored the use of a photonic crystal resonator to induce localized heating required for TPT [166]. Their experiment showed a similar effect of DNA concentration enhancement.

4.6. Other Electrokinetic Methods

There are some other methods of analyte concentration which cannot be classified into the above reviewed categories. Khandurina et al. reported [167] a microfabricated injection valve incorporating a porous membrane structure to concentrate DNA samples. The porous membrane was fabricated in the microchannel with two channels separated from each other and connected by a thin porous silicate layer. Large molecules, such as DNA, accumulate before the membrane due to their hindered transport through the membrane, and the concentration enhancement of 2 orders of magnitude can be achieved within 3 min. Later, the same technique was also used to preconcentrate proteins [168]. Similarly, Kuo et al. [169] developed a micro-CE chip for DNA preconcentration and separation using a normally closed valve which can be activated by pneumatic suction. The negatively charged DNA was blocked and trapped by a nanoscale channel formed by the normally closed valve with anionic surface charges. An approximate 41 times concentration enhancement was obtained after 100 s. However, the normally closed valve brings complexity in design and fabrication of microchips, and also such device is prone to mechanical failure.

Kuo et al. [170] developed an on-column concentration and separation of dsDNA using gradient capillary electrophoresis. To concentration DNA prior to separation, they introduced concentration gradient of polymers along the capillary, such as PEO (polyethylene oxide) and EtBr (ethidium bromide). The concentration of DNA is mainly due to the sieving and the change in viscosity as DNA migrates from sample zone to the polymer solution. Several ten-fold sensitivity improvements were demonstrated in the separation of DNA mixtures. Park and Swerdlow [171] also developed an on-line DNA sample concentration method for enhancing the sensitivity of capillary electrophoresis. The method allows an effective capture of DNA fragments from a flowing sample stream which is appropriately opposed by a strong electric field. The captured DNA fragments form a concentrated band by simply turning off the electric field. In addition, an even more concentrated band of DNA can be recovered when reversing the polarity of the electric field during the elution process.

Wanunu et al. [172] studied the focusing of DNA into solid-sate nanoscale pores with a salt gradient (Figure 14). More DNA molecules are captured when ionic gradients are established across the pore and the capture rate is increased as increasing the salt gradients (Figure 14a,b). The nanopore is negatively charged, and thus only cations can pass through the nanopore from *trans* to *cis*. Such selective transport of cations leads to the formation of a zone on the *cis* side (reddish area in Figure 14c), which mainly contains cations. The cation concentration inside this zone is decreasing as the distance is away from the pore, which induces an enhancement of the local electric field around the pore (Figure 14d). Therefore, more molecules are electrophoretically focused into the pore, raising the possibility of using nanopores to analyze unamplified DNA samples. High throughput detection of picomolar DNA concentrations was demonstrated with a 20-fold salt gradient. Instead of using a salt gradient, Paik et al. [173] exploited the use of electrically-gated nanopores to achieve a flexible control of DNA focusing. It was demonstrated that the DNA capture rate could be adjusted over 3 orders

of magnitude with gate voltage less than 1 V. Such efficient control of DNA focusing arises from the appropriate balance between electrophoresis and electroosmosis.

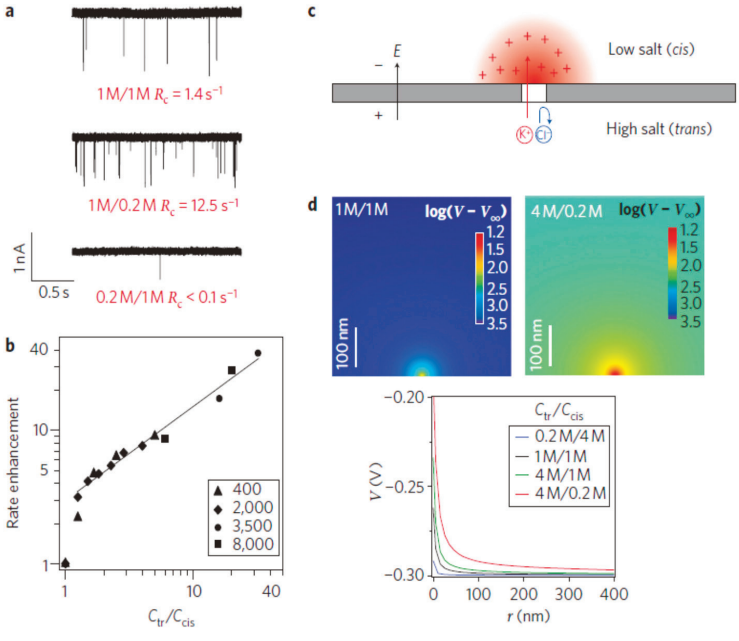

Figure 14. Intensified DNA molecules focusing into a solid-sate 3.5-nm nanoscale pore by salt gradients. (**a**) Measured continuous traces with 400 bp DNA for different KCl concentration (C_{tr}/C_{cis}) ratios. R_c value in each case is the average capture rate; (**b**) enhancement of DNA capture rate with C_{tr}/C_{cis} for four different DNA lengths; (**c**) schematic showing of the selective transport of cations (K^+) from *trans* to *cis* for the case of $C_{tr}/C_{cis} > 1$, leading to a local accumulation of cations near the pore on the *cis* side (reddish area), which enhances capture rate; (**d**) numerical electric potential distributions around the pore at the *cis* side, for both symmetric (top left) and asymmetric (top right) KCl concentrations. The bottom center of each image is where the pore is located. Reprint from Ref. [172].

Dhopeshwarkar et al. [174] developed an electrokinetic focusing method using bipolar electrode (BPE) in a microchannel, where the electrophoretic velocity of anions is balanced by the electroosmotic velocity due to the control of local electric filed by BPE. Theoretical description and numerical simulations were also reported to shed light on the complex local interplay among electrokinetics, hydrodynamics, and electrochemistry involved [175]. Perdue et al. [176] extended the method by using discontinuous BPEs to show that concentration enrichment is coincident with the onset of faradaic electrochemistry at the BPE. About 70-fold concentration enrichment was achieved within 160 s.

Dghighi and Li [177] proposed an electrokinetic method for concentrating DNA molecules in a straight microchannel with two closed ends. The concentration is a joint effect of electroosmotic flow, electrophoresis and the flow induced by back pressure. The concentration process and the transport of DNA molecules feature a flexible control by the manipulation of the voltages via three electrodes. 91-fold concentration enrichment can be obtained within 115 s. Separation of the focused DNA with different mobilities also can be realized while transporting them downstream along the microchannel.

5. Summary and Conclusions

Lab-on-a-chip can integrate various laboratory and analytical protocols ranging from mixing, pumping to concentration, separation and detection etc. into a single microchip. It is an emerging microfluidic technology which is believed to have the great potential to revolutionize chemical and biological analyses. However, Lab-on-a-chip devices normally suffer from low analysis sensitivity due to the inherently poor detection limits in microchannels. To improve the analysis sensitivity of lab-on-a-chip devices has prompted the need of on-chip preconcentration of analytes. A variety of microfluidic techniques have been developed for analytes concentration. This paper reviews these techniques and focuses on discussing their physical principles and advantages/disadvantages. The reviewed concentration techniques are categorized into three major groups according to the concentration mechanisms involved.

The first group of concentration techniques termed as stacking methods is based on the difference in analyte velocity within two different moving buffer zones when analytes migrate from a faster velocity zone into a slower velocity zone and so being concentrated. Among the sample stacking techniques, one widely used is the sweeping method, in which analytes are incorporated into the micelles when micelles in the running buffer penetrate the sample zone and their mobility is considerably decreased in the stacking zone. However, the sweeping method is useful only for small hydrophobic analytes with a high affinity to a mobile micellar phase. For the field amplified sample stacking (FASS), the change of velocity is produced by low- and high-conductivity buffers. The concentration could be fairly high with FASS, but multi buffers are required. Isotachophoresis (ITP) is a technique using variable ion mobility zones for sample focusing and separation. Both ITP and FASS commonly need relatively long channels to preconcentrate larger sample volumes. Moreover, in sample stacking processes, the concentration enhancement is limited by the magnitude of analyte velocity change ratio, and also it is not easy to control the concentrated samples due to their motion.

The second group of analyte concentration methods is termed as field gradient focusing methods, in which analytes are focused at a unique equilibrium point where analyte net velocity is zero. The concentration enhancement in focusing techniques is determined by the rate at which analytes are transported to the focusing zone and the duration of the application of the focusing field, allowing for higher concentration enhancement in comparison with the stacking methods. Isoelectric focusing (IEF) technique is frequently used for the concentration and separation of proteins. In IEF, analytes is focused at their respective isoelectric points along a pH gradient. IEF however has limited applications since it is only applicable to analytes that have an accessible isoelectric point. In addition, most proteins are weakly soluble at their isoelectric points, which severely limits the extent of protein focusing with IEF. Electric field gradient focusing (EFGF) technique utilizes electric field gradient to suppress the net analyte velocity at a point in a channel where analyte focusing is achieved. In EFGF, the electrophoretic velocity gradient is created by manipulating electric field in the channel through an arrangement of electrodes, which however involves complex design and fabrication processes. In the family of field gradient focusing methods, temperature gradient focusing (TGF) is relatively new. In TGF, the concentration of sample analytes is achieved by balancing the electrophoretic motion of analytes against the bulk flow of buffer solution. The electrophoretic velocity gradient is created by using a temperature gradient along the channel with an appropriate buffer. TGF allows the concentration and separation of charged analytes in simple microfluidic structures with relatively short microchannels. Furthermore, TGF does not involve multi-buffers, embedded electrodes, membranes or nanostructures. Specifically, Joule heating induced TGF which has compact structure design can achieve the possibly high concentration enhancement in a short time, making it well suited for the development of integrated microfluidic systems.

The third group of analyte concentration methods utilizes various trapping mechanisms, such as electrokinetic trapping, dielectrophoretic trapping, immunocapture based trapping, magnetic beads assisted trapping and thermophoretic trapping. Electrokinetic trapping relies on the force due to ion concentration polarization for trapping analyte particles, dielectrophoretic trapping

and thermophoretic trapping use dielectrophoretic force and thermophoretic force, respectively. Immunocapture based trapping utilizes the immunochemistry to immobilize analytes of interest on solid substrates. Magnetic beads assisted trapping uses magnetic force to trap the samples which are magnetized by adsorption of magnetic nanobeads. Usually, electrokinetic trapping performs much better than dielectrophoretic and thermophoretic trapping. Immunocapture based trapping and magnetic beads assisted trapping are specially used to concentrate biological cells, mostly CTCs. Some other emerging microfluidic concentration techniques are also briefly discussed.

Finally, here we provide a more quantitative comparison for the reviewed techniques. Figure 15 presents the concentration factor vs. concentration time for various microfluidic concentration techniques reviewed in the present work. The concentration factors in this figure correspond to the highest values documented in the literature. The concentration methods located on the bottom right of the figure suggests a better concentration performance, indicating a higher concentration factor achieved in a shorter time. This plot in combination with characteristics of each technique (such as application background, advantages and limitations) discussed above can be used to guide the choice of microfluidic concentration techniques for specific applications.

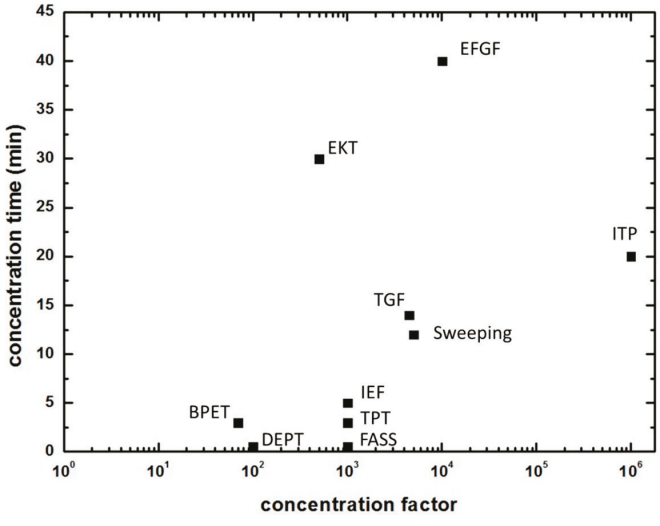

Figure 15. Concentration enhancement factor vs. concentration time for a variety of microfluidic sample concentration techniques. TGF, temperature gradient focusing (with Joule heating); IEF, Isoelectric focusing; EFGF, electric field gradient focusing; FASS, field amplified sample stacking; ITP, isotachophoresis; EKT, electrokinetic trapping; DEPT, dielectrophoretic trapping; TPT, thermophoretic trapping; BPET, bipolar electrode trapping.

Acknowledgments: The work was supported by Tier 1 Academic Research Grant (RG 83/15) from the Ministry of Education of Singapore. C.Z. is also supported by the "Top Young Talent Support Plan" from Xi'an Jiaotong University.

Author Contributions: C.Z. and C.Y. conceived the idea of this topical review; Z.G. prepared the preliminary draft of this review; C.Z. proposed the structure of the review and made substantial contributions to enrich the content of this review; C.Y. supervised the research.

Conflicts of Interest: The authors declare no conflict of interest.

References

1. Psaltis, D.; Quake, S.R.; Yang, C. Developing optofluidic technology through the fusion of microfluidics and optics. *Nature* **2006**, *442*, 381–386. [CrossRef] [PubMed]
2. Yager, P.; Edwards, T.; Fu, E.; Helton, K.; Nelson, K.; Tam, M.R.; Weigl, B.H. Microfluidic diagnostic technologies for global public health. *Nature* **2006**, *442*, 412–418. [CrossRef] [PubMed]
3. Whitesides, G.M. The origins and the future of microfluidics. *Nature* **2006**, *442*, 368–373. [CrossRef] [PubMed]
4. Dittrich, P.S.; Tachikawa, K.; Manz, A. Micro total analysis systems. Latest advancements and trends. *Anal. Chem.* **2006**, *78*, 3887–3908. [PubMed]
5. Scriba, G.K.E. Pharmaceutical and biomedical applications of chiral capillary electrophoresis and capillary electrochromatography: An update. *Electrophoresis* **2003**, *24*, 2409–2421. [CrossRef] [PubMed]
6. Verpoorte, E. Microfluidic chips for clinical and forensic analysis. *Electrophoresis* **2002**, *23*, 677–712. [CrossRef]
7. Crompton, T.R. *Preconcentration Techniques for Natural and Treated Waters: High Sensitivity Determination of Organic and Organometallic Compounds, Cations and Anions*; Taylor & Francis: Oxon, UK, 2002.
8. Pérez-Bendito, D.; Rubio, S. Chapter 5: Preconcentration of environmental samples. In *Comprehensive Analytical Chemistry: Environmental Analytical Chemistry*; Weber, S.G., Ed.; Elsevier: Amsterdam, The Netherlands, 1999; pp. 185–215.
9. Chirila, E.S.; Draghici, C.; Dobrinas, S. Sampling and sample pretreatment for enviromental analysis. In *Chemicals as Intentional and Accidental Global Environmental Threats*; Simeonov, L., Chirila, E., Eds.; Springer: Dordrecht, The Netherlands, 2006; pp. 7–28.
10. Marczenko, Z.; Balcerzak, M. Chapter 1—Separation and preconcentration of elements. In *Analytical Spectroscopy Library*; Zygmunt, M., Maria, B., Eds.; Elsevier: Amsterdam, The Netherlands, 2000; pp. 5–25.
11. Giakisikli, G.; Anthemidis, A.N. Magnetic materials as sorbents for metal/metalloid preconcentration and/or separation. A review. *Anal. Chim. Acta* **2013**, *789*, 1–16. [CrossRef] [PubMed]
12. Paulus, A.; Klockow, A. Detection of carbohydrates in capillary electrophoresis. *J. Chromatogr.* **1996**, *720*, 353–376. [CrossRef]
13. Breadmore, M.C.; Haddad, P.R. Approaches to enhancing the sensitivity of capillary electrophoresis methods for the determination of inorganic and small organic anions. *Electrophoresis* **2001**, *22*, 2464–2489. [CrossRef]
14. Malá, Z.; Křivánková, L.; Gebauer, P.; Boček, P. Contemporary sample stacking in CE: A sophisticated tool based on simple principles. *Electrophoresis* **2007**, *28*, 243–253. [CrossRef] [PubMed]
15. Quirino, J.P.; Terabe, S. Exceeding 5000-fold concentration of dilute analytes in micellar electrokinetic chromatography. *Science* **1998**, *282*, 465–468. [CrossRef] [PubMed]
16. Quirino, J.P.; Terabe, S. Sweeping of analyte zones in electrokinetic chromatography. *Anal. Chem.* **1999**, *71*, 1638–1644. [CrossRef]
17. Aranas, A.T.; Guidote, A.M.; Quirino, J.P. Sweeping and new on-line sample preconcentration techniques in capillary electrophoresis. *Anal. Bioanal. Chem.* **2009**, *394*, 175–185. [CrossRef] [PubMed]
18. Quirino, J.P.; Kim, J.-B.; Terabe, S. Sweeping: Concentration mechanism and applications to high-sensitivity analysis in capillary electrophoresis. *J. Chromatogr.* **2002**, *965*, 357–373. [CrossRef]
19. Kitagawa, F.; Otsuka, K. Recent applications of on-line sample preconcentration techniques in capillary electrophoresis. *J. Chromatogr.* **2014**, *1335*, 43–60. [CrossRef] [PubMed]
20. Quirino, J.P.; Terabe, S. Approaching a million-fold sensitivity increase in capillary electrophoresis with direct ultraviolet detection: Cation-selective exhaustive injection and sweeping. *Anal. Chem.* **2000**, *72*, 1023–1030. [CrossRef] [PubMed]
21. Burgi, D.S.; Chien, R.L. Optimization in sample stacking for high-performance capillary electrophoresis. *Anal. Chem.* **1991**, *63*, 2042–2047. [CrossRef]
22. Palmer, J.; Munro, N.J.; Landers, J.P. A universal concept for stacking neutral analytes in micellar capillary electrophoresis. *Anal. Chem.* **1999**, *71*, 1679–1687. [CrossRef] [PubMed]
23. Zhang, C.-X.; Thormann, W. Head-column field-amplified sample stacking in binary system capillary electrophoresis: A robust approach providing over 1000-fold sensitivity enhancement. *Anal. Chem.* **1996**, *68*, 2523–2532. [CrossRef] [PubMed]
24. Jung, B.; Bharadwaj, R.; Santiago, J.G. Thousandfold signal increase using field-amplified sample stacking for on-chip electrophoresis. *Electrophoresis* **2003**, *24*, 3476–3483. [CrossRef] [PubMed]

25. Bharadwaj, R.; Santiago, J.G. Dynamics of field-amplified sample stacking. *J. Fluid Mech.* **2005**, *543*, 57–92. [CrossRef]
26. Sustarich, J.M.; Storey, B.D.; Pennathur, S. Field-amplified sample stacking and focusing in nanofluidic channels. *Phys. Fluids* **2010**, *22*, 112003. [CrossRef]
27. Wei, S.-Y.; Wang, L.-F.; Yang, Y.-H.; Yeh, H.-H.; Chen, Y.-C.; Chen, S.-H. Sample stacking by field-amplified sample injection and sweeping for simultaneous analysis of acidic and basic components in clinic application. *Electrophoresis* **2012**, *33*, 1571–1581. [CrossRef] [PubMed]
28. Dziomba, S.; Kowalski, P.; Bączek, T. Field-amplified sample stacking–sweeping of vitamins B determination in capillary electrophoresis. *J. Chromatogr.* **2012**, *1267*, 224–230. [CrossRef] [PubMed]
29. Gebauer, P.; Boček, P. Recent progress in capillary isotachophoresis. *Electrophoresis* **2002**, *23*, 3858–3864. [CrossRef] [PubMed]
30. Urbánek, M.; Křivánková, L.; Boček, P. Stacking phenomena in electromigration: From basic principles to practical procedures. *Electrophoresis* **2003**, *24*, 466–485. [CrossRef] [PubMed]
31. Ma, B.; Zhou, X.; Wang, G.; Huang, H.; Dai, Z.; Qin, J.; Lin, B. Integrated isotachophoretic preconcentration with zone electrophoresis separation on a quartz microchip for UV detection of flavonoids. *Electrophoresis* **2006**, *27*, 4904–4909. [CrossRef] [PubMed]
32. Jung, B.; Bharadwaj, R.; Santiago, J.G. On-chip millionfold sample stacking using transient isotachophoresis. *Anal. Chem.* **2006**, *78*, 2319–2327. [CrossRef] [PubMed]
33. Jung, B.; Zhu, Y.; Santiago, J.G. Detection of 100 aM fluorophores using a high-sensitivity on-chip CE system and transient isotachophoresis. *Anal. Chem.* **2007**, *79*, 345–349. [CrossRef] [PubMed]
34. Khurana, T.K.; Santiago, J.G. Sample zone dynamics in peak mode isotachophoresis. *Anal. Chem.* **2008**, *80*, 6300–6307. [CrossRef] [PubMed]
35. Bottenus, D.; Hossan, M.R.; Ouyang, Y.; Dong, W.-J.; Dutta, P.; Ivory, C.F. Preconcentration and detection of the phosphorylated forms of cardiac troponin I in a cascade microchip by cationic isotachophoresis. *Lab Chip* **2011**, *11*, 3793–3801. [CrossRef] [PubMed]
36. Bottenus, D.; Jubery, T.Z.; Ouyang, Y.; Dong, W.-J.; Dutta, P.; Ivory, C.F. 10000-fold concentration increase of the biomarker cardiac troponin I in a reducing union microfluidic chip using cationic isotachophoresis. *Lab Chip* **2011**, *11*, 890–898. [CrossRef] [PubMed]
37. Bottenus, D.; Jubery, T.Z.; Dutta, P.; Ivory, C.F. 10000-fold concentration increase in proteins in a cascade microchip using anionic ITP by a 3-D numerical simulation with experimental results. *Electrophoresis* **2011**, *32*, 550–562. [CrossRef] [PubMed]
38. Shackman, J.G.; Ross, D. Counter-flow gradient electrofocusing. *Electrophoresis* **2007**, *28*, 556–571. [CrossRef] [PubMed]
39. Righetti, P.G.; Bossi, A. Isoelectric focusing of proteins and peptides in gel slabs and in capillaries1. *Anal. Chim. Acta* **1998**, *372*, 1–19. [CrossRef]
40. Ivory, C.F. Several new electrofocusing techniques. *Electrophoresis* **2007**, *28*, 15–25. [CrossRef]
41. Shimura, K. Recent advances in capillary isoelectric focusing: 1997–2001. *Electrophoresis* **2002**, *23*, 3847–3857. [CrossRef] [PubMed]
42. Kilár, F. Recent applications of capillary isoelectric focusing. *Electrophoresis* **2003**, *24*, 3908–3916. [CrossRef] [PubMed]
43. Shim, J.; Dutta, P.; Ivory, C.F. Effects of ampholyte concentration on protein behavior in on-chip isoelectric focusing. *Electrophoresis* **2008**, *29*, 1026–1035. [CrossRef]
44. Montgomery, R.; Jia, X.; Tolley, L. Dynamic isoelectric focusing for proteomics. *Anal. Chem.* **2006**, *78*, 6511–6518. [CrossRef] [PubMed]
45. Mosher, R.A.; Thormann, W. High-resolution computer simulation of the dynamics of isoelectric focusing: In quest of more realistic input parameters for carrier ampholytes. *Electrophoresis* **2008**, *29*, 1036–1047. [CrossRef] [PubMed]
46. Yang, K.S.; Clementz, P.; Park, T.J.; Lee, S.J.; Park, J.P.; Kim, D.H.; Lee, S.Y. Free-flow isoelectric focusing microfluidic device with glass coating by sol–gel methods. *Curr. Appl. Phys.* **2009**, *9*, e66–e70. [CrossRef]
47. Kelly, R.T.; Woolley, A.T. Electric field gradient focusing. *J. Sep. Sci.* **2005**, *28*, 1985–1993. [CrossRef] [PubMed]
48. Meighan, M.M.; Staton, S.J.R.; Hayes, M.A. Bioanalytical separations using electric field gradient techniques. *Electrophoresis* **2009**, *30*, 852–865. [CrossRef] [PubMed]

49. Koegler, W.S.; Ivory, C.F. Focusing proteins in an electric field gradient. *J. Chromatogr.* **1996**, *726*, 229–236. [CrossRef]
50. Petsev, D.N.; Lopez, G.P.; Ivory, C.F.; Sibbett, S.S. Microchannel protein separation by electric field gradient focusing. *Lab Chip* **2005**, *5*, 587–597. [CrossRef] [PubMed]
51. Tolley, H.D.; Wang, Q.; LeFebre, D.A.; Lee, M.L. Equilibrium gradient methods with nonlinear field intensity gradient: A theoretical approach. *Anal. Chem.* **2002**, *74*, 4456–4463. [CrossRef] [PubMed]
52. Humble, P.H.; Kelly, R.T.; Woolley, A.T.; Tolley, H.D.; Lee, M.L. Electric field gradient focusing of proteins based on shaped ionically conductive acrylic polymer. *Anal. Chem.* **2004**, *76*, 5641–5648. [CrossRef] [PubMed]
53. Liu, J.; Sun, X.; Farnsworth, P.B.; Lee, M.L. Fabrication of conductive membrane in a polymeric electric field gradient focusing microdevice. *Anal. Chem.* **2006**, *78*, 4654–4662. [CrossRef] [PubMed]
54. Kelly, R.T.; Li, Y.; Woolley, A.T. Phase-changing sacrificial materials for interfacing microfluidics with ion-permeable membranes to create on-chip preconcentrators and electric field gradient focusing microchips. *Anal. Chem.* **2006**, *78*, 2565–2570. [CrossRef] [PubMed]
55. Sun, X.; Li, D.; Woolley, A.T.; Farnsworth, P.B.; Tolley, H.D.; Warnick, K.F.; Lee, M.L. Bilinear electric field gradient focusing. *J. Chromatogr.* **2009**, *1216*, 6532–6538. [CrossRef] [PubMed]
56. Sun, X.; Farnsworth, P.B.; Tolley, H.D.; Warnick, K.F.; Woolley, A.T.; Lee, M.L. Performance optimization in electric field gradient focusing. *J. Chromatogr.* **2009**, *1216*, 159–164. [CrossRef] [PubMed]
57. Ansell, R.J.; Tunon, P.G.; Wang, Y.; Myers, P.; Ivory, C.F.; Keen, J.N.; Findlay, J.B.C. Electrophoretic field gradient focusing with on-column detection by fluorescence quenching. *Analyst* **2009**, *134*, 226–229. [CrossRef] [PubMed]
58. Ross, D.; Locascio, L.E. Microfluidic temperature gradient focusing. *Anal. Chem.* **2002**, *74*, 2556–2564. [CrossRef] [PubMed]
59. Balss, K.M.; Ross, D.; Begley, H.C.; Olsen, K.G.; Tarlov, M.J. DNA hybridization assays using temperature gradient focusing and peptide nucleic acids. *J. Am. Chem. Soc.* **2004**, *126*, 13474–13479. [CrossRef] [PubMed]
60. Balss, K.M.; Vreeland, W.N.; Howell, P.B.; Henry, A.C.; Ross, D. Micellar affinity gradient focusing: A new method for electrokinetic focusing. *J. Am. Chem. Soc.* **2004**, *126*, 1936–1937. [CrossRef] [PubMed]
61. Balss, K.M.; Vreeland, W.N.; Phinney, K.W.; Ross, D. Simultaneous concentration and separation of enantiomers with chiral temperature gradient focusing. *Anal. Chem.* **2004**, *76*, 7243–7249. [CrossRef] [PubMed]
62. Hoebel, S.J.; Balss, K.M.; Jones, B.J.; Malliaris, C.D.; Munson, M.S.; Vreeland, W.N.; Ross, D. Scanning temperature gradient focusing. *Anal. Chem.* **2006**, *78*, 7186–7190. [CrossRef] [PubMed]
63. Munson, M.S.; Danger, G.; Shackman, J.G.; Ross, D. Temperature gradient focusing with field-amplified continuous sample injection for dual-stage analyte enrichment and separation. *Anal. Chem.* **2007**, *79*, 6201–6207. [CrossRef] [PubMed]
64. Munson, M.S.; Meacham, J.M.; Locascio, L.E.; Ross, D. Counterflow rejection of adsorbing proteins for characterization of biomolecular interactions by temperature gradient focusing. *Anal. Chem.* **2008**, *80*, 172–178. [CrossRef] [PubMed]
65. Munson, M.S.; Meacham, J.M.; Ross, D.; Locascio, L.E. Development of aptamer-based affinity assays using temperature gradient focusing: Minimization of the limit of detection. *Electrophoresis* **2008**, *29*, 3456–3465. [CrossRef] [PubMed]
66. Lin, H.; Shackman, J.G.; Ross, D. Finite sample effect in temperature gradient focusing. *Lab Chip* **2008**, *8*, 969–978. [CrossRef] [PubMed]
67. Huber, D.E.; Santiago, J.G. Taylor–Aris dispersion in temperature gradient focusing. *Electrophoresis* **2007**, *28*, 2333–2344. [CrossRef] [PubMed]
68. Huber, D.E.; Santiago, J.G. Ballistic dispersion in temperature gradient focusing. *Proc. R. Soc.* **2008**, *464*, 595–612. [CrossRef]
69. Becker, M.; Mansouri, A.; Beilein, C.; Janasek, D. Temperature gradient focusing in miniaturized free-flow electrophoresis devices. *Electrophoresis* **2009**, *30*, 4206–4212. [CrossRef] [PubMed]
70. Maynes, D.; Webb, B.W. Fully developed electro-osmotic heat transfer in microchannels. *Int. J. Heat Mass Transf.* **2003**, *46*, 1359–1369. [CrossRef]
71. Maynes, D.; Webb, B.W. Fully-developed thermal transport in combined pressure and electro-osmotically driven flow in microchannels. *J. Heat Transf.* **2003**, *125*, 889–895. [CrossRef]

72. Zhao, C.; Yang, C. Joule heating induced heat transfer for electroosmotic flow of power-law fluids in a microcapillary. *Int. J. Heat Mass Transf.* **2012**, *55*, 2044–2051. [CrossRef]
73. Horiuchi, K.; Dutta, P.; Hossain, A. Joule-heating effects in mixed electroosmotic and pressure-driven microflows under constant wall heat flux. *J. Eng. Math.* **2005**, *54*, 159–180. [CrossRef]
74. Horiuchi, K.; Dutta, P. Joule heating effects in electroosmotically driven microchannel flows. *Int. J. Heat Mass Transf.* **2004**, *47*, 3085–3095. [CrossRef]
75. Tang, G.Y.; Yang, C.; Chai, C.J.; Gong, H.Q. Modeling of electroosmotic flow and capillary electrophoresis with the joule heating effect: The Nernst−Planck equation versus the Boltzmann distribution. *Langmuir* **2003**, *19*, 10975–10984. [CrossRef]
76. Tang, G.Y.; Yang, C.; Chai, J.C.; Gong, H.Q. Joule heating effect on electroosmotic flow and mass species transport in a microcapillary. *Int. J. Heat Mass Transf.* **2004**, *47*, 215–227. [CrossRef]
77. Xuan, X.; Sinton, D.; Li, D. Thermal end effects on electroosmotic flow in a capillary. *Int. J. Heat Mass Transf.* **2004**, *47*, 3145–3157. [CrossRef]
78. Kim, S.M.; Sommer, G.J.; Burns, M.A.; Hasselbrink, E.F. Low-power concentration and separation using temperature gradient focusing via Joule heating. *Anal. Chem.* **2006**, *78*, 8028–8035. [CrossRef] [PubMed]
79. Sommer, G.J.; Kim, S.M.; Littrell, R.J.; Hasselbrink, E.F. Theoretical and numerical analysis of temperature gradient focusing via Joule heating. *Lab Chip* **2007**, *7*, 898–907. [CrossRef] [PubMed]
80. Tang, G.; Yang, C. Numerical modeling of Joule heating-induced temperature gradient focusing in microfluidic channels. *Electrophoresis* **2008**, *29*, 1006–1012. [CrossRef] [PubMed]
81. Ge, Z.; Yang, C.; Tang, G. Concentration enhancement of sample solutes in a sudden expansion microchannel with Joule heating. *Int. J. Heat Mass Transf.* **2010**, *53*, 2722–2731. [CrossRef]
82. Ge, Z.; Wang, W.; Yang, C. Towards high concentration enhancement of microfluidic temperature gradient focusing of sample solutes using combined AC and DC field induced Joule heating. *Lab Chip* **2011**, *11*, 1396–1402. [CrossRef] [PubMed]
83. Ge, Z.; Jin, L.; Yang, C. Microfluidic concentration of sample solutes using Joule heating effects under a combined AC and DC electric field. *Int. J. Heat Mass Transf.* **2015**, *85*, 158–165. [CrossRef]
84. Ge, Z.; Wang, W.; Yang, C. Rapid concentration of deoxyribonucleic acid via Joule heating induced temperature gradient focusing in poly-dimethylsiloxane microfluidic channel. *Anal. Chim. Acta* **2015**, *858*, 91–97. [CrossRef] [PubMed]
85. Kim, S.J.; Song, Y.-A.; Han, J. Nanofluidic concentration devices for biomolecules utilizing ion concentration polarization: Theory, fabrication, and applications. *Chem. Soc. Rev.* **2010**, *39*, 912–922. [CrossRef] [PubMed]
86. Schoch, R.B.; Han, J.; Renaud, P. Transport phenomena in nanofluidics. *Rev. Mod. Phys.* **2008**, *80*, 839–883. [CrossRef]
87. Son, S.Y.; Lee, S.; Lee, H.; Kim, S.J. Engineered nanofluidic preconcentration devices by ion concentration polarization. *BioChip J.* **2016**, *10*, 251–261. [CrossRef]
88. Dai, J.; Ito, T.; Sun, L.; Crooks, R.M. Electrokinetic trapping and concentration enrichment of DNA in a microfluidic channel. *J. Am. Chem. Soc.* **2003**, *125*, 13026–13027. [CrossRef] [PubMed]
89. Hahn, T.; O'Sullivan, C.K.; Drese, K.S. Microsystem for field-amplified electrokinetic trapping preconcentration of DNA at poly(ethylene terephthalate) membranes. *Anal. Chem.* **2009**, *81*, 2904–2911. [CrossRef] [PubMed]
90. Wang, Y.-C.; Stevens, A.L.; Han, J. Million-fold preconcentration of proteins and peptides by nanofluidic filter. *Anal. Chem.* **2005**, *77*, 4293–4299. [CrossRef] [PubMed]
91. Wang, Y.-C.; Han, J. Pre-binding dynamic range and sensitivity enhancement for immuno-sensors using nanofluidic preconcentrator. *Lab Chip* **2008**, *8*, 392–394. [CrossRef] [PubMed]
92. Li, M.; Anand, R.K. Recent advancements in ion concentration polarization. *Analyst* **2016**, *141*, 3496–3510. [CrossRef] [PubMed]
93. Ko, S.H.; Song, Y.-A.; Kim, S.J.; Kim, M.; Han, J.; Kang, K.H. Nanofluidic preconcentration device in a straight microchannel using ion concentration polarization. *Lab Chip* **2012**, *12*, 4472–4482. [CrossRef] [PubMed]
94. Liu, V.; Song, Y.-A.; Han, J. Capillary-valve-based fabrication of ion-selective membrane junction for electrokinetic sample preconcentration in PDMS chip. *Lab Chip* **2010**, *10*, 1485–1490. [CrossRef] [PubMed]
95. Lee, J.H.; Song, Y.-A.; Han, J. Multiplexed proteomic sample preconcentration device using surface-patterned ion-selective membrane. *Lab Chip* **2008**, *8*, 596–601. [CrossRef] [PubMed]

96. Kim, S.J.; Han, J. Self-sealed vertical polymeric nanoporous-junctions for high-throughput nanofluidic applications. *Anal. Chem.* **2008**, *80*, 3507–3511. [CrossRef] [PubMed]
97. Choi, J.; Huh, K.; Moon, D.J.; Lee, H.; Son, S.Y.; Kim, K.; Kim, H.C.; Chae, J.-H.; Sung, G.Y.; Kim, H.-Y.; Hong, J.W.; Kim, S.J. Selective preconcentration and online collection of charged molecules using ion concentration polarization. *RSC Adv.* **2015**, *5*, 66178–66184. [CrossRef]
98. Kwak, R.; Kang, J.Y.; Kim, T.S. Spatiotemporally defining biomolecule preconcentration by merging ion concentration polarization. *Anal. Chem.* **2016**, *88*, 988–996. [CrossRef]
99. Phan, D.-T.; Shaegh, S.A.M.; Yang, C.; Nguyen, N.-T. Sample concentration in a microfluidic paper-based analytical device using ion concentration polarization. *Sens. Actuators* **2016**, *222*, 735–740. [CrossRef]
100. Yang, R.-J.; Pu, H.-H.; Wang, H.-L. Ion concentration polarization on paper-based microfluidic devices and its application to preconcentrate dilute sample solutions. *Biomicrofluidics* **2015**, *9*, 014122. [CrossRef] [PubMed]
101. Phan, D.-T.; Yang, C.; Nguyen, N.-T. Fabrication of nanoporous junctions using off-the-shelf Nafion membrane. *J. Micromech. Microeng.* **2015**, *25*, 115019. [CrossRef]
102. Jones, T.B. *Electromechanics of Particles*; Cambridge University Press: Cambridge, UK, 1995.
103. Asbury, C.L.; Engh, G.v.d. Trapping of DNA in nonuniform oscillating electric fields. *Biophys. J.* **1998**, *74*, 1024–1030. [CrossRef]
104. Yang, L.; Banada, P.P.; Chatni, M.R.; Seop Lim, K.; Bhunia, A.K.; Ladisch, M.; Bashir, R. A multifunctional micro-fluidic system for dielectrophoretic concentration coupled with immuno-capture of low numbers of Listeria monocytogenes. *Lab Chip* **2006**, *6*, 896–905. [CrossRef]
105. Park, K.; Suk, H.-J.; Akin, D.; Bashir, R. Dielectrophoresis-based cell manipulation using electrodes on a reusable printed circuit board. *Lab Chip* **2009**, *9*, 2224–2229. [CrossRef] [PubMed]
106. Lee, H.-Y.; Voldman, J. Optimizing micromixer design for enhancing dielectrophoretic microconcentrator performance. *Anal. Chem.* **2007**, *79*, 1833–1839. [CrossRef] [PubMed]
107. Gadish, N.; Voldman, J. High-throughput positive-dielectrophoretic bioparticle microconcentrator. *Anal. Chem.* **2006**, *78*, 7870–7876. [CrossRef] [PubMed]
108. Du, J.-R.; Juang, Y.-J.; Wu, J.-T.; Wei, H.-H. Long-range and superfast trapping of DNA molecules in an AC electrokinetic funnel. *Biomicrofluidics* **2008**, *2*, 044103. [CrossRef] [PubMed]
109. Du, J.-R.; Wei, H.-H. Focusing and trapping of DNA molecules by head-on AC electrokinetic streaming through join asymmetric polarization. *Biomicrofluidics* **2010**, *4*, 034108. [CrossRef] [PubMed]
110. Loucaides, N.G.; Ramos, A.; Georghiou, G.E. Initial concentration and fluidic effects on the dielectrophoretic trapping of DNA. *Phys. Status Solidi* **2010**, *7*, 2755–2758. [CrossRef]
111. Loucaides, N.G.; Ramos, A.; Georghiou, G.E. Dielectrophoretic and AC electroosmotic trapping of DNA: Numerical simulation incorporating fluid dynamics and steric particle effects. *J. Electrostat.* **2011**, *69*, 111–118. [CrossRef]
112. Cummings, E.B.; Singh, A.K. Dielectrophoresis in microchips containing arrays of insulating posts: Theoretical and experimental results. *Anal. Chem.* **2003**, *75*, 4724–4731. [CrossRef] [PubMed]
113. Chou, C.-F.; Tegenfeldt, J.O.; Bakajin, O.; Chan, S.S.; Cox, E.C.; Darnton, N.; Duke, T.; Austin, R.H. Electrodeless dielectrophoresis of single- and double-stranded DNA. *Biophys. J.* **2002**, *83*, 2170–2179. [CrossRef]
114. Lapizco-Encinas, B.H.; Simmons, B.A.; Cummings, E.B.; Fintschenko, Y. Dielectrophoretic concentration and separation of live and dead bacteria in an array of insulators. *Anal. Chem.* **2004**, *76*, 1571–1579. [CrossRef] [PubMed]
115. Lapizco-Encinas, B.H.; Simmons, B.A.; Cummings, E.B.; Fintschenko, Y. Insulator-based dielectrophoresis for the selective concentration and separation of live bacteria in water. *Electrophoresis* **2004**, *25*, 1695–1704. [CrossRef] [PubMed]
116. Mela, P.; van den Berg, A.; Fintschenko, Y.; Cummings, E.B.; Simmons, B.A.; Kirby, B.J. The zeta potential of cyclo-olefin polymer microchannels and its effects on insulative (electrodeless) dielectrophoresis particle trapping devices. *Electrophoresis* **2005**, *26*, 1792–1799. [CrossRef] [PubMed]
117. Chen, D.; Du, H.; Tay, C. Rapid Concentration of Nanoparticles with DC dielectrophoresis in focused electric fields. *Nanoscale Res. Lett.* **2009**, *5*, 55–60. [CrossRef] [PubMed]
118. Lewpiriyawong, N.; Yang, C.; Lam, Y.C. Electrokinetically driven concentration of particles and cells by dielectrophoresis with DC-offset AC electric field. *Microfluid. Nanofluid.* **2012**, *12*, 723–733. [CrossRef]

119. Zhao, K.; Peng, R.; Li, D. Separation of nanoparticles by a nano-orifice based DC-dielectrophoresis method in a pressure-driven flow. *Nanoscale* **2016**, *8*, 18945–18955. [CrossRef] [PubMed]
120. Hawkins, B.G.; Kirby, B.J. Electrothermal flow effects in insulating (electrodeless) dielectrophoresis systems. *Electrophoresis* **2010**, *31*, 3622–3633. [CrossRef] [PubMed]
121. Sridharan, S.; Zhu, J.; Hu, G.; Xuan, X. Joule heating effects on electroosmotic flow in insulator-based dielectrophoresis. *Electrophoresis* **2011**, *32*, 2274–2281. [CrossRef] [PubMed]
122. Pratt, E.D. How to Sort Circulating Tumor Cells Part II: Immunocapture. 2012. Available online: https://pratted.wordpress.com/2012/11/13/how-to-sort-circulating-tumor-cells-part-ii-immunocapture/#comments (accessed on 17 January 2017).
123. Nagrath, S.; Sequist, L.V.; Maheswaran, S.; Bell, D.W.; Irimia, D.; Ulkus, L.; Smith, M.R.; Kwak, E.L.; Digumarthy, S.; Muzikansky, A.; et al. Isolation of rare circulating tumour cells in cancer patients by microchip technology. *Nature* **2007**, *450*, 1235–1239. [CrossRef] [PubMed]
124. Dharmasiri, U.; Njoroge, S.K.; Witek, M.A.; Adebiyi, M.G.; Kamande, J.W.; Hupert, M.L.; Barany, F.; Soper, S.A. High-Throughput Selection, Enumeration, Electrokinetic manipulation, and molecular profiling of low-abundance circulating tumor cells using a microfluidic system. *Anal. Chem.* **2011**, *83*, 2301–2309. [CrossRef] [PubMed]
125. Gleghorn, J.P.; Pratt, E.D.; Denning, D.; Liu, H.; Bander, N.H.; Tagawa, S.T.; Nanus, D.M.; Giannakakou, P.A.; Kirby, B.J. Capture of circulating tumor cells from whole blood of prostate cancer patients using geometrically enhanced differential immunocapture (GEDI) and a prostate-specific antibody. *Lab Chip* **2010**, *10*, 27–29. [CrossRef] [PubMed]
126. Yang, L.; Lang, J.C.; Balasubramanian, P.; Jatana, K.R.; Schuller, D.; Agrawal, A.; Zborowski, M.; Chalmers, J.J. Optimization of an enrichment process for circulating tumor cells from the blood of head and neck cancer patients through depletion of normal cells. *Biotechnol. Bioeng.* **2009**, *102*, 521–534. [CrossRef] [PubMed]
127. Lara, O.; Tong, X.; Zborowski, M.; Chalmers, J.J. Enrichment of rare cancer cells through depletion of normal cells using density and flow-through, immunomagnetic cell separation. *Exp. Hematol.* **2004**, *32*, 891–904. [CrossRef] [PubMed]
128. Liu, Z.; Fusi, A.; Klopocki, E.; Schmittel, A.; Tinhofer, I.; Nonnenmacher, A.; Keilholz, U. Negative enrichment by immunomagnetic nanobeads for unbiased characterization of circulating tumor cells from peripheral blood of cancer patients. *J. Transl. Med.* **2011**, *9*, 70. [CrossRef] [PubMed]
129. Mok, J.; Mindrinos, M.N.; Davis, R.W.; Javanmard, M. Digital microfluidic assay for protein detection. *Proc. Natl. Acad. Sci. USA* **2014**, *111*, 2110–2115. [PubMed]
130. Wang, S.; Esfahani, M.; Gurkan, U.A.; Inci, F.; Kuritzkes, D.R.; Demirci, U. Efficient on-chip isolation of HIV subtypes. *Lab Chip* **2012**, *12*, 1508–1515. [CrossRef] [PubMed]
131. Thege, F.I.; Lannin, T.B.; Saha, T.N.; Tsai, S.; Kochman, M.L.; Hollingsworth, M.A.; Rhim, A.D.; Kirby, B.J. Microfluidic immunocapture of circulating pancreatic cells using parallel EpCAM and MUC1 capture: Characterization, optimization and downstream analysis. *Lab Chip* **2014**, *14*, 1775–1784. [CrossRef] [PubMed]
132. Hughes, A.D.; King, M.R. Use of naturally occurring halloysite nanotubes for enhanced capture of flowing cells. *Langmuir* **2010**, *26*, 12155–12164. [CrossRef] [PubMed]
133. Wang, S.; Wang, H.; Jiao, J.; Chen, K.-J.; Owens, G.E.; Kamei, K.-I.; Sun, J.; Sherman, D.J.; Behrenbruch, C.P.; Wu, H.; Tseng, H.-R. Three-dimensional nanostructured substrates toward efficient capture of circulating tumor cells. *Angew. Chem. Int. Ed.* **2009**, *48*, 8970–8973. [CrossRef] [PubMed]
134. Wang, L.; Asghar, W.; Demirci, U.; Wan, Y. Nanostructured substrates for isolation of circulating tumor cells. *Nano Today* **2013**, *8*, 374–387. [CrossRef]
135. Stott, S.L.; Hsu, C.-H.; Tsukrov, D.I.; Yu, M.; Miyamoto, D.T.; Waltman, B.A.; Rothenberg, S.M.; Shah, A.M.; Smas, M.E.; Korir, G.K.; et al. Isolation of circulating tumor cells using a microvortex-generating herringbone-chip. *Proc. Natl. Acad. Sci. USA* **2010**, *107*, 18392–18397. [CrossRef] [PubMed]
136. Wang, S.; Liu, K.; Liu, J.; Yu, Z.T.F.; Xu, X.; Zhao, L.; Lee, T.; Lee, E.K.; Reiss, J.; Lee, Y.-K.; et al. Highly Efficient capture of circulating tumor cells by using nanostructured silicon substrates with integrated chaotic micromixers. *Angew. Chem. Int. Ed.* **2011**, *50*, 3084–3088. [CrossRef] [PubMed]
137. Powell, A.A.; Talasaz, A.H.; Zhang, H.; Coram, M.A.; Reddy, A.; Deng, G.; Telli, M.L.; Advani, R.H.; Carlson, R.W.; Mollick, J.A.; et al. Single cell profiling of circulating tumor cells: Transcriptional heterogeneity and diversity from breast cancer cell lines. *PLoS ONE* **2012**, *7*, e33788. [CrossRef] [PubMed]

138. Mohamadi, R.M.; Svobodova, Z.; Bilkova, Z.; Otto, M.; Taverna, M.; Descroix, S.; Viovy, J.-L. An integrated microfluidic chip for immunocapture, preconcentration and separation of β-amyloid peptides. *Biomicrofluidics* **2015**, *9*, 054117. [CrossRef] [PubMed]
139. Hong, C.S.; Muller, L.; Boyiadzis, M.; Whiteside, T.L. Isolation and characterization of CD34+ blast-derived exosomes in acute myeloid leukemia. *PLoS ONE* **2014**, *9*, e103310. [CrossRef] [PubMed]
140. Ozalp, V.C.; Bayramoglu, G.; Kavruk, M.; Keskin, B.B.; Oktem, H.A.; Arica, M.Y. Pathogen detection by core–shell type aptamer-magnetic preconcentration coupled to real-time PCR. *Anal. Biochem.* **2014**, *447*, 119–125. [CrossRef] [PubMed]
141. Chen, H.-X.; Busnel, J.-M.; Gassner, A.-L.; Peltre, G.; Zhang, X.-X.; and Girault, H.H. Capillary electrophoresis immunoassay using magnetic beads. *Electrophoresis* **2008**, *29*, 3414–3421. [CrossRef] [PubMed]
142. Riethdorf, S.; Fritsche, H.; Müller, V.; Rau, T.; Schindlbeck, C.; Rack, B.; Janni, W.; Coith, C.; Beck, K.; Jänicke, F.; et al. Detection of circulating tumor cells in peripheral blood of patients with metastatic breast cancer: a validation study of the cellsearch system. *Clin. Cancer Res.* **2007**, *13*, 920–928. [CrossRef] [PubMed]
143. Cohen, S.J.; Punt, C.J.A.; Iannotti, N.; Saidman, B.H.; Sabbath, K.D.; Gabrail, N.Y.; Picus, J.; Morse, M.; Mitchell, E.; Miller, M.C.; et al. Relationship of circulating tumor cells to tumor response, progression-free survival, and overall survival in patients with metastatic colorectal cancer. *J. Clin. Oncol.* **2008**, *26*, 3213–3221. [CrossRef] [PubMed]
144. de Bono, J.S.; Scher, H.I.; Montgomery, R.B.; Parker, C.; Miller, M.C.; Tissing, H.; Doyle, G.V.; Terstappen, L.W.W.M.; Pienta, K.J.; Raghavan, D. Circulating tumor cells predict survival benefit from treatment in metastatic castration-resistant prostate cancer. *Clin. Cancer Res.* **2008**, *14*, 6302–6309. [CrossRef] [PubMed]
145. Huang, C.; Liu, H.; Bander, N.H.; Kirby, B.J. Enrichment of prostate cancer cells from blood cells with a hybrid dielectrophoresis and immunocapture microfluidic system. *Biomed. Microdevices* **2013**, *15*, 941–948. [CrossRef] [PubMed]
146. Smith, J.P.; Huang, C.; Kirby, B.J. Enhancing sensitivity and specificity in rare cell capture microdevices with dielectrophoresis. *Biomicrofluidics* **2015**, *9*, 014116. [CrossRef] [PubMed]
147. Smith, J.P.; Lannin, T.B.; Syed, Y.A.; Santana, S.M.; Kirby, B.J. Parametric control of collision rates and capture rates in geometrically enhanced differential immunocapture (GEDI) microfluidic devices for rare cell capture. *Biomed. Microdevices* **2014**, *16*, 143–151. [CrossRef] [PubMed]
148. Kirby, B.J.; Jodari, M.; Loftus, M.S.; Gakhar, G.; Pratt, E.D.; Chanel-Vos, C.; Gleghorn, J.P.; Santana, S.M.; He, L.; Smith, J.P.; et al. Functional characterization of circulating tumor cells with a prostate-cancer-specific microfluidic device. *PLoS ONE* **2012**, *7*, e35976. [CrossRef]
149. Santana, S.M.; Liu, H.; Bander, N.H.; Gleghorn, J.P.; Kirby, B.J. Immunocapture of prostate cancer cells by use of anti-PSMA antibodies in microdevices. *Biomed. Microdevices* **2012**, *14*, 401–407. [CrossRef] [PubMed]
150. Galletti, G.; Sung, M.S.; Vahdat, L.T.; Shah, M.A.; Santana, S.M.; Altavilla, G.; Kirby, B.J.; Giannakakou, P. Isolation of breast cancer and gastric cancer circulating tumor cells by use of an anti HER2-based microfluidic device. *Lab Chip* **2014**, *14*, 147–156. [CrossRef] [PubMed]
151. Sarioglu, A.F.; Aceto, N.; Kojic, N.; Donaldson, M.C.; Zeinali, M.; Hamza, B.; Engstrom, A.; Zhu, H.; Sundaresan, T.K.; Miyamoto, D.T.; et al. A microfluidic device for label-free, physical capture of circulating tumor cell clusters. *Nat. Methods* **2015**, *12*, 685–691. [CrossRef] [PubMed]
152. Miltenyi, S.; Müller, W.; Weichel, W.; Radbruch, A. High gradient magnetic cell separation with MACS. *Cytometry* **1990**, *11*, 231–238. [CrossRef] [PubMed]
153. Chen, P.; Huang, Y.-Y.; Hoshino, K.; Zhang, X. Multiscale immunomagnetic enrichment of circulating tumor cells: From tubes to microchips. *Lab Chip* **2014**, *14*, 446–458. [CrossRef] [PubMed]
154. Talasaz, A.H.; Powell, A.A.; Huber, D.E.; Berbee, J.G.; Roh, K.-H.; Yu, W.; Xiao, W.; Davis, M.M.; Pease, R.F.; Mindrinos, M.N.; et al. Isolating highly enriched populations of circulating epithelial cells and other rare cells from blood using a magnetic sweeper device. *Proc. Natl. Acad. Sci. USA* **2009**, *106*, 3970–3975. [CrossRef] [PubMed]
155. Horák, D.; Babič, M.; Macková, H.; Beneš, M.J. Preparation and properties of magnetic nano- and microsized particles for biological and environmental separations. *J. Sep. Sci.* **2007**, *30*, 1751–1772. [CrossRef] [PubMed]
156. Brian, D.P.; Shashi, K.M.; Laura, H.L. Fundamentals and application of magnetic particles in cell isolation and enrichment: A review. *Rep. Prog. Phys.* **2015**, *78*, 016601.

157. Hoshino, K.; Huang, Y.-Y.; Lane, N.; Huebschman, M.; Uhr, J.W.; Frenkel, E.P.; Zhang, X. Microchip-based immunomagnetic detection of circulating tumor cells. *Lab Chip* **2011**, *11*, 3449–3457. [CrossRef] [PubMed]
158. Plouffe, B.D.; Mahalanabis, M.; Lewis, L.H.; Klapperich, C.M.; Murthy, S.K. Clinically relevant microfluidic magnetophoretic isolation of rare-cell populations for diagnostic and therapeutic monitoring applications. *Anal. Chem.* **2012**, *84*, 1336–1344. [CrossRef] [PubMed]
159. Tsai, S.S.H.; Griffiths, I.M.; Stone, H.A. Microfluidic immunomagnetic multi-target sorting—A model for controlling deflection of paramagnetic beads. *Lab Chip* **2011**, *11*, 2577–2582. [CrossRef] [PubMed]
160. Luo, W.-Y.; Tsai, S.-C.; Hsieh, K.; Lee, G.-B. An integrated microfluidic platform for negative selection and enrichment of cancer cells. *J. Micromech. Microeng.* **2015**, *25*, 084007. [CrossRef]
161. Wang, Z.; Wu, W.; Wang, Z.; Tang, Y.; Deng, Y.; Xu, L.; Tian, J.; Shi, Q. Ex vivo expansion of circulating lung tumor cells based on one-step microfluidics-based immunomagnetic isolation. *Analyst* **2016**, *141*, 3621–3625. [CrossRef] [PubMed]
162. Braun, D.; Libchaber, A. Trapping of DNA by thermophoretic depletion and convection. *Phys. Rev. Lett.* **2002**, *89*, 188103. [CrossRef] [PubMed]
163. Duhr, S.; Braun, D. Why molecules move along a temperature gradient. *Proc. Natl. Acad. Sci. USA* **2006**, *103*, 19678–19682. [CrossRef] [PubMed]
164. Mast, C.B.; Braun, D. Thermal trap for DNA replication. *Phys. Rev. Lett.* **2010**, *104*, 188102. [CrossRef] [PubMed]
165. Duhr, S.; Braun, D. Optothermal molecule trapping by opposing fluid flow with thermophoretic drift. *Phys. Rev. Lett.* **2006**, *97*, 038103. [CrossRef] [PubMed]
166. Serey, X.; Mandal, S.; Chen, Y.-F.; Erickson, D. DNA transport and delivery in thermal gradients near optofluidic resonators. *Phys. Rev. Lett.* **2012**, *108*, 048102. [CrossRef] [PubMed]
167. Khandurina, J.; Jacobson, S.C.; Waters, L.C.; Foote, R.S.; Ramsey, J.M. Microfabricated porous membrane structure for sample concentration and electrophoretic analysis. *Anal. Chem.* **1999**, *71*, 1815–1819. [CrossRef] [PubMed]
168. Foote, R.S.; Khandurina, J.; Jacobson, S.C.; Ramsey, J.M. Preconcentration of proteins on microfluidic devices using porous silica membranes. *Anal. Chem.* **2005**, *77*, 57–63. [CrossRef] [PubMed]
169. Kuo, C.-H.; Wang, J.-H.; Lee, G.-B. A microfabricated CE chip for DNA pre-concentration and separation utilizing a normally closed valve. *Electrophoresis* **2009**, *30*, 3228–3235. [CrossRef] [PubMed]
170. Kuo, I.T.; Chiu, T.-C.; Chang, H.-T. On-column concentration and separation of double-stranded DNA by gradient capillary electrophoresis. *Electrophoresis* **2003**, *24*, 3339–3347. [CrossRef] [PubMed]
171. Park, S.-R.; Swerdlow, H. Concentration of DNA in a flowing stream for high-sensitivity capillary electrophoresis. *Anal. Chem.* **2003**, *75*, 4467–4474. [CrossRef] [PubMed]
172. Wanunu, M.; Morrison, W.; Rabin, Y.; Grosberg, A.Y.; Meller, A. Electrostatic focusing of unlabelled DNA into nanoscale pores using a salt gradient. *Nat. Nano* **2010**, *5*, 160–165. [CrossRef] [PubMed]
173. Paik, K.-H.; Liu, Y.; Tabard-Cossa, V.; Waugh, M.J.; Huber, D.E.; Provine, J.; Howe, R.T.; Dutton, R.W.; Davis, R.W. Control of DNA capture by nanofluidic transistors. *ACS Nano* **2012**, *6*, 6767–6775. [CrossRef] [PubMed]
174. Dhopeshwarkar, R.; Hlushkou, D.; Nguyen, M.; Tallarek, U.; Crooks, R.M. Electrokinetics in microfluidic channels containing a floating electrode. *J. Am. Chem. Soc.* **2008**, *130*, 10480–10481. [CrossRef] [PubMed]
175. Hlushkou, D.; Perdue, R.K.; Dhopeshwarkar, R.; Crooks, R.M.; Tallarek, U. Electric field gradient focusing in microchannels with embedded bipolar electrode. *Lab Chip* **2009**, *9*, 1903–1913. [CrossRef] [PubMed]
176. Perdue, R.K.; Laws, D.R.; Hlushkou, D.; Tallarek, U.; Crooks, R.M. Bipolar electrode focusing: the effect of current and electric field on concentration enrichment. *Anal. Chem.* **2009**, *81*, 10149–10155. [CrossRef] [PubMed]
177. Daghighi, Y.; Li, D. Numerical studies of electrokinetic control of DNA concentration in a closed-end microchannel. *Electrophoresis* **2010**, *31*, 868–878. [CrossRef] [PubMed]

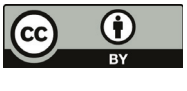

micromachines

MDPI

Article

Frequency-Dependent Electroformation of Giant Unilamellar Vesicles in 3D and 2D Microelectrode Systems

Qiong Wang [1], Xiaoling Zhang [2,*], Ting Fan [1,2], Zhong Yang [3], Xi Chen [1], Zhenyu Wang [4], Jie Xu [5], Yuanyi Li [5], Ning Hu [1,2,*] and Jun Yang [1,*]

1 Key Laboratory of Biorheological Science and Technology (Chongqing University), Ministry of Education, Bioengineering College, Chongqing University, Chongqing 400030, China; wangqiong@cqu.edu.cn (Q.W.); 20126461@cqu.edu.cn (T.F.); 20121913019t@cqu.edu.cn (X.C.)

2 Chongqing Engineering Research Center of Medical Electronics Technology (Chongqing University), Bioengineering College, Chongqing University, Chongqing 400030, China

3 Department of Laboratory Medicine, Southwest Hospital, Third Military Medical University, Chongqing 400038, China; zyang@tmmu.edu.cn

4 College of Biomedical Engineering, Chongqing Medical University, Chongqing 400016, China; wangzhenyu20090306@gmail.com

5 Chongqing Jinshan Science & Technology (Group) Co., Ltd., Chongqing 401120, China; kyxuj@jinshangroup.com (J.X.); liyy@jinshangroup.com (Y.L.)

* Correspondence: zhangxiaoling@cqu.edu.cn (X.Z.); huning@cqu.edu.cn (N.H.); bioyangjun@cqu.edu.cn (J.Y.); Tel.: +86-23-6511-1931 (X.Z., N.H. & J.Y.)

Academic Editors: Xiangchun Xuan and Shizhi Qian
Received: 23 September 2016; Accepted: 9 January 2017; Published: 16 January 2017

Abstract: A giant unilamellar vesicle (GUV), with similar properties to cellular membrane, has been widely studied. Electroformation with its simplicity and accessibility has become the most common method for GUV production. In this work, GUV electroformation in devices with traditional 3D and new 2D electrode structures were studied with respect to the applied electric field. An optimal frequency (10 kHz in the 3D and 1 kHz in the 2D systems) was found in each system. A positive correlation was found between GUV formation and applied voltage in the 3D electrode system from 1 to 10 V. In the 2D electrode system, the yield of the generated GUV increased first but decreased later as voltage increased. These phenomena were further confirmed by numerically calculating the load that the lipid film experienced from the generated electroosmotic flow (EOF). The discrepancy between the experimental and numerical results of the 3D electrode system may be because the parameters that were adopted in the simulations are quite different from those of the lipid film in experiments. The lipid film was not involved in the simulation of the 2D system, and the numerical results matched well with the experiments.

Keywords: electroformation; yield; monodispersity; lipid film

1. Introduction

Giant unilamellar vesicles (GUVs), a particular type of lipid vesicles, have been widely accepted as cellular membrane models because of their similar properties [1]. The last few decades have witnessed many methods being developed to prepare GUVs. Hydration, the original and simple method, is a completely spontaneous process because of natural flows resulting in very low formation efficiency. Gradually, many other methods were realized that introduced some external energy sources to accelerate the formation process and improve the formation efficiency significantly with the help of a faster convective flow. This kind of method included reverse evaporation [2], sonication [3,4],

electroformation [5], extrusion, etc. Electroformation, since first described by Angelova and Dimitrov in 1986, became the most common method for GUV production for its simplicity and accessibility [6]. Different from the hydration method, electroformation involves the presence of an external electric field following the hydration process of a dry lipid film deposited on a substrate.

In electroformation, the most widely used was a sandwiched chamber consisting of two plates of electrodes and a spacer held between them. Based on this, many effective methods have been developed in order to improve the monodispersity and yield of the formed vesicles. For example, microcontact printing based on microfabrication techniques allowed the patterning of controllable-sized lipids and then formed controllable-sized liposomes. Two kinds of microstamps have been used to date: polydimethylsiloxane (PDMS) stamps suitable for organic solvent-soluble lipids [7] and biocompatible hydrogel stamps suitable for aqueous solutions [8]. Analogously, fabricating arrays of microwells on the substrate and trying to achieve the same sized liposomes was another innovative method [9] that can be combined with some techniques such as the electrospray deposition (ESD) method to realize selective patterning of the lipid film. In addition, a coplanar interdigitated electrode system, often used in cell electromanipulation [10,11], micromixers, and micropumps [12,13], has also been used in electroformation [1,14]. Arrays of interdigitated electrodes on the substrate reduced the electrode interval to several tens of micrometers, and thus reduced the required voltage significantly. The last one (the coplanar interdigitated electrode system) appeared to obtain the best yield at present.

For different electroformation devices, the applied electric field also a critical factor is often overlooked. Some research simply mentioned that the frequency exceeding a few hundred Hertz would fail with electroformation and was generally fixed at 10 Hz [5,9]. As a matter of fact, a frequency of thousands of Hertz obtained a better result but a theoretical understanding remains unknown [1,15]. In this work, a traditional method of a 3D electrode system containing a top and bottom electrode and a spacer between them, and the most effective method of a 2D coplanar electrode system which was fabricated with many microelectrode arrays on the substrate were chosen to study experimentally with respect to the applied electric field. An optimal frequency was found in each system. In addition, positive correlation was found between GUV formation and the applied voltage in the 3D electrode system from 1 to 10 V, but was not found in the 2D electrode system. GUVs with a wide size distribution were formed in the 3D electrode system and was improved in the 2D electrode system in both yield and size distribution, which is consistent with those previous results. The experimental results were further confirmed by numerical simulation for the first time in which an optimal frequency was also found in each system.

2. Experimental

2.1. Materials

L-α-phosphatidylcholine (PC, 1,2-diacyl-sn-glycero-3-phosphocholine) and fluorescent dye (DiI, 1,1′-dihexadecyl-3,3,3′,3′-tetramethylindocarbo-cyanie perchlorate, ex/em: 549/564 nm, Molecular Probes) were purchased from Sigma-Aldrich (St. Louis, MO, USA). Glass slides, polydimethylsiloxane (PDMS) and polymethyl methacrylate (PMMA) were purchased from Kaivo (Zhuhai, China), Dow Corning (Midland, MI, USA), and Yikang (Shanghai, China), respectively. Sucrose (AR) was purchased from Sinopharm Chemical Reagent Co., Ltd. (Shanghai, China). Millipore Milli-Q water with a resistance of 18.25 MΩ·cm at 25 °C was used for solution preparation. All experiments were performed at 25 °C.

2.2. 3D Electrode System

The 3D electrode system was designed and constructed as schematically depicted in Figure 1a. It consisted of two indium tin oxide (ITO) planar electrodes (the red parts) and a sandwiched PDMS spacer (the blue part). The reactor consisted of a mixing chamber of 10 mm in diameter and 1 mm in height, and two channels of 2 mm in width. A curve side wall (2 mm radius and 65° angle) was used

to connect the mixing chamber and the channels in order to minimize the disturbance of the flow on the lipid film when loading the aqueous solution. The inlet and outlet were left open to avoid bubble formation when the experimental setup was completed. The miniaturized reactor was fabricated based on a well-established soft lithography technique following reference [16]. A PMMA mold was made first by a laser marking machine. A liquid mixture with PDMS and curing agent at a mass ratio of 10:1 was then poured into the PMMA mold, which was degassed to remove the air bubbles and cured at 70 °C for 2 h. The PDMS spacer was thus obtained by separating it from the PMMA mold. Finally, the PDMS spacer and a glass slide (10 cm × 10 cm) were treated with oxygen plasma for 30 s, and then were pressed together. The top glass slides were placed onto the PDMS spacer after lipid film formation to complete the preparation chip.

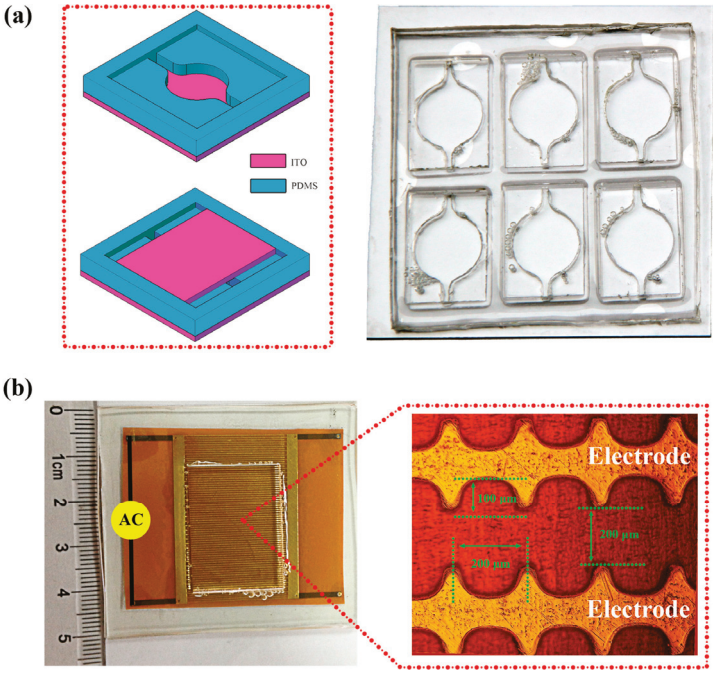

Figure 1. Illustration of the 3D and 2D experimental setup. (**a**) The 3D electrode system consists of a top and a bottom indium tin oxide (ITO) electrode separated by a polydimethylsiloxane (PDMS) spacer. The chip used in experiments contains six subcells and allows several groups of experiments to be carried out at the same time. (**b**) The 2D electrode system with many microelectrode arrays.

2.3. 2D Electrode System

A microchip with coplanar electrode arrays of symmetrical comb teeth shown in Figure 1b was designed and fabricated based on the flexible printed circuit board (FPCB) technique following reference [17]. The raised comb teeth in the polyimide substrate-based microchip formed a subcell for GUV formation on one hand, and strengthened the electric field on the other hand. The depth of the microchannel was fixed at 35 μm and other dimensions were listed in the diagram. The microelectrode arrays were fabricated on polyimide substrates which was glued on a glass slide. A PDMS spacer was fixed on the microelectrode arrays through curing some PDMS between them. Finally, a general coverslip was placed on the top of the PDMS spacer to hold aqueous solution.

2.4. Experimental Procedure

Solution of lipids at a concentration of 4 mg/mL composed of PC and DiI at a 99.5:0.5 mass ratio was prepared in diethyl ether. With the mixed organic solution, 20 μL was dripped onto the substrates of both the 3D and 2D electrode systems shown in Figure S1. The chips after film formation were placed in vacuum overnight to remove the solvent completely followed by covering the upper glasses. Finally, all the chambers were gently filled with 200 mm of sucrose solution and a sinusoidal alternating current (AC) signal was applied to induce vesicle formation.

3. Experimental Results

In these electroformation systems, the applied voltage decayed with increasing frequency since the bulk electrolyte was not a pure resistor but a load of resistance and capacitance. So the applied signal was always corrected by using an oscilloscope in each experiment.

3.1. GUV Electroformation in the 3D Electrode System

First, the amplitude was fixed at 12 V with varying frequency from 1 Hz to 10^5 Hz ($\times 10$ for the interval) to study the effect of the applied electric field on the GUV electroformation. At 10 Hz, an undesired result was obtained with sporadic super giant vesicles at the edge area and only swelling lipid membranes in the center. A better effect was observed as the frequency increased (Figure 2a, the GUV formation process in the edge and central area under 12 V and 1 kHz were displayed). Vesicles with a wide size distribution were generated, and big ones distributed at the edge area while small ones distributed in the center. This may be due to the non-uniform thickness of the lipid film in some degree. Both the monodispersity and the yield of the generated vesicles were continuously increased with increasing frequency until 10 kHz but did not change too much when the frequency continued to increase (Figure 2b). The experiment for each given frequency were carried out at least three times.

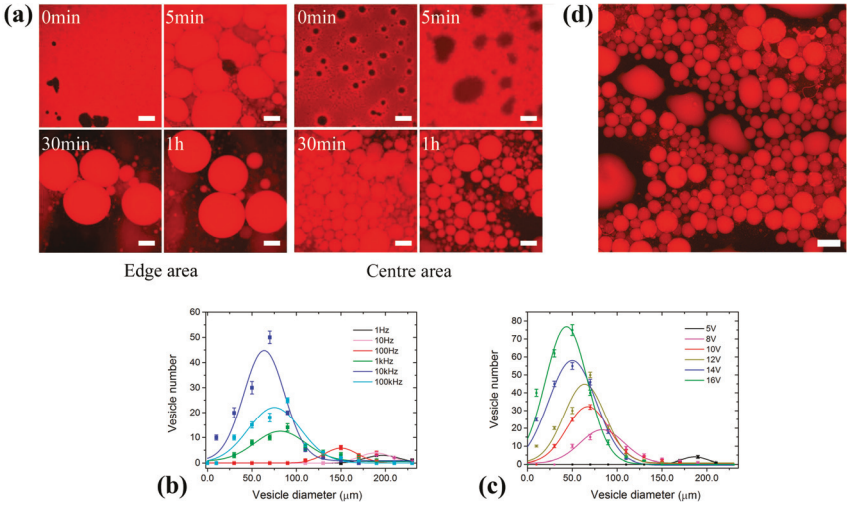

Figure 2. (**a**) The GUV formation process in the edge and central area, respectively, under the electric field of 12 V and 1 kHz. The deposited lipid film swelled into membrane domains first, then closed gradually and detached finally to form vesicles. (**b**,**c**) The scatter diagram and Gaussian fitting curves for GUV diameters at different frequencies (12 V) and voltages (10 kHz), respectively. Where, the GUV number was obtained by specifying a box (1 mm × 1 mm) at the center and edge, respectively, and then added them up. The GUVs with diameter within the interval of (0, 20) were classified into d = 10 μm, and so on. (**d**) The formed GUVs at 16 V and 10 kHz. The scale bar is 100 μm.

The frequency was then fixed at 10 kHz to study the effect of the applied voltage (Figure 2c). No vesicles except some swelling lipid membranes were formed in the center when the voltage was less than 5 V. More and more GUVs began to generate with increasing electric field strength and decreased in the average size when the amplitude was varied from 5 V to 16 V (Figure 2d, 16 V, 10 kHz).

3.2. GUV Electroformation in the 2D Electrode System

Preparation efficiency was improved significantly in the 2D electrode system (Figure 3a). When the amplitude was fixed at 8 V, the yield and the monodispersity of the formed GUVs increased with increasing frequency, and were maximized at 1 kHz (Figure 3b). When the frequency exceeded 1 kHz, both the yield and monodispersity of the formed GUVs decreased significantly. Compared with that in the 3D electrode system, the yield of the generated GUVs was obviously improved (Figures 2d and 3a). This may be due to the narrowed electrode interval in the 2D electrode system strengthening the electric field. The frequency was subsequently fixed at 1 kHz to study the effect of the applied voltage. It should be noted that the yield and the monodispersity of the formed vesicles increased when varying amplitude from 1 V to 10 V (Figure 3c). However, more and more lipid debris was observed gradually when the amplitude exceeds 10 V, which however has not been observed in the 3D electrode system.

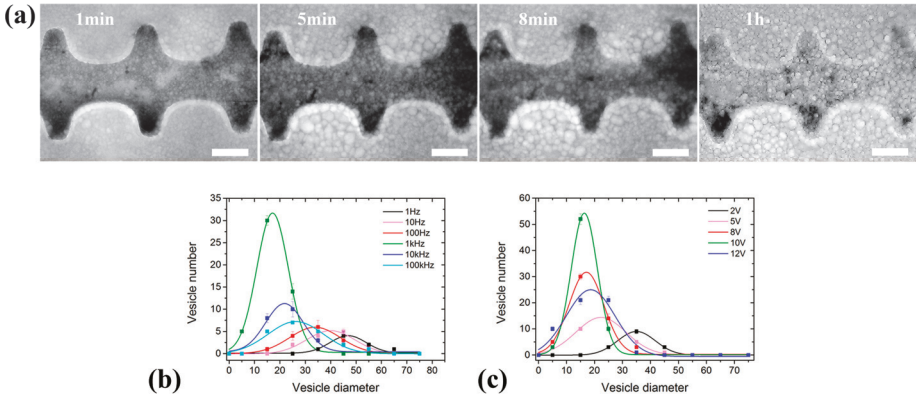

Figure 3. (**a**) The GUV formation process in the 2D electrode system at 8 V and 1 kHz. (**b**,**c**) The scatter diagram and Gaussian fitting curves for GUV diameters at different frequencies (8 V) and voltages (1 kHz), respectively. Where, the vesicle number was obtained in a subcell of the microchip. The GUVs with diameter within the interval of (0, 10) were classified into d = 5 μm, and so on. The scale bar is 100 μm.

In addition to the external electric field, the monodispersity of the generated GUVs in the 2D system is also related to the configuration of the microchip, such as the width of the electrode and the electrode interval. Therefore, a further improvement of the monodispersity of the generated GUVs could be achieved by optimizing the design of the microchip.

4. Numerical Analysis

Lipids deposited on the substrate rearrange to form regular bilayer sheets which would continuously fuse without external disturbance. The larger the external force, the earlier the inter-membrane fusion would be stopped, and the smaller and more GUVs would be formed. This phenomenon was captured by us and presented in another article. AC Electroosmotic flow (ACEO) of the aqueous solution, which is formed by the migration of net charges in the diffuse layer under a tangential electric field [11,18–20],

was widely accepted as the main driving force for electroformation [21], and often calculated by the Helmholtz-Smoluchowski (HS) velocity,

$$u = -\frac{\varepsilon_0 \varepsilon_r \zeta}{\mu}\mathbf{E} \tag{1}$$

where, ε_0 is the dielectric constant of the vacuum (8.85×10^{-12} F/m) and ε_r, μ are the relative dielectric constant and viscosity of the solution, respectively. $\mathbf{E}$ and ζ are the electric field vector and zeta potential, respectively. Two models in this work were built for calculating the EOF in the preparation chamber. The load the lipid film experienced from the ACEO was calculated by

$$\mathbf{T}_s = -n \cdot (-p\mathbf{I} + \mu(\nabla \mathbf{u})) \tag{2}$$

which was a sum of pressure and viscous forces and was used to characterize the effect of the applied electric field on GUV electroformation. The larger this load, the larger the yield of the generated GUVs.

In the 3D electrode system, the functional electric double layer (EDL) was formed near the chamber wall (made of PDMS) ignoring the deformation of the lipid film shown as Figure 4a. The formed EOF under an AC field thus depended on the zeta potential (ζ) of the chamber wall which was usually considered as uniform and constant under some assumptions [22] and was set to 50×10^{-3} V in this work. In the 2D electrode system, the AC applied field might act on its own induced diffuse charges near a polarizable electrode (Figure 4b). Compared with the 3D electrode system, the 2D one could concentrate the electric field on the substrate and the functional zeta potential was much higher related to the applied voltage.

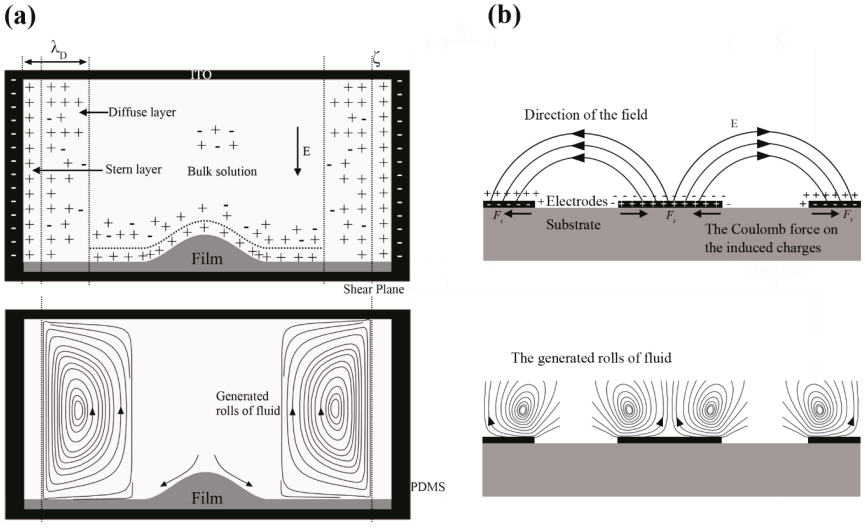

Figure 4. The formation mechanism of the ACEO in the 3D (**a**) and 2D (**b**) electrode system.

The conductivity of the used aqueous solution (200 mm sucrose solution) was measured by using the conductivity detector (METTLER TOLEDO, Columbus, OH, USA) which was 5×10^{-4} S/m. The properties of the liquid were assumed to be constant because the Joule-heating produced by the applied electric field can be neglected when the conductivity was so low. The properties of the aqueous solution, such as the relative dielectric constant of the solution ε_r ~80, density ρ ~1000 kg/m^3, viscosity μ ~9×10^{-4} Pa·s, temperature T ~293.15 K, and the dielectric constant of the lipid film ε_m ~5, were adopted and assumed to be constant. The thickness of lipid film was measured by a homemade surface

plasmon resonance (SPR) imaging device [23]. During the detection, the organic solution of the lipid mixture was diluted 1000 times to ensure the film thickness within the effective detection range of the device. The results were shown in Figure 5 and the average thickness of the lipid film d_m was 2 μm and assumed to be flat in the numerical simulation.

In addition, it should be noted that the lipid film covered the whole substrate of the 3D electrode system (Figure S1a). The complex impedances of the lipid film is $Z_m = 1/(j\omega C_m)$, $C_m = \varepsilon_0 \varepsilon_m / d_m$ is the capacitance of the lipid film. The complex impedances of the EDL are $Z_D = 1/(j\omega C_D)$ and $C_D = \varepsilon_0 \varepsilon_r / d_D$ and d_D is the capacitance and the thickness of the EDL near the electrode surfaces, respectively. Together with d_m/d_D ~10^3 and $\varepsilon_m/\varepsilon_r$ ~10, the impedance of the lipid film is thus several orders of magnitude (>10^2) larger than that of the EDL. Considering the lipid film and EDL are two capacitors and in series in the 3D electrode system, the EDL can thus be neglected. Whereas, in the 2D electrode system, the lipid film only deposited in the electrode intervals (Figure S1b) and did not affect the electric circuit thus could be neglected. Overall, the model of the 3D electrode system consists of a resistance (the bulk solution) and a capacitor (the lipid film) in series, and so does the model of the 2D one (the bulk solution and the EDL). The lipid film in the 3D system, because of its infinitesimal thickness compared with the bulk solution, an effective boundary condition was thus necessary to avoid failure on meshing, as well as the EDL in the 2D electrode system. Laminar flow was adopted in both models because the Reynolds number is extremely low [12,24]. All the calculations were carried out in a commercial finite element package, COMSOL Multiphysics 4.4 (COMSOL Inc., Los Angeles, CA, USA).

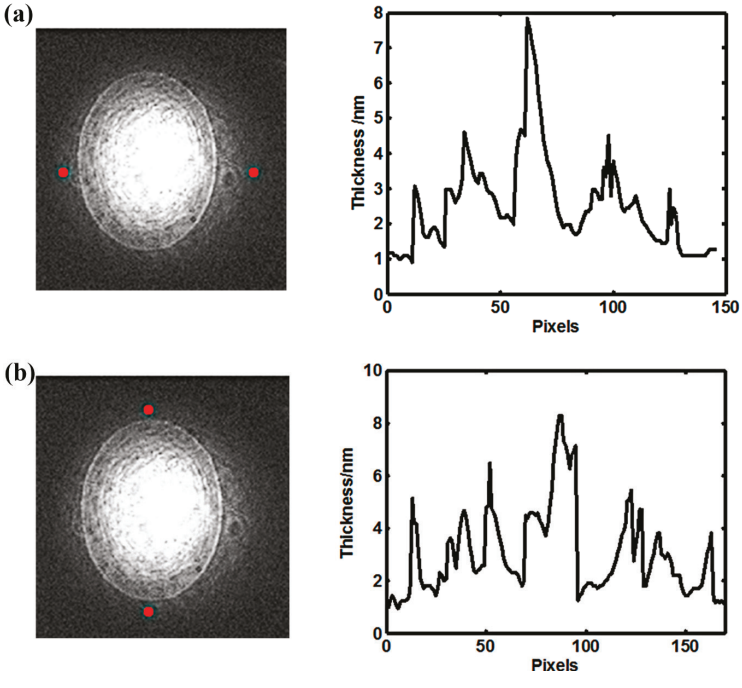

Figure 5. The thickness distribution of the lipid film deposited on the substrate including the transverse distribution (**a**) and the vertical distribution (**b**).

4.1. Modeling of the Systems

4.1.1. The 3D Electrode System

The cylindrical cell in the 3D electrode system, because of its characteristic of symmetry, was simplified into a 2D symmetric model. Only the shaded area was calculated and all the results could be obtained by rotating this plane about *z*-axis (Figure 6a). On the bottom electrode, the film and the electrode were combined into a boundary, and a Robin-type boundary condition which involved the conductivity, permittivity, and thickness of the film was used. The conductivity of the aqueous solution (5×10^{-4} S/m) was larger than that of the lipid film (~10^{-6} S/m [25], and ~5×10^{-7} [26,27]) by several orders of magnitude. The conductivity property of the lipid film was thus neglected during the computation.

Equations in the frequency domain in *Electric Currents* were used to obtain the steady sinusoidal response to the external AC signal [28–30]. The governing equation for the electric field in the frequency domain can be expressed as:

$$\nabla \cdot (\sigma + j\omega\varepsilon)\nabla\widetilde{\phi} = 0 \tag{3}$$

where $\widetilde{\phi}$ was the phasor of electric potential which was a complex with $\phi = \mathrm{Re}\left(\widetilde{\phi}e^{j\omega t}\right)$, and $\omega = 2\pi f$ was the angular frequency of the AC signal. When neglecting the dielectric properties of the solution, Equation (1) can be simplified as:

$$\nabla^2\widetilde{\phi} = 0 \tag{4}$$

As the lipid film was deposited on the bottom surface, the Robin-type boundary condition $\widetilde{\phi}$ was imposed on the bottom electrode surface,

$$\frac{\widetilde{\phi} - \widetilde{\phi}_0}{Z_m} = \sigma\left(\hat{n} \cdot \nabla\widetilde{\phi}\right) \tag{5}$$

therefore,

$$\widetilde{\phi} = \widetilde{\phi}_0 + \sigma Z_m\left(\hat{n} \cdot \nabla\widetilde{\phi}\right) \tag{6}$$

and no lipid film was on the top surface, then the boundary condition on the top electrode was set to $\widetilde{\phi} = -\widetilde{\phi}_0$. The PDMS wall was considered as insulated, $\hat{n} \cdot \nabla\widetilde{\phi} = 0$, shown in Figure 6a. Here, $\widetilde{\phi}_0$ was the amplitude of the applied AC signal with $\phi_0 = \mathrm{Re}\left(\widetilde{\phi}_0 e^{j\omega t}\right)$, and $\hat{n}$ was the unit vector normal to the membrane surface.

Due to extremely low Reynolds number for the flow, the Stokes equation was used to describe the flow field:

$$\nabla \cdot \mathbf{u} = 0 \tag{7}$$

$$-\nabla p + \mu\nabla^2\mathbf{u} = 0 \tag{8}$$

with a boundary condition of the HS slip velocity on the PDMS wall [31],

$$u_z = -\frac{\varepsilon_0\varepsilon_r\zeta}{\mu}\widetilde{\mathbf{E}}_t = \frac{\varepsilon_0\varepsilon_r\zeta}{\mu}\left[\mathrm{Re}\left(\frac{\partial\widetilde{\phi}}{\partial z}\right) + \mathrm{Im}\left(\frac{\partial\widetilde{\phi}}{\partial z}\right)\right] \tag{9}$$

$$u_r = 0 \tag{10}$$

and no slip on the two electrode surfaces. Here u was the time-averaged velocity field with z component u_z, and r component u_r. p was the pressure, and $\widetilde{\mathbf{E}}_t$ was the z component of the electric field vector near the PDMS wall.

4.1.2. The 2D Electrode System

The length of the microelectrode was infinite compared with the electrode intervals within the 2D electrode system, which was thus simplified as a vertically 2D model as that in Figure 6b. Average values of the electrode width (200 μm) and interval (300 μm) were used. ACEO flow near the electrode surface was formed and may be much stronger than the EOF formed in the 3D electrode system because of a larger zeta potential. Similarly to the 3D electrode system, a Robin-type boundary condition was also applied to the EDL here.

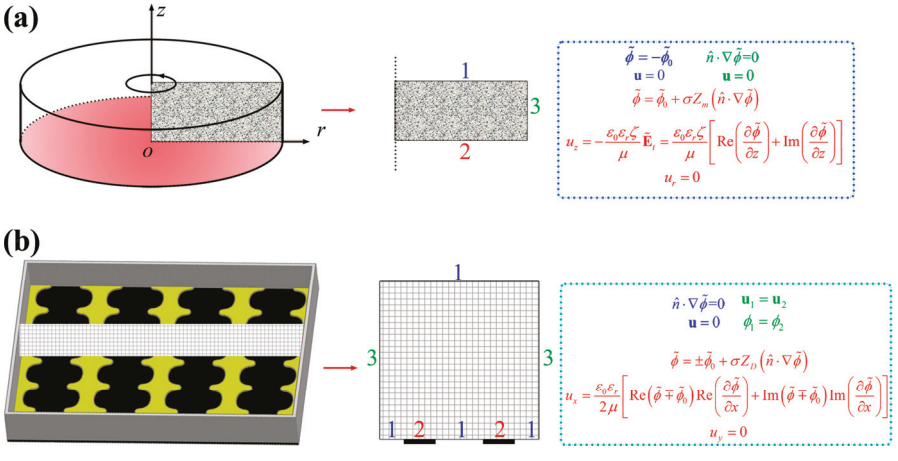

Figure 6. The schematic diagrams of the 3D (**a**) and 2D (**b**) electrode system, and their corresponding boundary conditions.

Equations in the frequency domain were also used here similar to that of the 3D electrode system, with the Robin-type boundary condition $\tilde{\phi}$ at the electrode surfaces,

$$\tilde{\phi} = \pm\tilde{\phi}_0 + \sigma Z_D\left(\hat{n}\cdot\nabla\tilde{\phi}\right) \tag{11}$$

as well as periodic condition and electric insulation on the vertical boundaries and the remaining boundaries, respectively. Boundary conditions for the flow field included a HS slip velocity parallel to the electrode surfaces,

$$u_x = \frac{\varepsilon_0\varepsilon_r}{2\mu}\left[\mathrm{Re}\left(\tilde{\phi}\mp\tilde{\phi}_0\right)\mathrm{Re}\left(\frac{\partial\tilde{\phi}}{\partial x}\right)+\mathrm{Im}\left(\tilde{\phi}\mp\tilde{\phi}_0\right)\mathrm{Im}\left(\frac{\partial\tilde{\phi}}{\partial x}\right)\right] \tag{12}$$

$$u_y = 0 \tag{13}$$

and periodic flow condition and no slip on the vertical boundaries and the remaining boundaries, respectively.

4.2. Simulation Results and Discussion

4.2.1. The 3D Electrode System

The impact of frequency (from 1 Hz to 1 GHz, ×10 for interval) was calculated when ϕ_0 was fixed at 12 V. Vortexes were formed in the preparation chamber. Most of the applied voltage dropped across the lipid film and the bulk electrolyte when the frequency was lower and higher than 100 kHz, respectively. When the frequency was lower than 100 kHz, the electric field in the bulk electrolyte was

reversed with respect to the applied electric field, as well as the formed vortex shown in Figure 7a. This may be due to the lipid film being treated as a capacitor in this work which would store the energy and discharge to the solution at low frequency. It implies that the reversal of the direction of the formed ACEO can be induced by the frequency. The maximum value of the load (T_s) the lipid film experienced from the ACEO was shown in Figure 7b. It maximized at 100 kHz, which suggested that a characteristic frequency did exist in the 3D electrode system. In addition, the ACEO also maximized at this frequency, which was not consistent with the previous result that ACEO predominated at low frequencies and attenuated with increasing frequency [22].

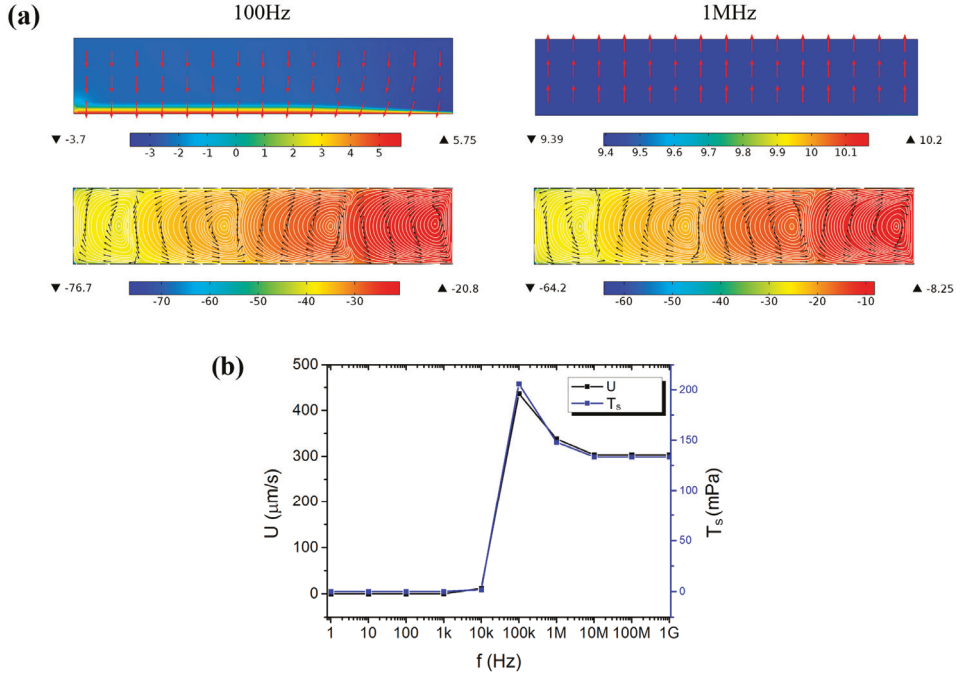

Figure 7. Numerical results of the 3D electrode system. (**a**) The electric field and the formed EOF in a vertical section at 100 Hz and 1 MHz, respectively. The surface plot used a logarithmic scale. (**b**) The frequency-dependent maximum value of the velocity amplitude (U) and the load (T_s) the lipid film experienced from the ACEO.

However, the characteristic frequency of 100 kHz was different from the experimental result where the optimal frequency was 10 kHz. This may be due to the present model adopting the properties of cell membrane, while the lipid film in experiments was not regular multiple bilayers but lipid aggregates with many interspaces. The aggregate interspaces would allow electrolyte to penetrate through and lead to a large discrepancy in the electrical properties (conductivity and dielectric constant) from the cell membrane. In addition, when the frequency exceeded the characteristic one (100 kHz), T_s slightly decreased and in some degree confirmed the experimental result that the yield of the formed GUVs did not decrease that much when the frequency exceeded 10 kHz. The characteristic frequency was expressed previously as [28]:

$$\omega_0 \approx \frac{\sigma}{\varepsilon_0 \varepsilon_m} \frac{d_m}{h} \tag{14}$$

where h is the electrode gap.

4.2.2. The 2D Electrode System

The impact of frequency (from 1 Hz to 1 GHz, ×10 for interval) was also calculated in the 2D electrode system when ϕ_0 was fixed at 3.6 V in order to obtain the same external electric field as that in the 3D one (1.2×10^4 V/m). Two symmetric counter-rotating rolls of fluid flow were formed on each electrode surface. Like that of the 3D electrode system, most of the applied voltage dropped across the EDL and the bulk electrolyte when the frequency was lower and higher than 1 kHz, respectively. When the frequency was lower than 1 kHz, the electric field in the bulk electrolyte was reversed with respect to the applied one, as well as the formed ACEO (Figure 8a). The maximum value of the load the lipid film experienced (T_s) was shown in Figure 8b and maximized at 1 kHz. This suggested that a characteristic frequency also did exist in the 2D electrode system. When the frequency exceeded the characteristic one (1 kHz), T_s decreased sharply and in some degree confirmed the experimental result that the yield of the generated GUVs decreased very remarkably when the frequency exceeded 1 kHz.

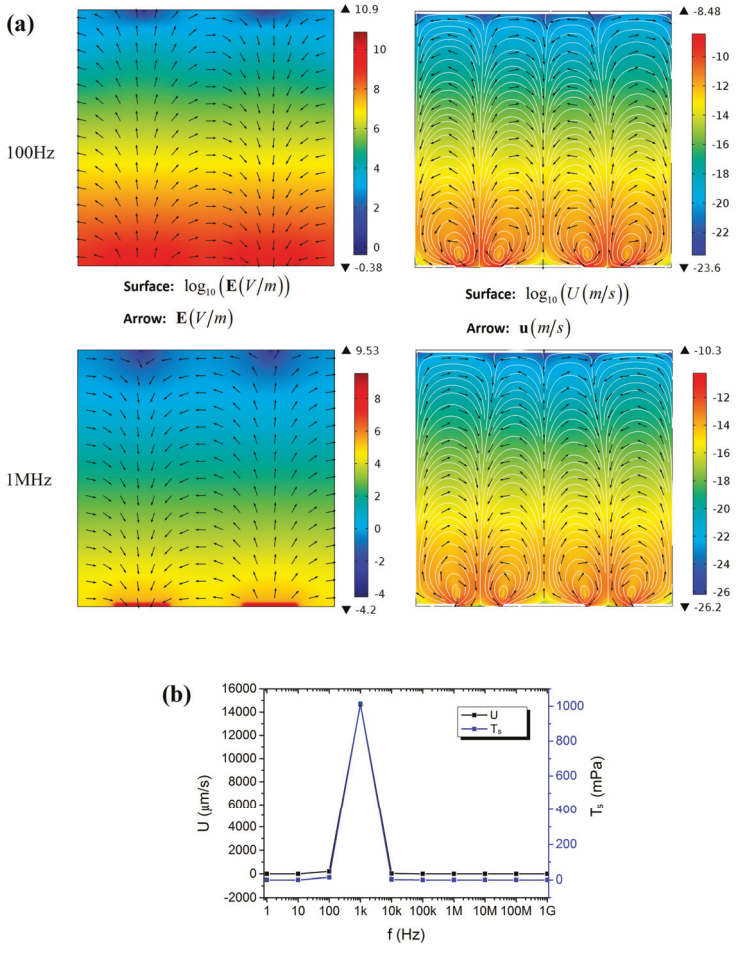

Figure 8. Simulation results of the 2D electrode system. (**a**) The electric field and the formed EOF in a vertical section at 100 Hz and 1 MHz, respectively. The surface plot used a logarithmic scale. (**b**) The frequency-dependent maximum value of the velocity amplitude (U) and the load (T_s) the lipid film experienced from the ACEO.

It should also be noted that the simulation results of the 3D and 2D electrode systems were different even though the same external electric field was applied. At the characteristic frequency, the load the lipid film experienced in the 2D electrode system was much higher than that in the 3D one. Therefore, more GUVs were formed in the 2D electrode system than in the 3D one, and a saturation phenomenon was observed in the 2D but not in the 3D electrode system experimentally. As mentioned above, this may be also due to the strengthened electric field by the narrowed electrode interval in the 2D electrode system.

5. Conclusions

Traditional 3D and a 2D electrode systems were investigated experimentally with respect to the applied electric field on electroformation of GUVs. An optimal frequency was found in each system (10 kHz in 3D system and 1 kHz in 2D system) under which a good yield and monodispersity of the generated vesicles can be achieved. This was not consistent with those reported results that low frequency was more suitable for GUV electroformation. The results were confirmed further by numerical modeling in which a characteristic frequency did exist for the resistor–capacitor (RC) circuit in each system (100 kHz in 3D system and 1 kHz in 2D system). Under this frequency, the load the lipid film experienced from the formed ACEO can be maximized. The discrepancy between the experimental (10 kHz) and numerical (100 kHz) results in the 3D electrode system were attributed to the uncertainty of the lipid film properties, since the lipid film in GUV electroformation was greatly different from the cell membrane. The 2D electrode system did not involve the lipid film and thus matched with the experiments better.

Supplementary Materials: The following are available online at www.mdpi.com/2072-666X/8/1/24/s1, Figure S1: Lipid film deposited on the substrate of the 3D and 2D electrode system, respectively.

Acknowledgments: This work was supported by the National Natural Science Foundation of China (Nos. 81371691, 31571005, 81501617), the Fundamental Research Funds for the Central Universities (Nos. 106112016CDJZR238807, 106112015CDJZR235514), and the Program of International S & T Cooperation (No. 2014DFG31380).

Author Contributions: N.H. and J.Y. conceived and designed the experiments; Q.W. and X.Z. performed the experiments; Z.W. and J.X. analyzed the data; T.F. and X.C. performed simulation; Z.Y. contributed 2D microchip fabrication; Q.W. wrote the paper; N.H. and J.Y. revised the paper.

Conflicts of Interest: The authors declare no conflict of interest.

References

1. Bi, H.; Yang, B.; Wang, L.; Cao, W.; Han, X. Electroformation of giant unilamellar vesicles using interdigitated ITO electrodes. *J. Mater. Chem. A* **2013**, *1*, 7125–7130. [CrossRef]
2. Szoka, F.; Papahadjopoulos, D. Procedure for preparation of liposomes with large internal aqueous space and high capture by reverse-phase evaporation. *Proc. Natl. Acad. Sci. USA* **1978**, *75*, 4194–4198. [CrossRef] [PubMed]
3. Johnson, S. The effect of charge and cholesterol on the size and thickness of sonicated phospholipid vesicles. *Biochim. Biophys. Acta Biomembr.* **1973**, *307*, 27–41. [CrossRef]
4. Helfrich, W. The size of bilayer vesicles generated by sonication. *Phys. Lett. A* **1974**, *50*, 115–116. [CrossRef]
5. Wang, Z.; Hu, N.; Yeh, L.-H.; Zheng, X.; Yang, J.; Joo, S.W.; Qian, S. Electroformation and electrofusion of giant vesicles in a microfluidic device. *Colloids Surf. B Biointerfaces* **2013**, *110*, 81–87. [CrossRef] [PubMed]
6. Angelova, M.I.; Dimitrov, D.S. Liposome electroformation. *Faraday Discuss. Chem. Soc.* **1986**, *81*, 303–311. [CrossRef]
7. Taylor, P.; Xu, C.; Fletcher, P.D.; Paunov, V.N. A novel technique for preparation of monodisperse giant liposomes. *Chem. Commun.* **2003**, 1732–1733. [CrossRef]
8. Kang, Y.J.; Wostein, H.S.; Majd, S. A simple and versatile method for the formation of arrays of giant vesicles with controlled size and composition. *Adv. Mater.* **2013**, *25*, 6834–6838. [CrossRef] [PubMed]
9. Le Berre, M.; Yamada, A.; Reck, L.; Chen, Y.; Baigl, D. Electroformation of giant phospholipid vesicles on a silicon substrate: Advantages of controllable surface properties. *Langmuir* **2008**, *24*, 2643–2649. [CrossRef] [PubMed]
10. Ramos, A.; Morgan, H.; Green, N.; Castellanos, A. AC electrokinetics: A review of forces in microelectrode structures. *J. Phys. D Appl. Phys.* **1998**, *31*, 2338. [CrossRef]

11. Oh, J.; Hart, R.; Capurro, J.; Noh, H.M. Comprehensive analysis of particle motion under non-uniform AC electric fields in a microchannel. *Lab Chip* **2009**, *9*, 62–78. [CrossRef] [PubMed]
12. Song, H.; Cai, Z.; Noh, H.M.; Bennett, D.J. Chaotic mixing in microchannels via low frequency switching transverse electroosmotic flow generated on integrated microelectrodes. *Lab Chip* **2010**, *10*, 734–740. [CrossRef] [PubMed]
13. Studer, V.; Pépin, A.; Chen, Y.; Ajdari, A. An integrated AC electrokinetic pump in a microfluidic loop for fast and tunable flow control. *Analyst* **2004**, *129*, 944–949. [CrossRef] [PubMed]
14. Tonry, C.; Patel, M.; Bailey, C.; Desmuliez, M.; Cargill, S.; Yu, W. Modelling of the electric field assisted capillarity effect used for the fabrication of hollow polymer microstructures. In Proceedings of the 2012 13th International Conference on Thermal, Mechanical and Multi-Physics Simulation and Experiments in Microelectronics and Microsystems (EuroSimE), Cascais, Portugal, 16–18 April 2012.
15. Politano, T.J.; Froude, V.E.; Jing, B.; Zhu, Y. AC-electric field dependent electroformation of giant lipid vesicles. *Colloids Surf. B Biointerfaces* **2010**, *79*, 75–82. [CrossRef] [PubMed]
16. Li, W.; Wang, Q.; Yang, Z.; Wang, W.; Cao, Y.; Hu, N.; Luo, H.; Liao, Y.; Yang, J. Impacts of electrical parameters on the electroformation of giant vesicles on ITO glass chips. *Colloids Surf. B Biointerfaces* **2016**, *140*, 560–566. [CrossRef] [PubMed]
17. Liu, L.; Zhao, L.; Yang, J.; Wan, X.; Hu, N.; Yeh, L.H.; Joo, S.W.; Qian, S. Low-voltage pulsed electric field sterilization on a microfluidic chip. *Electroanalysis* **2013**, *25*, 1301–1309. [CrossRef]
18. Ai, Y.; Zhang, M.; Sang, W.J.; Cheney, M.A.; Qian, S. Effects of electroosmotic flow on ionic current rectification in conical nanopores. *J. Phys. Chem. C* **2010**, *114*, 3883–3890. [CrossRef]
19. Qian, S.; Bau, H.H. A chaotic electroosmotic stirrer. *Anal. Chem.* **2002**, *74*, 3616–3625. [CrossRef] [PubMed]
20. Qian, S.; Bau, H.H. Theoretical investigation of electro-osmotic flows and chaotic stirring in rectangular cavities. *Appl. Math. Model.* **2005**, *29*, 726–753. [CrossRef]
21. Okumura, Y.; Zhang, H.; Sugiyama, T.; Iwata, Y. Electroformation of giant vesicles on a non-electroconductive substrate. *J. Am. Chem. Soc.* **2007**, *129*, 1490–1491. [CrossRef] [PubMed]
22. Yang, C.; Ooi, K.; Wong, T.; Masliyah, J. Frequency-dependent laminar electroosmotic flow in a closed-end rectangular microchannel. *J. Colloid Interface Sci.* **2004**, *275*, 679–698.
23. Liu, L.; Wang, Q.; Yang, Z.; Wang, W.; Hu, N.; Luo, H.; Liao, Y.; Zheng, X.; Yang, J. Characterization of lipid films by an angle-interrogation surface plasmon resonance imaging device. *Colloids Surf. B Biointerfaces* **2015**, *128*, 287–295. [CrossRef] [PubMed]
24. Sasaki, N.; Kitamori, T.; Kim, H.-B. AC electroosmotic micromixer for chemical processing in a microchannel. *Lab Chip* **2006**, *6*, 550–554. [CrossRef] [PubMed]
25. Sens, P.; Isambert, H. Undulation instability of lipid membranes under an electric field. *Phys. Rev. Lett.* **2002**, *88*, 128102. [CrossRef] [PubMed]
26. Pucihar, G.; Krmelj, J.; Reberšek, M.; Napotnik, T.B.; Miklavčič, D. Equivalent pulse parameters for electroporation. *IEEE Trans. Biomed. Eng.* **2011**, *58*, 3279–3288. [CrossRef] [PubMed]
27. Pucihar, G.; Miklavcic, D. A numerical approach to investigate electrofusion of cells of different sizes. In *5th European Conference of the International Federation for Medical and Biological Engineering*; Springer: Berlin/Heidelberg, Germany, 2011.
28. Urbanski, J.P.; Levitan, J.A.; Burch, D.N.; Thorsen, T.; Bazant, M.Z. The effect of step height on the performance of three-dimensional AC electro-osmotic microfluidic pumps. *J. Colloid Interface Sci.* **2007**, *309*, 332–341. [CrossRef] [PubMed]
29. Hong, F.; Bai, F.; Cheng, P. A parametric study of electrothermal flow inside an AC ewod droplet. *Int. Commun. Heat Mass Transf.* **2014**, *55*, 63–70. [CrossRef]
30. Hong, F.; Bai, F.; Cheng, P. Numerical simulation of AC electrothermal micropump using a fully coupled model. *Microfluid. Nanofluid.* **2012**, *13*, 411–420. [CrossRef]
31. Reppert, P.M.; Morgan, F.D. Frequency-dependent electroosmosis. *J. Colloid Interface Sci.* **2002**, *254*, 372–383. [CrossRef] [PubMed]

micromachines

MDPI

Article

Electrokinetic Phenomena in Pencil Lead-Based Microfluidics

Yashar Bashirzadeh, Venkat Maruthamuthu and Shizhi Qian *

Department of Mechanical & Aerospace Engineering, Old Dominion University, Norfolk, VA 23529, USA; ybash001@odu.edu (Y.B.); vmarutha@odu.edu (V.M.)

* Correspondence: sqian@odu.edu; Tel.: +1-757-683-3304

Academic Editors: Xiangchun Xuan and Nam-Trung Nguyen

Received: 2 October 2016; Accepted: 12 December 2016; Published: 15 December 2016

Abstract: Fabrication of microchannels and associated electrodes to generate electrokinetic phenomena often involves costly materials and considerable effort. In this study, we used graphite pencil-leads as low cost, disposable 3D electrodes to investigate various electrokinetic phenomena in straight cylindrical microchannels, which were themselves fabricated by using a graphite rod as the microchannel mold. Individual pencil-leads were employed as the micro-electrodes arranged along the side walls of the microchannel. Efficient electrokinetic phenomena provided by the 3D electrodes, including alternating current electroosmosis (ACEO), induced-charge electroosmosis (ICEO), and dielectrophoresis (DEP), were demonstrated by the introduced pencil-lead based microfluidic devices. The electrokinetic phenomena were characterized by micro-particle image velocimetry (micro-PIV) measurements and microscopy imaging. Highly efficient electrokinetic phenomena using 3D pencil-lead electrodes showed the affordability and ease of this technique to fabricate microfluidic devices embedded with electrodes for electrokinetic fluid and particle manipulations.

Keywords: alternating current electroosmosis (ACEO); induced-charge electroosmosis (ICEO); dielectrophoresis (DEP); 3D electrode

1. Introduction

Microfluidic technology has become an important multi-disciplinary field for controlling and sensing in areas as diverse as electronics and tissue engineering. Small volumes of solvent, samples and reagents have been transported through microchannels embedded in a chip, and, additionally, micro-electrodes of different materials have been used for manipulation, control and/or detection of fluids and samples [1,2].

Electrokinetic transport processes such as electroosmosis, induced charge electroosmosis (ICEO) and dielectrophoresis (DEP) using electric fields have become important techniques to manipulate fluids and particles in various microfluidic applications [3,4]. ICEO flow is a nonlinear electro-osmotic flow and typically occurs around a conductive surface or floating electrode under an external direct current (DC) or low frequency alternating current (AC) electric field [5]. Alternating current electroosmosis (ACEO) flow is generated at electrode surfaces subject to an applied AC electric field [6]. DEP refers to the motion of particles caused by dielectric polarization effects induced by a spatially non-uniform electric field [7]. The aforementioned electrokinetic phenomena, including ACEO, ICEO and DEP, have been widely used for pumping, mixing, trapping, focusing and separating samples/particles in various microfluidic applications [8–10]. To achieve the aforementioned electrokinetic phenomena, micro-electrodes must be fabricated within the microfluidic device for either applying the electric field (in ACEO and DEP applications) or inducing charges at the surface of the floating electrode (in ICEO applications).

Several methods for fabricating micro-electrodes in microfluidic devices have been developed in the literature. Common methods use photolithography followed by metal deposition and the lift-off process [11,12]. A conventional deposition process is sputtering, and it requires expensive equipment to deposit the metal or alloy film on the substrate. Another common conventional process electroplates a superior metal on a base metal. Even though this process can be low in cost for a thin film of deposited metal, it is costly and time-consuming for thicker coats of metal. Uniformity of such coats on the base metal has also been an issue [13]. An alternative approach injects low melting point liquid metals or alloys in a mold aligned to the microchannel [14]. Doped silicon [15] and insulating posts have also been used to produce non-uniform fields generated by metal electrodes for DEP applications. Insulating posts require application of high voltages to the system [16], and the cost of fabrication using doped silicon is a concern [17].

Use of low-cost and biocompatible 3D electrodes possessing good mechanical properties has always been of great interest in microfluidics to simplify the laborious fabrication process and lower its cost while providing efficient outputs. Use of 3D carbon-based electrodes [18] can be suitable for this purpose. Glass-like 3D carbon electrodes, for example, have been used to manipulate particles and biomolecules under low voltages [19,20]. Glass-like carbon electrodes can be fabricated by the carbonization process [20]. To achieve this, a two-step photolithography process was used to fabricate the precursor SU-8 structures, which were then converted into 3D carbon electrodes through pyrolysis, heating the structures up to high temperatures (900 °C for SU-8) [21]. Low voltage DEP using carbon electrodes fabricated using this low-cost method combines advantages of metal electrodes and insulator-based DEP. Even though carbon electrodes are electrically more resistive than highly conductive metals such as gold, there are some advantages associated with them over metals. Carbon possesses excellent mechanical properties and polarizes at lower voltages while minimizing the possibility of sample electrolysis [17]. Therefore, accessible and ready-made yet low-cost allotropes of carbon can further facilitate microfluidic device fabrication. Sub-mm pencil-lead, mechanical pencil core made of graphite mixed with clay, sounds promising for achieving this goal. Electrically, graphite is a semi-metal, conductive in its basal plane and an insulator normal to the basal plane [22]. Its special properties have led to several applications in electronics, semiconductor and energy industries. Its high heat and electrical conductivity, durability, and stability have provided researchers with electrodes capable of working at a wide range of operating conditions. In small scale applications, graphite pencil cores are capable of playing important roles in paper-based electronics [23,24] and microfluidics [25,26]. Graphite rods are fabricated in various types and diameters ranging from 200 micrometers to a few millimeters suitable for microfluidic applications. They have been embossed in a channel substrate of a planar fuel cell or mounted in the machined cavity of a 3D array fuel cell to serve as electrodes [27].

The present paper uses 3D graphite pencil-leads to provide a straightforward single-step device fabrication method complementing other challenging conventional fabrication techniques that require multiple steps and processes. For instance, conventional photolithography techniques pattern expensive photoresists, such as SU-8, on clean surfaces as molds. These molds provide only vertical sidewalls when they are exposed to ultraviolet (UV) light and developed. As mentioned, conventional electrode fabrication processes deposit a thin layer of metal such as gold on a substrate surface to be used often as a planar electrode. Here, pencil-leads provided us with simple 3D side-wall electrodes that could be aligned with the microchannel. The major advantage of using 3D electrodes as bulky polarizable objects over planar conductive surfaces is the generation of more efficient electrokinetic phenomena. Faster ICEO and ACEO flows using 3D electrodes [28], and superior filtering efficiencies of DEP using 3D carbon electrodes [21] compared to that generated by planar metal electrodes are some examples. Due to the ready-made pencil-leads being rigid rods, they also served as microchannel molds (a blunt end needle can also be used for this purpose) without any need to use costly fabrication apparatuses such as sputtering machines in clean rooms. Use of these graphite rods as both molds and 3D electrodes enables us to fabricate cylindrical microchannels and apply electric fields at different directions to study the electrokinetic phenomena in polydimethylsiloxane

(PDMS)/glass or PDMS/PDMS microfluidic devices. Common conductive rods in microfluidic devices are wires, micro wires [29], and allotropes of carbon such as graphite [30]. Pencil-lead was used here as a highly conductive 3D electrode, since it is accessible and disposable, and can be aligned with an identical pencil-lead mold due to its rigidity. However, this comes with a drawback: pencil-leads are fragile and more likely to break. Here, the molds and electrodes were embedded into an elastomer stamp made of PDMS in a single-step process and the microchannel mold (central lead) was gently removed from the cured PDMS without breakage. The cured PDMS was simply bonded to the glass or PDMS substrate to complete the fabrication process. Electrokinetic phenomena including ICEO, ACEO, and DEP in the pencil-lead-based microfluidic device were illustrated and characterized by micro-particle image velocimetry (micro-PIV) measurement and microscopy imaging.

2. Experimental Methods

2.1. Device Fabrication

A simple single-step fabrication method was used here to fabricate a cylindrical channel with 3D bulky electrodes. The microfluidic device consisted of a microchannel, two reservoirs on both ends of the microchannel, and sidewall pencil-lead electrodes. As shown in Figure 1a, four coverslip stacks of the same height (2–5 mm) were placed in a Petri dish. A 0.3 or 0.5 mm pencil-lead (mirochannel mold) was placed at the center of the Petri dish on two coverslip stacks (reservoir molds) from both ends. Sidewall pencil-leads (electrodes) were placed on the other two coverslips. Their positions were adjusted so that they were perpendicular to the microchannel mold. PDMS (Sylgard184 Silicone ElastomerKit, Dow Corning Corp., Freeland, MI, USA) with prepolymer and curing agent weight ratio of 10:1 was cast in the Petri dish covering the molds and electrode array (position of pencil-leads can be readjusted in case they are displaced). PDMS was cured at room temperature after 36 h (curing on a hot plate is quicker, but it may lead to displacement of the leads if they are not fixed). As shown in Figure 1b, the cured PDMS containing the embedded molds and electrodes was gently peeled off, and the coverslip stacks were then removed. The central pencil-lead (mirochannel mold) was peeled off, and the sides of the cured PDMS were cut and removed so that the electrodes could be connected to the power supply. Two holes were then punched on top of the two reservoirs. In case some graphite remained in the microcochannel, it was cleaned and then rinsed with deionized (DI) water. Before bonding, we ensured that the microchannel was not blocked. Figure 1c shows the final fabrication step. The PDMS slab containing the microchannel and a glass slide were cleaned, treated and bonded. Flow inlet and outlet tubes connected to the reservoirs provided the fluid flow through the punched holes (in order for the tubes to be fixed in their positions, they can be connected to the reservoirs through small pieces of PDMS bonded to the reservoirs as shown in Figure 1c). Figure 1d shows the functionality of the microfluidic device before connecting the inlet and outlet tubes. As shown in the figure, food dye was used as a colorant to test the ability of the device in order to properly allow the fluid to pass through the microchannel. One can use multiple pencil-leads to form the mold of a more complicated microfluidic channel, and an optical microscope can be used to align pencil-leads in desired positions. For example, a microchannel with two inlets and outlets is fabricated for the DEP experiments, as shown in Section 3.3.

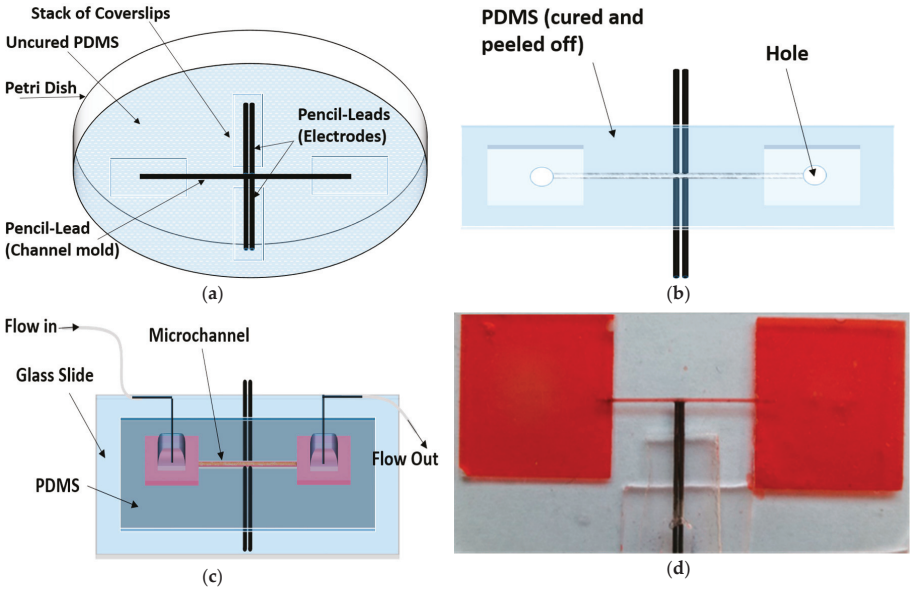

Figure 1. Device fabrication. (**a**) Pencil-leads were positioned on stacks of coverslips sitting on the Petri dish and the polydimethylsiloxane (PDMS) was cast and cured; (**b**) PDMS including the embedded pencil-leads and coverslips was gently peeled off and the coverslip stacks were removed. The unmolded PDMS was placed on the workbench with the side containing the reservoirs face up, and the central lead (microchannel mold) was removed. The sides of the cured PDMS were cut and removed so that the electrodes could be connected to the power supply. Then, holes were punched into the reservoirs; (**c**) the PDMS containing the microchannel was cleaned, treated and bonded to a treated clean glass slide. Finally, the inlet and outlet tubes were connected to the reservoirs (optionally, the tubes were connected to the reservoirs through small pieces of PDMS bonded to the parts of the device containing the holes in order for inlet and outlet tubes to be fixed tightly in their positions); (**d**) functionality of the microchannel was tested before connecting the tubes.

2.2. Flow Characterization by Micro-PIV

To examine electrokinetic phenomena in the pencil-lead-based microfluidic device, micro-PIV was used to quantify the fluid velocity field within the microchannel. In addition, 1 μm fluorescent micro-beads (Invitrogen, Eugene, OR, USA) suspended in the working fluid were used as flow tracers. Tween 20 (Thermo Fisher Scientific, Fremont, CA, USA) was also added to the suspension for reducing particle adhesion and for stable dispersion of tracer particles [31], and the suspension was sonicated to homogeneously disperse the particles in the fluid prior to the experiment. The microfluidic device was then placed on an inverted optical microscope (TE2000-U, Nikon Eclipse Ti, Nikon Instruments, Tokyo, Japan) equipped with a fluorescence light source and a high-resolution (1376 pixel × 1040 pixel) 15 Hz charge-coupled device (CCD) camera (PowerviewTM, TSI Inc., Shoreview, MN, USA) to capture the flow. Pressure-driven flows of fixed flow rates were provided by an infusion syringe pump (Harvard Apparatus, PHD 2000, Holliston, MA, USA). To generate electrokinetic flows, an AC function generator (Tektronix AFG 3102, Beaverton, OR, USA) was used to apply a sinusoidal AC electric field amplified by a high voltage amplifier (Tegam, Model 2340, Geneva, OH, USA) between the pencil-lead electrodes.

PIVlab [32] (Version 1.41), an open source MATLAB program (R2015b, MathWorks, Natick, MA, USA) for cross-correlation, was used to process the sequence of images taken from the fluorescent tracer particles. First, some image preprocessing such as defining a region of interest (ROI), creating masks and removing background noise prepared the image sequences for velocimetry. PIVlab then used

50% overlapped interrogation windows to quantify the displacement of particles between each pair of images with a certain time interval defined by the camera frame rate, resulting in a velocity vector field for each pair. PIVlab was able to post-process the obtained vector fields including interpolation of missing data, outlier removal and data smoothing as necessary. Ensemble-averaging the velocity vectors of all image pairs at each point resulted in the final averaged velocity vector field.

The micro-PIV measurement was validated by a steady pressure-driven flow passing through the cylindrical microchannel, which was provided by the syringe pump at a fixed flow rate. DI water was used as the working fluid and 1 μm carboxylate-modified fluorescent micro-beads suspended in the DI water were used as flow tracers. Figure 2a shows the velocity vector field of pressure-driven flow at a volume rate of 12 μL/h. Figure 2b demonstrates the validity of the velocity distribution when compared to the parabolic velocity profile of an incompressible laminar pipe flow with no slip on walls. R and u_{max} are the microchannel radius and the averaged maximum velocity (in the neighborhood of the centerline). The experimental data points show the average dimensionless velocities at each radial position. The error bars show the minimum and maximum dimensionless velocities of each radial position at different cross sections along the flow direction. As expected, micro-PIV provided less accurate information about velocities in the vicinity of the microchannel wall. Interrogation windows overlapped with the stationary surface regions (wall) is a source of this error [33].

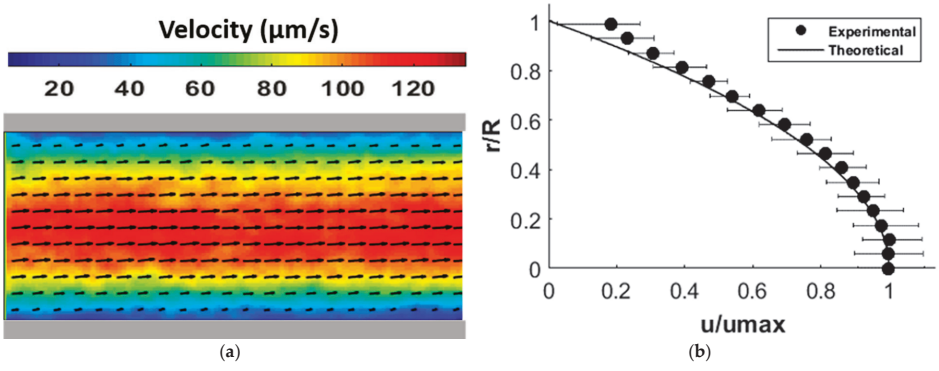

Figure 2. (**a**) Velocity distribution of pressure-driven flow with a volume flow rate of 12 μL/h through a microchannel 0.3 mm in diameter; (**b**) validation of the pressure-driven velocity field in (**a**).

3. Results

The main objective of the present study was simple fabrication of microchannels with embedded 3D sidewall electrodes (shown in black in Figures 3–6) to generate electrokinetic transport phenomena. We demonstrated ICEO, ACEO and DEP with the devices fabricated with the developed method. Since the pencil-lead is relatively big (0.3 to 0.5 mm), multiple experiments can be conducted in the same device.

3.1. ICEO

To achieve ICEO, the sidewall electrodes made of pencil-leads are floating, and an external AC electric field is applied through two pencil-leads inserted into the two holes of the reservoirs. In most of the existing studies, ICEO was typically induced in the vicinity of a thin layer of floating polarizable surface, such as a gold film, fabricated by an electrical sputtering system [34]. In addition to the high cost, the thin metal layer also suffers from a short life time due to its small thickness [35]. Here, highly conductive and durable bulk pencil-leads are used as 3D polarizable objects to overcome these deficiencies.

Here, 1 μm carboxylate-modified fluorescent micro-beads were used to demonstrate ICEO flow of 1 mM KCl solution in a fabricated microchannel with a side wall pencil-lead. A pencil-lead of 0.5 mm in diameter was used as the microchannel mold, and only one pencil-lead of 0.5 mm in diameter was embedded as the side wall electrode. Figure 3 shows the base of the pencil-lead (as a conductive surface) as part of the sidewall of a microchannel where ICEO flow was generated by applying an AC field between the two reservoirs. Video S1 (in Supplementary Information) shows the ICEO results under different applied voltages. For a floating electrode, a symmetric ICEO flow is expected [36]. Briefly, when the electric field is applied, part of the floating lead is positively charged and the rest is negatively charged, and an induced electrical double layer is formed in the vicinity of the floating pencil-lead. The interaction between the applied electric field and the net charges within the induced electrical double layer creates an electrostatic force and accordingly an ICEO flow. Due to the presence of opposite charges, two eddies with opposite flow directions are formed near the floating lead, as shown in Figure 3. Figure 3a–c also shows that the ICEO flow speed is highly dependent on electric field strength, and the ICEO flow is nearly symmetric with respect to the center of the lead. One can have multiple sidewall pencil-leads to further enhance the ICEO flow within the microchannel. By using pencil-leads of a few hundred microns, one can thus obtain results related to ICEO flow around one or multiple cylinders shown by Canpolat et al. [31,37], who fabricated the cylindrical rod by the electroplating technique. In contrast, use of the commercial pencil-lead is simpler and cheaper.

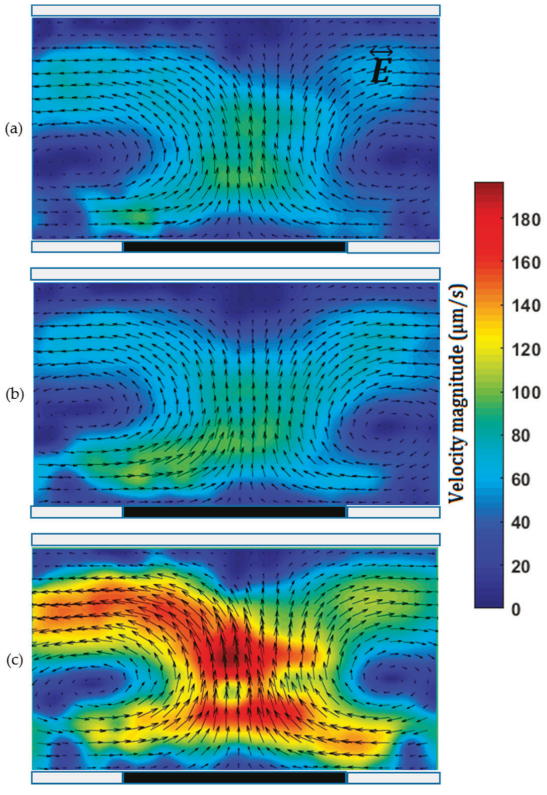

Figure 3. Induced-charge electroosmosis (ICEO) flow in front of a 0.5 mm pencil-lead in a channel of 0.5 mm diameter under an applied alternating current (AC) voltage of (**a**) 400 $V_{p\text{-}p}$; (**b**) 450 $V_{p\text{-}p}$; (**c**) 500 $V_{p\text{-}p}$ with a frequency of 500 Hz between two pencil-lead electrodes positioned about 11 mm apart in reservoirs.

3.2. ACEO

Different from the above ICEO flow where the sidewall electrode(s) are just floating, a potential applied to the sidewall electrode is used for generating ACEO flow. To achieve ACEO flow, we fabricate a microchannel with a pair of sidewall pencil-lead electrodes positioned either side-by-side (Figure 4) or face-to-face (Figure 5). Video S2 (in Supplementary Information) shows the ACEO flow around a pair of side-by-side pencil-leads under different voltages. The pair of pencil-leads connect to the AC function generator amplified by the high-voltage amplifier. Different AC voltages of fixed frequency were applied to the pair of sidewall pencil-lead electrodes. ACEO flow results from the interaction between the applied electric field and the net charges within the electrical double layer of each working electrode. The major advantage of using simple 3D electrodes as bulk polarizable objects over planar conductive surfaces is the enhancement in ACEO flow velocity [38]. The introduced fabrication method can also be used to provide stepped 3D pencil-lead electrodes. The flow rate and frequency range capable of ACEO pumping were enhanced significantly when planar electrodes were replaced by stepped 3D electrodes [39]. Figures 4 and 5 show ACEO flow of a 1 mM KCl solution (ACEO is limited to electrolytes with low ionic strength [40]) under different AC fields applied across a pair of side-by-side and face-to-face pencil-lead electrodes, respectively. It should be noted that, for the 1 mM KCl solution with molar electric conductivity of 146.88×10^{-4} Sm^2/mol [41] (conductivity of 0.014 S/m), ACEO dominated other electrohydrodynamic effects such as dielectrophoresis and electrothermal effects in the microchannel due to the low frequency employed here [42].

In case of parallel electrodes shown in Figure 4, the ICEO flow near one electrode is stronger than that near the other, and the flow is not symmetric with respect to the center of the gap between the two electrodes. This is the minimum gap achieved through the fabrication process and was measured by the microscope. This gap can be adjusted under the microscope at the beginning of the fabrication process. For parallel planar electrodes, a symmetric ACEO flow is expected [43]; however, the cross sections of both the microchannel and each electrode are circular in our device, which is the main reason for the asymmetric ICEO flow observed here. Comparison of velocity fields around the vortices shown in Figure 4a–c depicts that the strength of the ACEO flow increases approximately quadratically with increase in the applied AC voltage, which qualitatively agrees with the results from the literature [44]. In the experiments, we found that drastic decrease in frequency (from the range of kHz to Hz) or increase in the AC voltage (>60 $V_{p\text{-}p}$) increased the risk of electrolysis, resulting in the creation of bubbles around the electrodes.

For the case of face-to-face pencil-leads (Figure 5), at a relatively low AC voltage, the flow is mainly directed from one electrode towards the other and two opposite circulations are formed, as shown by Figure 5a. As the voltage increases, the flow is directed toward each electrode, which is clearly shown in Figure 5c. As the voltage increases, both the magnitude and the region of the ACEO flow increase. The ACEO flow velocity with face-to-face electrodes is stronger than that with side-by-side electrodes. In both cases, increasing the frequency (to 1 MHz) in the reported range of applied voltages did not show a notable change in flow velocity. However, the ACEO flow decayed drastically when the frequency exceeded 2 MHz.

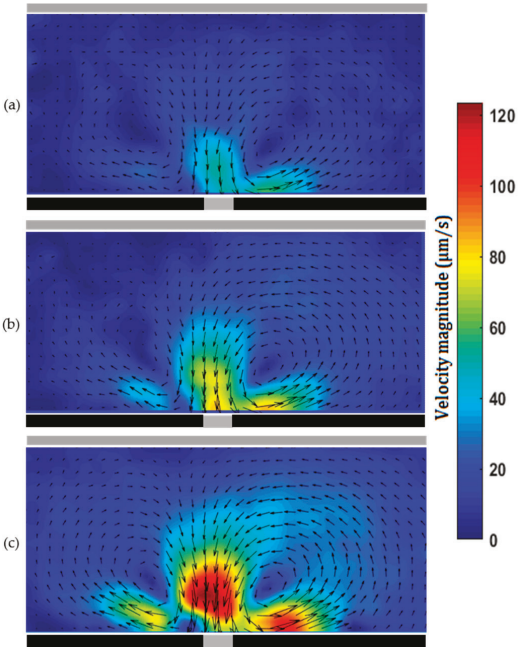

Figure 4. Alternating current electroosmosis (ACEO) flow of 1 mM KCl solution between two parallel 0.3 mm pencil-lead electrodes with a gap of 40 μm in a microchannel of 0.3 mm diameter. AC voltage of (**a**) 30 $V_{p\text{-}p}$; (**b**) 35 $V_{p\text{-}p}$; (**c**) 40 $V_{p\text{-}p}$ with a frequency of 50 kHz.

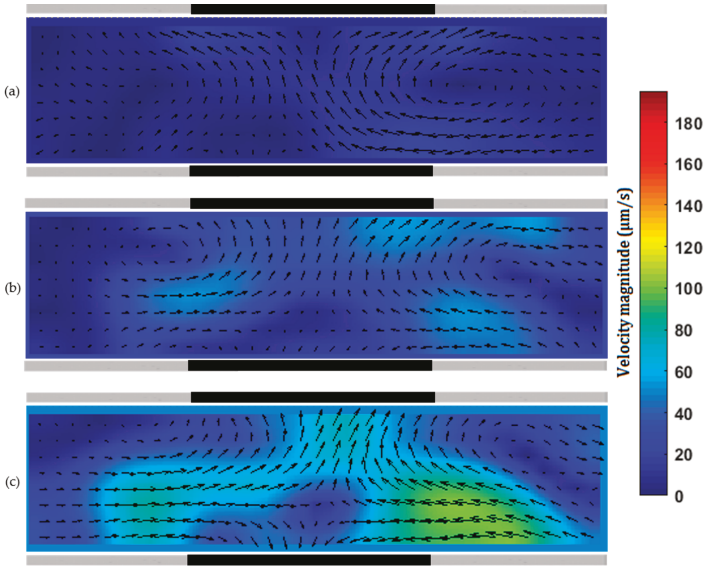

Figure 5. ACEO flow of 1 mM KCl solution between two 0.5 mm pencil-lead electrodes facing each other in a microchannel of 0.3 mm diameter. AC voltage of (**a**) 30 $V_{p\text{-}p}$; (**b**) 35 $V_{p\text{-}p}$; (**c**) 40 $V_{p\text{-}p}$ with a frequency of 50 kHz.

One can use a syringe pump to pump sample through the microchannel with pencil-lead sidewall electrodes. Since the Reynolds numbers in microchannels are very small, the flow is laminar and mixing is challenging. One can apply AC voltage through a pair of pencil-lead sidewall electrodes to generate secondary ACEO flow, which will perturb the main pressure-driven flow. Figure 6 shows the superposition of the pressure-driven and ACEO flows using both electrode configurations. Without the ACEO flow, the velocity profile in the pressure-driven flow is nearly parabolic, as shown in Figure 2. Clearly the pressure-driven flow is perturbed in the region with the ACEO flow, and the formed vortex can be used for mixing enhancement. To create chaotic advection for mixing enhancement, one can have multiple pairs of sidewall electrodes made of pencil-lead, and alternately apply an AC voltage to the sidewall electrodes [45,46]. In addition to the combination of the pressure-driven and ACEO flows for mixing enhancement, one can also apply a DC electric field through two pencil-leads inserted into the two reservoirs to generate electroosmotic flow. Under DC field, ICEO flow also forms on the floating sidewall pencil-leads. The formed secondary ICEO flow can perturb the main electroosmotic flow for mixing enhancement.

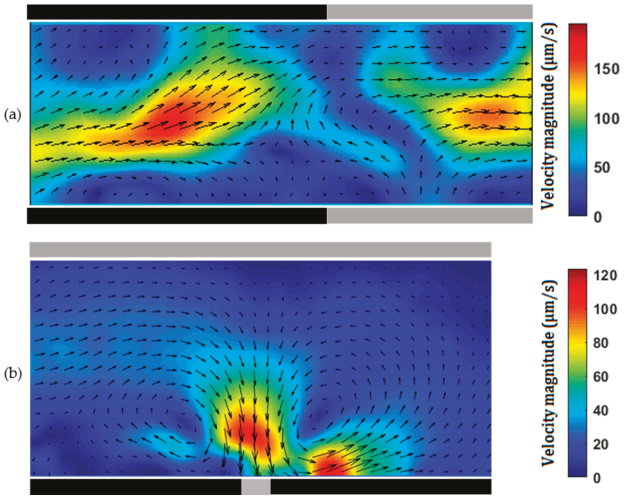

Figure 6. (**a**) Combination of a pressure-driven flow with a volume flow rate of 12 μL/h and ACEO flow between two 0.5 mm pencil-lead electrodes facing each other in a microchannel of 0.3 mm diameter with an AC voltage of 40 V_{p-p} at 50 kHz; (**b**) combination of a pressure-driven flow with a volume flow rate of 6 μL/h and ACEO flow in a microchannel of 0.3 mm diameter with two parallel 0.3 mm pencil-lead electrodes between which the gap is 40 μm. The applied AC voltage on the electrodes is 40 V_{p-p} at 50 kHz.

3.3. DEP

DEP refers to the migration of polarizable objects in an aqueous solution under a spatially non-uniform electric field [7]. Complex Clausius–Mossotti (CM) factor (a function of the ratio of the particle and electrolyte polarizability [47]) determines whether the particles experience positive or negative DEP. Use of the pencil-lead sidewall electrodes enables us to locally apply a voltage and generate spatially non-uniform AC field, and accordingly a DEP force acting on the particle. We used 10 μm polystyrene fluospheres to demonstrate DEP here. We used the method described in Section 2.1 to fabricate a microfluidic device similar to that fabricated by Puttaswamy et al. [48]. The main microchannel has two inlets on one side and two outlets at the other end, as shown in Figure 7a. Two parallel pencil-leads of 0.5 mm diameter are placed near outlet 1, and the gap between the two pencil-lead electrodes is about 200 μm as positioned under microscope. Figure 7a shows

the functionality of the device. Sheath flow with a flow rate of 4.5 μL/min pumps pure DI water without particles through one inlet, and the other inlet pumps DI water mixed with 10 μm polystyrene fluospheres at a flow rate of 1.6 μL/min. Without applying a voltage to the pencil-lead electrodes, particles flow through outlet 1, and no particles exit from outlet 2, as shown in Figure 7b. When an AC voltage of 100 V_{p-p} with a frequency of 5 MHz is applied between the two pencil-leads, particles flow to the second outlet, as shown in Figure 7c. Video S3 (in Supplementary Information) shows the particles' motion before and after application of the electric field. Under our experimental condition, the CM factor is negative, confirming that the particle experiences negative DEP. In addition, due to the high frequency, ACEO is negligible. Due to negative DEP, particles are pushed away from the electrodes, and then are carried by the faster sheath flow to outlet 2. Since the DEP force is proportional to the particle size, the deflection distance from the wall depends on the particle size. Thus, one can add more outlets to the device to achieve DEP-based particle separation by size.

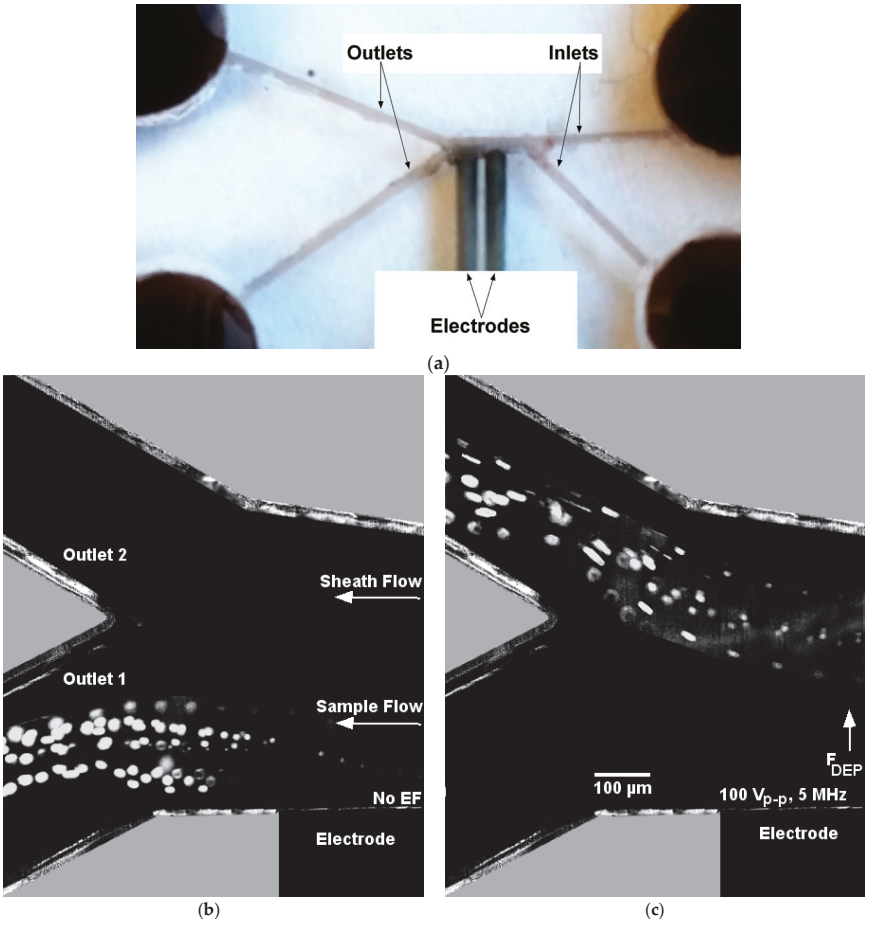

Figure 7. Microfluidic device for dielectrophoresis (DEP)-based particle switching. (**a**) A fabricated device having two inlets and outlets. Parallel pencil-lead electrodes were aligned near one outlet to apply the desired AC field in the microchannel; (**b**) superimposed trajectories of 10 μm fluorescent particles suspended in deionized (DI) water exiting the microchannel under no electric field; (**c**) DEP force generated by AC voltage of 100 V_{p-p} at a frequency of 5 MHz repelled the particles to outlet 2.

4. Discussion

The demonstrated electrokinetic phenomena using our cheap and straightforward device fabrication method show a promising way for manipulating fluids and particles beneficial for various microfluidic applications. For instance, 3D pencil-leads embedded into PDMS-based microfluidic devices could offer highly polarizable floating electrodes for generating strong ICEO flow, yet ACEO flow created under low voltages between these low cost graphite rods could efficiently mix fluids. DEP control of particles under non-uniform AC fields generated by these aligned highly conductive pencil-leads is able to achieve particle focusing, separation and trapping. Obviously, the pencil-lead-based microfluidic devices also have certain disadvantages. Since the pencil-lead is rigid, it can only fabricate straight microchannels of a few hundreds microns in diameter. The size and shape of the microchannel and electrode are constrained by that of the pencil-lead. The position and alignment of pencil-leads are not as accurate as in conventional photolithography techniques. However, they provide a cheap and quick method to fabricate a microfluidic device with 3D electrodes to generate various electrokinetic phenomena for various applications without the use of expensive fabrication facilities.

5. Conclusions

A pencil-lead-based microfluidic channel was developed and tested by implementation of multiple electrokinetic phenomena. The microchannel mold was a pencil-lead instead of the typical mold made of SU-8 photoresist, and pencil-leads also constituted the 3D sidewall electrodes. The use of these accessible molds and electrodes eliminates time-consuming and expensive conventional fabrication procedures such as coating, UV exposing, developing and sputtering. This facile, low cost technique allows one to fabricate microchannels of different dimensions using different diameter pencil-leads as well as configure different geometries by using multiple pencil-leads as sidewall electrodes at various positions. As shown in this paper, one can easily implement various electrokinetic phenomena including EOF, ICEO, ACEO and DEP in the fabricated device. One can also combine pressure-driven flow with the aforementioned electrokinetic phenomena to manipulate samples for various microfluidic applications. A significant advantage of using these bulk electrodes is to increase the electrokinetic flow velocity. Micro-PIV measurements of the phenomena illustrated in this paper underscore the capability of the fabricated devices for several microfluidic applications such as local mixing, fluid pumping and particle manipulation.

Supplementary Materials: The following are available online at www.mdpi.com/2072-666X/7/12/235/s1, Video S1: ICEO flow described in Section 3.1, Video S2: ACEO flow described in Section 3.2, Video S3: DEP described in Section 3.3.

Author Contributions: Shizhi Qian conceived and designed the experiments; Venkat Maruthamuthu contributed with data analysis and manuscript revision; Yashar Bashirzadeh conducted the experiments, analyzed the data and wrote the manuscript.

Conflicts of Interest: The authors declare no conflict of interest. The funding sponsors had no role in the design of the study; in the collection, analyses, or interpretation of data; in the writing of the manuscript, and in the decision to publish the results.

References

1. Mondal, K.; Ali, M.A.; Srivastava, S.; Malhotra, B.D.; Sharma, A. Electrospun functional micro/nanochannels embedded in porous carbon electrodes for microfluidic biosensing. *Sens. Actuators B Chem.* **2016**, *229*, 82–91. [CrossRef]
2. Matteucci, M.; Heiskanen, A.; Zór, K.; Emnéus, J.; Taboryski, R. Comparison of ultrasonic welding and thermal bonding for the integration of thin film metal electrodes in injection molded polymeric lab-on-chip systems for electrochemistry. *Sensors* **2016**, *16*, 1795. [CrossRef] [PubMed]

3. Mirzajani, H.; Cheng, C.; Wu, J.; Ivanoff, C.S.; Aghdam, E.N.; Ghavifekr, H.B. Design and characterization of a passive, disposable wireless AC-electroosmotic lab-on-a-film for particle and fluid manipulation. *Sens. Actuators B Chem.* **2016**, *235*, 330–342. [CrossRef]
4. Çetin, B.; Özer, M.B.; Çağatay, E.; Büyükkoçak, S. An integrated acoustic and dielectrophoretic particle manipulation in a microfluidic device for particle wash and separation fabricated by mechanical machining. *Biomicrofluidics* **2016**, *10*, 014112. [CrossRef] [PubMed]
5. Bazant, M.Z.; Squires, T.M. Induced-charge electrokinetic phenomena. *Curr. Opin. Colloid Interface Sci.* **2010**, *15*, 203–213. [CrossRef]
6. Bazant, M.Z.; Squires, T.M. Induced-charge electrokinetic phenomena: Theory and microfluidic applications. *Phys. Rev. Lett.* **2004**, *92*, 066101. [CrossRef] [PubMed]
7. Pohl, H.A. *Dielectrophoresis: The Behavior of Neutral Matter in Nonuniform Electric Fields*; Cambridge University Press: Cambridge, UK, 1978; Volume 80.
8. Feng, H.; Wong, T.N.; Che, Z. Chaotic micromixer utilizing electro-osmosis and induced charge electro-osmosis in eccentric annulus. *Phys. Fluids* **2016**, *28*, 062003. [CrossRef]
9. Wu, X.; Ramiah Rajasekaran, P.; Martin, C.R. An alternating current electroosmotic pump based on conical nanopore membranes. *ACS Nano* **2016**, *10*, 4637–4643. [CrossRef] [PubMed]
10. Chung, C.-C.; Glawdel, T.; Ren, C.L.; Chang, H.-C. Combination of AC electroosmosis and dielectrophoresis for particle manipulation on electrically-induced microscale wave structures. *J. Micromech. Microeng.* **2015**, *25*, 035003. [CrossRef]
11. Li, S.; Li, M.; Hui, Y.S.; Cao, W.; Li, W.; Wen, W. A novel method to construct 3D electrodes at the sidewall of microfluidic channel. *Microfluid. Nanofluid.* **2013**, *14*, 499–508. [CrossRef]
12. Vulto, P.; Huesgen, T.; Albrecht, B.; Urban, G. A full-wafer fabrication process for glass microfluidic chips with integrated electroplated electrodes by direct bonding of dry film resist. *J. Micromech. Microeng.* **2009**, *19*, 077001. [CrossRef]
13. Schlesinger, M.; Paunovic, M. *Modern Electroplating*; John Wiley & Sons: Hoboken, NJ, USA, 2011; Volume 55.
14. So, J.-H.; Dickey, M.D. Inherently aligned microfluidic electrodes composed of liquid metal. *Lab Chip* **2011**, *11*, 905–911. [CrossRef] [PubMed]
15. Iliescu, C.; Xu, G.L.; Samper, V.; Tay, F.E. Fabrication of a dielectrophoretic chip with 3D silicon electrodes. *J. Micromech. Microeng.* **2004**, *15*, 494. [CrossRef]
16. Cummings, E.B.; Singh, A.K. Dielectrophoresis in microchips containing arrays of insulating posts: Theoretical and experimental results. *Anal. Chem.* **2003**, *75*, 4724–4731. [CrossRef] [PubMed]
17. Martinez-Duarte, R. Microfabrication technologies in dielectrophoresis applications—A review. *Electrophoresis* **2012**, *33*, 3110–3132. [CrossRef] [PubMed]
18. Wang, C.; Madou, M. From MEMS to NEMS with carbon. *Biosens. Bioelectron.* **2005**, *20*, 2181–2187. [CrossRef] [PubMed]
19. Martinez-Duarte, R.; Camacho-Alanis, F.; Renaud, P.; Ros, A. Dielectrophoresis of lambda-DNA using 3D carbon electrodes. *Electrophoresis* **2013**, *34*, 1113–1122. [CrossRef] [PubMed]
20. Martinez-Duarte, R.; Renaud, P.; Madou, M.J. A novel approach to dielectrophoresis using carbon electrodes. *Electrophoresis* **2011**, *32*, 2385–2392. [CrossRef] [PubMed]
21. Martinez-Duarte, R.; Gorkin, R.A., III; Abi-Samra, K.; Madou, M.J. The integration of 3D carbon-electrode dielectrophoresis on a CD-like centrifugal microfluidic platform. *Lab Chip* **2010**, *10*, 1030–1043. [CrossRef] [PubMed]
22. Pierson, H.O. *Handbook of Carbon, Graphite, Diamonds and Fullerenes: Processing, Properties and Applications*; William Andrew: Norwich, NY, USA, 2012.
23. Li, W.; Qian, D.; Li, Y.; Bao, N.; Gu, H.; Yu, C. Fully-drawn pencil-on-paper sensors for electroanalysis of dopamine. *J. Electroanal. Chem.* **2016**, *769*, 72–79. [CrossRef]
24. Lee, S.H.; Ban, J.Y.; Oh, C.H.; Park, H.K.; Choi, S. A solvent-free microbial-activated air cathode battery paper platform made with pencil-traced graphite electrodes. *Sci. Rep.* **2016**, *6*, 28588. [CrossRef] [PubMed]
25. Adkins, J.; Boehle, K.; Henry, C. Electrochemical paper-based microfluidic devices. *Electrophoresis* **2015**, *36*, 1811–1824. [CrossRef] [PubMed]
26. Dossi, N.; Toniolo, R.; Pizzariello, A.; Impellizzieri, F.; Piccin, E.; Bontempelli, G. Pencil-drawn paper supported electrodes as simple electrochemical detectors for paper-based fluidic devices. *Electrophoresis* **2013**, *34*, 2085–2091. [CrossRef] [PubMed]

27. Kjeang, E.; McKechnie, J.; Sinton, D.; Djilali, N. Planar and three-dimensional microfluidic fuel cell architectures based on graphite rod electrodes. *J. Power Sources* **2007**, *168*, 379–390. [CrossRef]
28. Bazant, M.Z.; Ben, Y. Theoretical prediction of fast 3D AC electro-osmotic pumps. *Lab Chip* **2006**, *6*, 1455–1461. [CrossRef] [PubMed]
29. Jia, Y.; Jiang, J.; Ma, X.; Li, Y.; Huang, H.; Cai, K.; Cai, S.; Wu, Y. PDMS microchannel fabrication technique based on microwire-molding. *Chin. Sci. Bull.* **2008**, *53*, 3928–3936. [CrossRef]
30. Agustini, D.; Bergamini, M.F.; Marcolino-Junior, L.H. Low cost microfluidic device based on cotton threads for electroanalytical application. *Lab Chip* **2016**, *16*, 345–352. [CrossRef] [PubMed]
31. Canpolat, C.; Qian, S.; Beskok, A. Micro-PIV measurements of induced-charge electro-osmosis around a metal rod. *Microfluid. Nanofluid.* **2013**, *14*, 153–162. [CrossRef]
32. Thielicke, W.; Stamhuis, E. PIVlab–towards user-friendly, affordable and accurate digital particle image velocimetry in MATLAB. *J. Open Res. Softw.* **2014**, *2*, 30. [CrossRef]
33. Westerweel, J.; Geelhoed, P.; Lindken, R. Single-pixel resolution ensemble correlation for micro-PIV applications. *Exp. Fluids* **2004**, *37*, 375–384. [CrossRef]
34. Yalcin, S.E.; Sharma, A.; Qian, S.; Joo, S.W.; Baysal, O. Manipulating particles in microfluidics by floating electrodes. *Electrophoresis* **2010**, *31*, 3711–3718. [CrossRef] [PubMed]
35. Li, Q.; Yuan, Y.J. Application of vertical electrodes in microfluidic channels for impedance analysis. *Micromachines* **2016**, *7*, 96. [CrossRef]
36. Tao, Y.; Ren, Y.; Liu, W.; Wu, Y.; Jia, Y.; Lang, Q.; Jiang, H. Enhanced particle trapping performance of induced charge electroosmosis. *Electrophoresis* **2016**, *37*, 1326–1336. [CrossRef] [PubMed]
37. Canpolat, C.; Zhang, M.; Rosen, W.; Qian, S.; Beskok, A. Induced-charge electroosmosis around touching metal rods. *J. Fluids Eng.* **2013**, *135*, 021103. [CrossRef]
38. Rouabah, H.A.; Park, B.Y.; Zaouk, R.B.; Morgan, H.; Madou, M.J.; Green, N.G. Design and fabrication of an AC-electro-osmosis micropump with 3D high-aspect-ratio electrodes using only SU-8. *J. Micromech. Microeng.* **2011**, *21*, 035018. [CrossRef]
39. Senousy, Y.; Harnett, C. Fast three dimensional AC electro-osmotic pumps with nonphotolithographic electrode patterning. *Biomicrofluidics* **2010**, *4*, 036501. [CrossRef] [PubMed]
40. Srivatsan, T.S. *Microfluidic Devices in Nanotechnology: Fundamental Concepts*; Kumar, C.S., Ed.; Wiley: Hoboken, NJ, USA, 2010.
41. Lide, D.R. *CRC Handbook of Chemistry and Physics*; CRC Press: Boca Raton, FL, USA, 2004; Volume 85.
42. Castellanos, A.; Ramos, A.; Gonzalez, A.; Green, N.G.; Morgan, H. Electrohydrodynamics and dielectrophoresis in microsystems: Scaling laws. *J. Phys. D Appl. Phys.* **2003**, *36*, 2584. [CrossRef]
43. Urbanski, J.P.; Thorsen, T.; Levitan, J.A.; Bazant, M.Z. Fast AC electro-osmotic micropumps with nonplanar electrodes. *Appl. Phys. Lett.* **2006**, *89*, 143508. [CrossRef]
44. Green, N.G.; Ramos, A.; González, A.; Morgan, H.; Castellanos, A. Fluid flow induced by nonuniform AC electric fields in electrolytes on microelectrodes. I. Experimental measurements. *Phys. Rev. E* **2000**, *61*, 4011. [CrossRef]
45. Qian, S.; Bau, H.H. A chaotic electroosmotic stirrer. *Anal. Chem.* **2002**, *74*, 3616–3625. [CrossRef] [PubMed]
46. Qian, S.; Bau, H.H. Theoretical investigation of electro-osmotic flows and chaotic stirring in rectangular cavities. *Appl. Math. Model.* **2005**, *29*, 726–753. [CrossRef]
47. Qian, S.; Ai, Y. *Electrokinetic Particle Transport in Micro-/Nanofluidics: Direct Numerical Simulation Analysis*; CRC Press: Boca Raton, FL, USA, 2012; Volume 153.
48. Puttaswamy, S.V.; Xue, P.; Kang, Y.; Ai, Y. Simple and low cost integration of highly conductive three-dimensional electrodes in microfluidic devices. *Biomed. Microdevices* **2015**, *17*, 1–5. [CrossRef] [PubMed]

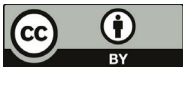

micromachines

MDPI

Article

An Enhanced Electroosmotic Micromixer with an Efficient Asymmetric Lateral Structure

Teng Zhou [1,2], Hanlin Wang [1], Liuyong Shi [1], Zhenyu Liu [3,*] and Sang Woo Joo [2,*]

1 Mechanical and Electrical Engineering College, Hainan University, Haikou 570228, Hainan, China; zhouteng@hainu.edu.cn (T.Z.); hanlinwang@gmail.com (H.W.); liuyongshi@gmail.com (L.S.)
2 School of Mechanical Engineering, Yeungnam University, Gyongsan 712-719, Korea
3 Changchun Institute of Optics, Fine Mechanics and Physics (CIOMP), Chinese Academy of Science, Changchun 130033, Jilin, China
* Correspondence: liuzy@ciomp.ac.cn (Z.L.); swjoo@yu.ac.kr (S.W.J.); Tel.: +86-431-86176025 (Z.L.); +82-53-810-2568 (S.W.J.)

Academic Editors: Xiangchun Xuan and Shizhi Qian
Received: 30 September 2016; Accepted: 24 November 2016; Published: 1 December 2016

Abstract: Homogeneous and rapid mixing in microfluidic devices is difficult to accomplish, owing to the low Reynolds number associated with most flows in microfluidic channels. Here, an efficient electroosmotic micromixer based on a carefully designed lateral structure is demonstrated. The electroosmotic flow in this mixer with an asymmetrical structure induces enhanced disturbance in the micro channel, helping the fluid streams' folding and stretching, thereby enabling appreciable mixing. Quantitative analysis of the mixing efficiency with respect to the potential applied and the flow rate suggests that the electroosmotic microfluidic mixer developed in the present work can achieve efficient mixing with low applied potential.

Keywords: microfluidics; micromixer; electroosmotic; active mixer; computational fluid dynamics

1. Introduction

In many biochemical processes, efficient reagent mixing is often required [1–4]. In macro-scale devices, mixing of fluids usually relies mainly on convection effects, which tend to weaken as the geometrical scale decreases. In microfluidic channels, it is difficult to rapidly and homogenously mix different fluids due to the low Reynolds number associated with the microscale fluid flow. A number of micro mixing methods have been demonstrated to enhance the distance for interaction of the two samples and shorten the mixing distance required.

Many ingenious micromixers developed in recent years can be divided into two broad categories: passive [5–9] and active types [10–18]. Active micromixers utilize externally-induced mixing, such as electric [11–15,19], magnetic [18,20–24], acoustic [25], and moving parts [26] upon the flow field. Passive micromixers do not require external energy, except for that used to drive the flows [5,27,28]. Mostly, passive micromixers exploit the micromixers' geometry to produce complex flow fields for effective mixing [27,28]. Compared to the passive method, the active type relies on external stimuli or energy to enhance the mixing of the reagent in the channel, and can show better mixing capabilities. Among the passive mixers, the electroosmotic flow (EOF) mixer is particularly effective in small channels, and suitable for fluids with low Reynolds numbers, and makes use of a DC voltage across the regions with positive and negative charges on the same substrate in a microchannel [10–12,15]. In general, the DC voltage can generate in-plane vortices, which can be simulated by two-dimensional (2D) computations.

In the present work, we present an EOF mixer with an efficient lateral structure with DC voltage across two coplanar groups of electrodes. The lateral structure is obtained based on the topography

optimization method [8,29–31]. By adding four electrodes and adjusting their distribution, the channel with DC-EOF produces in-plane microvortices, helping the reagent mixing. Compared with traditional EOF mixers consisting of two circles [10], the efficiency of the proposed EOF micromixer with a lateral structure is significantly improved by the enhanced fluid motion. Besides, the electric field is not time-dependent, but stationary. The proposed mixer can thus be more compact and suitable for connection with other parts of a microfluidic system.

2. Mathematical Model and Numerical Method

We consider a two-dimensional (2D) viscous flow in a microchannel with with a mixing region, as shown in Figure 1b. The channel depth-to-width ratio is assumed to be large enough for the three-dimensional effect of top and bottom to be neglected. The original mixer (shown in Figure 1a as a reference) is composed of two circular boundaries, while the optimized mixer of the present study is composed of two lateral structures, as designed by the authors using a topography optimization method.

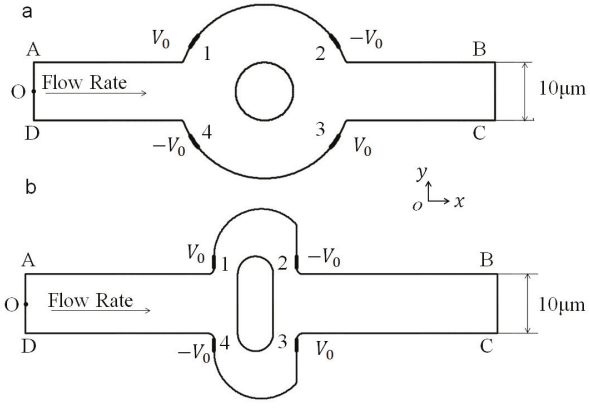

Figure 1. Configuration of (**a**) the original mixer structure with four symmetric electrodes on the wall of the mixing chamber; and (**b**) the optimized mixer. AD: inlet, BC: outlet, O: midpoint of boundary AD.

In both mixers, an electric potential is applied externally from inlet AO and OD to grounded outlets BC. The incompressible electroosmotic flow in the fluid domain Ω_f is described by a coupled system of the Navier–Stokes equation, the Laplace equation for the electrical potential ϕ in in the channel, and the convection–diffusion equation for the concentration c of the dissolved substances in the fluid, as follows:

$$\nabla \cdot [p\mathrm{I} - \eta(\nabla \mathbf{u} + \nabla \mathbf{u}^{\mathrm{T}})] + \rho \mathbf{u} \cdot \nabla \mathbf{u} = \mathbf{f}, \tag{1}$$

$$\nabla \cdot \mathbf{u} = 0, \tag{2}$$

$$\nabla^2 \phi = 0, \tag{3}$$

$$\mathbf{u} \cdot \nabla c = \nabla \cdot (\mathrm{D} \nabla c), \tag{4}$$

where ρ, η, $\mathbf{u}$, I, p, D are the fluid density, viscosity, velocity vector, identity tensor, pressure field, and diffusion coefficient, respectively. For water as the carrier fluid, $\rho = 1000\ \mathrm{kg/m^3}$ and $\eta = 0.001\ \mathrm{Pa{\cdot}s}$, with the diffusion coefficient $\mathrm{D} = 10^{-11}\ \mathrm{m^2/s}$.

Along the inlets 1 and 2, a uniform flow is imposed,

$$\mathbf{u} = U_{01}\mathbf{n} \quad \text{at} \quad \Gamma_{AO}, \tag{5}$$

$$\mathbf{u} = U_{02}\mathbf{n} \quad \text{at} \quad \Gamma_{OB}. \tag{6}$$

Here, U_{01}, U_{02}, and $\mathbf{n} = (n_x, n_y)$ are the magnitude of the velocity of inlet AO, inlet OB, and the normal vector of the surface, respectively. In this work, $U_{01} = U_{02} = U_0$ is set. The thicknesses of the electric double layer (EDL) adjacent to the charged channel wall are very thin in comparison to the widths of the channel, and so the Smoluchowski slip boundary condition for Newtonian electroosmotic flow is applied on the charged channel wall AB and CD:

$$\mathbf{u} = \mathbf{u}_w = \frac{\varepsilon_f \zeta_w}{\mu}(\mathbf{I} - \mathbf{nn}) \cdot \nabla\phi \quad \text{at} \quad \Gamma_{wall}, \tag{7}$$

where $\mathbf{u}_w$ is the fluid velocity on the channel wall, and ε_f and ζ_w are, respectively, the fluid permittivity and the zeta potential of the channel wall, which are set to 80.2 and -0.1 V. The ambient pressure and no-traction condition are applied at outlet BC:

$$p = 0 \quad \text{at} \quad \Gamma_{outlet} \tag{8}$$

$$\eta(\nabla\mathbf{u} + \nabla\mathbf{u}^{\mathrm{T}}) \cdot \mathbf{n} = \mathbf{0} \quad \text{at} \quad \Gamma_{outlet}. \tag{9}$$

With the Laplace equation, the local electric field $\mathbf{E}$ can be calculated from the electric potential ϕ by

$$\mathbf{E} = -\nabla\phi \quad \text{in } \Omega_f. \tag{10}$$

In this chip, a potential shift is applied across the electrodes (1,3) and (2,4), so the boundary conditions for ϕ on the entrance and exits of the microchannel are

$$\phi = \phi_0 \quad \text{on } 1, 3 \tag{11}$$

and

$$\phi = -\phi_0 \quad \text{on } 2, 4. \tag{12}$$

Other boundaries (including the channel wall (Γ_{wall}), except on electrodes), inlet (Γ_{inlet}) and outlet (Γ_{outlet}) are electrically insulating, yielding

$$\mathbf{n} \cdot \nabla\phi = 0 \quad \text{on other boundaries.} \tag{13}$$

For the steady convection–diffusion equation, the concentrations at inlets 1 and 2 are specified as

$$c = 1 \text{ mol/m}^3 \quad \text{at} \quad \Gamma_{inlet1} \tag{14}$$

$$c = 0 \text{ mol/m}^3 \quad \text{at} \quad \Gamma_{inlet2}, \tag{15}$$

while the condition of no species flux is imposed at channel walls,

$$(c\mathbf{u} - \mathrm{D}\nabla c) \cdot \mathbf{n} = 0 \quad \text{at} \quad \Gamma_{wall}. \tag{16}$$

The boundary condition along the outlet is

$$(\mathrm{D}\nabla c) \cdot \mathbf{n} = 0 \quad \text{at} \quad \Gamma_{outlet}. \tag{17}$$

The mixing effect of the two flows with an anticipated distribution of the concentration near the outlet can be expressed using the least-square type optimization objective as [8,30,32], which is used as our mixing efficiency index,

$$\sigma = \sqrt{\frac{\int_\Gamma (c - \bar{c})^2}{L\bar{c}^2}}, \tag{18}$$

where c is the concentration of the reagent, $\bar{c}$ denotes the average concentration, Γ is the cross line from which we measure the concentration; in this work, line BC is chosen as the cross line, and L is the length of the cross line. Complete mixing and complete segregation are then defined by $\sigma = 0$ and $\sigma = 1$, respectively. Therefore, the lower the value is, the better is the performance of the mixer.

The above system is solved numerically using the commercial finite element package COMSOL Multiphysics (Version 4.3a, COMSOL Group, Stockholm, Sweden). The coupled system of hydrodynamic, electrical, and concentration field is solved simultaneously.

3. Results and Discussion

In this section, the mixing process is presented using the concentration surface plot, the fluid streamlines, and electric potential lines for the original chip and revised chip with and without an electric field. Furthermore, the mixing efficiency index σ of chip versus the potential and the inlet mean velocity is analyzed to show the influence of the potential and the inlet mean velocity.

3.1. Mixing Process and Mechanism

For two mixers, the two fluids in the channel are also well separated at the outlet, because the flow is laminar and the diffusion coefficient is very small when the electric field is not applied; that is, $V_0 = 0$ V, as shown in Figure 2. The mean inlet velocity of the two mixers is $U_0 = 10^{-3}$ m/s, and the concentrations at the upper and lower inlet are set as 1 mol/m^3 and 0 mol/m^3. The streamlines in Figure 2 demonstrate that there is no lateral flow, which would be vertical main flow with other fluctuations, owing to the slow mean velocity and low Reynolds number. Furthermore, the distance for the diffusion of two samples is not long enough. Thus the two solutions with different concentrations stay split, with an obvious interface in both the original and the revised chip.

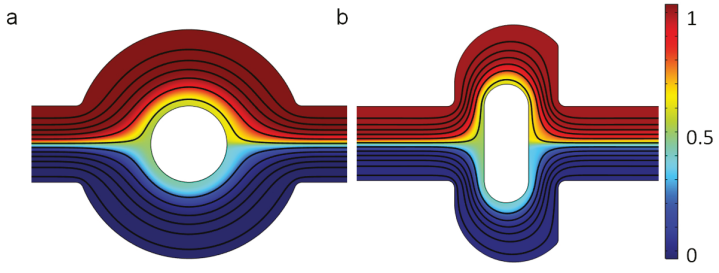

Figure 2. Fluid streamlines in the channel, and the concentration surface plot of (**a**) the original chip and (**b**) revised chip in the absence of an electric field and the mean inlet velocity $U_0 = 10^{-3}$ m/s. The unit for the concentration is mol/m^3.

When the electric field is applied, the fluctuations in the flow increase considerably, as shown by the streamlines in Figure 3, due to the electroosmotic flow. In both mixers, there are some vortices near the electrodes. The applied voltage for both mixers is $V_0 = 1$ V, which generates a uniform electric intensity in the channel (Figure 4). Comparing the electric potential lines in the channels of the mixer, it is found that the nonuniformity is reinforced by the lateral structure of the revised chip due to the asymmetry, which can also be easily manufactured by standard photolithography [6]. Therefore, the rotating vortices caused by the electroosmotic flow due to the electrical field (which disturbs the main flow) is much more irregular near the electrodes in the revised chip, compared with the original chip (as shown in Figure 3). The vortices in the channel will fold and stretch the fluid element of two reagents, inducing an efficient mixing in the mixer (Figure 5). Furthermore, the range of influence for the vortex of the revised chip is stronger than that of the original mixer. From Figure 3, it can be seen that the vortex of the revised chip extends further into the main channel than that of the original

chip. Figure 5 qualitatively illustrates the concentration before and after the expansion part of channel. Before the expansion part, the concentration of the two mixers is the same, while the two streams are much more homogeneous for the mixer with the lateral structure than the original mixer near the outlet, as observed in Figure 5.

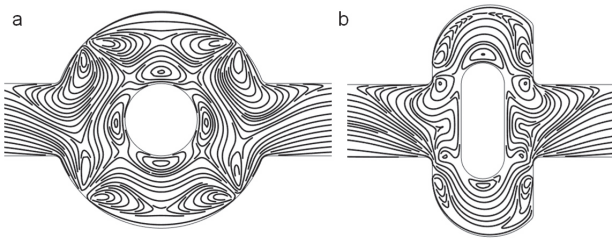

Figure 3. Fluid streamlines in (**a**) the original chip and (**b**) revised chip in the channel when the device uses the potentials $V_0 = 1$ V and the inlet velocity $U_0 = 10^{-3}$ m/s.

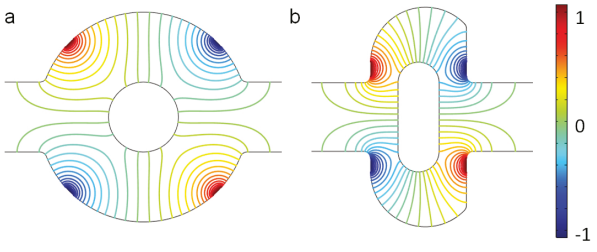

Figure 4. Electric potential lines in (**a**) the original chip and (**b**) the revised chip when the device uses the potentials $V_0 = 1$ V and the inlet mean velocity $U_0 = 10^{-3}$ m/s.

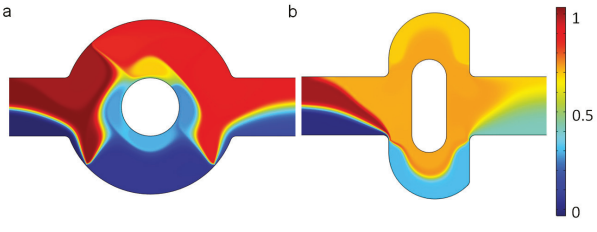

Figure 5. The concentration surface plot of (**a**) the original chip and (**b**) the revised chip when the device uses the potentials $V_0 = 1\,V$ and the mean inlet velocity $U_0 = 10^{-3}$ m/s. The unit for the concentration is mol/m^3.

3.2. Mixing Efficiency

In this part, we calculate the mixing efficiency index σ quantitatively based on the corresponding simulation result for the two mixers, considering the electrical potential and flow rate while the mixing efficiency index σ of 1 indicates unmixed fluids, and a mixing efficiency index σ of 0.0 indicates complete mixing. As the Smoluchowski slip velocity is proportional to the electric field intensity, the mixing level will be influenced as a result of enhanced disturbance induced in the microfluidic channel (Figure 6). Moreover, the mixing behavior will vary with the inlet mean velocity, because the mixing time will decrease with increasing flow rate (Figure 7).

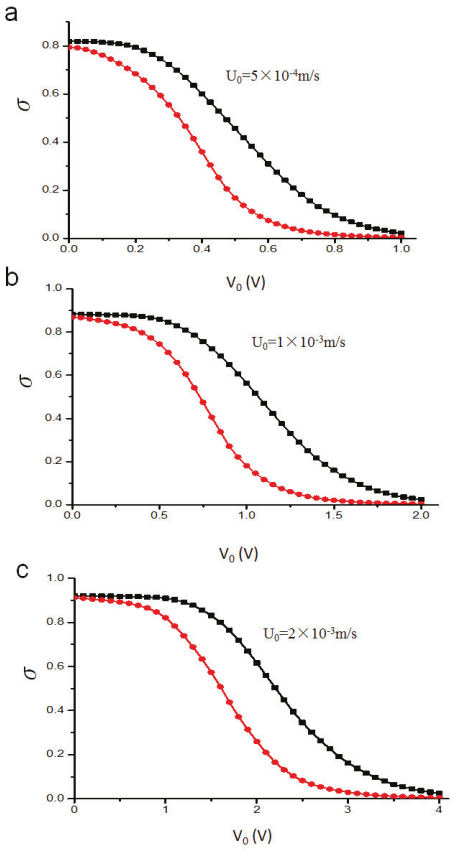

Figure 6. The mixing efficiency index σ versus the potential V_0, where the inlet mean velocity U_0 is (**a**) 5×10^{-4} m/s; (**b**) 1×10^{-3} m/s; (**c**) 2×10^{-3} m/s. Black line with square symbols: original chip; Red line with circular symbols: revised chip.

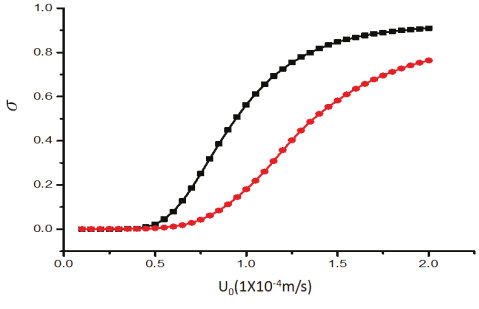

Figure 7. The mixing efficiency index σ of mixer versus the inlet mean velocity U_0 for $V_0 = 1$ V. The horizontal and vertical axes depict the inlet mean velocity U_0 and mixing efficiency index σ, respectively. The unit for the inlet mean velocity U_0 is 1×10^{-4} m/s. Black line with square symbols: original chip. Red line with circular symbols: revised chip.

Figure 6 compares the mixing efficiency index σ near the outlet along with the potentials V_0 for three different inlet mean velocities: (a) 5×10^{-4} m/s, (b) 1×10^{-3} m/s, (c) 2×10^{-3} m/s, in both the original and the revised mixer. From the result, it is found that the higher levels of mixing can be achieved when the electrical intensity increases for both mixers. Two species almost achieve complete mixing from poor mixing when the potentials V_0 raise from 0 to 1 V (2 V and 4 V), as shown in Figure 6a (Figure 6b and Figure 6c). However, the revised chip will improve the mixing of the samples much further as the electric potential V_0 is increased. This means that the stirring effect in the original mixer caused by EOF is less significant than the mixer with the lateral structure to substantially enhance mixing performance for the original mixer at the same V_0.

The mixing efficiency index σ near the outlet is shown as a function of the inlet mean velocity U_0 at the electrical potential $V_0 = 1$ V of the two mixers in Figure 6. For both mixers, the mixing effect will weaken when the flow rate is increased, due the reduction of mixing time, as manifested in Figure 7. This holds true for all values of U_0, though the proposed mixer outperforms the original one.

4. Conclusions

An efficient electroosmotic micromixer is designed by improving an existing electroosmotic micromixer with an asymmetric lateral structure. The mixing is achieved by the additional fluctuations in the flow due to this structure with the EOF generated by the electric field. The simulation results suggest that this enhanced mixer folds and stretches fluid samples in the channel more effectively than the original mixer. The influences of the electric potential applied and the flow rate are investigated to compare the performance of the two mixers. In all parametric studies, the modified structure considerably outperforms the original mixer. The results also indicate that the reagents can reach complete mixing in the enhanced mixer with lower potential and higher throughput compared to the original mixer. An experimental verification of the present numerical analysis is necessary for actual application of the proposed mixer, and will be the subject of future investigation.

Acknowledgments: This work is funded by the Grant NRF-2015-002423 of the National Research Foundation of Korea.

Author Contributions: Teng Zhou and Zhenyu Liu conceived and designed the experiments; Teng Zhou and Liuyong Shi performed the experiments; Teng Zhou and Hanlin Wang analyzed the data; Sang Woo Joo and Zhenyu Liu contributed reagents/materials/analysis tools; Teng Zhou, Hanlin Wang, Zhenyu Liu and Sang Woo Joo wrote the paper.

Conflicts of Interest: The authors declare no conflicts of interest.

References

1. Lee, C.Y.; Chang, C.L.; Wang, Y.N.; Fu, L.M. Microfluidic mixing: A review. *Int. J. Mol. Sci.* **2011**, *12*, 3263–3287.
2. Suh, Y.K.; Kang, S. A Review on Mixing in Microfluidics. *Micromachines* **2010**, *1*, 82–111.
3. Wang, G.; Yang, F.; Zhao, W. There can be turbulence in microfluidics at low Reynolds number. *Lab Chip* **2014**, *14*, 1452–1458.
4. You, J.B.; Kang, K.; Tran, T.T.; Park, H.; Hwang, W.R.; Kim, J.M.; Im, S.G. PDMS-based turbulent microfluidic mixer. *Lab Chip* **2015**, *15*, 1727–1735.
5. Amini, H.; Lee, W.; Di Carlo, D. Inertial microfluidic physics. *Lab Chip* **2014**, *14*, 2739–2761.
6. Zhou, T.; Liu, Z.; Wu, Y.; Deng, Y.; Liu, Y.; Liu, G. Hydrodynamic particle focusing design using fluid-particle interaction. *Biomicrofluidics* **2013**, *7*, 054104.
7. Zhang, J.; Li, W.; Li, M.; Alici, G.; Nguyen, N.T. Particle inertial focusing and its mechanism in a serpentine microchannel. *Microfluid. Nanofluid.* **2014**, *17*, 305–316.
8. Zhou, T.; Xu, Y.; Liu, Z.; Joo, S.W. An enhanced one-layer passive microfluidic mixer with an optimized lateral structure with the Dean effect. *J. Fluids Eng.* **2015**, *137*, 091102.
9. Chen, X.; Li, T. A novel design for passive misscromixers based on topology optimization method. *Biomed. Microdevices* **2016**, *18*, 1–15.

10. Chen, H.; Zhang, Y.; Mezic, I.; Meinhart, C.; Petzold, L. Numerical Simulation of an Electroosmotic Micromixer. In Proceedings of the ASME 2003 International Mechanical Engineering Congress and Exposition, Washington, DC, USA, 15–21 November 2003; pp. 653–658.
11. Sasaki, N.; Kitamori, T.; Kim, H.B. Experimental and theoretical characterization of an AC electroosmotic micromixer. *Anal. Sci.* **2010**, *26*, 815–819.
12. Cartier, C.A.; Drews, A.M.; Bishop, K.J.M. Microfluidic mixing of nonpolar liquids by contact charge electrophoresis. *Lab Chip* **2014**, *14*, 4230–4236.
13. Qian, S.; Bau, H.H. A chaotic electroosmotic stirrer. *Anal. Chem.* **2002**, *74*, 3616–3625.
14. Sasaki, N.; Kitamori, T.; Kim, H.B. AC electroosmotic micromixer for chemical processing in a microchannel. *Lab Chip* **2006**, *6*, 550–554.
15. Huang, S.H.; Wang, S.K.; Khoo, H.S.; Tseng, F.G. AC electroosmotic generated in-plane microvortices for stationary or continuous fluid mixing. *Sens. Actuators B* **2007**, *125*, 326–336.
16. Zhou, T.; Yeh, L.H.; Li, F.C.; Mauroy, B.; Joo, S. Deformability-Based Electrokinetic Particle Separation. *Micromachines* **2016**, *7*, 170.
17. Wang, G.; Yang, F.; Zhao, W.; Chen, C.P. On micro-electrokinetic scalar turbulence in microfluidics at a low Reynolds number. *Lab Chip* **2016**, *16*, 1030–1038.
18. Liang, L.; Xuan, X. Diamagnetic particle focusing using ferromicrofluidics with a single magnet. *Microfluid. Nanofluid.* **2012**, *13*, 637–643.
19. Qian, S.; Bau, H.H. Theoretical investigation of electro-osmotic flows and chaotic stirring in rectangular cavities. *Appl. Math. Model.* **2005**, *29*, 726–753.
20. Qian, S.; Bau, H.H. Magneto-hydrodynamic stirrer for stationary and moving fluids. *Sens. Actuators B* **2005**, *106*, 859–870.
21. Wen, C.Y.; Liang, K.P.; Chen, H.; Fu, L.M. Numerical analysis of a rapid magnetic microfluidic mixer. *Electrophoresis* **2011**, *32*, 3268–3276.
22. Qian, S.; Bau, H.H. Magnetohydrodynamic flow of RedOx electrolyte. *Phys. Fluids* **2005**, *17*, 067105.
23. Qian, S.; Zhu, J.; Bau, H.H. A stirrer for magnetohydrodynamically controlled minute fluidic networks. *Phys. Fluids* **2002**, *14*, 3584–3592.
24. Qian, S.; Bau, H.H. Magneto-hydrodynamics based microfluidics. *Mech. Res. Commun.* **2009**, *36*, 10–21.
25. Cardoso, V.F.; Knoll, T.; Velten, T.; Rebouta, L.; Mendes, P.M.; Lanceros-Mendez, S.; Minas, G. Polymer-based acoustic streaming for improving mixing and reaction times in microfluidic applications. *RSC Adv.* **2014**, *4*, 4292–4300.
26. Shang, X.; Huang, X.; Yang, C. Mixing enhancement by the vortex in a microfluidic mixer with actuation. *Exp. Therm. Fluid Sci.* **2015**, *67*, 57–61.
27. Lee, M.G.; Shin, J.H.; Bae, C.Y.; Choi, S.; Park, J.K. Label-free cancer cell separation from human whole blood using inertial microfluidics at low shear stress. *Anal. Chem.* **2013**, *85*, 6213–6218.
28. SadAbadi, H.; Packirisamy, M.; Wuthrich, R. High performance cascaded PDMS micromixer based on split-and-recombination flows for lab-on-a-chip applications. *RSC Adv.* **2013**, *3*, 7296–7305.
29. Liu, Z.; Deng, Y.; Lin, S.; Xuan, M. Optimization of micro Venturi diode in steady flow at low Reynolds number. *Eng. Optim.* **2012**, *44*, 1389–1404.
30. Deng, Y.; Liu, Z.; Zhang, P.; Liu, Y.; Gao, Q.; Wu, Y. A flexible layout design method for passive micromixers. *Biomed. Microdevices* **2012**, *14*, 929–945.
31. Deng, Y.; Zhang, P.; Liu, Y.; Wu, Y.; Liu, Z. Optimization of unsteady incompressible Navier-Stokes flows using variational level set method. *Int. J. Numer. Methods Fluids* **2013**, *71*, 1475–1493.
32. Lee, M.G.; Choi, S.; Park, J.K. Rapid laminating mixer using a contraction-expansion array microchannel. *Appl. Phys. Lett.* **2009**, *95*, 051902.

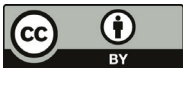

micromachines

MDPI

Article

Numerical Model of Streaming DEP for Stem Cell Sorting

Rucha Natu and Rodrigo Martinez-Duarte *

Multiscale Manufacturing Laboratory, Department of Mechanical Engineering, Clemson University, Clemson, SC 29634, USA; rnatu@g.clemson.edu

* Correspondence: rodrigm@clemson.edu; Tel.: +1-864-656-5634

Academic Editors: Xiangchun Xuan and Shizhi Qian

Received: 1 October 2016; Accepted: 25 November 2016; Published: 30 November 2016

Abstract: Neural stem cells are of special interest due to their potential in neurogenesis to treat spinal cord injuries and other nervous disorders. Flow cytometry, a common technique used for cell sorting, is limited due to the lack of antigens and labels that are specific enough to stem cells of interest. Dielectrophoresis (DEP) is a label-free separation technique that has been recently demonstrated for the enrichment of neural stem/progenitor cells. Here we use numerical simulation to investigate the use of streaming DEP for the continuous sorting of neural stem/progenitor cells. Streaming DEP refers to the focusing of cells into streams by equilibrating the dielectrophoresis and drag forces acting on them. The width of the stream should be maximized to increase throughput while the separation between streams must be widened to increase efficiency during retrieval. The aim is to understand how device geometry and experimental variables affect the throughput and efficiency of continuous sorting of SC27 stem cells, a neurogenic progenitor, from SC23 cells, an astrogenic progenitor. We define efficiency as the ratio between the number of SC27 cells over total number of cells retrieved in the streams, and throughput as the number of SC27 cells retrieved in the streams compared to their total number introduced to the device. The use of cylindrical electrodes as tall as the channel yields streams featuring >98% of SC27 cells and width up to 80 μm when using a flow rate of 10 μL/min and sample cell concentration up to 10^5 cells/mL.

Keywords: streaming dielectrophoresis; neural stem cells; numerical simulation

1. Introduction

Next-generation therapeutics such as cellular therapy and tissue regeneration are largely based on the use of stem cells [1]. These cells are characterized by a varying capacity for growth and the ability to either differentiate into specialized cells or maintain their stem cell phenotype. Neural stem cells are of special interest given their potential for neurogenesis to treat spinal cord injuries and other nervous disorders [2–4]. Neural stem cells can be differentiated as three types of cells in the central nervous system: neurons, astrocytes, and oligodendrocytes [5], with neurons being the most sought-after type of cell. Neurons obtained from the neurogenic progenitors play an important role in the treatment on Parkinson's disease, spinal cord injuries, and motor neuron diseases and also to restore lost neuronal populations [6]. However, the dynamic nature of stem cells and their susceptibility to environmental changes demand technology to monitor, characterize, and manipulate living cells [7].

Currently, the most common methods used to quantitatively characterize stem cells include fluorescence-activated cell sorting (FACS) [8], magnetic bead-coupled cell separation [9] and micropipette aspiration [10]. These methods normally use specific labels or formulation of certain probes for detection of the stem or differentiated cells. However, there is no clear set of surface markers with sufficient specificity to identify promising cells, such as neural stem cells, from a background. This limits investigation of lineage-biased progenitors and their potential use as therapeutic agents.

Hence, alternatives to traditional techniques are needed. The use of membrane capacitance and dielectrophoresis (DEP) as a label-free technique to discriminate targeted cells from a background is presented here. We focus on studying the impact of device design and experimental protocol on the throughput and efficiency when separating neurogenic progenitor cells (SC27) from astrogenic ones (SC23) in a sample of neural stem/progenitor stem cells (NSPCs). The study presented here is based on the experimental results by Labeed and co-workers where they demonstrated that the capacitance of neurogenic progenitors, SC27, differs from astrogenic progenitors, SC23, in a human NSPC population even when their size is virtually identical. Furthermore, they demonstrated that membrane capacitance increases with age of NSPCs [11]. The ultimate goal is an in-line module for cell sorting that could be incorporated in the bio manufacturing of therapeutic cells, such as after cell expansion [12].

Dielectrophoresis (DEP) refers to movement induced on the cells by an electric field gradient [13]. When the cell is less polarized than the medium, the cell moves away from the field gradient and such movement is commonly known as negative DEP. When the cell is more polarized than the medium, it moves towards the field gradient, which is known as positive DEP. Hence, by tailoring such behavior, one can direct the cells to specific locations to allow for sorting. For example, cells can be attracted to the electrodes using positive DEP. The response of the cell to a polarizing field gradient of a given frequency and when suspended in a specific medium depends on its membrane capacitance as detailed in the theoretical section below for frequencies below the MHz range. The membrane capacitance of a cell depends on its surface area and surface topography, which change as a response to various internal processes and external stimuli. Thus, membrane capacitance is used as a label-free, non-destructive quantitative indicator of cell identity and in combination with DEP to enable cell separation [11,14–19]. For example, besides their work with human stem cells, Labeed and colleagues have demonstrated the separation of mice neurogenic progenitors from a mixture [11] while Bagnaninchi et al. used membrane capacitance to detect differentiated adipocytes and osteoblasts from their progenitors [19]. Membrane capacitance has also been used to identify six main leucocyte subpopulations in hematopoietic lineage [18], while Stephens et al. have characterized how the membrane capacitance of *Clostridium difficile* can be used for separation from peripheral blood cell harvest and Talary et al. demonstrated the separation and enrichment of hematopoietic stem cells that express CD34+ from bone marrow and peripheral blood [20,21]. Furthermore, Flanagan et al. concluded that distinct changes in the dielectrophoretic properties of the neural stem cells are observed before the presence of specific cell-surface proteins (antigens) can be detected [7] and Vykoukal et al. used DEP coupled with field flow fractionation to enrich putative stem cells from adipose tissue [22].

In this paper, we use numerical simulation to assess the potential for continuous separation of Human Neural Stem/Progenitor Cells (HuNPSC) using streaming DEP. Streaming DEP refers to the focusing of targeted cells into specific streams to facilitate their retrieval from the channel. The width of the stream should be maximized to increase throughput while the separation between streams must be widened to increase efficiency during retrieval. The goal is to understand the factors that impact the forming of these streams. Here we are interested in forming streams of neurogenic progenitors (SC27) to facilitate their separation from astrogenic (SC23) progenitor cells. To this end, we assess the impact of electrode geometry, experimental flow rate and sample concentration on the efficiency and throughput of streaming DEP. We define efficiency as the ratio between the number of SC27 cells over total number of cells retrieved in the streams, and throughput as the number of SC27 cells retrieved in the streams compared to their total number input to the device. The implemented model can be applied for different electrode materials and DEP technologies. However, our goal is to use this model for the optimization of carbon electrodes. These glass-like carbon electrodes are made by carbonization of SU-8 photoresist and have been demonstrated in a number of DEP applications [23–27].

2. Operating Principle of Streaming Dielectrophoresis (DEP)

Cells can be attracted to a field gradient around the electrodes using positive DEP or repelled from it using negative DEP. The theory behind this is shown in the next section. Streaming DEP is the focusing of targeted cells into streams either collinearly with the electrodes by using positive DEP or between the electrodes using negative DEP. This is illustrated in Figure 1, where the red particles are attracted to the electrodes and eluted away in lines collinear with the electrodes. This is due to the fact that the drag and DEP forces acting on the cell are in equilibrium. Increasing the DEP force will lead to particle trapping while increasing the drag force. Increasing flow velocity will lead to hydrodynamic focusing only. The combination of DEP with hydrodynamic focusing is desired to increase the resolution of the system since hydrodynamic focusing depends mainly on the particle size [28]. The blue particles in the figure are focused in streams between electrodes using negative DEP, as in this case is where the field gradient is of less magnitude. Once focused in streams, the retrieval of cells can be facilitated by geometries as those shown in the figure. By choosing the frequency of the polarizing waveform appropriately, one can induce a positive DEP force on specific cells while inducing negative DEP on the rest. Here, we will study how the device geometry, such as electrode cross-section and height relative to the channel, and experimental parameters, such as flow rate and sample concentration, impact the width T and cell composition of these streams. We strive to understand how these parameters need to be optimized to enable streams featuring all of the SC27 cells introduced in the system (100% throughput) without contamination with SC23 cells (100% efficiency). The design of the retrieval geometries is beyond the scope of the work presented here.

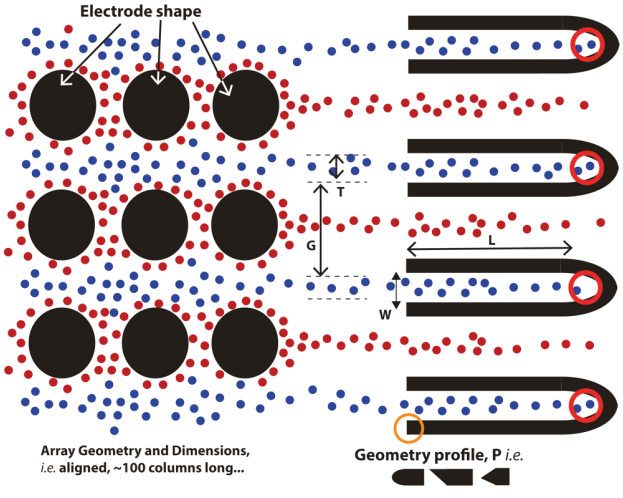

Figure 1. Schematic of the working principle of streaming dielectrophoresis (DEP). Cells can be focused into streams of specific width T and separation G between each other. Retrieval geometries can be used for continuous extraction from the channel. The impact of device geometry and experimental parameters on the composition and width of the streams is studied here. Specifically, we study the impact of electrode shape (circles, diamonds, lens-shaped) and height (10%, 50% and 100% of the channel height) as well as flow rate and cell concentration in the sample.

3. Materials and Methods

3.1. Theoretical Framework

Labeed et al. [11] have shown how the membrane capacitances of SC27 and SC23 huNSPCs are different even though they are remarkably similar in their size and levels of nestin and SOX2 markers.

Their experimental results are replicated here in Figure 2 with SC23 cells displaying a membrane capacitance value of 9.9 ± 0.2 mF/m^2 and SC27 cells of 7.6 ± 0.3 mF/m^2 and both overlapping in the size range of 6.57 to 7.75 µm.

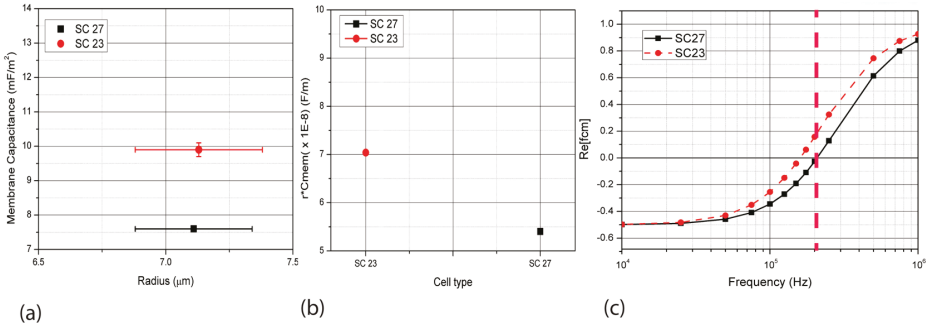

Figure 2. (**a**) The radius and membrane capacitance of different cells considered in this work as obtained experimentally by Labeed et al. [11]. The membrane capacitance of SC23 cells is 9.9 $\pm$ 0.2 mF/m^2 while that of SC27 is 7.6 ± 0.3 mF/m^2. The cell radius lies between 6.57 and 7.75 µm; (**b**) The product of radius and membrane capacitance for SC23 and SC27 is different and can be used to further distinguish the two types of cells. The values of rC_{mem} for SC27 and SC23 used here are $(5.40 \pm 0.06) \times 10^{-8}$ F/m and $(7.50 \pm 0.05) \times 10^{-8}$ F/m respectively. Note the small deviation on the average values (**c**). The values of the real part of the Clausius Mossotti factor $Re[f_{CM}]$ for SC23 and SC27 as frequency changes are obtained using Equation (2) using the r and C_{mem} values shown in Figure 2a. At the frequency of 200 kHz (dashed red line), the cells SC23 and SC27 show the highest difference in their $Re[f_{CM}]$ values, whereas SC23s show a positive value of 0.15, and SC27s show a slight negative -0.02.

Dielectrophoresis is the motion of electrically polarizable particles induced by the interaction between an electrical dipole induced on the cell and an electric field gradient [13]. The product rC_{mem} gives the cells a specific signature which will dictate the movement of the cell either towards, positive DEP, or away, negative DEP, from the electric field gradient established around the electrodes. The DEP force F_{DEP} for a spherical particle is given by Equation (1) and depends on the size of the particle r, gradient of the square of the electric field ∇E^2_{rms}, permittivity of the medium ε_m and the magnitude of the real part of the Clausius Mossotti factor f_{CM}.

$$F_{DEP} = 2\pi r^3 Re\left[f_{CM}\right] \nabla E^2_{rms} \tag{1}$$

Several authors have detailed the use of the crossover frequency method to determine the Clausius Mossotti factor of a cell experimentally [29,30]. In this method, $Re[f_{CM}]$ is given by Equation (2):

$$Re\left[f_{CM}\right] = \frac{\left(\sqrt{2}\pi r C_{mem} f\right)^2 - \sigma_m^2}{\left(\sqrt{2}\pi r C_{mem} f\right)^2 + 2\sigma_m^2} \tag{2}$$

where f is the frequency of the polarizing signal and σ_m is the electrical conductivity of the suspending medium. The dependence of $Re[f_{CM}]$ on frequency for SC27 and SC23 cells when suspended in a medium with conductivity of 0.05 S/m is calculated using Equation (2) and shown in Figure 2c when using values of r and C_{mem} obtained experimentally by Labeed et al. [11]. A polarizing frequency of 200 kHz is used in this work to model separation between different cell types, since at this frequency the difference between the $Re[f_{CM}]$ of SC23 (0.15) and SC27 (-0.02) is the maximum.

In order to implement continuous separation using cell focusing into elution streams by streaming DEP, the interaction between DEP force and hydrodynamic drag acting on the particles must be analyzed. The Stokes drag force F_{DRAG} is given by Equation (3) where the dynamic viscosity of the medium is η, the radius of the spherical particle r, the flow velocity u and the particle velocity v.

$$F_{\mathrm{DRAG}} = 6\pi\eta\,(u - v) \tag{3}$$

The sedimentation force on the cells resulting from gravity and cell buoyancy is also important and is given by Equation (4), where F_{s} is the sedimentation force, d_{p} is the density of the cell, d is the density of the medium and g is the gravitational constant.

$$F_{\mathrm{s}} = \frac{4}{3}\pi r^3\,(d_{\mathrm{p}} - d)\,g \tag{4}$$

Hence, the motion of the particle in the microfluidic channel is influenced by the total force F_{t} which is calculated by vector summation of F_{DEP}, F_{DRAG} and F_{s}:

$$F_{\mathrm{t}} = F_{\mathrm{DRAG}} + F_{\mathrm{DEP}} + F_{\mathrm{s}} \tag{5}$$

According to Newton's second law of motion, the total force F_{t} can also be expressed as,

$$m_{\mathrm{p}}\frac{dv}{dt} = F_{\mathrm{t}} \tag{6}$$

where the mass of the particle is m_{p} and v is particle velocity. The total force acting on a particle is given by Equation (7) by combining the Equations (1)–(6)

$$m_{\mathrm{p}}\frac{dv}{dt} = 6\pi\eta r(u - v) + 2\pi\varepsilon_{\mathrm{m}} r^3 Re\,[f_{\mathrm{CM}}]\,\nabla E_{\mathrm{rms}}^2 + \frac{4}{3}\pi r^3(d_{\mathrm{p}} - d)g \tag{7}$$

Equation (7) can be considered a general equation from which the sum of forces on a particle can be obtained. After proper manipulation [17], the vector of particle velocity can be obtained with Equation (8)

$$\boldsymbol{v} = \boldsymbol{u} + \frac{\boldsymbol{F_{\mathrm{DEP}}} + F_{\mathrm{s}}}{6\pi\eta r} \tag{8}$$

where $\boldsymbol{v}$ is the particle velocity vector at a given point, $\boldsymbol{u}$ is the flow velocity vector; $\boldsymbol{F_{\mathrm{DEP}}}$ is the force vector given by Equation (1) for a specific cell and experimental conditions; and F_{s} is the sedimentation force assuming a constant density throughout the medium. The 3D flow velocity field in the device as well as the electric field gradient that is required to calculate the DEP force acting on a particle throughout the device are calculated using COMSOL Multiphysics (Version 4.4, Stockholm, Sweden). The particle velocity vectors are then used to compute the position of the particle by the Lagrangian tracking method and originate streamlines of potential particle trajectories in the device [31].

There are two other important considerations that need to be taken into account when designing devices for cell sorting. The first one is the effect of shear stress on the cell. Shear stress is the tractive force produced by a moving viscous fluid on a solid body in relative motion with the fluid [32]. Although physiological levels of shear stress in the aortas of adults and embryos have been observed as 15 and 5 dyne/cm^2 respectively, magnitudes down to 1.5 dyne/cm^2 are known to effect adult blood phenotypes [33–35]. Exposure of embryonic stem cells to shear stress values of 1.5 to 15 dyne/cm^2 for 2 days promoted differentiation of embryonic stem cells [36]. Since the intended application of this work is the sorting of neurogenic progenitors, a conservative upper limit of shear stress on the cell is taken as 1.5 dyne/cm^2. This reduces the possibility of introducing undesired changes in the manipulated cells. It is important to note that the transit time of cells through the device when using streaming DEP will likely be in the order of few seconds and thus long exposure to shear stress is not taken into account here.

The other important consideration is the impact of the electric field on the cell. For example, Salmanzadeh et al. reported on DEP experiments using insulator structures (insulator-based DEP or iDEP) where tumor cells remain viable after a 30 min exposure to an electric field gradient squared around 10^{14} V^2/m^3 in the frequency range of 100–600 kHz [37]. Su et al. conducted DEP trapping of the anaerobic microbe *Clostridium difficile* on insulator-based electrodes using similar gradient conditions, thoughin the frequency range of 0.1–5 MHz. Cell viability was intact after repeated occasional exposure to the field swept over 5 min for three hours [38]. In the case of manufacturing therapeutic cells, maintaining cell viability is obviously required but not enough since changes induced on the manipulated cells can later impact the properties of their progeny. Lu et al. reported that neural stem/progenitor cells suspended in a medium with conductivity of 0.01 S/m undergo undesirable changes in their DNA when exposed to a gradient of electric field squared at around 10^{14} V^2/m^3 at frequencies in the range near the crossover frequency of the neural stem/progenitor which is 50–100 kHz [39]. In this work, the range of the crossover frequency of cells is 100–200 kHz and a similar behavior is expected. Hence, a minute is taken here as the upper limit in the exposure time of the cells to the field gradient.

3.2. Computational Model

COMSOL Multiphysics 4.4 (Stockholm, Sweden) was used to build the model to solve for the flow field and electric field in a microfluidics channel containing an array of electrodes. An Intel® Xeon® CPU E5-1650 v2 @ 3.50 GHz processor with a RAM of 32 GB and a 64-bit operating system was used for these simulations. The simplified top view of the geometrical model used is illustrated in Figure 3. The dimensions of the model are based on experimental DEP devices made with carbon electrodes and validated using different cells [24,40–42]. 3D electrodes spanning 10%, 50%, 75% and 100% of a 100 μm-high channel were simulated. The length of the channel was 9000 μm. Three types of electrode cross-sections were used: circle, diamond and lens. The characteristic dimension for each of them was 50 μm as diameter for circles and side for lens and diamond (see Figure 3). The channel width was around 700 μm and varied slightly depending on the shape of the electrode since the distance between the outer edge of the array and the channel wall was kept constant at 45 μm. The surface of the electrodes was arbitrarily polarized with voltages of 0 and 3 V to maintain a maximum electric field of 9.69×10^4 V/m and field gradient of 8.49×10^{14} V^2/m^3 to reduce the possibility of changes to the cells [43]. Flow rates from 5 to 20 μL/min were implemented since a flow rate of 20 μL/min was calculated to be the maximum value before inducing shear stress above 1.5 dyne/cm^2 on cells using the channel and electrode dimensions explored here. Given the length of the channel and flow rates simulated here, the maximum residence time of the cell in the channel is 40 s when using a flow rate of 1 μL/min.

The Laminar Flow and Electric Currents physics modules available in the software were used to compute the flow velocity and electric field gradient to calculate the drag and DEP force fields acting in the simulation domain at steady state. Gravitational and buoyancy forces were used to consider cell sedimentation. Equations presented in the theory section were solved to obtain the force fields. A mesh featuring ~4.0 million tetrahedral elements was implemented and controlled by the fluid flow physics. The average element quality achieved was 0.66. The grid used is a fine-meshed COMSOL grid with the maximum element size of 20 μm and minimum element size of 1.5 μm. Simulations were also performed with the maximum element thicknesses of 15 and 7.5 μm. The stream widths were calculated in each of these cases and the maximum deviation in stream width was calculated to be <6 μm. Since this error is smaller than the radius of the cells of interest here, the stream width does not vary significantly to affect the cell retrieval. Grid value is restricted by limited memory sources available for this study. Given the limited computational power available to us and the desire to model high cell concentrations, we did not model cells as spherical particles moving through the device. Instead, we modeled potential cell trajectories as the streamlines obtained by taking the particle velocity vectors calculated using Equation (8) and used them to compute the position of the particle

by the Lagrangian tracking method [31]. Both flow velocity and electric field gradient were obtained using COMSOL Muliphysics. The starting points of as many streamlines necessary to simulate a given cell concentration in the channel were randomly determined by generating random values in MATLAB (2014a, MathWorks, Natick, NA, USA) and feeding them back to COMSOL as starting positions. Such protocol enabled the simulation of cell dispersion throughout the channel cross-section at the inlet as will be expected in experiments. At least three different simulations were performed for each case of interest. Random starting points were used for each of these cases and hence the error bars shown in the results. From this point on in this manuscript, we refer to cell trajectories and locations as those that can be expected from modeling the streamlines in the channel.

The fact that the cells are simulated as streams introduces certain limitations in the calculations of stream widths. The thickness of the cell is not taken into account while simulating the streams. Hence, two streams which can come very close to each other (closer than the value of cell diameter) will not appropriately depict cell behavior. Also, the number of cells that can be trapped on the electrodes is restricted. This is because as the cells accumulate at the electrode, they cover a certain positive area of the electrode. As more and more cells attract towards the electrode, less area is available for cell trapping. This restriction is not present in the case of the streamlines. In spite of these limitations, the streamlines help to depict potential paths taken by individual cells in the channel.

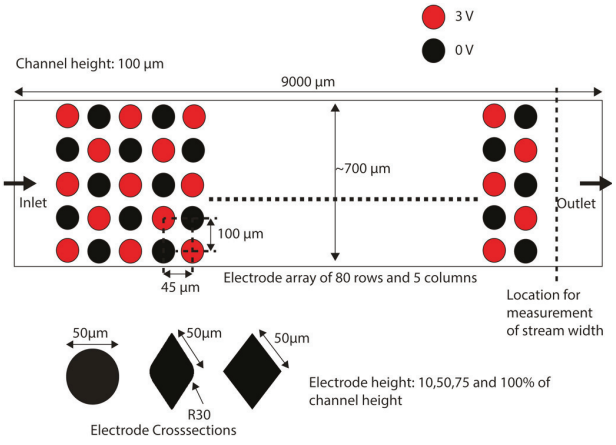

Figure 3. The top view of the model used for numerical analysis with the dimensions and electrode polarity is shown in the figure. The electrodes are arranged in a manner that they lie in straight rows and symmetrical rows. However, the electrodes are polarized alternately using either 3 or 0 V. The three cross-sections studied in this work are shown: circles, lens and diamonds. The model shown is not true to the scale, but represents the actual shape of the electrodes and channel.

All the streams were released in the channel at one time with the inlet velocities depending on their starting position and corresponding to a parabolic flow profile in the channel. Furthermore, the electric field was assumed to not be affected by local field gradients around electrodes derived from particles already trapped on the electrode surface. All modeled materials were considered to be non-porous, while the properties of the medium are uniform throughout the channel. Since flow occurred at Reynolds numbers lower than unity, a creeping flow was assumed. The electrodes and channel boundaries were assigned a slip condition. This consideration was to address the experimentally observed behavior of the cells slipping around the electrode and channel surfaces rather than abruptly sticking to them when coming in contact with such a boundary. We initially implemented a no-slip boundary condition, but this led to streamlines abruptly terminating on electrodes and channel walls, which is not true to experimental observations when using different cell types [24,40,44]. Cells are

only observed to be held on the surface electrode against a flow when the DEP force is significantly higher than the drag force. However, the cells are released and eluted as soon as the electrodes are de-polarized and the DEP force disappears.

The values for $Re[f_{CM}]$ of SC23 (0.15) and SC27 (-0.09) corresponding to the frequency of 200 kHz were used. This value was chosen based on Figure 2c which shows that the $Re[f_{CM}]$ values for the two types of cells show maximum difference; hence DEP force acting on the two types of cells will differ significantly. The values of radius for the different cells were also taken as shown in Figure 2a. Other simulation parameters are specified in Table S1 in Supplementary Information.

The electric field in the domain was derived using the equations solved in the electric currents domains, for a stationary study as,

$$E = -\nabla V \tag{9}$$

where E is the electric field computed in the domain and V is the voltage assigned to the electrode surface. X, Y and Z components for F_{DEP} were calculated here by using the equations in Table S2 (in Supplementary Information) for Electric Currents in stationary domain for the SC23 and SC27 cells.

The flow velocity u for the laminar flow field was calculated using Equations (10) and (11) where fluid density is denoted by ρ, u is the flow velocity, I is the identity matrix, and T represents the transpose of the matrix.

$$\rho\,(u \cdot \nabla)\,u = \nabla \cdot \left[-\rho I + \mu(\nabla u) + (\nabla u)^T\right] + F_t \tag{10}$$

$$\rho \nabla \cdot u = 0 \tag{11}$$

These values for the flow velocity and the F_{DEP} were used to simulate the particle motion with the particle velocity v given by Equation (8). Streamlines were simulated by using the velocity represented by Equation (8) with different inlet positions of the cells. The medium conductivity used was 0.05 S/m which has been shown to not affect the cell viability of stem cells, as was recently shown by Lu et al. as long as the cell is exposed for less than a minute [39].

3.3. Data Analysis

COMSOL data points corresponding to the ends of the streamlines were exported to MATLAB 2014a for post processing. MATLAB was used to filter the streams which represent the SC23 and SC27 cells that get captured at the electrodes and only the streams which reach the outlet were selected. Plots were generated for the end points of the streamlines at the channel outlet. This data is converted to a histogram wherein the channel width is divided into small bars (or datasets) for the range of around 6 μm width along the channel. This width was arbitrarily selected. Thus, the channel of ~700 μm-width is divided into around 115 bars. The number of streamlines reaching the outlet in the width of such a bar is stored and this data is used for calculating the percent purity of both SC23 and SC27 types of streams in the domain. This is calculated using Equation (12), where X can take the value of 3 and 7 depending on the cell type being analyzed (SC23 or SC27). Equation (13) is used to calculate the throughput of the system.

$$\%\text{ purity of SC2}X\text{ cells in a bar}: \frac{\text{total number of SC2}X\text{ streamlines in the bar} \times 100}{\text{total number of streamlines in the bar}} \tag{12}$$

$$\%\text{ throughput of SC2}X\text{ cells} = \frac{\text{total number of SC2}X\text{ streamlines in the bar} \times 100\%}{\text{total number of streamlines of SC2}X\text{ at inlet}} \tag{13}$$

4. Results

The results are resumed in the graphs shown in Figure 4a–d for different cases of electrode shape or cross-section, electrode height, flow rate and cell concentration in the sample. The x-axis in each case shows the distance along the channel with the scale marks denoting the center position of the

electrodes (45, 185, 345, 495 and 645 µm). The percentage of SC23 (red) and SC27 (blue) streamlines flowing at that particular location is denoted in the *y*-axis. The cells of interest here are SC27 cells, given their neurogenic properties. A blue stripe spanning the complete height of the graph marks the specific location where a 100% pure SC27 cell stream can be retrieved. We calculated throughput as the ratio between the number of SC27 in the streams and those entered into the system. Hence, a 100% throughput means recovery of all cells entered in the system. The throughput is reported in tab:micromachines-07-00217-t001. The goal of this work is to study the impact of different electrode geometries and experimental parameters on the efficiency and throughput of streaming DEP.

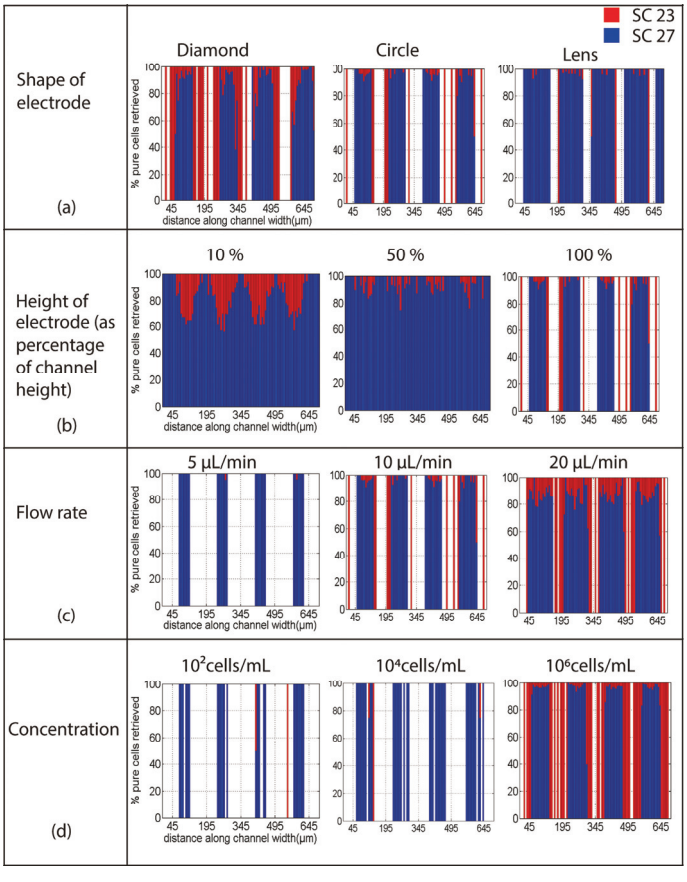

Figure 4. The percentage of SC23 and SC27 retrieved in different conditions considered in the numerical simulations. The stacked histogram in *y*-axis shows the percentage of SC23 and SC27 streams retrieved at different channel locations (from 0 to 700 µm). The *x*-axis in each case denotes the distance along the channel width and the grid points at 45, 195, 345, 495 and 645 µm mark the position of the center of each electrode in the channel. (**a**) The impact of electrode cross-section on cell separation; (**b**) Impact of electrode height relative to the channel. The purity of the streams increases with the increase in electrode height; (**c**) Impact of flow rate. 100% pure streams of SC23 cells can be obtained linearly to the electrodes as the flow rate increases. The purity of SC27 decreases at the same time; (**d**) Impact of cell concentration on the separation efficiency between cell types at 10 µL/min. SC23 cells are trapped at low concentrations and are not received, the array becomes saturated at high cell concentrations and SC23 streams start appearing collinear with the electrodes.

Table 1. The average percentage throughput in each of the cases in the simulation for SC23 and SC27 streams calculated using Equation (13). The throughput represents the percentage of total incoming streams of each type that are present in the streams after the electrode array. Since most of the SC23 streams show positive dielectrophoresis (DEP) and get captured at the electrodes, the throughput for this case is generally low. SC27 cells show negative DEP, no significant trapping and thus a high throughput is obtained.

Parameter Studied	Value	Throughput for SC23	Throughput for SC27
Shape of electrode	Lens	0.3%	69.43%
	Circle	2.40%	62.09%
	Diamond	8.51%	61.54%
Height of electrode as percentage of channel height	10%	11.31%	55.86%
	50%	3.37%	64.35%
	100%	2.40%	62.09%
Flow Rate	1 μL/min	0%	0%
	5 μL/min	0%	33.33%
	10 μL/min	2.40%	68.09%
	20 μL/min	14.48%	81.40%
Cell Concentration	10^2 cells/mL	10.61%	41.92%
	10^4 cells/mL	2.88%	68.18%
	10^6 cells/mL	2.36%	62.52%

4.1. Shape of Electrodes

The electrode shape plays an important role in determining the trapping capability when using DEP as well as the flow around it. For example, the use of sharp angles may lead to sharper electric field gradients and possible turbulence at high flow rates. Although the use of cylindrical electrodes is prominent in DEP [24,45,46], other shapes of electrodes or insulator structures have been studied. For example, Saucedo-Espinoza et al. explored insulator structures with diamond and circular cross-sections and width of ~80 μm. The use of a square shape was concluded to provide the highest trapping capacity due to the presence of large volumes with high electric field square gradient. However, the diamond and circle shapes were proven beneficial for cell focusing [47]. In the case of streaming DEP, Cummings et al. studied the use of diamond and circular cross-sections [48,49] In the case of diamond shaped electrodes, particle concentration was seen to deplete as the particles moved along the channel showing high rate of particle capture, whereas in case of posts with circular cross-sections, the particles became more focused as they moved through the channel but showed less capture than the diamonds.

The results obtained when using electrodes of different cross-sections but with their height equal to 100% of the channel height are shown in Figure 4a with a flow rate of 10 μL/min and cell concentration of 2×10^5 cells/mL. The case of diamond cross-section yields a high amount of SC23 cells being trapped in the array due to the sharp corners of the electrodes and the high field gradients that are generated. Only 8.51% of the SC23 population input in the model could be retrieved and hence the predominance of blue in the figure. About 61.54% of the SC27 cells could be retrieved at the array exit. Although the retrieval throughput of SC27 is high, the purity is only around 90% in most regions, with 95% in a few regions. In the case of circle cross-section, the retrieval of SC27 is about 62.09% whereas SC23 streams have a throughput of 2.40%, showing less trapping of SC23 cells compared to diamonds. For circles, well defined regions with SC27 purity greater than 95% can be seen in the figure. The use of the lens cross-section yields a throughput of 69.43% for SC27 cells, comparable to that of circles, but features the least percentage of SC23 retrieval among the three, only 0.3% SC23, thereby indicating high trapping and the predominant white regions aligned with the electrodes. The purity obtained in the case of lens is higher than that obtained when using the other two cross-sections; close to 100% pure SC27 streams can be seen throughout the width of the channel.

4.2. Height of Electrodes

The height of the electrode with respect to the height of the channel was varied and studied to see the effect it has on the capture and effective focusing of the SC23 and SC27 streams. The obtained results are shown in Figure 4b when the electrodes are 10%, 50% and 100% of the channel height (100 μm here). These results were obtained when using circular electrodes, a flow rate of 200 μL/min and concentration of 2×10^5 cells/mL. When the electrode height is 10% of the channel height, the throughput for SC23 is about 11.31%, whereas the throughput for SC27 is about 55.86%, indicating poor trapping for both cell types which is beneficial for continuous sorting. However, the average purity obtained at this electrode height for SC23 streams is around 20% (max. 25%), while the average purity for SC27 streams is around 70% (max. 75%). The electrodes with a height 10% of the channel are not a good choice for separation of the two species. For the electrodes with a height 50% of that of the channel, there is improvement in the trapping of the SC23 streams and the purity of SC27 streams. Around 3.37% of SC23 streams and 64.35% of SC27 streams can be retrieved. These electrodes show high trapping of SC23 streams, but the focusing of SC27 streams by negative DEP is limited. The case when the electrodes are as tall as the channel shows high improvement over the previous cases. Though the throughput of SC23 decreased to only 2.40% in this case, 68.09% SC27 streams were retrieved. The retrieval of highly focused SC23 and SC27 streams with purity higher than 95% is possible in some regions of the channel as seen in the graph. These results reinforce experimental results previously reported where the use of 3D carbon electrodes yielded better trapping efficiency [40].

4.3. Flow Rate

An important parameter to study when aiming at increasing device throughput is flow rate. The upper limit on the flow rate value is given by the necessity to prevent cell damage by shear stress. Hence, a maximum flow rate of 20 μL/min is used in this work. We report on the results obtained when increasing the flow rate from 5 to 20 μL/min at a concentration of 2×10^5 cells/mL. Simulations using flow rate of 5 μL/min illustrate how all SC23 cells get captured due to dominance of dielectric force over the drag force. As the flow rate increases to 10 μL/min, the drag force starts to dominate the dielectric force and hence the number of trapped SC23 decreases, and around 2.40% of them can be retrieved. Up to 68.09% of SC27 streams are retrieved. Though the retrieval of SC27 streams is high, the purity in this case is affected as some SC23 streams are seen in the same region as the SC27. At 20 μL/min, the maximum purity in SC27 streams that can be expected is around 85% while the throughput is around 81.04%. The throughput of SC23 is 14.48% indicating the decrease in capture of SC23 as the flow rate increases from 10 μL/min to 20 μL/min. The average purity of SC27 streams is higher (85%–90%) in the regions closer to the electrodes than in the regions in between the electrodes where it is around 70%. This is because SC27 flowing near the electrodes are effectively diverted by the dielectric forces, whereas the SC23 streams in this region are attracted to the electrodes. These phenomena decrease as the cells flow deeper into the region between the electrodes, where the SC23 and SC27 are less affected by dielectric force, and more by the drag force. Being similar in size, there is no significant discrimination between them. At the flow rate of 20 μL/min, 100% pure SC23 can be obtained in regions immediately next to the electrodes. The dielectric force is very high in these regions and SC23 streams are directed towards the electrodes. However, given the high drag force at high flow rates, the SC23 cells no longer get captured but instead are focused and eluted collinearly to the electrodes. The SC23 cells that are not affected by the DEP force attracting them to the electrodes decrease the purity of the SC27 cell stream flowing in between electrodes.

4.4. Cell Concentration

The results obtained when simulating different cell concentrations at the flow rate of 10 μL/min when using 100 μm-high circular electrodes are shown in Figure 4d. The concentration increased from 10^2 to 10^6 cells/mL. The case with 10^2 cells/mL corresponds to one cell flowing through the modeled

channel at a given time. Similarly, 10^4 cells correspond to 100 cells. For the case of 10^2–10^3 cells/mL, random coordinates were generated to determine the starting position of the cells. For the case of 10^3 cells/mL, ten different coordinates were generated to obtain a more realistic model. Three repetitions were done for cases 10^4 and 10^5 cells/mL, while only one trial was implemented for the case of 10^6 cells. The results shown in Figure 4d are representative of each case. In all cases, high purity SC27 streams are obtained from regions in between the electrodes, while mostly all the SC23s in the channel are trapped when concentration is less than 10^5 cells/mL. At the concentration of 10^6 cells of each type, the concentration is so high that not all SC23s are trapped anymore because the array starts to be saturated and the cells are eluted in characteristic streams linearly with the electrodes.

5. Discussion

The width of the elution stream, T, and the separating gap between the streams, G, are important design parameters in streaming DEP to enable continuous separation as shown in Figure 1. Depending on their values, one can design geometries with an optimized opening W for continuous extraction of the targeted cells from the channel. Photolithography is a technique that is amenable for the fabrication of such geometries [50]. If using photolithography, the minimal width of these retrieval geometries is likely to be in the tens of micrometers, with separation between each other in the same range. The width of these retrieval geometries, W, would ideally be less than the width of the cell stream, T, since this will allow for a buffer zone to mitigate contamination with other cells at the edges of the retrieval geometries. Although the downside to this will be the loss of targeted cells and a decrease in throughput, this may be less significant if the yield of cell expansion and differentiation during cell manufacturing is high.

The change of stream width according to the parameters studied here is presented in Figure 5. All points shown in this figure correspond to stream widths with purity >98% as calculated using Equation (12). Since the diameter of the SC27 cells is ~15 μm, streams narrower than this value are not considered. The effect of electrode cross-section is shown in Figure 5a. Similar to the results obtained when varying electrode height and cell concentration (Figure 5b,c, respectively), a peak on the stream width can be observed when varying the electrode cross-section. This peak occurs at 10 μL/min in the case of circular electrodes and 5 μL/min for diamonds and lens. Before these peak values, the increase on stream width is due to the combined effect of high trapping of SC23 cells on the electrodes and sharp focusing of SC27 streams by negative DEP. With the increase in flow rate beyond the corresponding peak values, not all SC23s are remain trapped and they start being eluted. The purity and width of the SC27 streams are thus reduced. At their peak values, the circular electrodes yield the widest retrieval zones at 83.16 ± 6.93 μm-width. Lens and diamonds yield 51.97 ± 8.94 μm and 64.68 ± 8.00 μm respectively at their peak values at 5 μL/min flow rate. The lens shape can be described as a combination between circle and diamond shape. Hence, it has regions with high gradients along the curved edges, like circles, which facilitate cell movement along the electrode surface. It also features sharp points like diamonds which are useful for positive DEP of SC23 due to the high electric field gradient generated at such points. In contrast to the case of diamonds where the stream width decreases rapidly after 5 μL/min of flow rate, the decrease in the case of lens is gradual. This is due to the focusing of SC23 towards the electrodes decreasing gradually when compared to diamonds.

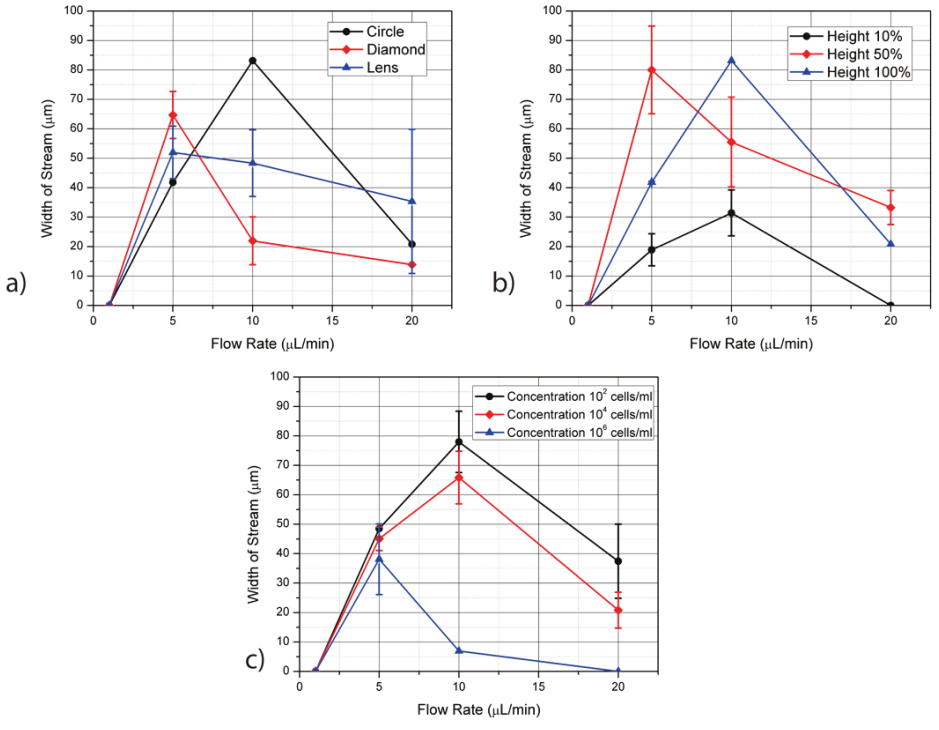

Figure 5. (**a**) The width of stream or zone obtained in the case of each electrode such that >98% pure streams of SC27 can be retrieved in the zone. The width of the zone initially increases with the increase in flow rate until it reaches a peak value before it starts decreasing. The circle shape features the widest zone for the flow rate of 10 μL/min followed by the lens and the diamond shape. However, the width of the zone decreases rapidly as the flow rate increases; (**b**) The width of the streams for obtaining >98% pure SC27 streams at different heights of the cylindrical electrodes as the flow rate varies. The stream width for the case of heights 50% and 100% of the channel are comparable as seen in this figure and are much higher than the case of height 10% of the channel. This reiterates the effect of height of the electrode for focusing. In this case, the stream width decreases with increase in flow rate; (**c**) The study of concentration of streams was conducted for stream purities of 98% and above with the increase in flow rates. The zone width increases with flow rate and shows a peak at the flow rate of 10 μL/min, after which it decreases. The zone width increases as the concentration of the cells decrease, mostly owing to less contamination of SC27 cells by SC23 cells that are retrieved through the zones.

A peak on the stream width can be observed when varying the other parameters of interest as well. In the case of electrode height, the use of electrodes as tall as the channel (100% height) leads to a maximum stream width of 83.16 ± 6.93 μm at 10 μL/min. The use of shorter electrodes does not yield stream widths as wide. In the case of electrodes spanning half the channel height, the peak value of stream width is seen at 5 μL/min but the value drops at higher flow rates since the drag force starts dominating the DEP force. The SC23 streams are not attracted to the electrodes as effectively and start flowing from the retrieval regions for SC27. The use of short electrodes only addresses the particles flowing close to the channel floor and hence their separation performance is poor. The region with active electric field is present only at the 10% of the channel height and hence the stream widths obtained in this case are smaller than the electrodes covering 50% and 100% of the channel height.

Using cell concentration of 10^2 cells/mL results on the widest stream width (77.96 ± 10.39 μm) followed by 10^4 cells/mL (65.83 ± 8.94 μm) and 10^6 cells/mL (6.93 μm). A peak on the stream width is again observed at 10 μL /min for the concentrations of 10^2 and 10^4 cells/mL. An important observation here is with the cell concentration of 10^5 cells/mL considered in the case of Figure 5a,b. In these cases, the cell concentration of 10^5 cells/mL show a high stream width of around 83.16 μm. Thus the stream width is seen to decrease beyond this value of cell concentration. The use of flow rates of 20 μL/min leads to a significant decrease on the width of streams with >98% purity of SC27 cells. For a fixed stream width, a lower cell concentration ~10^2 cells/mL with a high flow rate can give a device with high efficiency, but with a low throughput. Using samples with high concentrations ~10^6 cells/mL at a low flow rate can give a high throughput but with a low efficiency. The parameters to be implemented can thus be optimized based on the requirement of throughput and efficiency depending on the application.

The behavior of stream width and composition depending on electrode geometry, flow rate and sample concentration has been studied here. Implementing a flow rate of 10 μL/min leads to SC27 cell streams featuring purity >98% and as wide as 80 μm when using cylindrical electrodes that are as tall as the channel and a sample concentration in the range 10^2–10^5 cells/mL. However, the throughput changes on the cell concentration, from 41.92% at 10^2 cells/mL to 61.52% at 10^5 cells/mL.

The number of cells currently required for neuron-based therapy is around 10^5 per dose [51]. At a flow rate in the device of 10 μL/min, a sample concentration of 10^5 cells/mL, a throughput of 62.09%, and assuming that up to 50% of the sample are cells of interest, the purification of SC27 cells using streaming DEP with the device modeled here will take around 6 h. At these conditions, an individual cell undergoes shear stress lower than 1.5 dynes/cm^2. Future work will be on increasing the flow rate through the device while maintaining low levels of shear stress. For example, the channel cross-section will be significantly expanded to increase the flow rate thanks to the increase of cross-section only. This will likely require the fabrication of improved 3D electrodes and the optimization of their polarizing voltage depending on the electrode material.

Once the streams are formed, retrieval geometries will be implemented. The length of the retrieval geometry L in Figure 1 plays an important role to sustain the retrieved cells. A short geometry will cause quick accumulation and clogging of the retrieval geometry. Also, at high flow rates, the inflowing stream will cause transient flow in the collection geometry and will build back pressure in the zone. To avoid this, the retrieval geometry should be sufficiently long to allow continuation of the flow developed in the channel. The design of the entrance profile marked as P in the Figure 4 also affects the dynamics of the streaming geometry. For example, at a flow rate of 10 μL/min, a discrete separation between SC27 and SC23 streams is obtained and a pointed entrance profile will cut through the flow without affecting the cell streaming. The pointed entrance with the sloping edge facing the retrieval geometry can be used where the streams for pure SC27 cells are discretely defined and all the streams which are enclosed by the edges are collected. When the boundaries of the streams show a mixture of the two types of cells and it is desired to eliminate these cells, the sloping edge facing the outward side of the retrieval zone would enable their flow out of the geometry. With higher flow rates, the pointed profile will create obstructions in the flow and can create pressure drop or back flow as the stream enters the retrieval region, whereas the curved entrance profile will create a more gradual gradient of pressure as the stream transits from the channel to the retrieval geometry. Further investigations into the microchannel flow dynamics for the design of retrieval geometries are necessary and will be conducted in future work.

6. Conclusions

The results presented demonstrate the potential to continuously separate SC27 from SC23 cells using streaming dielectrophoresis (DEP). The impact of electrode geometry, flow rate and sample concentration on the generation of cell streams with purity >98% was studied. The use of circle and lens cross-section prove beneficial for obtaining high stream widths, but the circle cross-section offers

better reproducibility. The use of electrodes as tall as the channel was concluded to be ideal due to the wide streams obtained at the flow rate of 10 μL/min. The stream widths show a peak with the increase in flow rate initially as the effect of DEP and drag forces aid the stream formation, but the stream width decreases further as the flow rate increases. Increasing the cell concentration above 10^5 cells/mL was seen to generate narrower stream widths. The throughput obtained in the case of electrodes with 100% height and circular cross-section is 62.09% and varies with electrode shape and flow rate in the channel. The use of cylindrical electrodes as tall as the channel leads to the generation of streams with width up to 80 μm which facilitates the fabrication of retrieval geometries using photolithography. The time required to generate a therapeutic dose using the parameters optimized here can be as long as 6 h. This is deemed too long for a practical application and further work is required to shorten this time to less than 30 min. However, these initial results allow for identifying the effect of different parameters on the equilibrium between the DEP and drag forces required for streaming DEP. Streaming DEP can enable continuous separation of cells in a microfluidic chip. Further optimization of parameters like electrode shape, dimensions and flow rate are needed to decrease the processing times of relevant sample volumes for cell manufacturing.

Supplementary Materials: The following are available online at www.mdpi.com/2072-666X/7/12/217/s1. Table S1: Parameters defined for the simulation. Table S2: Equations defined for the simulation.

Acknowledgments: The authors acknowledge Rohan Galgalikar for his help during data processing using MATLAB R2014a.

Author Contributions: R.N. and R.M.-D. conceived and designed the experiments as well as analyzed the data; R.N. performed the experiments.

Conflicts of Interest: The authors declare no conflict of interest.

References

1. Zandstra, P.W.; Nagy, A. Stem cell bioengineering. *Annu. Rev. Biomed. Eng.* **2001**, *3*, 275–305. [CrossRef] [PubMed]
2. Koeppe, R.A.; Cortex, C.; Petrides, M.; Alivisatos, B.; Meyer, E.; Evans, A.C.; Natl, P.; Sci, A.; Owen, A.M.; Evans, A.C.; et al. Generalized potential of adult neural stem cells. *Science* **2000**, *288*, 1660–1663.
3. Martino, G.; Martino, G.; Pluchino, S.; Pluchino, S. The therapeutic potential of neural stem cells. *Nat. Rev. Neurosci.* **2006**, *7*, 395–406. [CrossRef] [PubMed]
4. Okada, S.; Ishii, K.; Yamane, J.; Iwanami, A.; Ikegami, T.; Katoh, H.; Iwamoto, Y.; Nakamura, M.; Miyoshi, H.; Okano, H.J.; et al. In vivo imaging of engrafted neural stem cells: Its application in evaluating the optimal timing of transplantation for spinal cord injury. *FASEB J.* **2005**, *19*, 1839–1841. [CrossRef] [PubMed]
5. Kennea, N.L.; Mehmet, H. Neural stem cells. *J. Pathol.* **2002**, *197*, 536–550. [CrossRef] [PubMed]
6. Goldman, S. Stem and progenitor cell-based therapy of the human central nervous system. *Nat. Biotechnol.* **2005**, *23*, 862–871. [CrossRef] [PubMed]
7. Flanagan, L.A.; Lu, J.; Wang, L.; Marchenko, S.A.; Jeon, N.L.; Lee, A.P.; Monuki, E.S. Unique dielectric properties distinguish stem cells and their differentiated progeny. *Stem Cells* **2008**, *26*, 656–665. [CrossRef] [PubMed]
8. Uchida, N.; Buck, D.W.; He, D.; Reitsma, M.J.; Masek, M.; Phan, T.V.; Tsukamoto, A.S.; Gage, F.H.; Weissman, I.L. Direct isolation of human central nervous system stem cells. *Proc. Natl. Acad. Sci. USA* **2000**, *97*, 14720–14725. [CrossRef] [PubMed]
9. Spangrude, G.J.; Heimfeld, S.; Weissman, I.L. Purification and characterization of mouse hematopoietic stem cells. *Science* **1988**, *241*, 58–62. [CrossRef] [PubMed]
10. Hochmuth, R.M. Micropipette aspiration of living cells. *J. Biomech.* **2000**, *33*, 15–22. [CrossRef]
11. Labeed, F.H.; Lu, J.; Mulhall, H.J.; Marchenko, S.A.; Hoettges, K.F.; Estrada, L.C.; Lee, A.P.; Hughes, M.P.; Flanagan, L.A. Biophysical characteristics reveal neural stem cell differentiation potential. *PLoS ONE* **2011**, *6*, e25458. [CrossRef] [PubMed]
12. Schnitzler, A.C.; Verma, A.; Kehoe, D.E.; Jing, D.; Murrell, J.R.; Der, K.A.; Aysola, M.; Rapiejko, P.J.; Punreddy, S.; Rook, M.S. Bioprocessing of human mesenchymal stem/stromal cells for therapeutic use: Current technologies and challenges. *Biochem. Eng. J.* **2015**, *108*, 3–13. [CrossRef]

13. Pethig, R. Dielectrophoresis: Status of the theory, technology, and applications. *Biomicrofluidics* **2010**, *4*, 22811. [CrossRef] [PubMed]
14. Huang, Y.; Joo, S.; Duhon, M.; Heller, M.; Wallace, B.; Xu, X. Dielectrophoretic cell separation and gene expression profiling on microelectronic chip arrays. *Anal. Chem.* **2002**, *74*, 3362–3371. [CrossRef] [PubMed]
15. Pethig, R.; Talary, M.S. Dielectrophoretic detection of membrane morphology changes in Jurkat T-cells undergoing etoposide-induced apoptosis. *IET Nanobiotechnol.* **2007**, *1*, 2–9. [CrossRef] [PubMed]
16. Yang, J.; Huang, Y.; Wang, X.; Wang, X.-B.; Becker, F.F.; Gascoyne, P.R.C. Dielectric properties of human leukocyte subpopulations determined by electrorotation as a cell separation criterion. *Biophys. J.* **1999**, *76*, 3307–3314. [CrossRef]
17. Pethig, R.; Bressler, V.; Carswell-Crumpton, C.; Chen, Y.; Foster-Haje, L.; García-Ojeda, M.E.; Lee, R.S.; Lock, G.M.; Talary, M.S.; Tate, K.M. Dielectrophoretic studies of the activation of human T lymphocytes using a newly developed cell profiling system. *Electrophoresis* **2002**, *23*, 2057–2063. [CrossRef]
18. Vykoukal, D.M.; Gascoyne, P.R.C.; Vykoukal, J. Dielectric characterization of complete mononuclear and polymorphonuclear blood cell subpopulations for label-free discrimination. *Integr. Biol. (Camb.)* **2009**, *1*, 477–484. [CrossRef] [PubMed]
19. Bagnaninchi, P.; Drummond, N.; Giaever, I. Real-time label-free monitoring of adipose-derived stem cell differentiation with electric cell-substrate impedance sensing. *Proc. Natl. Acad. Sci. USA* **2011**, *108*, 6462–6467. [CrossRef] [PubMed]
20. Stephens, M.; Talary, M.S.; Pethig, R.; Burnett, A.K.; Mills, K.I. The dielectrophoresis enrichment of CD34+ cells from peripheral blood stem cell harvests. *Bone Marrow Transplant.* **1996**, *18*, 777–782. [PubMed]
21. Talary, M.S.; Mills, K.I.; Hoy, T.; Burnett, A.K.; Pethig, R. Dielectrophoretic separation and enrichment of CD34 cell subpopulations from bone marrow. *Med. Biol. Eng. Comput.* **1995**, *33*, 235–237. [CrossRef] [PubMed]
22. Vykoukal, J.; Vykoukal, D.M.; Freyberg, S.; Alt, E.U.; Gascoyne, P.R.C. Enrichment of putative stem cells from adipose tissue using dielectrophoretic field-flow fractionation. *Lab Chip* **2008**, *8*, 1386–1393. [CrossRef] [PubMed]
23. Islam, M.; Natu, R.; Larraga-Martinez, M.F.; Martinez-Duarte, R. Enrichment of diluted cell populations from large sample volumes using 3D carbon-electrode dielectrophoresis. *Biomicrofluidics* **2016**, *10*, 033107. [CrossRef] [PubMed]
24. Martinez-Duarte, R.; Camacho-Alanis, F.; Renaud, P.; Ros, A. Dielectrophoresis of lambda-DNA using 3D carbon electrodes. *Electrophoresis* **2013**, *34*, 1113–1122. [CrossRef] [PubMed]
25. Martinez-Duarte, R. Carbon-electrode dielectrophoresis for bioparticle manipulation. *ECS Trans.* **2014**, *61*, 11–22. [CrossRef]
26. Martinez-Duarte, R.; Andrade-Roman, J.; Martinez, S.O.; Madou, M. A high throughput multi-stage, multi-frequency filter and separation device based on carbon dielectrophoresis. *NSTI-Nanotech* **2008**, *3*, 316–319.
27. Teixidor, G.T.; Zaouk, R.B.; Park, B.Y.; Madou, M.J. Fabrication and characterization of three-dimensional carbon electrodes for lithium-ion batteries. *J. Power Sources* **2008**, *183*, 730–740. [CrossRef]
28. Kralj, J.G.; Lis, M.T.W.; Schmidt, M.A.; Jensen, K.F. Continuous dielectrophoretic size-based particle sorting. *Anal. Chem.* **2006**, *78*, 5019–5025. [CrossRef] [PubMed]
29. Das, C.M.; Becker, F.; Vernon, S.; Noshari, J.; Joyce, C.; Gascoyne, P.R.C. Dielectrophoretic segregation of different human cell types on microscope slides. *Anal. Chem.* **2005**, *77*, 2708–2719. [CrossRef] [PubMed]
30. Adams, T.N.G.; Turner, P.A.; Janorkar, A.V.; Zhao, F.; Minerick, A.R. Characterizing the dielectric properties of human mesenchymal stem cells and the effects of charged elastin-like polypeptide copolymer treatment. *Biomicrofluidics* **2014**, *8*, 1–15. [CrossRef] [PubMed]
31. Kang, K.H.; Kang, Y.; Xuan, X.; Li, D. Continuous separation of microparticles by size with direct current-dialectrophoresis. *Electrophoresis* **2006**, *27*, 694–702. [CrossRef] [PubMed]
32. Dewey, C.F., Jr.; Bussolari, S.R.; Gimbrone, M.A., Jr.; Davies, P.F. The dynamic response of vascular endothelial cells to fluid shear stress. *J. Biomech. Eng.* **1981**, *103*, 177–185. [CrossRef] [PubMed]
33. Adamo, L.; Naveiras, O.; Wenzel, P.L.; McKinney-Freeman, S.; Mack, P.J.; Gracia-Sancho, J.; Suchy-Dicey, A.; Yoshimoto, M.; Lensch, M.W.; Yoder, M.C.; et al. Biomechanical forces promote embryonic haematopoiesis. *Nature* **2009**, *459*, 1131–1135. [CrossRef] [PubMed]

34. Fukuda, S.; Schmid-Schönbein, G.W. Regulation of CD18 expression on neutrophils in response to fluid shear stress. *Proc. Natl. Acad. Sci. USA* **2003**, *100*, 13152–13157. [CrossRef] [PubMed]
35. Gerszten, R.E.; Lim, Y.C.; Ding, H.T.; Snapp, K.; Kansas, G.; Dichek, D.A.; Cabañas, C.; Sánchez-Madrid, F.; Gimbrone, M.A.; Rosenzweig, A.; et al. Adhesion of monocytes to vascular cell adhesion molecule-1-transduced human endothelial cells: Implications for atherogenesis. *Circ. Res.* **1998**, *82*, 871–878. [CrossRef] [PubMed]
36. Wolfe, R.P.; Ahsan, T. Shear stress during early embryonic stem cell differentiation promotes hematopoietic and endothelial phenotypes. *Biotechnol. Bioeng.* **2013**, *110*, 1231–1242. [CrossRef] [PubMed]
37. Salmanzadeh, A.; Romero, L.; Shafiee, H.; Gallo-Villanueva, R.C.; Stremler, M.A.; Cramer, S.D.; Davalos, R.V. Isolation of prostate tumor initiating cells (TICs) through their dielectrophoretic signature. *Lab Chip* **2012**, *12*, 182–189. [CrossRef] [PubMed]
38. Su, Y.H.; Warren, C.A.; Guerrant, R.L.; Swami, N.S. Dielectrophoretic monitoring and interstrain separation of intact clostridium difficile based on their S(Surface)-layers. *Anal. Chem.* **2014**, *86*, 10855–10863. [CrossRef] [PubMed]
39. Lu, J.; Barrios, C.A.; Dickson, A.R.; Nourse, J.L.; Lee, A.P.; Flanagan, L.A. Advancing practical usage of microtechnology: A study of the functional consequences of dielectrophoresis on neural stem cells. *Integr. Biol.* **2012**, *4*, 1223. [CrossRef] [PubMed]
40. Martinez-Duarte, R.; Renaud, P.; Madou, M.J. A novel approach to dielectrophoresis using carbon electrodes. *Electrophoresis* **2011**, *32*, 2385–2392. [CrossRef] [PubMed]
41. Elitas, M.; Martinez-Duarte, R.; Dhar, N.; McKinney, J.D.; Renaud, P. Dielectrophoresis-based purification of antibiotic-treated bacterial subpopulations. *Lab Chip* **2014**, *14*, 1850–1857. [CrossRef] [PubMed]
42. Jaramillo, M.D.C.; Martínez-Duarte, R.; Hüttener, M.; Renaud, P.; Torrents, E.; Juárez, A. Increasing PCR sensitivity by removal of polymerase inhibitors in environmental samples by using dielectrophoresis. *Biosens. Bioelectron.* **2013**, *43*, 297–303. [CrossRef] [PubMed]
43. Teissié, J.; Rols, M.P. An experimental evaluation of the critical potential difference inducing cell membrane electropermeabilization. *Biophys. J.* **1993**, *65*, 409–413. [CrossRef]
44. Martinez-Duarte, R.; Rouabah, H.A.; Green, N.G.; Madou, M.; Morgan, H. Higher efficiency and throughput in particle separation with 3D dielectrophoresis with C-MEMS. In Proceedings of the 11th International Conference on Miniaturized Systems for Chemistry and Life Sciences, microTAS 2007, Paris, France, 7–11 October 2007; Volume 1, pp. 826–828.
45. Xu, H.; Malladi, K.; Wang, C.; Kulinsky, L.; Song, M.; Madou, M. Carbon post-microarrays for glucose sensors. *Biosens. Bioelectron.* **2008**, *23*, 1637–1644. [CrossRef] [PubMed]
46. Wang, C.; Taherabadi, L.; Jia, G.; Kassegne, S.; Zoval, J.; Madou, M. Carbon-MEMS architectures for 3D microbatteries. *Proc. SPIE* **2004**, *5455*, 295–302.
47. Saucedo-Espinosa, M.A.; Lapizco-Encinas, B.H. Design of insulator-based dielectrophoretic devices: Effect of insulator posts characteristics. *J. Chromatogr. A* **2015**, *1422*, 325–333. [CrossRef] [PubMed]
48. Cummings, E.B. Streaming dielectrophoresis for continuous-flow microfluidic devices. *IEEE Eng. Med. Biol. Mag.* **2003**, *22*, 75–84. [CrossRef] [PubMed]
49. Cummings, E.B.; Singh, A.K. Dielectrophoresis in microchips containing arrays of insulating posts: Theoretical and experimental results. *Anal. Chem.* **2003**, *75*, 4724–4731. [CrossRef] [PubMed]
50. Rogers, J.A.; Nuzzo, R.G. Recent progress in soft lithography. *Mater. Today* **2005**, *8*, 50–56. [CrossRef]
51. Serra, M.; Brito, C.; Correia, C.; Alves, P.M. Process engineering of human pluripotent stem cells for clinical application. *Trends Biotechnol.* **2012**, *30*, 350–359. [CrossRef] [PubMed]

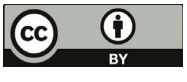

micromachines

MDPI

Article

Microfluidic Mixing and Analog On-Chip Concentration Control Using Fluidic Dielectrophoresis

Nicholas Mavrogiannis, Mitchell Desmond, Kenny Ling, Xiaotong Fu and Zachary Gagnon *

Department of Chemical and Biomolecular Engineering, Johns Hopkins University, Maryland Hall 220A, Baltimore, MD 21218, USA; nmavrog1@jhu.edu (N.M.); mdesmond42@gmail.com (M.D.); kling2@jhu.edu (K.L.); xfu7@jhu.edu (X.F.)

* Correspondence: zgagnon1@jhmi.edu; Tel.: +1-410-516-8489

Academic Editors: Xiangchun Xuan and Shizhi Qian

Received: 4 October 2016; Accepted: 14 November 2016; Published: 23 November 2016

Abstract: Microfluidic platforms capable of complex on-chip processing and liquid handling enable a wide variety of sensing, cellular, and material-related applications across a spectrum of disciplines in engineering and biology. However, there is a general lack of available active microscale mixing methods capable of dynamically controlling on-chip solute concentrations in real-time. Hence, multiple microfluidic fluid handling steps are often needed for applications that require buffers at varying on-chip concentrations. Here, we present a novel electrokinetic method for actively mixing laminar fluids and controlling on-chip concentrations in microfluidic channels using fluidic dielectrophoresis. Using a microfluidic channel junction, we co-flow three electrolyte streams side-by-side so that two outer conductive streams enclose a low conductive central stream. The tri-laminar flow is driven through an array of electrodes where the outer streams are electrokinetically deflected and forced to mix with the central flow field. This newly mixed central flow is then sent continuously downstream to serve as a concentration boundary condition for a microfluidic gradient chamber. We demonstrate that by actively mixing the upstream fluids, a variable concentration gradient can be formed dynamically downstream with single a fixed inlet concentration. This novel mixing approach offers a useful method for producing variable on-chip concentrations from a single inlet source.

Keywords: mixing; fluidic dielectrophoresis; microfluidics; laminar flow; chemical gradient

1. Introduction

Microfluidics is emerging as a fundamental engineering science for development of lab-on-a-chip (LOC) and point-of-care diagnostic platforms. A primary objective for LOC design is to miniaturize conventional chemical and biological analysis processes so they can function without human intervention on-chip. The benefits of using microfluidics to support LOC technology are well known and include shorter analysis times, reduced sample volume, and significantly reduced manufacturing and operation costs. One challenge in designing miniaturized LOC processes is reagent mixing. Common laboratory tasks such as protein immunoassays [1,2], DNA hybridization [3,4], and cell culture [5] all require well-controlled mixing. Mixing at low Reynolds number [6], however, can be challenging since inertial contributions to fluid motion are small and macromolecules such as protein and DNA often have low diffusion coefficients. Additionally, microfluidic mixing is often binary in nature. A fluid, for example, with an initial solute concentration is often combined and mixed together with another fluid to create a new, but fixed, solute concentration that is different from the original solution. The ability to dynamically control solute concentration during this process is challenging, and microfluidic processes often require significant off-chip sample preparation and multiple mixing steps on-chip to create mixed solutions at desired on-chip concentrations.

Microfluidic mixing can be accomplished either passively with secondary flow fields or actively using externally applied fluid forces. Because the Reynolds number is often well below one, these passive methods create mixing by stretching the interface between two liquid streams to decrease the distance over which diffusion occurs. Passive mixing approaches focus on increasing mixing fluid contact area or contact time to promote enhanced diffusion between flows. One popular passive mixing method uses microfluidic lamination, where multiple streams a forced to split and then later gather as a multitude of smaller streams in order to increase the contact area between the flows [7]. While lamination can provide fast mixing times and shorter mixing lengths [8], it typically requires complex fabrication methods and a complicated network of microchannels. Other passive mixers rely on the use of patterned surface chemistry [9], 3-D serpentine structures [10,11] and baffles or obstacles to create secondary flows for mixing [12–16]. While effective, passive methods create disperse samples, and the final on-chip solute concentration is diluted as it spreads out longitudinally into neighboring buffer during the mixing process. Additionally, while passive mixing devices can typically mix within 55–300 ms, many devices result in lower mixing efficiency, and therefore require a longer mixing to achieve optimal mixing.

An alternative to passive mixing is active mixing, where fluid streams are combined with the use of an external driving force [17,18]. Common active methods include mixing by peristaltic pumps [19], magnetic particles [20–22] or surface acoustic waves [23,24]. Because active mixing can often produce flow fields with larger fluid velocities than passive methods, active mixing methods generally have shorter on-chip mixing dimensions and mixing times. One way to actively drive fluid mixing is to use electrokinetics. In this approach, an electrical field is introduced into a microchannel. The field interacts with regions of non-neutral space charge to drive fluid motion. These electrokinetic flows can then be harnessed to drive the mixing of two of more fluidic streams.

While many microfluidic mixing methods exist, they are all based on the principle of binary dilution, where two or more flow volumes are combined to produce a larger volume at a fixed diluted concentration. While both active and passive mixing techniques have been effective in combating the lack of inertial influence at low Reynolds number, it is currently very difficult to control on-chip concentration in real-time during mixing. Here, we present a novel electrokinetic mixing approach for dynamically tuning and controlling the on-chip solute concentration of fluid flows. Mixing is accomplished using an externally applied alternating current (AC) electric field dropped across a microchannel with three co-flowing liquid streams. Two outer streams contain a solute to be mixed with the central stream, while the inner central stream flows downstream to a chemical gradient generator. The laminar flow field is electrokinetically driven across the microchannel by the electric field and the magnitude of fluid motion can be controlled by varying the frequency and electric field strength. We show that on-chip solute concentration in the central flow stream can be dynamically controlled and demonstrate usefulness of this method by controlling the concentration in a downstream microfluidic gradient generator.

2. Experimental Section

Electrokinetic mixing experiments were performed using a two-stage microfluidic device (Figure 1). An upstream stage was used to electrokinetically mix multiple laminar streams into a single stream at a desired concentration. This mixed stream was then continuously fed into a downstream stage where it was used to create a stable microfluidic gradient. The overall two-stage design offered a means to assess fluidic mixing by our electrokinetic approach, and to demonstrate dynamic on-chip concentration control.

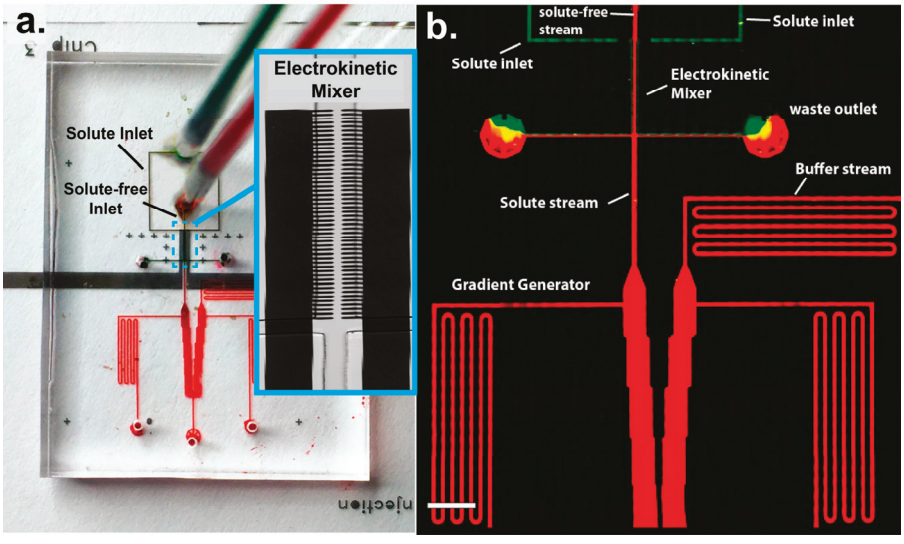

Figure 1. (**a**) Microfludic device with embedded electrodes. The solute and solute-free streams are delivered to the top and bottom inlets respectively. The electrokinetic mixer, boxed in blue, is shown in a magnified brightfield image; (**b**) Montage of the dual-stage microfluidic device. The upstream stage consists of an electrokinetic mixer which is fed continuously downstream to a gradient generator. An electric field is used to inject two solute streams into a central solute-free stream. This stream then serves as an input to the downstream gradient generator. Scale bar, 100 μm.

The upstream electrokinetic mixing was performed using a combination of laminar and field-induced electrokinetic flow. An array of point electrodes drive fluid into motion by electrokinetic flow using fluidic dielectrophoresis (fDEP). In fDEP, laminar liquid interfaces are polarized and driven into motion by an externally applied AC electric field [25]. To produce fDEP mixing, three different fluid streams were introduced into a main flow channel using an external constant pressure source and made to flow side-by-side in a main flow channel. The electrical properties of the two outer streams were adjusted such that they had a higher conductivity and lower dielectric constant than the inner fluid stream. Therefore, two electrical liquid interfaces were produced that could then be polarized and driven into motion with an electric field. The fluidic channel network was designed such that the two outer streams were driven into waste outlets, while the central stream remained in the device and was sent continuously downstream to a gradient chamber. Therefore, only a "clean" central fluid is sent downstream, while the two outer, high conductive green streams are forced to flow to outlet waste streams. In this work, we demonstrate that fDEP can be used to mix the contents of the two outer fluids with the central fluid. When an AC electric field is applied across the three streams, the two fluid interfaces polarize and deflect, and forcibly inject their contents into the center stream (Figure 2). This injection rate can be exploited to control the concentration in a downstream microfluidic system.

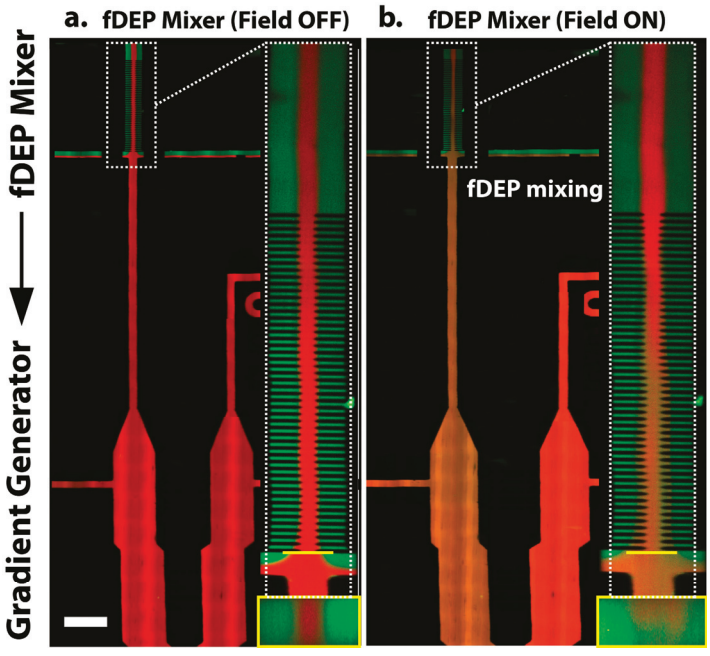

Figure 2. (**a**) Left: The microfluidic device consists of two stages: an upstream mixing stage with embedded electrodes and a downstream gradient chamber. The microchannel network is designed such that when no alternating current (AC) field is applied, only the low conductive central red stream flows to the gradient chamber. Right: A magnified micrograph of the mixing section. A yellow line depicts the spatial location where a 3D cross-sectional image was capture, shown under the zoomed in image; (**b**) When an AC electric field was applied, mixing occurred and influence the solute concentration supplied to the gradient chamber. The mixing section shows that while the red stream enters the mixing zone and exits with a slight orange hue due to mixing with the two outer streams. Scale bar, 200 μm.

2.1. Device Design and Fabrication

Mixing experiments were performed using a microfluidic channel network with embedded planar electrodes, as shown in Figure 1. Each device was fabricated using a combination of standard soft lithography and microfabrication techniques. Briefly, microchannel electrodes were fabricated using wet chemical etching. Glass cover slips (50 × 30 mm—#1, Fisher Scientific, Hampton, NH, USA) were first coated with 2 nm of chrome and 50 nm of gold using electron beam evaporation. The cover slips were then patterned with photoresist (Shipley 1813) and exposed metal film was etched away with gold and chrome etchant to create an array of metal electrodes. The polymer microfluidic device, which sits atop the glass coverslip was fabricated in PDMS (Momentive, Freemont, CA, USA, RTV 615A). Channels were fabricated in PDMS using a polymer mold constructed out of SU-8 photoresist (Microchem, Westborough, MA, USA). SU-8 was lithographically fabricated onto a silicon wafer using contact lithography. The polymer mold consisted of two different layers—one 3 μm layer and a second 65 μm-tall layer. The 3 μm layer was used to form an array of gradient channels while the 65 μm layer formed the upstream mixing and fluidic routing channels and gradient chambers. First a thin 3 μm layer of SU-8 was patterned onto a silicon water. The layer was patterned using contact lithography and developed. Next, a second 65 μm layer of SU-8 was spin coated onto the wafer and patterned and developed, to produce a dual-layer device. A 1:10 mixture of PDMS elastomer

and curing agent was poured atop the SU-8 polymer mold, cured and gently peeled off. Fluid ports were punched into the PDMS using a 0.75 mm biopsy punch (Ted Pella, Inc., Redding, CA, USA). The microchannel and coverslip were exposed to oxygen plasma (Jelight, Irvine, CA, USA, Model 42A) and immediately aligned and sealed under an inverted microscope. The completed device consisted of a network of flow channels 100 μm wide and 65 μm high connected to a series of perpendicular downstream gradient channels. Point electrodes were embedded in the main upstream channel. They were axially separated by 20 μm and symmetrically bridged the channel width. The downstream gradient chamber consisted of two reservoirs, one with an inlet stream consisting entirely of a low conductive buffer. The adjacent reservoir was fed liquid from the upstream, main flow channel. Electrodes with sharp points were utilized in order to maximize the electric field strength across the liquid interface, as the sharp point serves to focus the electric field to the tip of the electrode.

2.2. Electrokinetic Flow

AC electric fields have long been exploited to manipulate the fluidic contents of microfluidic systems. Fluid motion is produced through an interaction between an applied electric field and interfacial charge, and when an electric field is applied to a charged surface or liquid domain, an electrical stress is produced that can be used to drive fluid flow. In liquids, these electrokinetic flows occur when a field is applied tangential to polarized surface (e.g., electro-osmosis) or across regions of fluid with spatial gradients in electrical properties (e.g., electrothermal flow). Recently, a new type of electrokinetic flow was discovered in the vicinity of laminar liquid interfaces formed between two miscible aqueous liquids [26]. The phenomenon is known as fluidic dielectrophoresis (fDEP), which describes the frequency-dependent fluid motion of a laminar liquid interface in response to an AC electric field. Interfacial fluid motion is produced using a series of parallel electrodes integrated into a microfluidic t-channel device with three co-flowing liquids (Figure 2a). Each liquid has a different electrical conductivity and dielectric constant such that a large electrical mismatch exists at the interface formed between the two liquids. When an AC field is delivered across the three co-flowing streams, the two fluid interfaces polarize and displace into the center of the microchannel (Figure 2b). The displacement is driven by conductive and dielectric charging (e.g., polarization) at each fluid interface, and is dependent on the electrical properties of each fluid stream and the AC electric field frequency. For a liquid interface subjected to a time varying monochromatic electric field, the displacement is directly proportional to the real part of the interface polarizability factor, $K(\omega)$, which is function of field frequency (ω), electrical conductivity and permittivity:

$$Re\left[K(\omega)\right] = \frac{(\varepsilon_2 - \varepsilon_1)\,\tau^2\omega^2}{(\varepsilon_2 + \varepsilon_1)\,(\tau^2\omega^2 + 1)} + \frac{(\sigma_2 - \sigma_1)\,\tau^2\omega^2}{(\sigma_2 + \sigma_1)\,(\tau^2\omega^2 + 1)} \tag{1}$$

where $\tau = \left(\frac{\varepsilon_2 + \varepsilon_1}{\sigma_2 + \sigma_1}\right)$ is the characteristic Maxwell-Wagner charge relaxation timescale at the interface between the two liquids. fDEP offers a useful method for initiating fluid motion because interface displacement behavior is very sensitive to the relative conductive and dielectric differences across the interface. At frequencies on the order of 100 kHz, for example, the interface displacement is governed solely by differences in the electrical conductivity at interfaces between two co-flowing fluids. At high frequency (typically >10 MHz), however, the displacement is driven by differences in permittivity. fDEP naturally compliments on-chip mixing because these processes often require the combination of two or more fluids with different electrical properties. In the next section of this work we discuss how these fluid properties can be controlled to produce an fDEP response.

2.3. Chemicals and Reagents

Fluid motion by fDEP requires a polarizable liquid interface. In this work, liquid interfaces were composed of three fluids with different electrical conductivity (σ) and dielectric constant (ε). When forced to flow side-by-side at low Reynolds number these three fluids formed two interfaces, each with a large electrical mismatch. Each stream was injected at a constant flow rate (10 μL/min) into the

device using a low-cost flow controller equipped with an externally pressurized fluid-filled cryogenic vial [27]. We labelled each fluid with a different Alexa Fluor fluorescent dye to accurately image the interface position using confocal microscopy. The electrical interface was formed by flowing two outer (green) diluted phosphate buffered saline streams ($\sigma_1 = 1.60$ mS/cm; $\varepsilon_1 = 78$) with 10 ng/mL of Alexa Fluor 488 (Invitrogen, Carlsbad, CA, USA). The center (red) high dielectric stream ($\sigma_2 = 19$ µS/cm; $\varepsilon_2 = 110$) was comprised of 0.8 M 6-aminohexanoic acid (Sigma-Aldrich, St. Louis, MO, USA) (AHA) labeled with 10 ng/mL of Alexa Fluor 594 (Invitrogen). AHA is a water-soluble zwitterion used for increasing the dielectric constant of aqueous solution. Prior to fluorescent labeling, the AHA solution was polished with 1 g/mL Dowex MR-3 (Sigma-Aldrich) ion exchange resin to remove trace salts and reduce solution conductivity.

2.4. Characterizing the Magnitude of Mixing

To analyze the degree of mixing and the voltage dependence, measurements were taken over a 100 × 100 square µm section directly above the electrode array. Interfacial motion was captured using a confocal microscope (Nikon/Prairie Technologies) equipped with an Andor iXon 897 camera, two 50 mW solid-state lasers for excitation at 488 nm and 561 nm, respectively, and a triggered Piezo Z stage for capturing 3-dimensional micrographs of the microchannel cross-section. When fDEP was used to drive fluid motion, the resulting mixing was calculated by capturing a fluorescent intensity profile over the microchannel cross section depicted in Figure 3. Using these confocal images, the intensity profile in the central fluidic stream was analyzed approximately 30 µm above the channel surface across the entire channel width. Each intensity profile was normalized to the fluorescent background (~126 intensity units) when no AC electric field was applied (Figure 3a). Mixing was then quantified by averaging the fluorescent intensity of the Alexa Fluor 488 across the channel width, normalizing this value with the background intensity profile and then dividing by the theoretical max intensity.

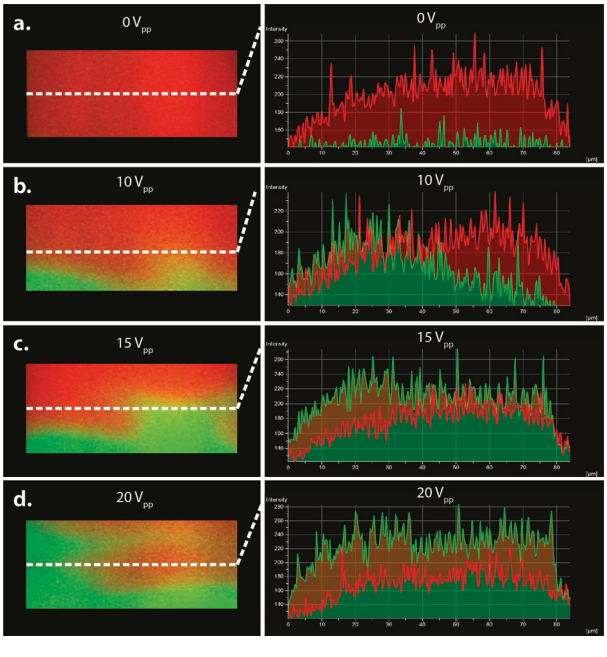

Figure 3. 3D cross-sectional image of the device at the entrance of the gradient chamber. Fluorescent profiles (**a**) 0 Vpp; (**b**) 10 Vpp; (**c**) 15 Vpp and (**d**) 20 Vpp is applied across the tri-laminar flow streams The fluorescent measurements were taken in center of the microchannel cross-section and indicated by the dotted white line.

3. Results and Discussion

3.1. Mixing with Fluidic Dielectrophoresis

We first sought to investigate the ability to mix multiple fluidic streams using fDEP. We observed rapid mixing between three co-flowing fluid streams when an AC voltage was applied across the microchannel. Mixing was observed to occur when the high conductive (green) stream forcibly displaced into the low conductive (red) stream. In order to better investigate the mechanism by which mixing occurs, confocal images of the channel cross-section were taken for three different voltages—10, 15 and 20 V_{pp}. The degree of mixing between the red and green streams was quantified using fluorescent intensity profiles captured over the microchannel cross-section (Figure 3). Shown in Figure 3, mixing occurs when the central green stream is forcibly displaced into the low conductive red stream. When the applied voltage was sufficiently large the rate of injection is so great that an electrokinetic vortical flow formed down the axis of the mixing electrode array, as shown in Figure 4. Therefore, fDEP served to electrokinetically inject fluid from the outer two flow streams and to satisfy conservation of mass, fluid volume from the central stream was dispelled outward to the two outer streams. Therefore, the electrokinetic mixer offers a means to mix with less dilution since newly injected flow of the outer fluid is accompanied by an equal outward flow of the inner fluid.

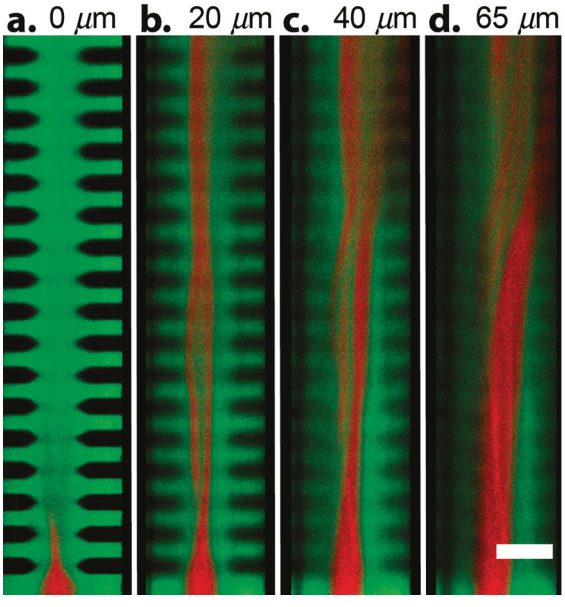

Figure 4. A confocal montage captures fluid motion down the axial length of the mixing channel captured at different positions along the channel height. (**a**) Bottom surface of the microfluidic device. Upon entering the array with an applied voltage of 20 MHz at 1 MHz, the outer green streams inject into the center occupying the entire bottom of the channel; (**b**) 1/3 from the bottom of the device; (**c**) 2/3 from the bottom of the device; (**d**) Top of the microchannel device. Scale bar, 50 μm.

3.2. The Influence of Field Frequency and Voltage on Mixing

There are several important properties of the AC electric field that will influence fluid mixing. The field frequency will affect the direction of interfacial displacement. A low frequency field, for example, will force high conductive fluid from the two outer streams to displace into the central low conductive stream. Alternatively, if a high frequency electric field is applied across the fluid

interfaces the center high dielectric stream displaces into the two adjacent low dielectric streams. In this case, no mixing was observed. Thus, for this system where we sought to inject solute from the two outer flows, the frequency regime significant for the experiments was at low frequency (<5 MHz). The influence of AC frequency on mixing is shown in Figure 5. For the frequency ranges from 1 to 5 MHz the average normalized concentration of the high conductive stream is not significantly influenced by the AC field frequency. The observed solute concentration entering the gradient chamber (C_{in}) was normalized by the theoretical maximum concentration. However, it was apparent that the applied voltage impacted the mixing concentration. Therefore, we next investigated the effects of applied voltage on mixing. To do this, three different AC voltages—10, 15 and 20 V_{pp}—were applied across the fluid interfaces at a constant field frequency of 5 MHz. While we could have selected any frequency between our 1–5 MHz experimental range based on the data in Figure 5, we based our concentration data on the largest experimental frequency simply because higher frequency electric fields are known to be less likely to produce Faradaic reactions and Joule heating in conductive buffers. Shown in Figure 6, we observed a linear correlation between the applied voltage and degree of mixing. In particular, as the applied voltage increases, the degree of mixing also increases.

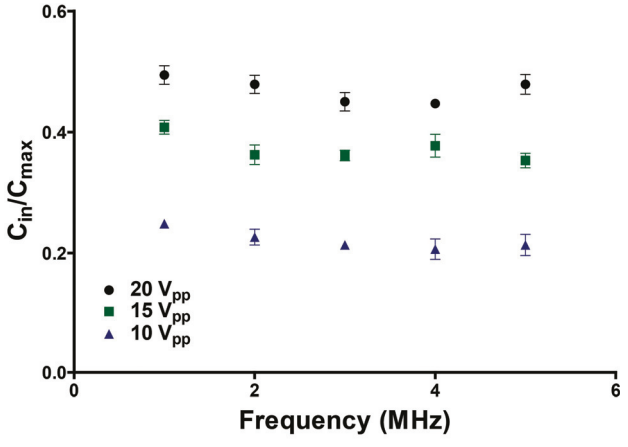

Figure 5. Quantification of the degree of concentration perturbation (C_{in}/C_{max}) versus frequency. The concentration is normalized based on the theoretical max concentration.

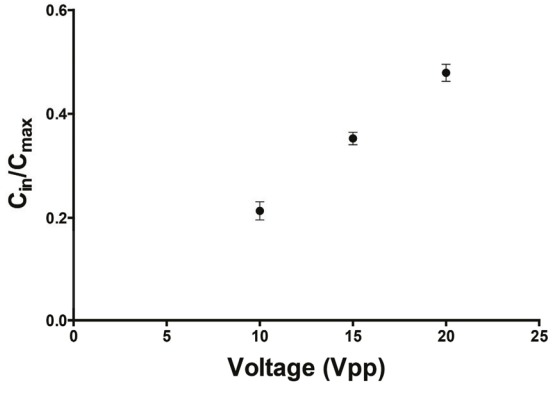

Figure 6. Plot of C_{in}/C_{max} versus applied voltage. The concentration of solute increases linearly with increasing applied voltage.

3.3. Using AC Electrokinetic Mixing to Create Finely Tunable Concentration Gradients

Finally, with the ability to induce mixing and control the solute concentration within the central stream, we investigated the ability to integrate the upstream electrokinetic mixer with a downstream concentration gradient generator. Shown in Figure 2a, when no AC electric field is applied, no fluid injection occurs and the flow central fluid stream, which is fed into the downstream chamber consists entirely of the low conductive fluid (red stream). However, when an AC electric field was applied upstream, fluidic mixing occurred and altered the downstream fluidic concentration. Figure 7 shows the gradient chamber when an upstream AC electric field of 5 MHz, 20 V_{pp} was applied. A series of consecutive micrograph images were captured at different time intervals to illustrate the rate at which the gradient is generated when upstream mixing is initiated. After the electric field was activated, a concentration gradient is formed within the gradient channels, where one chamber consists entirely of the low conductive (red) buffer and the adjacent stream consists of a mixture of the high conductive (green) and low conductive (red) buffers. When differing voltages are applied, the time for gradient generation, as well as the gradient steepness differ due to differing magnitudes of mixing and different rates of fluid injection. With lower applied voltages, less mixing occurs which produces a lower concentration gradient. Larger applied voltages result in a greater rate of fluidic injection and produce a steeper gradient.

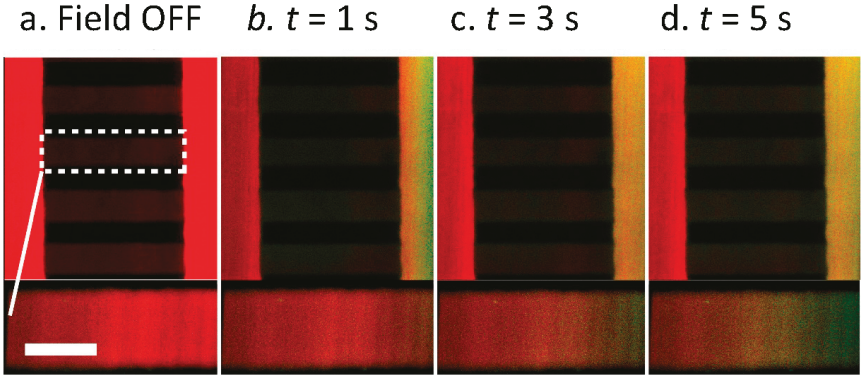

Figure 7. Magnified view of the microfluidic gradient chamber. Images were captured at varying time points after the electric field was applied over a period of 5 s. When a 5 MHz, 20 V_{pp} AC electric field is applied upstream it modifies the concentration of mixed solution that enters the gradient chamber. (**a**) When the electric field is off, the connecting gradient side channel lacks any fluid from the tri-laminar outer streams. However, when the field is switched on a chemical gradient forms across the connecting channel, which increases with over a time period of 5 s; (**b**) 1 s; (**c**) 3 s and (**d**) 5 s. Scale bar, 40 μm.

4. Conclusions

In this paper, we have presented a novel method for electrokinetic mixing in a microfluidic device using fluidic dielectrophoresis. Using an AC electric field, the two laminar liquid interfaces between three co-flowing fluids were actively mixed through the use of interfacial electrokinetic stresses. When an electric field was applied across these interfaces, they polarized and forcibly injected the contents of the two outer streams into the center stream. The degree of mixing was monitored by labeling each fluid stream and measuring the fluorescent intensity profiles over the microfluidic channel cross-section. Mixing was shown to be influenced by both the frequency and voltage of the applied AC electric field. As the voltage increased, the magnitude of mixing increased. It was shown that there exists a linear relationship between the degree of mixing and applied voltage. Finally,

we coupled this upstream mixing device with a downstream passive gradient chamber to demonstrate the usefulness of this proposed method. Upstream, an AC electric field was used to induce mixing. This led to a change in solute concentration that was sent downstream to the gradient chamber. By controlling the degree of mixing, we can alter the steepness of the concentration gradient. Future work will focus on applying this novel electrokinetic mixing component in order to create tunable on-chip concentrations.

Acknowledgments: We gratefully acknowledge support from the National Science Foundation under CBET CAREER grant 1351253 and CBET grant 1511185.

Author Contributions: Nicholas Mavrogiannis, Mitchell Desmond, and Zachary Gagnon conceived and designed the experiments. Nicholas Mavrogiannis, Mitchell Desmond, Kenny Ling, and Xiaotong Fu performed experiments. Nicholas Mavrogiannis and Mitchell Desmond analyzed the data. Nicholas Mavrogiannis wrote the manuscript; Zachary Gagnon revised the manuscript.

Conflicts of Interest: The authors declare no conflict of interest.

References

1. Anwar, K.; Han, T.; Yu, S.; Kim, S.M. Integrated micro/nano-fluidic system for mixing and preconcentration of dissolved proteins. *Microchim. Acta* **2011**, *173*, 331–335. [CrossRef]
2. Gambin, Y.; VanDelinder, V.; Ferreon, A.C.M.; Lemke, E.A.; Groisman, A.; Deniz, A.A. Visualizing a one-way protein encounter complex by ultrafast single-molecule mixing. *Nat. Methods* **2011**, *8*, 239–241. [CrossRef] [PubMed]
3. Ko, Y.-J.; Maeng, J.-H.; Ahn, Y.; Hwang, S.Y. DNA ligation using a disposable microfluidic device combined with a micromixer and microchannel reactor. *Sens. Actuators B Chem.* **2011**, *157*, 735–741. [CrossRef]
4. Wang, X.; Chen, X.; Ma, X.; Kong, X.; Xu, Z.; Wang, J. Fast DNA hybridization on a microfluidic mixing device based on pneumatic driving. *Talanta* **2011**, *84*, 565–571. [CrossRef] [PubMed]
5. Yang, Y.; Swennenhuis, J.F.; Rho, H.S.; Le Gac, S.; Terstappen, L.W. Parallel Single Cancer Cell Whole Genome Amplification Using Button-Valve Assisted Mixing in Nanoliter Chambers. *PLoS ONE* **2014**, *9*, e107958. [CrossRef] [PubMed]
6. Viktorov, V.; Mahmud, M.R.; Visconte, C. Design and characterization of a new H-C passive micromixer up to Reynolds number 100. *Chem. Eng. Res. Des.* **2016**, *108*, 152–163. [CrossRef]
7. Tofteberg, T.; Skolimowski, M.; Andreassen, E.; Geschke, O. A novel passive: Lamination in a planar channel system. *Microfluid. Nanofluid.* **2010**, *8*, 209–215. [CrossRef]
8. Buchegger, W.; Wagner, C.; Lendl, B.; Kraft, M.; Vellekoop, M. A highly uniform lamination micromixer with wedge shaped inlet channels for time resolved infrared spectroscopy. *Microfluid. Nanofluid.* **2011**, *10*, 889–897. [CrossRef]
9. Jain, M.; Nandakumar, K. Novel index for micromixing characterization and comparative analysis. *Nanofluidics* **2010**, *4*, 031101. [CrossRef] [PubMed]
10. Chen, Z.; Bown, M.R.; O'Sullivan, B.; MacInnes, J.M.; Allen, R.W.K.; Mulder, M.; Blom, M.; van't Oever, R. Performance analysis of a folding flow micromixer. *Microfluid. Nanofluid.* **2009**, *7*, 783–794. [CrossRef]
11. Kang, T.G.; Singh, M.K.; Anderson, P.D.; Meijer, H.E.H. A Chaotic Serpentine Mixer Efficient in the Creeping Flow Regime: From Design Concept to Optimization. *Microfluid. Nanofluid.* **2010**, *6*, 763–774. [CrossRef]
12. Lee, C.-Y.; Wang, W.-T.; Liu, C.-C.; Fu, L.-M. Passive mixers in microfluidic systems: A review. *Chem. Eng. J.* **2016**, *288*, 146–160. [CrossRef]
13. Matlock-Colangelo, L.; Colangelo, N.; Fenzl, C.; Frey, M.; Baeumner, A. Passive Mixing Capabilities of Micro- and Nanofibres When Used in Microfluidic Systems. *Sensors* **2016**, *16*, 1238. [CrossRef] [PubMed]
14. Lynn, N.S., Jr.; Martínez-López, J.-I.; Bocková, M.; Adam, P.; Coello, V.; Siller, H.R.; Homola, J. Biosensing enhancement using passive mixing structures for microarray-based sensors. *Biosens. Bioelectron.* **2014**, *54*, 506–514. [CrossRef] [PubMed]
15. Losey, M.W.; Jackman, R.J.; Firebaugh, S.L. Design and fabrication of microfluidic devices for multiphase mixing and reaction. *J. Microelectromech. Syst.* **2002**, *11*, 462–469. [CrossRef]
16. Jacobson, S.C.; McKnight, T.E.; Ramsey, J.M. Microfluidic Devices for Electrokinetically Driven Parallel and Serial Mixing. *Anal. Chem.* **1999**, *71*, 4455–4459. [CrossRef]

17. Biswas, S.K.; Das, T.; Chakraborty, S. Nontrivial augmentations in mixing performance through integrated active and passive mixing in serpentine microchannels. *J. Appl. Phys.* **2012**, *111*, 054904. [CrossRef]
18. Ober, T.J.; Foresti, D.; Lewis, J.A. Active mixing of complex fluids at the microscale. *Proc. Natl. Acad. Sci. USA* **2015**, *112*, 12293–12298. [CrossRef] [PubMed]
19. Glasgow, I.; Aubry, N. Enhancement of microfluidic mixing using time pulsing. *Lab Chip* **2003**, *3*, 114–120. [CrossRef] [PubMed]
20. Lu, L.-H.; Ryu, K.S.; Liu, C. A magnetic microstirrer and array for microfluidic mixing. *J. Microelectromech. Syst.* **2002**, *11*, 462–469.
21. Cao, Q.; Han, X.; Li, L. An active microfluidic mixer utilizing a hybrid gradient magnetic field. *Int. J. Appl. Electromagn. Mech.* **2015**, *47*, 583–592.
22. Scherr, T.F.; Ryskoski, H.B.; Doyle, A.B.; Haselton, F.R. A two-magnet strategy for improved mixing and capture from biofluids. *Biomicrofluidics* **2016**, *10*, 024118. [CrossRef] [PubMed]
23. Bui, T.; Morana, B.; Scholtes, T.; Chu Duc, T.; Sarro, P.M. A mixing surface acoustic wave device for liquid sensing applications: Design, simulation, and analysis. *J. Appl. Phys.* **2016**, *120*, 074504. [CrossRef]
24. Shilton, R.; Tan, M.K.; Yeo, L.Y.; Friend, J.R. Particle concentration and mixing in microdrops driven by focused surface acoustic waves. *J. Appl. Phys.* **2008**, *104*, 014910. [CrossRef]
25. Mavrogiannis, N.; Desmond, M.; Gagnon, Z.R. Fluidic dielectrophoresis: The polarization and displacement of electrical liquid interfaces. *Electrophoresis* **2014**, *36*, 1386–1395. [CrossRef] [PubMed]
26. Desmond, M.; Mavrogiannis, N.; Gagnon, Z. Maxwell-Wagner polarization and frequency-dependent injection at aqueous electrical interfaces. *Phys. Rev. Lett.* **2012**, *109*, 187602. [CrossRef] [PubMed]
27. Mavrogiannis, N.; Ibo, M.; Fu, X.; Crivellari, F.; Gagnon, Z. Microfluidics made easy: A robust low-cost constant pressure flow controller for engineers and cell biologists. *Biomicrofluidics* **2016**, *10*, 034107. [CrossRef] [PubMed]

micromachines

MDPI

Article

Power Generation by Reverse Electrodialysis in a Microfluidic Device with a Nafion Ion-Selective Membrane

Tsung-Chen Tsai, Chia-Wei Liu and Ruey-Jen Yang *

Department of Engineering Science, National Cheng Kung University, Tainan 70101, Taiwan; tsungchen0329@gmail.com (T.-C.T.); N96044353@mail.ncku.edu.tw (C.-W.L.)
* Correspondence: rjyang@mail.ncku.edu.tw; Tel.: +886-6-2757575-63343

Academic Editors: Xiangchun Xuan and Shizhi Qian
Received: 18 September 2016; Accepted: 4 November 2016; Published: 10 November 2016

Abstract: An energy conversion microchip consisting of two circular microchambers and a Nafion-filled microchannel is fabricated using standard micro-electro-mechanical systems (MEMS) techniques. When the chambers are filled with KCl solutions with different concentrations, the Nafion microchannel acts as a cation-selective membrane and results in the generation of electrical power through a reverse electrodialysis (RED) process. The current-potential characteristics of the Nafion membrane are investigated for devices with various microchannel lengths and electrolyte concentration ratios. It is shown that for a given voltage, the current and generated power increase with a reducing channel length due to a lower resistance. In addition, a maximum power density of 755 mW/m^2 is obtained given an electrolyte concentration ratio of 2000:1 (unit is mM). The optimal device efficiency is found to be 36% given a channel length of 1 mm and a concentration ratio of 1000:1 (mM). Finally, no enhancement of the short circuit current is observed at higher concentration ratios.

Keywords: reverse electrodialysis; salinity gradient power; Gibbs free energy; Nafion membrane; energy conversion

1. Introduction

Most of today's energy is produced from fossil fuels (e.g., coal, oil and natural gas). However, this has serious implications for the environment, including most notably, the emission of greenhouse gases (CO_2, SO_2 and NO_x) and global warming. To address the problems of environmental pollution and climate change and to prevent future resource depletion, it is necessary to develop alternative green energy sources, such as salinity gradient energy [1–3], biomass conversion [4], wind power [5], solar energy [6], and others. Of these various technologies, salinity gradient energy is one of the most attractive since seawater accounts for almost 70% of the planet's surface. In the salinity gradient method, power is generated from the Gibbs free energy produced during the mixing of seawater and fresh water. The method was first proposed by Weinstein and Leitz [7] and has an estimated theoretical output capacity of up to 1.4–2.6 TW [8]. Suda et al. [9] investigated the performance of a dialytic battery consisting of 59 compartments made with 29 ion-exchange membrane pairs, each with an effective area of 80 cm^2 per sheet. The results showed that while the output power reduced over time, a power density of 259 mW/m^2 was possible during the initial mixing of seawater and river water. Veerman et al. [10] showed that for a scaled-up reverse electrodialysis (RED) stack consisting of 50 cells with a size of 25 cm × 75 cm, a maximum power density of 930 mW/m^2 could be achieved given an appropriate hydrodynamic design of the stack.

Advances in micro-electro-mechanical systems (MEMS) techniques have facilitated device miniaturization in many applications [11], including biomedical implants, micro-sensors, micro-batteries and portable personal electronics [12]. Furthermore, when combined with nanofluidics technology, MEMS-based devices provide the means to generate energy not only from large-scale systems, but also from micro/nano-scale devices [13]. The problem of power generation by RED in ion-selective microchannels has attracted significant attention in the recent literature. The application of micro-RED systems can be used for some resource-limited settings while travelling outdoors and could also be used as a counterpart of a solar-driven satellite just in case of power insufficiency. Kim et al. [14] showed that for silica nanochannels with heights of 4, 26 and 80 nm, respectively, the ion selectivity increased with a reducing concentration gradient and channel height. Thus, the optimal performance (a power density of 7.7 W/m^2 and an efficiency of 31%) was obtained in the device with a channel height of 4 mm. Kang et al. [15] investigated the RED effect in anodic alumina nanopores given various pore lengths, pore radii and electrolyte concentrations. Overall, the results showed that a power output density of 9.9 W/m^2 could be achieved given a suitable specification of the engineering parameters. Chang and Yang [16] presented a theoretical model based on a modified Onsager reciprocal relation and the Poisson–Boltzmann model for predicting the electrokinetic energy conversion efficiency in short-length nanofluidic channels. It was shown that the results obtained from the proposed model were in good agreement with those of the Poisson–Nernst–Planck (PNP) model in the absence of concentration polarization effects at the reservoirs. In a later study by the same group (Chang and Yang [17]), it was shown that the electrokinetic energy conversion efficiency of ion-selective nanopores could be increased to more than 40% by imposing a hydrodynamic slip ratio greater than 0.7.

Guo et al. [18] presented a fully-abiotic single-pore nanofluidic energy-harvesting system, developed by chemically-etching the nanopores, which achieved a system with a maximum power output of 26 pW. Tandon et al. [19] investigated the electroosmotic mobility properties of ion-selective microfluidic devices fabricated from hydrophobic polymers and showed that a higher ion mobility resulted in a greater diffusion current and an improved power. Cao et al. [20] compared the RED performance of single ion-selective nanopores for three different electrolytes, namely KCl, NaCl and LiCl. The results confirmed that the electric power and energy conversion efficiency are both dependent on a well-matched charge selectivity and ionic composition. In particular, it was shown that for the considered nanopores, the highest diffusion coefficient and power generation (45 pW) were obtained using the KCl solution. Chang et al. [21] investigated the diffusion potential and power generation performance of a microchip containing a Nafion ion-selective membrane given the use of three different electrolyte solutions with pH values of 3.8, 5.6 and 10.3, respectively. The performance of the device was found to improve with an increasing pH value, with a diffusion potential of 135 mV and a power generation of 339 pW observed for the electrolyte with a pH value of 10.3.

The present study fabricates a simple energy conversion microchip consisting of two circular microchambers connected by a Nafion-filled microchannel. When the chambers are filled with KCl solutions with different concentrations, the Nafion microchannel acts as a cation-selective membrane, and hence, electrical power is generated as the result of RED. The current-potential (*I-V*) characteristics, power generation performance and electrokinetic conversion efficiency of the proposed device are systematically examined for various values of the microchannel length and electrolyte concentration ratio.

2. Material and Methods

A mold consisting of the two microchambers and the inter-connecting microchannel was patterned on a silicon wafer using standard MEMS techniques. A polydimethylsiloxane (PDMS) structure was then produced using a simple replication method. The PDMS structure was bonded to a blank glass substrate by an oxygen plasma treatment process in order to form the final RED chip. Nafion solution purchased from DuPont (DE-2021, Wilmington, DE, USA) was diluted with deionized (DI) water in a proportion of 5:1, then injected into one reservoir and allowed to fill the microchannel and the

other reservoir under the effects of capillary forces (see Figure 1). The chip was then stored at room temperature for 8 h; causing the Nafion to solidify within the microchannel and reservoirs [22,23]. The solidified Nafion in the two reservoirs can be easily peeled off. The Nafion remaining in the microchannel acts as a cation-selective membrane and results in the generation of electrical power through a reverse electrodialysis (RED) process.

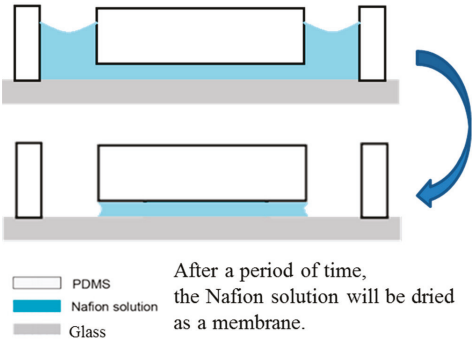

Figure 1. Fabrication of the Nafion ion-selective membrane in the microchannel.

Figure 2 shows the basic configuration of the fabricated chip. Three devices were produced with microchannel lengths of 1, 2 and 3 mm, respectively. In every case, the microchannel had a height of 23 μm and a width of 500 μm. The dimensions of the fabricated microchannels were measured using ImageJ software and were found to deviate by no more than 13% from the corresponding design values. The RED experiments were performed using Ag/AgCl electrodes and KCl electrolyte solution with a pH value of 5.6 ± 0.2. Four different electrolyte concentration ratios (C_H:C_L) were considered, namely 10:1, 100:1, 1000:1 and 2000:1 (unit is mM). In each experiment, the potential and current were measured using a Keithley 2400 source meter (Keithley Instruments, Cleveland, OH, USA). Each case is conducted at least for four independent measurements.

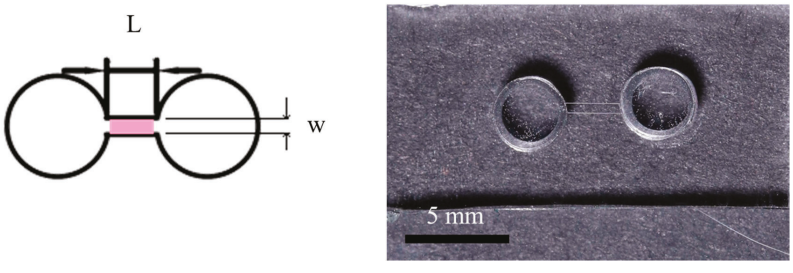

Figure 2. Basic configuration and photograph of the reverse electrodialysis (RED) device.

3. Results and Discussion

Figure 3a shows a schematic illustration of the RED process in the proposed device. As shown, the left (anode) and right (cathode) reservoirs are filled with high- and low-concentration KCl solutions, respectively. As a consequence, a salinity gradient is formed along the length of the microchannel. Due to the ion-selectivity of the membrane, the cations and anions diffuse toward the low-concentration reservoir at different rates. Consequently, a difference in the positive and negative charges is produced at the two ends of the membrane. This difference results in the formation of a diffusion potential, which is subsequently converted into electrical energy through a process of reverse electrodialysis. Figure 3b

shows the equivalent electrical circuit for the experimental setup used to evaluate the performance of the proposed RED device. Note that V_{app} is the potential applied by the source meter; E_{redox} is the potential produced by the redox reactions at the electrodes; E_{diff} is the diffusion potential; $R_{channel}$ is the resistance of the microchannel filled with Nafion; and I is the output current generated by the microchip. The redox potential produced at different concentration ratios (C_H:C_L) can be expressed by the following Nernst relation [24,25]:

$$E_{redox} = \frac{RT}{zF} \ln \frac{\gamma_{C_H} C_H}{\gamma_{C_L} C_L} \quad (1)$$

where R, T, z, F and γ are the gas constant, absolute temperature, charge number, Faraday constant and mean activity coefficient, respectively. The diffusion potential can be expressed as [21]:

$$E_{diff} = (2t_+ - 1) \frac{RT}{zF} \ln \frac{\gamma_{C_H} C_H}{\gamma_{C_L} C_L} \quad (2)$$

where t_+ is the transference number for the cations and can be expressed as $t_+ = j_+/(j_+ + j_-)$, where j_+ and j_- are the cation and anion fluxes, respectively. The transference number provides an index of the ion selectivity of the membrane. More specifically, $t_+ = 1$ indicates that the membrane has full cation selectivity, while $t_+ = 0$ indicates that the membrane has full anion selectivity.

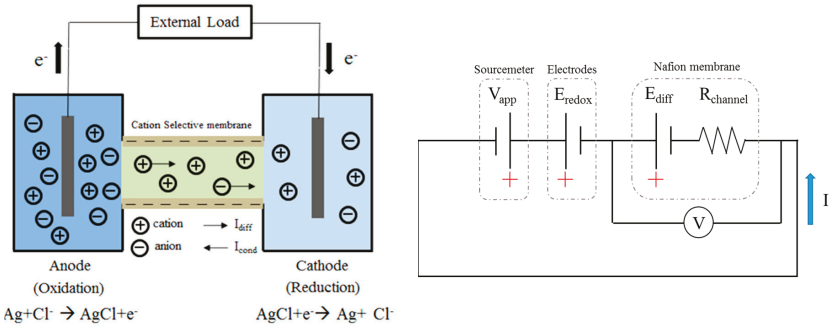

Figure 3. (**a**) Schematic illustration of the RED process in the cation-selective channel; and (**b**) the equivalent electrical circuit of the experimental setup.

When the system is connected to an external load, the output power is given by:

$$V = E_{diff} - IR_{channel} = V_{app} - E_{redox} \quad (3)$$

$$P_{out} = IV = \frac{E_{diff}^2 R_{load}}{(R_{load} + R_{channel})^2} \quad (4)$$

The maximum output power is obtained when $R_{load} = R_{channel}$ and can be computed as [21,26]:

$$P_{max} = \frac{E_{diff}^2}{4R_{channel}} \quad (5)$$

Figure 4a–c show the measured I-V curves of the three RED devices with different microchannel lengths given KCl concentration ratios of 10:1, 100:1 and 1000:1 (mM), respectively. It is seen that for all values of the concentration ratio, the channel resistance ($R = V/I$) reduces with a reducing

microchannel length. As a result, the power generated by the RED device reduces as the microchannel length increases.

Figures 5 and 6 show the variations of the diffusion potential and transference number, respectively, with the electrolyte concentration ratio given a microchannel length of 1 mm. As shown in Figure 5, the diffusion current increases with an increasing concentration ratio due to the corresponding increase in the diffusion potential. However, a limiting effect occurs as the concentration ratio is increased beyond 1000:1 (mM). Similarly, Figure 6 shows that the transference number increases (i.e., the Nafion membrane becomes increasingly cation selective) as the concentration ratio is increased from 10:1 to 1000:1 (mM), but reduces as the concentration ratio is further increased to 2000:1 (mM).

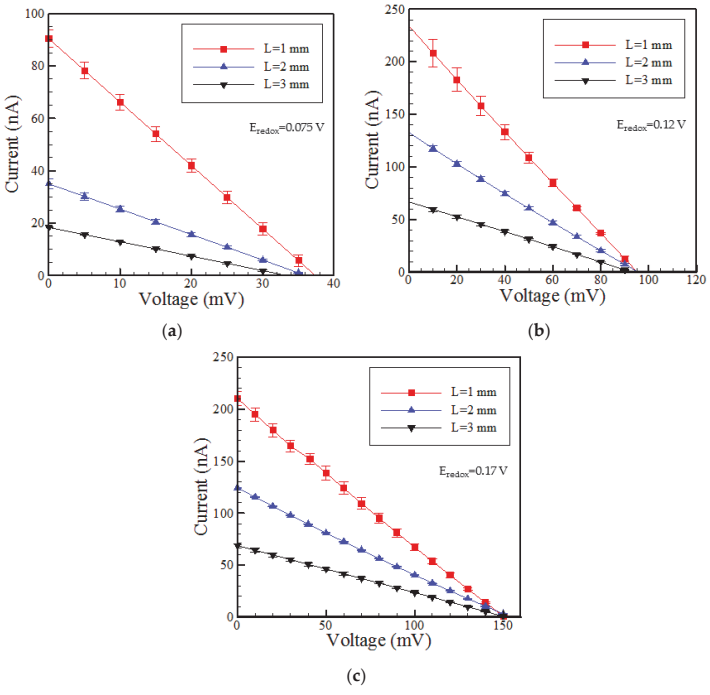

Figure 4. Current-potential curves for RED devices with different microchannel lengths and concentration ratios of: (**a**) 10:1; (**b**) 100:1; and (**c**) 1000:1 (unit is mM).

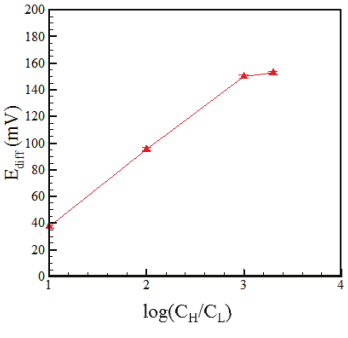

Figure 5. Variation of diffusion potential with concentration ratio given microchannel length of 1 mm.

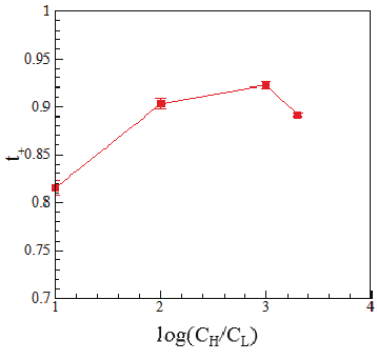

Figure 6. Variation of transference number with the concentration ratio given a microchannel length of 1 mm.

For an RED system, the energy conversion efficiency is defined as the ratio of the output electrical energy to the input Gibbs free energy of mixing. Moreover, the efficiency obtained under the maximum power condition, $\eta_{max,\ power}$, can be expressed as [21,27]:

$$\eta_{max,\ power} = \frac{(2t_+ - 1)^2}{2} \quad (6)$$

Figure 7 shows the maximum power density (i.e., the maximum power divided by the membrane area) in the RED device with a microchannel length of 1 mm given concentration ratios of 10:1, 100:1, 1000:1 and 2000:1 (mM). It is seen that the maximum power density has a value of 755 mW/m^2 and is achieved in the device with a concentration ratio of 2000:1 (mM). By contrast, the highest conversion efficiency is achieved in the device with a concentration gradient of 1000:1 (mM) and is found to have a value of 36%, as shown in Figure 8. Figure 9a–c show the *I-V* characteristics of the RED devices with channel lengths of 3, 2 and 1 mm, respectively, given three different electrolyte concentration ratios (10:1, 100:1 and 1000:1 (mM)) in each case. It is seen that for all values of the microchannel length, the short circuit current does not monotonically increase as the concentration ratio is increased. This finding can be explained as follows. Since cation migration flux from the high-concentration reservoir to the low-concentration reservoir increases with the concentration ratio, the amount of cations accumulated at the lower concentration reservoir would result in an opposite electrical field to the anode side (see Figure 3a). The opposite electrical field and the cation diffusion flux would therefore counteract and reach an equilibrium condition.

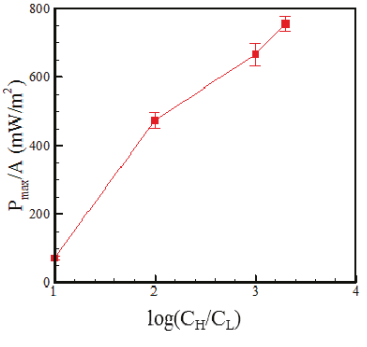

Figure 7. Variation of the maximum power density with concentration ratio given a microchannel length of 1 mm.

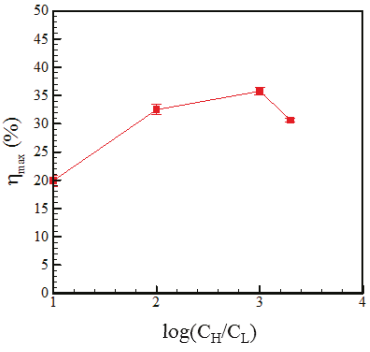

Figure 8. Variation of the energy conversion efficiency with the concentration ratio given a microchannel length of 1 mm.

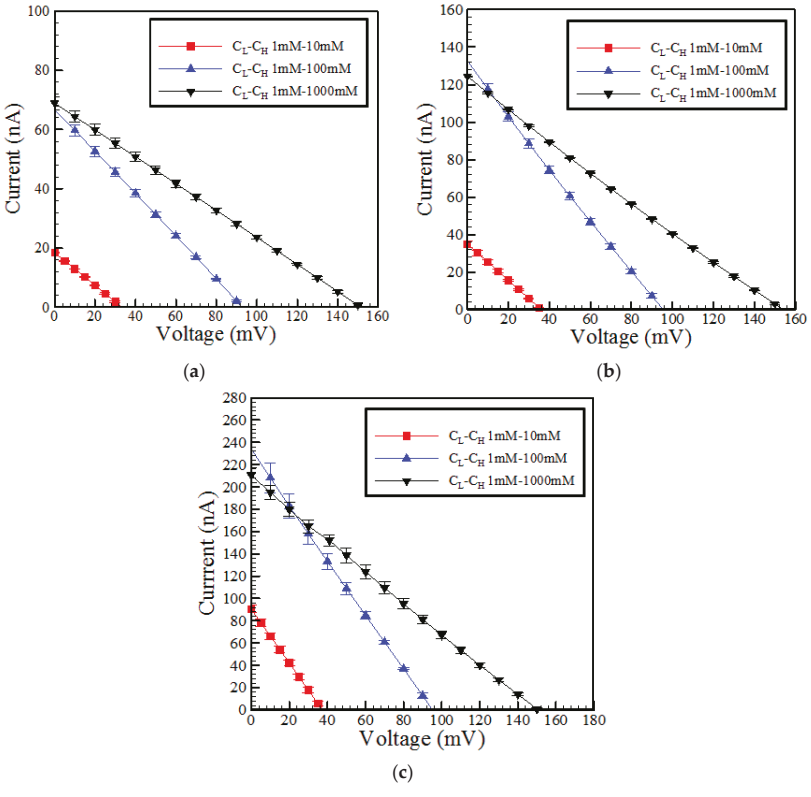

Figure 9. Current-potential curves for the different concentration ratios in RED devices with microchannels of lengths of: (**a**) 3 mm; (**b**) 2 mm; and (**c**) 1 mm.

4. Conclusions

This study has fabricated a salinity-gradient RED device consisting of two microchambers connected by a straight Nafion-filled microchannel. The power generation performance of the proposed device has been evaluated for three different microchannel lengths (1, 2 and 3 mm) and four different

KCl electrolyte concentration ratios (10:1, 100:1, 1000:1 and 2000:1 (mM)). The results have shown that the output current and power increase with a reducing microchannel length due to a lower channel resistance. For the RED device with a microchannel length of 1 mm, a maximum power density of 755 mW/m^2 is achieved using a concentration ratio of 2000:1 (mM), while a maximum efficiency of 36% is obtained for a concentration ratio of 1000:1 (mM). Finally, the short circuit current does not monotonically increase as the concentration ratio is increased. The short circuit current is constrained at higher electrolyte concentration ratios since the higher electric field impedes the migration of the cations to the low-concentration reservoir.

Acknowledgments: The authors gratefully acknowledge the financial support provided to this study by the Ministry of Science and Technology of Taiwan under Project Number MOST 103-2221-E-006-093-MY3. The acknowledgement is extended to the National Nano-Device Laboratory for providing microfabrication facilities.

Author Contributions: T.-C.T. performed the experiment and prepared the experimental images. C.-W.L. and R.-J.Y. contributed to the analysis and summarized the results. All authors commented on the paper.

Conflicts of Interest: The authors declare no conflict of interest.

References

1. Yeh, H.C.; Chang, C.C.; Yang, R.J. Reverse electrodialysis in conical-shaped nanopores: Salinity gradient-driven power generation. *RSC Adv.* **2014**, *4*, 2705–2714. [CrossRef]
2. Wick, G.L. Power from salinity gradient. *Energy* **1978**, *3*, 95–100. [CrossRef]
3. Lee, S.; Kim, H.; Kim, D.K. Power generation from concentration gradient by reverse electrodialysis in dense silica membranes for microfluidic and nanofluidic systems. *Energies* **2016**, *9*, 49. [CrossRef]
4. Demirbas, A. Biomass resource facilities and biomass conversion processing for fuels and chemicals. *Energy Convers. Manag.* **2001**, *42*, 1357–1378. [CrossRef]
5. Ackermann, T. Wind energy technology and current status a review. *Int. J. Heat Mass Transf.* **2000**, *4*, 315–374. [CrossRef]
6. Mahian, O.; Kianifar, A.; Kalogirou, S.A.; Pop, I.; Wongwises, S. A review of the applications of nanofluids in solar energy. *Int. J. Heat Mass Transf.* **2013**, *57*, 582–594. [CrossRef]
7. Weinstein, J.N.; Leitz, F.B. Electric power from differences in salinity: The dialytic battery. *Science* **1976**, *191*, 557–559. [CrossRef] [PubMed]
8. Isaacs, J.D.; Seymour, R.J. The ocean as a power resource. *Int. J. Environ. Stud.* **1973**, *4*, 201–205. [CrossRef]
9. Suda, F.; Matsuo, T.; Ushioda, D. Transient changes in the power output from the concentration difference cell (dialytic battery) between seawater and river water. *Energy* **2007**, *32*, 165–173. [CrossRef]
10. Veerman, J.; Saakes, M.; Metz, S.; Harmsen, G. Reverse electrodialysis: Performance of a stack with 50 cells on the mixing of sea and river water. *J. Membr. Sci.* **2009**, *327*, 136–144. [CrossRef]
11. Whitesides, G.M. The origins and the future of microfluidics. *Nature* **2006**, *442*, 368–373. [CrossRef] [PubMed]
12. Pennathur, S.; Eijkel, J.C.T.; van den Berg, A. Energy conversion in microsystems: Is there a role for micro/nanofluidics? *Lab Chip* **2007**, *7*, 1234–1237. [PubMed]
13. Eijkel, J.C.; Van Den Berg, A. Nanofluidics: What is it and what can we expect from it? *Microfluid. Nanofluid.* **2005**, *1*, 249–267. [CrossRef]
14. Kim, D.K.; Duan, C.; Chen, Y.F.; Majumdar, A. Power generation from concentration gradient by reverse electrodialysis in ion-selective nanochannels. *Microfluid. Nanofluid.* **2010**, *9*, 1215–1224. [CrossRef]
15. Kang, B.D.; Kim, H.J.; Lee, M.G.; Kim, D.-K. Numerical study on energy harvesting from concentration gradient by reverse electrodialysis in anodic alumina nanopores. *Energy* **2015**, *86*, 525–538. [CrossRef]
16. Chang, C.C.; Yang, R.J. Electrokinetic energy conversion in micrometer-length nanofluidic channels. *Microfluid. Nanofluid.* **2009**, *9*, 225–241. [CrossRef]
17. Chang, C.C.; Yang, R.J. Electrokinetic energy conversion efficiency in ion-selective nanopores. *Appl. Phys. Lett.* **2011**, *99*, 083102. [CrossRef]
18. Guo, W.; Cao, L.; Xia, J.; Nie, F.Q.; Ma, W.; Xue, J.; Song, Y.; Zhu, D.; Wang, Y.; Jiang, L. Energy harvesting with single-ion-selective nanopores: A concentration-gradient-driven nanofluidic power source. *Adv. Funct. Mater.* **2010**, *20*, 1339–1344. [CrossRef]

19. Tandon, V.; Bhagavatula, S.K.; Nelson, W.C.; Kirby, B.J. Zeta potential and electroosmotic mobility in microfluidic devices fabricated from hydrophobic polymers: 1. The origins of charge. *Electrophoresis* **2008**, *29*, 1092–1101. [CrossRef] [PubMed]
20. Cao, L.; Guo, W.; Ma, W.; Wang, L.; Xia, F.; Wang, S.; Wang, Y.; Jiang, L.; Zhu, D. Towards understanding the nanofluidic reverse electrodialysis system: Well matched charge selectivity and ionic composition. *Energy Environ. Sci.* **2011**, *4*, 2259. [CrossRef]
21. Chang, C.R.; Yeh, C.H.; Yeh, H.C.; Yang, R.J. Energy conversion from salinity gradient using microchip with nafion membrane. In *International Journal of Modern Physics: Conference Series*; World Scientific Publishing Company: Singapore, 2016; Volume 42, pp. 1660183-1–1660183-12.
22. Lee, J.H.; Song, Y.A.; Han, J. Multiplexed proteomic sample preconcentration device using surface-patterned ion-selective membrane. *Lab Chip* **2008**, *8*, 596–601. [CrossRef] [PubMed]
23. Yoon, J.; Cho, Y.; Han, S.; Lim, C.S.; Lee, J.H.; Chung, S. Microfluidic in-reservoir pre-concentration using a buffer drain technique. *Lab Chip* **2014**, *14*, 2778–2782. [CrossRef] [PubMed]
24. Lakshminarayanaiah, N. *Transport Phenomena In Membranes*; Academic Press: New York, NY, USA, 1969.
25. Bard, A.J.; Faulkner, L.R. Fundamentals and applications. In *Electrochemical Methods*, 2nd ed.; Wiley: New York, NY, USA, 2001.
26. Koryta, J.; Dvorak, J.; Kavan, L. *Principles of Electrochemistry*; Wiley: New York, NY, USA, 1993.
27. Fair, J.C.; Osterle, J.F. Reverse electrodialysis in charged capillary membranes. *J. Chem. Phys.* **1971**, *54*, 3307–3316. [CrossRef]

micromachines

MDPI

Article

Electro-Deformation of Fused Cells in a Microfluidic Array Device

Yan Liu [1,†], Xiaoling Zhang [1,†], Mengdi Chen [1], Danfen Yin [1], Zhong Yang [2], Xi Chen [1], Zhenyu Wang [3], Jie Xu [4], Yuanyi Li [4], Jun Qiu [5], Ning Hu [1,*] and Jun Yang [1,*]

1 Key Laboratory of Biorheological Science and Technology, Chongqing University, Ministry of Education, and Key Laboratory of Vision Loss, Regeneration and Restoration, Chongqing, Bioengineering College, Chongqing University, Chongqing 400030, China; 20141902049@cqu.edu.cn (Y.L.); zhangxiaoling@cqu.edu.cn (X.Z.); 20161902047@cqu.edu.cn (M.C.); 20161902048@cqu.edu.cn (D.Y.); 20121913019t@cqu.edu.cn (X.C.)

2 Department of Laboratory Medicine, Southwest Hospital, Third Military Medical University, Chongqing 400038, China; zyang@tmmu.edu.cn

3 College of Biomedical Engineering, Chongqing Medical University, Chongqing 400016, China; wangzhenyu20090306@gmail.com

4 Chongqing Jinshan Science & Technology (Group) Co., Ltd., Chongqing 401120, China; kyxuj@jinshangroup.com (J.X.); liyy@jinshangroup.com (Y.L.)

5 Department of Information, Southwest Hospital, Third Military Medical University, Chongqing 400038, China; qiujun1982@gmail.com

* Correspondence: huning@cqu.edu.cn (N.H.); bioyangjun@cqu.edu.cn (J.Y.); Tel.: +86-23-6511-1931 (N.H. & J.Y.)

† These authors contributed equally in this study.

Academic Editors: Xiangchun Xuan and Shizhi Qian

Received: 21 September 2016; Accepted: 3 November 2016; Published: 9 November 2016

Abstract: We present a new method of analyzing the deformability of fused cells in a microfluidic array device. Electrical stresses—generated by applying voltages (4–20 V) across discrete co-planar microelectrodes along the side walls of a microfluidic channel—have been used to electro-deform fused and unfused stem cells. Under an electro-deformation force induced by applying an alternating current (AC) signal, we observed significant electro-deformation phenomena. The experimental results show that the fused stem cells were stiffer than the unfused stem cells at a relatively low voltage (<16 V). However, at a relatively high voltage, the fused stem cells were more easily deformed than were the unfused stem cells. In addition, the electro-deformation process is modeled based on the Maxwell stress tensor and structural mechanics of cells. The theoretical results show that a positive correlation is found between the deformation of the cell and the applied voltage, which is consistent with the experimental results. Combined with a numerical analysis and experimental study, the results showed that the significant difference of the deformation ratio of the fused and unfused cells is not due to their size difference. This demonstrates that some other properties of cell membranes (such as the membrane structure) were also changed in the electrofusion process, in addition to the size modification of that process.

Keywords: electro-deformation; microfluidic; fused cell; mechanical properties

1. Introduction

Cell fusion is a method to asexually fuse two or more cells and produce a mono- or multi-nucleated fused cell in vitro [1]. The fused cell has new genetic or biological properties, as it integrates genetic material (i.e., genome and extranuclear genes) from both parent cells. Present research on fused cells has focused on the reprogramming of somatic cells [2,3], genetic analysis [4], developing antibodies [5],

cloning mammals, and cancer immunotherapy [6]. In the cell fusion process, the mechanical properties of fused cells change during the cell fusion and bilayer reconstitution process, due to the mobility of the lipid. In addition, the existence of a membrane protein would also affect the mobility of the lipid to change the mechanical properties of the fused cell membrane [7,8].

As the mechanical properties can reveal some important information regarding the fusion process, such as the membrane protein structure, and potential applications in cell separation or tumor cell detection based on the mechanical properties, several well-known tools have been used to measure the mechanical properties of cells, including optical tweezers [9–11], micropipette aspiration (MPA) [12], atomic force microscopy (AFM) [13], and electro-deformation (ED) [14–18]. Among these methods, ED is more amenable to lab-on-a-chip implementation and does not require complicated equipment. When biological cells are in a nonuniform electric alternating current (AC) field, Maxwell–Wagner polarization occurs, resulting in dielectrophoresis (DEP), electrorotation (ER), and electro-deformation. DEP can be used to trap cells in a non-uniform electric field. With an increase in the strength of the electric field, cells can be stretched, which is called electro-deformation [19].

In the research described above, cell deformation has been demonstrated to be a potent method of illuminating cell denaturation. Considering that fusion manipulation induces membrane reconstruction, membrane protein structure modifications, and intracellular substance integration, great changes in mechanical properties occur during this process. Detection of the mechanical properties of fused cells has the potential to reveal some important information and afford a potential unmarked fused cell separation technique. However, the mechanical properties of the fused cells have not been investigated. To detect the differences between the mechanical properties of fused stem cells and unfused stem cells, a discrete co-planar microelectrode device was designed to generate non-uniform electric fields. The cells on the chip were trapped on the microelectrode under DEP and then deformed under a sufficient electric field. The whole process of cell deformation was recorded by a charge-coupled device (CCD) camera connected to a microscope. In addition, numerical simulations were performed to model cell electro-deformation based on the Maxwell stress tensor and structural mechanics of the cells.

2. Materials and Methods

2.1. Cells and Media

Cells were maintained in a standard cell culture incubator (5% CO_2, 95% humidity, 37 °C). Unfused stem cells were from a mouse embryonic stem cell (mESC) line (MESPU35) that was cultured with irradiated embryonic fibroblasts as the feeder. These cells were derived from 12.5 day ICR mouse embryos and C-ray irradiated to arrest cell division at the third passage of culture to maintain mESCs in the undifferentiated state. They were cultured in high-glucose dulbecco's modified eagle medium (H-DMEM, Hyclone, Logan, UT, USA) supplemented with 10% fetal bovine serum (FBS, Hyclone), 2 mmol/L glutamine, 100 μg/mL penicillin–streptomycin, 1000 IU/mL leukemia inhibitory factor, 0.1 mmol/L β-mercaptoethanol, and 0.1 mmol/L nonessential amino acid. Fused stem cells [20] were cultured in mESC culture media. When collecting the cells, they were trypsinized using 0.25/0.02% trypsin/Ethylenediaminetetraacetic acid (EDTA) for approximately 1 min, arrested by H-DMEM containing 10% FBS, centrifuged at 1000 rpm for 5 min, and washed in 0.01 mol/L PBS (pH 7.2). The medium used for electrodeformation experiments was a medium buffer with low electrical conductivity (~0.001 $S \cdot m^{-1}$). Before the experiments, the cells were washed three times and resuspended in the medium buffer at low densities (1×10^6/mL).

2.2. Fabrication of the Microfluidic Device, Operation, and Data Analysis

A discrete co-planer vertical sidewall microelectrode device was used to produce the electro-deformation force. This device was designed and fabricated on a silicon-on-insulator (SOI) wafer [21]. The device contained a serpentine-shaped microchannel with 22,500 pairs of vertical

sidewall microelectrodes patterned on two opposite vertical sidewalls of the microchannel, and could produce a non-uniform electric field in the microchannel.

The operation procedures are described briefly as follows. The microchip was connected to an electrical signal generator. A sinusoidal electric potential of different amplitudes was applied to capture and deform cells. The microchannel was first rinsed and washed with fresh medium buffer. After loading, cells were randomly placed inside the microchannel. A small AC signal (1 $V_{p\text{-}p}$, 1 MHz) was applied to attract cells to the electrodes due to DEP. The applied voltage was then increased 4 V per step from 4 V to 20 V and kept steady at each step for 60 s, and the cell behavior was observed and recorded with a CCD camera (Motic 3000, Motic, Xiamen, China) during the experiments. To measure the deformation ratio of each cell relative to the voltage applied, measurements of the cell dimensions were carried out manually using the ellipse-fitting and measurement tools of the Graphic Image Manipulation Program (GIMP v.2, The GIMP Development Team, International). The deformation ratio was defined as the ratio between the elongation of the cell parallel to the electric field after ED and the original radius of the cell before ED, which was calculated as

$$\gamma = \frac{a}{a_0}, \tag{1}$$

where a_0 is the original radius of the cell and a is the length of the ellipse major axis after deformation, as shown in Figure 1.

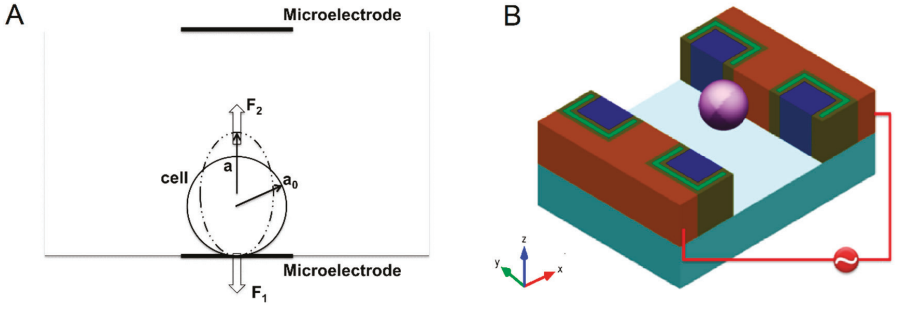

Figure 1. Schematic of electro-deformation (**A**) 2D and (**B**) 3D. The microelectrodes (red) on each sidewall are separated by coplanar SiO_2 (dark green)–Polysilicon (light green)–SiO_2 (dark green)/silicon (blue) insulators.

2.3. Numerical Simulation of ED Process

Modelling of the ED process was conducted in COMSOL Multiphysics 4.3b (COMSOL, Inc., Palo Alto, CA, USA) using the *Electric Currents*, *Frequency domain*, and *Solid*, *Stationary* application modes. The cell was modeled as a sphere with radius a_0. First, the distribution of the electric field was calculated in the microchannel, including the cell. Additionally, the ED forces exerted on the cell were computed by integrating the time-averaged Maxwell stress tensor over the cell surface [18]. Second, the cell was modeled as an incompressible linear elastic solid, which was described by a Neo-Hookean model [22]. *Solid* application mode was used to mimic the cell. A value of Young's modulus and Poisson's ratio of the cell was assumed, and the calculated ED forces were used as a load to calculate the cell deformation. Finally, the experiment results were used to fit the calculated deformations. The quantitative information used in the simulations is provided in tab:micromachines-07-00204-t001.

Table 1. Values of the constants and parameters used in the simulations.

Parameter	Value/Range	Reference
Medium conductivity (σ_{out})	0.001 S·m^{-1}	Measured
Medium permittivity (ε_{out})	80	[23]
Cytoplasmic conductivity (σ_{in})	0.3 S·m^{-1}	[23]
Cytoplasmic permittivity (ε_{in})	70	[18]
Cell membrane conductivity (σ_m)	5×10^{-7} S·m^{-1}	[23]
Cell membrane permittivity (ε_m)	10	[18]
Cell membrane thickness (d_m)	5 nm	[23]
Young's modulus	600 Pa	
Poisson's ratio of cell (μ)	0.499	

The electric potential inside and outside the cell was obtained by solving the equation in the frequency domain [16]

$$-\nabla\cdot\left(\left(\sigma_{out}+j\omega\varepsilon_0\varepsilon_{out}\right)\nabla\phi_{out}\right)=0, \tag{2}$$

$$-\nabla\cdot\left(\left(\sigma_{in}+j\omega\varepsilon_0\varepsilon_{in}\right)\nabla\phi_{in}\right)=0, \tag{3}$$

where ε_0 is the permittivity of the vacuum; ε_{out} and σ_{out} are, respectively, the relative permittivity and the conductivity of the medium; and ε_{in} and σ_{in} are, respectively, the relative permittivity and the conductivity of the cytoplasm. ω is the angular frequency of the AC electric field. $j=\sqrt{-1}$ is the imaginary unit. The voltage for ED (Φ_0) was applied via embedded discrete electrodes. Thus, the electrical boundary condition on the electrodes was assumed to be

$$\Phi=\Phi_0 \text{ or } 0 \tag{4}$$

The remaining walls of the microchannel were electrically insulated. The cell settled down the microelectrode (the highest electric field region) with forces F_1 and F_2 on two hemi-ellipsoids. These distributed forces on the cell led to elongation of the cell at an equilibrium location. The forces due to the electric field are calculated from the integration of the time-averaged Maxwell stress tensor over the cell's surface,

$$\mathbf{T}=\frac{\varepsilon_0\varepsilon_{out}}{4}\left(\mathbf{E}\mathbf{E}^*+\mathbf{E}^*\mathbf{E}-|\mathbf{E}|^2\,\mathbf{I}\right), \tag{5}$$

which is responsible for the steady deformation of the cell. **T** is the time-averaged Maxwell stress tensor, **E** is the applied external electric field, **E*** is the complex conjugate of **E**. **I** is the unit tensor. For trapped cells in the non-uniform electric field, we assumed that $\pm\left|F_1-F_2\right|/2$ were the forces acting on each half-sphere for electro-deformation, which stretched the cell approximately uniaxially. The total electroformation force is defined as

$$F=|F_1-F_2|. \tag{6}$$

At the cell membrane, a *Distributed Impedance* boundary condition was set to introduce the influence of the cell membrane:

$$\mathbf{n}\cdot\left(\mathbf{J_1}-\mathbf{J_2}\right)=\frac{\left(\sigma_m+j\omega\varepsilon_0\varepsilon_m\right)}{d_m}\left(V-V_{ref}\right). \tag{7}$$

Some constraints were set to prevent the cell from shifting in space; that is, the pole at the microelectrode cannot move at all, the lines at the *x*–*y* plane cannot move along the *z* axis, and the lines at the *x*–*z* plane cannot move along the *y* axis.

3. Results and Discussion

3.1. Simulation Results

As the electric properties of cells are mostly unknown, we used common values. As shown in Figure 2, as the applied voltage increased from 4 V to 20 V, the electrodeformation force changed from 7.6 nN to 190.4 nN for a cell with a_0 = 6 μm. Larger cells experience a larger electro-deformation force, but larger cells also require a large force to deform. Figure 3 depicts an example of the deformation of a cell with radius a_0 = 6 μm under 16 V of AC voltage when the Young's modulus of the cell is 600 Pa. The color represents the displacement along the x axis. The deformation ratio is ~1.555.

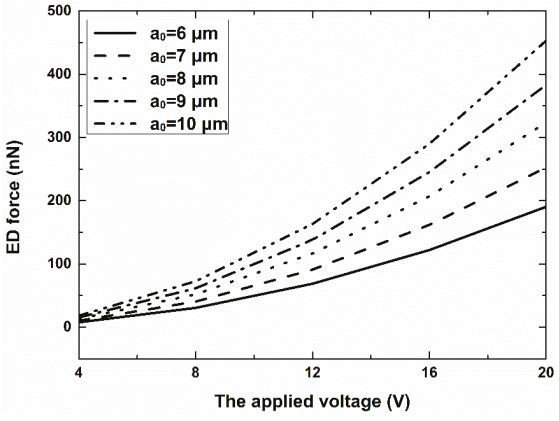

Figure 2. Electro-deformation (ED) forces as a function of the applied voltage and radius of the cell. The applied frequency was 1 MHz.

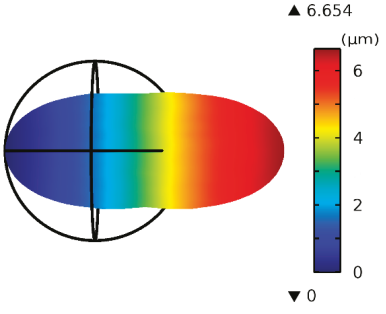

Figure 3. The deformation of a cell with a_0 = 6 μm under 16 V AC. The color represents the displacement along the x axis.

3.2. Cell Elongation

Firstly, a small AC signal (~1 $V_{p\text{-}p}$, 1 MHz) was applied on the microelectrode array to produce a non-uniform electric field. Considering that the relative permittivity of the cell sample was higher than the surrounding medium, the cells would move to the electrode under positive-DEP force induced by the non-uniform electric field. To avoid cell alignment phenomenon effects on cell electrodeformation detection, cells were loaded at a low density. After the cells were stably located at the desired place (attached to the microelectrode), AC signals (4–20 V) with different amplitudes were chosen to electrically deform the cells.

In addition to the amplitude, the frequency of the AC signals was also a very important parameter for cell electrodeformation. In DC or low frequency fields, most of the applied voltage drops across the cell membrane, so cell lysis is easy to occur. Whereas at very high frequencies, small electrodynamic forces are generated because the cell membrane becomes electrically transparent [16]. In our experiments, we chose a frequency of 1 MHz, which generated high electrodynamic forces and also reduced the electrolysis effect.

When subjected to electric fields, both the fused and unfused stem cells showed deformation parallel to the applied electric field lines, as shown in Figure 4. With the increase in applied voltage, the deformation degree also increased. When the applied voltage was significantly high, some cells could be very deformed and cross the middle of the microchannel, or even move to the opposite microelectrode.

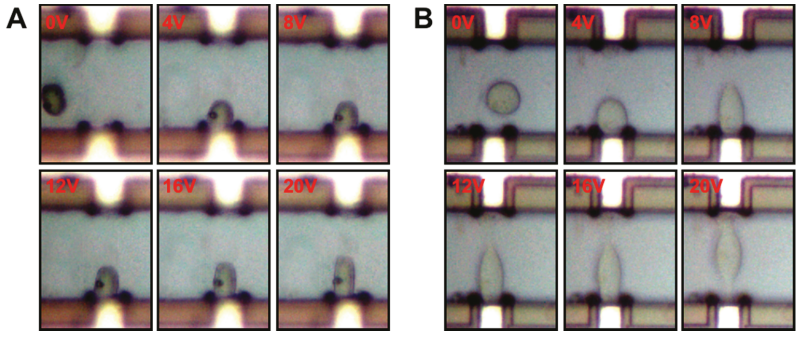

Figure 4. Deformation of (**A**) the unfused stem cell and (**B**) the fused stem cell as a function of the electric field strength.

3.3. Comparison of the Fused and Unfused Stem Cells

Figure 5 depicts the deformation ratio of the fused and unfused stem cells. For both types of cells, the deformation ratio increases as the applied voltage increases. However, the two cell types tested here were found to deform quite differently under identical ED conditions. The deformation ratios of the fused stem cell and unfused stem cell were, respectively, 1.205 ± 0.137 and 1.390 ± 0.256 at 16 $V_{p\text{-}p}$, and 1.517 ± 0.211 and 1.428 ± 0.243 at 20 $V_{p\text{-}p}$. No electrolysis was observed in the experiments. The fused stem cell was stiffer than the unfused stem cell at a relatively low voltage, and was less easily deformed by electrical stresses during ED. However, at 20 V, the fused stem cell was more easily deformed than the unfused stem cell. Above 20 V, the deformation of the fused stem cell was extremely large. This level of deformation may exceed the elastic limit of the fused stem cell, and some unwanted phenomena—such as electroporation on the cell membrane—occur. Because the mechanical properties of cells are largely determined by their cytoskeletons, this change may also arise from their different cytoskeletons.

For cell fusion, the largest radius of fused cells that we can obtain is $\sqrt[3]{2}R$, or $\sqrt{2}R$ after the fusion of two cells with radius R: (1) The volumes of the cells are assumed to be unchangeable, and the radius of the fused cell is $\sqrt[3]{2}R$; (2) the superficial areas of the cells are assumed to be unchangeable, and the radius of the fused cell is $\sqrt{2}R$. However, from our previous results, the radius of unfused stem cells is 7.55 ± 0.66 μm, but the radius of fused stem cells (8.88 ± 0.89 μm) is smaller than $\sqrt{2}R$ or $\sqrt[3]{2}R$. This result means that some part of the membrane of the cells was lost during the fusion process.

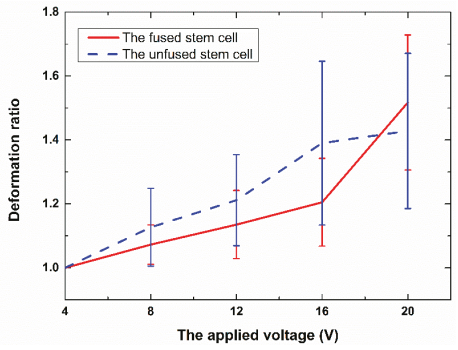

Figure 5. The deformation ratio vs. the applied voltage for the fused and unfused stem cells.

To compare with the experimental results, we assumed that the parameters of the cell membrane and cytoplasm were kept the same, and the same electric parameters of the fused and unfused cells were used in the simulation, except that the radius of the unfused stem cell was assumed to be 7.55 μm and the radius of the fused stem cell was assumed to be 8.88 μm. Note that a Young's modulus of 1500 Pa was used to approximate the deformation ratio of the fused cell. Under the same conditions (16 V), the deformation ratio of the fused stem cell is approximately 1.212, which is smaller than that of the unfused stem cell (~1.221). The deformation difference is then 0.009, but from the experimental results, the deformation difference is ~0.185. Thus, compared to the experimental results, this deformation difference was due to the radius not being large enough to cause a significant difference to the deformation ratio of the fused and unfused cells (Figure 6). It could be concluded that compared to the unfused stem cell, not only was the radius of the fused stem cell changed, but also—and more importantly—the properties of the cell membrane were changed after fusion.

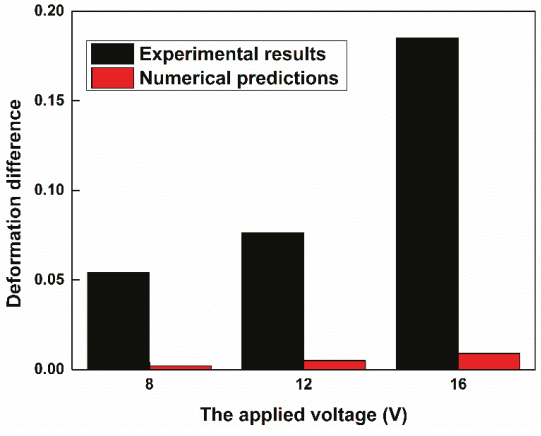

Figure 6. Deformation difference for the fused and unfused stem cells.

4. Conclusions

We present a method to analyze the deformability of fused cells. Electrical stresses, generated by a discrete co-planar microelectrode device with relatively low values of applied potential (4–20 V) have been used to electro-deform fused and unfused stem cells in suspension. The deformation ratios of the fused and unfused stem cells were, respectively, 1.205 ± 0.137 and 1.390 ± 0.256 at 16 $V_{p\text{-}p}$, and

1.517 ± 0.211 and 1.428 ± 0.243 at 20 $V_{p\text{-}p}$. Fused stem cells were stiffer than unfused stem cells at a relatively low voltage, and this trend was reversed at a relatively high voltage. It seems that the cytoskeletons of fused stem cells have been changed. The ED process is also modeled based on the Maxwell stress tensor and structural mechanics of cells. The simulation results showed that under the same conditions, the deformation ratio of fused stem cells is smaller than that of unfused stem cells, which is in qualitative agreement with the experimental observations. The numerical results also show that the significant difference in the deformation ratio of the fused and unfused stem cells is not due to their size difference; the change in deformability of the fused stem cells may be caused by the change in the cell membrane, and the properties of the cell membrane were changed after fusion.

Acknowledgments: This work was supported by the National Natural Science Foundation of China (Nos. 81371691, 31571005 and 81501617), the Fundamental Research Funds for the Central Universities (No. 106112016CDJZR238807) and the Program of International S&T Cooperation (No. 2014DFG31380).

Author Contributions: N.H. and J.Y. conceived and designed the experiments; X.Z., Y.L. and X.C. performed the experiments; M.C. and D.Y. performed simulation; J.X., Y.L. and J.Q. analyzed the data; Z.Y., and Z.W. contributed cell culture; X.Z. wrote the paper; N.H. and J.Y. revised the paper.

Conflicts of Interest: The authors declare no conflict of interest.

Abbreviations

The following abbreviations are used in this manuscript:

AC	Alternating current
ED	Electro-deformation
DEP	Dielectrophoresis
ER	Electrorotation
MPA	Micropipette aspiration
AFM	Atomic force microscopy
CCD	charge-coupled device
mESC	Mouse embryonic stem cell
H-DMEM	High-glucose dulbecco's modified eagle medium
EDTA	Ethylenediaminetetraacetic acid
FBS	Fetal bovine serum
PBS	Phosphate buffered saline
SOI	Silicon-on-insulator

References

1. Chen, E.H.; Olson, E.N. Unveiling the mechanisms of cell-cell fusion. *Science* **2005**, *308*, 369–373. [CrossRef] [PubMed]
2. Ambrosi, D.J.; Tanasijevic, B.; Kaur, A.; Obergfell, C.; O'Neill, R.J.; Krueger, W.; Rasmussen, T.P. Genome-wide reprogramming in hybrids of somatic cells and embryonic stem cells. *Stem Cells* **2007**, *25*, 1104–1113. [CrossRef] [PubMed]
3. Cowan, C.A.; Atienza, J.; Melton, D.A.; Eggan, K. Developmental biology: Nuclear reprogramming of somatic cells after fusion with human embryonic stem cells. *Science* **2005**, *309*, 1369–1373. [CrossRef] [PubMed]
4. Melancon, J.M.; Foster, T.P.; Kousoulas, K.G. Genetic analysis of the herpes simplex virus type 1 UL20 protein domains involved in cytoplasmic virion envelopment and virus-induced cell fusion. *J. Virol.* **2004**, *78*, 7329–7343. [CrossRef] [PubMed]
5. Dessain, S.K.; Adekar, S.P.; Stevens, J.B.; Carpenter, K.A.; Skorski, M.L.; Barnoski, B.L.; Goldsby, R.A.; Weinberg, R.A. High efficiency creation of human monoclonal antibody-producing hybridomas. *J. Immunol. Methods* **2004**, *291*, 109–122. [CrossRef] [PubMed]
6. Trevor, K.T.; Cover, C.; Ruiz, Y.W.; Akporiaye, E.T.; Hersh, E.M.; Landais, D.; Taylor, R.R.; King, A.D.; Walters, R.E. Generation of dendritic cell-tumor cell hybrids by electrofusion for clinical vaccine application. *Cancer Immunol. Immunother.* **2004**, *53*, 705–714. [CrossRef] [PubMed]

7. Niemela, P.S.; Miettinen, M.S.; Monticelli, L.; Hammaren, H.; Bjelkmar, P.; Murtola, T.; Lindahl, E.; Vattulainen, I. Membrane proteins diffuse as dynamic complexes with lipids. *J. Am. Chem. Soc.* **2010**, *132*, 7574–7575. [CrossRef] [PubMed]
8. Javanainen, M.; Hammaren, H.; Monticelli, L.; Jeon, J.-H.; Miettinen, M.S.; Martinez-Seara, H.; Metzler, R.; Vattulainen, I. Anomalous and normal diffusion of proteins and lipids in crowded lipid membranes. *Faraday Discuss.* **2013**, *161*, 397–417. [CrossRef] [PubMed]
9. Brandão, M.M.; Fontes, A.; Barjas-Castro, M.L.; Barbosa, L.C.; Costa, F.F.; Cesar, C.L.; Saad, S.T.O. Optical tweezers for measuring red blood cell elasticity: Application to the study of drug response in sickle cell disease. *Eur. J. Haematol.* **2003**, *70*, 207–211. [CrossRef] [PubMed]
10. Lim, C.T.; Dao, M.; Suresh, S.; Sow, C.H.; Chew, K.T. Large deformation of living cells using laser traps. *Acta Mater.* **2004**, *52*, 1837–1845. [CrossRef]
11. Lincoln, B.; Erickson, H.M.; Schinkinger, S.; Wottawah, F.; Mitchell, D.; Ulvick, S.; Bilby, C.; Guck, J. Deformability-based flow cytometry. *Cytometry A* **2004**, *59*, 203–209. [CrossRef] [PubMed]
12. Glenister, F.K.; Coppel, R.L.; Cowman, A.F.; Mohandas, N.; Cooke, B.M. Contribution of parasite proteins to altered mechanical properties of malaria-infected red blood cells. *Blood* **2002**, *99*, 1060–1063. [CrossRef] [PubMed]
13. Kirmizis, D.; Logothetidis, S. Atomic force microscopy probing in the measurement of cell mechanics. *Int. J. Nanomed.* **2010**, *5*, 137–145. [CrossRef]
14. Engelhardt, H.; Gaub, H.; Sackmann, E. Viscoelastic properties of erythrocyte membranes in high-frequency electric fields. *Nature* **1984**, *307*, 378–380. [CrossRef] [PubMed]
15. MacQueen, L.A.; Buschmann, M.D.; Wertheimer, M.R. Mechanical properties of mammalian cells in suspension measured by electro-deformation. *J. Micromech. Microeng.* **2010**, *20*, 065007. [CrossRef]
16. MacQueen, L.A.; Thibault, M.; Buschmann, M.D.; Wertheimer, M.R. Electromechanical deformation of mammalian cells in suspension depends on their cortical actin thicknesses. *J. Biomech.* **2012**, *45*, 2797–2803. [CrossRef] [PubMed]
17. Doh, I.; Lee, W.C.; Cho, Y.H.; Pisano, A.P.; Kuypers, F.A. Deformation measurement of individual cells in large populations using a single-cell microchamber array chip. *Appl. Phys. Lett.* **2012**, *100*, 173702–1737023. [CrossRef] [PubMed]
18. Chen, J.; Abdelgawad, M.; Yu, L.; Shakiba, N.; Chien, W.-Y.; Lu, Z.; Geddie, W.R.; Jewett, M.A.S.; Sun, Y. Electrodeformation for single cell mechanical characterization. *J. Micromech. Microeng.* **2011**, *21*, 054012. [CrossRef]
19. Gimsa, J. A comprehensive approach to electro-orientation, electrodeformation, dielectrophoresis, and electrorotation of ellipsoidal particles and biological cells. *Bioelectrochemistry* **2001**, *54*, 23–31. [CrossRef]
20. Qu, Y.; Hu, N.; Xu, H.; Yang, J.; Xia, B.; Zheng, X.; Yin, Z.Q. Somatic and stem cell pairing and fusion using a microfluidic array device. *Microfluid. Nanofluid.* **2011**, *11*, 633–641. [CrossRef]
21. Hu, N.; Yang, J.; Qian, S.; Zhang, X.; Joo, S.W.; Zheng, X. A cell electrofusion microfluidic chip using discrete coplanar vertical sidewall microelectrodes. *Electrophoresis* **2012**, *33*, 1980–1986. [CrossRef] [PubMed]
22. Luo, Y.N.; Chen, D.Y.; Zhao, Y.; Wei, C.; Zhao, X.T.; Yue, W.T.; Long, R.; Wang, J.B.; Chen, J. A constriction channel based microfluidic system enabling continuous characterization of cellular instantaneous young's modulus. *Sens. Actuators B Chem.* **2014**, *202*, 1183–1189. [CrossRef]
23. Kotnik, T.; Miklavčič, D.; Slivnik, T. Time course of transmembrane voltage induced by time-varying electric fields—A method for theoretical analysis and its application. *Bioelectrochem. Bioenerg.* **1998**, *45*, 3–16. [CrossRef]

micromachines

MDPI

Article

UV Light–Induced Aggregation of Titania Submicron Particles

Can Zhou, Yashar Bashirzadeh, Timothy A. Bernadowski Jr. and Xiaoyu Zhang *

Department of Mechanical & Aerospace Engineering, Old Dominion University, Norfolk, VA 23529, USA; czhou001@odu.edu (C.Z.); ybash001@odu.edu (Y.B.); tbern008@odu.edu (T.A.B.J.)

* Correspondence: x1zhang@odu.edu; Tel.: +1-757-683-4913

Academic Editors: Xiangchun Xuan and Shizhi Qian

Received: 30 September 2016; Accepted: 2 November 2016; Published: 8 November 2016

Abstract: In this study, aggregation of TiO_2 (rutile and anatase) submicron particles in deionized (DI) water under ultra-violet (UV) light irradiation was investigated. While no aggregation was observed in the dark, rutile and anatase submicron particles started aggregating upon application of UV light and ceased aggregation in about 2 and 8.4 h, respectively. It has been demonstrated that UV light directly mitigated the particle mobility of TiO_2, resulting in a neutralization effect of the Zeta potential. It was also observed that rutile particles aggregated much faster than anatase particles under UV radiation, indicating that the Zeta potential of as-prepared rutile is less than that of anatase in deionized (DI) water. In addition, the interaction energy of rutile and anatase particles was simulated using the Derjaguin–Landau–Verwey–Overbeek (DLVO) model. The results showed a significant reduction of barrier energy from 118.2 k_BT to 33.6 k_BT for rutile and from 333.5 k_BT to 46.1 k_BT for anatase, respectively, which further validated the remarkable influence of UV irradiation on the aggregation kinetics of rutile and anatase submicron particles. This work presents a further understanding of the aggregation mechanism of light-controlled submicron particles and has a promising potential application in environmental remediation.

Keywords: Derjaguin–Landau–Verwey–Overbeek (DLVO); Zeta potential; rutile; anatase; electrokinetics; mobility

1. Introduction

Aqueous micromotors driven by external energy from either a chemical reaction with an electrolyte or an environmental stimulus such as light, magnetic fields, temperature gradients, concentration gradients, etc., have drawn a lot of research interest [1–4]. Due to their small size and simple manipulation, micromotors composed of micro- or nanoparticles have promising applications in drug delivery, cell separation, bacterial degradation, and chemical decomposition [5–7]. Titania (TiO_2) particles have been commonly used in these micromotors. As an *n*-type semiconductor with strong photocatalytic activities, titania has been widely investigated for photoelectrochemical water splitting to produce hydrogen [8], following the work of technological pioneers Fujishima and Honda [9].

Light-induced behaviors of titania particles have become more researched over recent years. Anatase TiO_2 particles (0.2–2.5 μm) were reported to exhibit ultra-violet (UV)-induced microfireworks with tracer particles such as SiO_2 (2.34 μm) and amidine polystyrene (2.5 μm) [10]. Despite oppositely charged properties, both tracer particles would be repelled by TiO_2 particles in the dark whereas they would be attracted towards TiO_2 particles upon UV light exposure. According to the proposed diffusiophoretic model, the repeatable light switch effect was believed to be caused by the concentration gradient of photogenerated chemical species, osmotic propulsion, and surface charge interaction [10]. Photo-induced disaggregation of TiO_2 nanoparticles (27 ± 4 nm) was observed by Bennett et al. [11] and Zhou et al. [12]. It was reported that TiO_2 nanoparticles would disaggregate from core clusters

upon light irradiation and re-aggregate in the dark due to Brownian motion. Furthermore, infrared light was found to contribute to disaggregation of nanoparticles due to thermal energy input and induced vibration. The decrease of the Zeta potential under UV irradiation was insufficient to affect the balance of Derjaguin–Landau–Verwey–Overbeek (DLVO) forces. However, Sun et al. reported an opposite phenomenon in which UV light could induce aggregation of TiO_2 nanoparticles (21 nm) [13]. The results showed that the hydrodynamic size increased from 252 nm to 623 nm after 50 h of UV irradiation. It was explained that due to the formation of hydroxyl groups under UV irradiation, the surface charges of TiO_2 nanoparticles were reduced over time. It was concluded that the decrease of the repulsive force between nanoparticles facilitated TiO_2 aggregation. In addition to those investigations on pure TiO_2 particles, TiO_2-graphene (TiO_2: 70–80 nm) composite nanoparticles were reported to aggregate after 20 h of UV irradiation due to a decrease in hydrophilicity [14,15]. Those aforementioned studies mainly focused on the behaviors of TiO_2 particles induced by light at a nano-scale. As the particle size increases, TiO_2 may exhibit different photocatalytic properties and electrokinetic behaviors. To our best knowledge, the study of UV light–induced movements of micron or submicron TiO_2 particles is limited.

In this work, UV light–induced aggregation of submicron particles in aqueous suspensions was demonstrated using two different polymorphs of TiO_2, rutile and anatase. The objective was to investigate the factors that affect the particle aggregation, including irradiation duration, particle mobility, Zeta potential, and polymorphism. In addition, theoretical models were implemented to correlate and explain the experimental results.

2. Experiment

2.1. Aggregation Experiments

The aggregation experiments were conducted in an enclosed reservoir made of polydimethylsiloxane (PDMS) on a glass slide. The reservoir's dimensions are 40 mm $\times$ 10 mm $\times$ 2 mm. The suspensions of TiO_2 were injected into the reservoir and then sealed to prevent air intrusion. A 200 W solar simulator (Newport Corp., Irvine, CA, USA) with a Xe-Hg acr lamp was used as a light source. UV light was actuated using a dichroic mirror (Model 66217, Newport Corp.) that primarily reflects 260–320 nm light generated by the solar simulator. The experimental observations were performed via an optical microscope (Nikon TE2000-U, Nikon Instruments, Tokyo, Japan).

As-prepared rutile (500 nm) and anatase (325 mesh) powders were obtained from US-NANO and Sigma-Aldrich (St. Louis, MO, USA), respectively. It has been verified under the microscope that the particle size of anatase powder from Sigma-Aldrich is submicron. For preparation of TiO_2 suspension, rutile and anatase powders were directly added into deionized (DI) water, respectively, by a ratio of 3 mg:150 mL and the microsphere concentration was around 0.25 mM [16]. After manually stirring, an ultrasonic bath (VWR 501, Radnor, PA, USA) and/or magnetic stirring (Fisher Scientific Isotemp, Pittsburgh, PA, USA) at 1000 rpm was used to form suspensions and disaggregate large particles. Subsequently, the suspensions were injected into the prepared enclosed reservoir for experimentation. The actual particle sizes were around 1 μm for both rutile and anatase suspensions, possibly due to some difficulties encountered while breaking nano TiO_2 agglomerates in the ultrasonic bath [17].

2.2. Particle Mobility Measurement

The particle mobility under UV light in DI water was measured in a microchannel made of PDMS only. The microchannel consisted of a straight cylindrical conduit (Inner Diameter, ID = 0.3 mm) connected with two cubic reservoirs at both ends. An electric field was applied through two silver electrodes embedded outside the microchannel using a Direct current (DC) power supply (Circuit Specialists CSI20002S, Tempe, AZ, USA). Particle movement and velocity within the microchannel due to the electric field was visually recorded by the optical microscope. Lastly, the mobility was calculated by dividing the velocity of the particles by the strength of the electric field.

3. Theory

3.1. Particle Mobility and Zeta Potential

Zeta potential is an electrokinetic term that has been widely used to interpret the agglomeration and disaggregation of colloidal dispersions [18]. The Zeta potential represents the net electrical charge of a confined region. It is believed that when the Zeta potential becomes neutral, particles become more attractive so that they tend to agglomerate [13]. The aggregation of TiO_2 particles in the present research can be interpreted by using the Zeta potential if it incrementally becomes more neutral under UV irradiation.

Direct measurement of the Zeta potential was not a viable option in our lab; therefore, an indirect method, measuring the particle mobility, was adopted. The particle mobility has a direct relationship with the Zeta potential, as shown in Equation (1) below. The particle mobility (U) is defined as the ratio of the drift velocity (v_d) divided by the electric field (E_z): $U = v_d/E_z$. Note that practically, in these experiments, the PDMS microchannel is usually negatively charged in solution over a wide range of pH [19]. Therefore, an electrical double layer containing net cations forms near the PDMS/electrolyte interface, leaving net mobile anions inside the microchannel. Electroosmotic flows from anode to cathode are generated in the center of the microchannel when an electric field is applied. Such fluid motion affects the movement of TiO_2 particles. Hence, the measured mobility was actually the sum of the electrostatic mobility and electroosmotic flow: $U_m = U_{TiO_2} + U_{os}$. The Zeta potential of particles can be linearly correlated with electrostatic mobility based on Henry's equation: [20,21]

$$\zeta = \frac{2\mu U_{TiO_2}}{3\varepsilon_r \varepsilon_0} f(\kappa r) \tag{1}$$

$$f(\kappa r) = 1 + \frac{1}{2}\left[1 + \left(\frac{2.5}{\kappa r[1 + 2\exp(-\kappa r)]}\right)\right]^{-3} \tag{2}$$

where μ is the solution viscosity; ε_r and ε_0 are the relative dielectric constant and the vacuum electrical permittivity respectively; r is the particle diameter; κ is the inverse Debye length in which $\kappa = 2.32 \times 10^9 (\sum C_i Z_i^2)^{0.5}$, where C_i and Z_i are the concentration and valency value of ion i; $f(\kappa r)$ is Henry's function and varies from 1.0 to 1.5, depending on different situations.

3.2. DLVO Model

Another viable theory to interpret the aggregation of aqueous TiO_2 suspensions is the classical DLVO model. The DLVO model integrates the counteractions of the van der Waals attraction energy (V_{VDW}) and the electrical double layer (EDL) repulsion energy (V_{EDL}) among particles, which can be expressed using the following equations [16]:

$$V_{VDW} = -\frac{A_{131}}{6}\left[\frac{2r^2}{d(4r+d)} + \frac{2r^2}{(2r+d)^2} + \ln\frac{d(4r+d)}{(2r+d)^2}\right] \tag{3}$$

$$V_{EDL} = 2\pi r \varepsilon_r \varepsilon_0 \zeta^2 \ln[1 + \exp(-\kappa d)] \tag{4}$$

where A_{131} is the Hamaker constant for nanoparticle-water-nanoparticle (6×10^{-20} J) [13]; d is the distance between two particles; and n_∞ is the number concentrations of bulk ions.

The stability of a suspension is usually characterized by the total interaction energy (V_T), which is the summation of V_{VDW} and V_{EDL}. In a stable suspension, the total interaction energy acts as an energy barrier that resists particle aggregation. It is hypothesized that UV light affects the total interaction energy and results in a lower V_{EDL} and barrier energy. Consequently, particles start to aggregate, making the suspension unstable [13]. The DLVO model is similar to the Zeta potential and was validated by the experimental results.

4. Results and Discussion

4.1. Aggregation under UV Light

The aggregation of TiO_2 submicron particles was investigated through visualization using an optical microscope. Prior to the application of UV light, both rutile and anatase suspensions were kept in a dark environment for 10 h to ensure minimum aggregation. Figure 1 shows the changes of rutile (Figure 1a) and anatase suspensions (Figure 1b) under UV light over different time periods. It was observed that the aggregation rate of rutile particles was much faster than that of anatase particles. A quantified version of aggregation that shows the changes of particle sizes over time is illustrated in Figure 2. Both rutile and anatase suspensions went through a slow start-up and then a rapid increase in terms of particle size during aggregation. It was illustrated that the rutile particles coagulated significantly faster starting from about 1.5 h, with an average growing rate of 1.23 μm/s in diameter, until their average sizes peaked at 2 h. After this time, no further aggregation was clearly observed and the ultimate average particle diameter remained around 18.15 μm. In comparison, the accumulation of anatase particles in the suspension showed a similar trend but in a much slower process. The rapid growth of anatase particles started at 5.75 h and plateaued at 8.4 h. During that period, the average growing rate was 0.22 μm/s in diameter and the ultimate average particle size was around 25.7 μm.

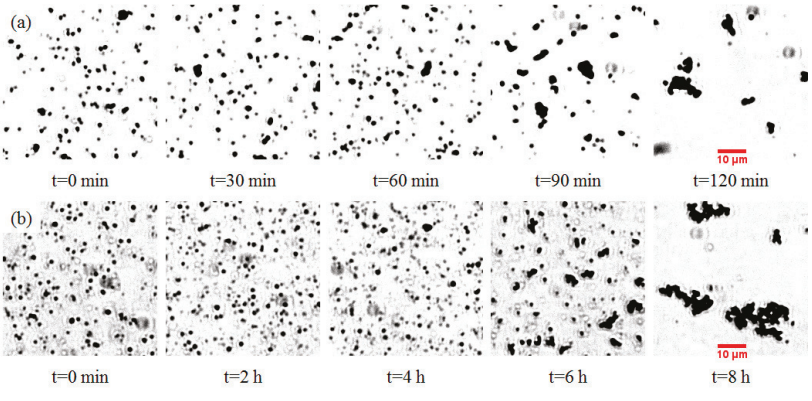

Figure 1. Microscopic images of ultra-violet (UV) light–induced aggregation of (**a**) rutile submicron particles over 120 min and (**b**) anatase submicron particles over 8 h in deionized (DI) water.

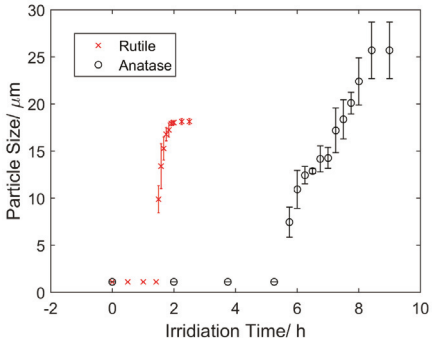

Figure 2. Size change of the rutile and anatase submicron particles in DI water as a function of irradiation time. The UV light was turned on at 0 h.

4.2. Particle Mobility

In order to further investigate the UV-induced aggregation electrokinetics, particle mobility tests were conducted using a lab-made microchannel. First, 20 V DC was applied through the electrodes which were spaced 20.2 mm apart. A regular mobility test was conducted under UV light with 5 min intervals, following a baseline test in the dark condition. The mobility tests lasted approximately 1 h, beyond which optical observations became difficult as sediments started blurring images in the microchannel. Particle movement in the microchannel is actually the net effect of the electroosmotic flow and electrostatic movement. The electroosmotic flow was assumed to remain stable throughout all the mobility tests. In addition, PDMS is highly transparent to UV light and its degradation under UV irradiation was assumed to be negligible.

The electrostatic movement of TiO_2 particles due to the surface potential exhibited the same variance with the measured mobility depending on the irradiation time, as shown in Figure 3. The mobility of both rutile and anatase immediately decreased upon application of UV light. During the first 15 min, the effect was remarkable, with a decrease of 2.32×10^{-8} $m^2 \cdot s/V$ for rutile and 3.51×10^{-8} $m^2 \cdot s/V$ for anatase. Over 1 h of UV irradiation, the overall magnitude decrease of mobility for rutile and anatase was about 60.8% and 46.4%, respectively. Rutile exhibited a lower mobility than anatase with an average difference of 1.37×10^{-8} $m^2 \cdot s/V$ throughout the test. This corresponded to a lower Zeta potential of 12.1 mV based on Equations (1) and (2), and indicated a lower surface charge, and thus faster aggregation rate for rutile particles.

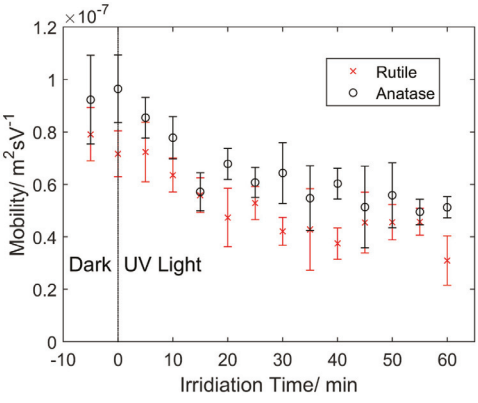

Figure 3. Measured particle mobility of the rutile and anatase submicron particles over time. The UV light was turned on at 0 h. The electric field strength was 0.99 V/mm.

4.3. Discussion

UV light–induced aggregation was observed in both aqueous rutile and anatase suspensions that contained submicron particles. Such a phenomenon was attributed to the strongly photocatalytic activities of TiO_2, which is an intrinsic *n*-type semiconductor with a wide bandgap (3.0–3.2 eV) [22]. Both rutile and anatase have been widely used as the photocatalysts for photoelectrochemical water splitting [8]. The wide bandgap of TiO_2 determines the threshold of the light frequencies required for exciting electrons from the valence band to the conduction band. Therefore, a UV light source was required in those experiments.

The changes of the Zeta potential over time can be used to interpret UV light–induced aggregation of TiO_2 particles observed in the experiments. Zeta potential has been used as an index of stability of colloidal dispersions [18]. The magnitude of the Zeta potential indicates the affinity between a particle and its adjacent ones. As the Zeta potential approaches neutral, the particles will have less resistance to

aggregation, and vice versa. The Zeta potential of TiO_2 particles is strongly relevant to the background pH value (or proton concentration) and the measured negative values in DI water (pH ≈ 6.5) [18]. Upon UV irradiation, it is believed that hydroxyl groups (·OH) form on the TiO_2 particle surfaces, resulting in a higher local proton concentration (lower local pH). Consequently, the Zeta potential increases and becomes more neutral. This electrochemical process has been explained and verified by Fujishima et al. [23–25]. When illuminated by UV light, photogenerated electron-hole pairs generated on the TiO_2 surfaces enable chemical redox reactions. Specifically, Ti^{4+} ions will combine with electrons and be reduced to Ti^{3+} ions, whereas the positive holes left will oxidize the bridging O atoms to produce oxygen vacancies in the lattice. Such vacancies then absorb water molecules and generate acidic bridging hydroxyls (pKa = 2.9) [13]. The chemically reactive hydroxyls are able to trap extra holes and subsequently dissociate water molecules. The final products are more concentrated protons, leading to the localized reduction of pH. Consequently, the Zeta potential of TiO_2 particles becomes more and more neutral.

The remarkable difference of the time duration of the aggregation between rutile and anatase was observed repeatedly in the experiments. As illustrated in Figure 3, the as-received rutile particles show less mobility than anatase ones. This indicates the initial Zeta potential of rutile was more neutral than that of anatase. However, none of the existing theory can be used to explain such a phenomenon, other than the possible different processes of powder synthesis from individual vendors, as pointed out in References [26,27]. Kosmulski et al. reviewed the research on the point zero charge (PZC) of rutile and anatase and their summary indicated that the Zeta potential of TiO_2 is not sensitive to its common crystal phases [26]. That conclusion basically excludes the cause due to different polymorphs of TiO_2. In addition, the particle sizes of those rutile and anatase submicron particles used in the experiments outlined in this work were similar. Therefore, the sizing effect on Zeta potential [28] cannot be fully used to justify the observations. More experiments are needed to validate whether the initial difference of the Zeta potential between rutile and anatase is attributed to the synthesis process or not.

The DLVO theoretical model was applied to quantitatively investigate the aggregation behaviors of rutile and anatase particles and the results are shown in Figure 4. The EDL repulsive force is determined by the particle surface charge. The initial Zeta potential of anatase was set to −30 mV in DI water (pH ≈ 6.5) as a reference point [17]. From the difference of measured mobility shown in Figure 3, the initial Zeta potential of rutile was calculated as −18.3 mV based on Equations (1) and (2). After 20, 40 and 60 min of UV irradiation, the Zeta potentials of rutile and anatase were reduced to −13.4, −11.9, −10.2 mV and −17.9, −14.2, −11.8 mV, respectively, according to the decrease of the particle mobility.

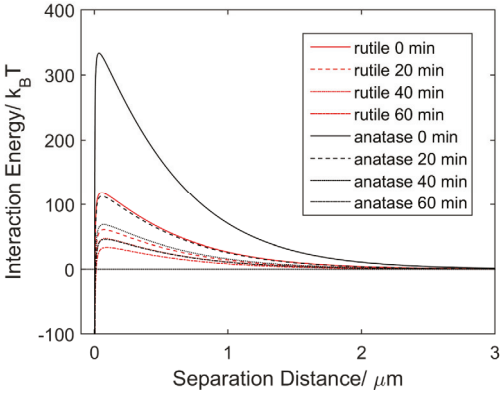

Figure 4. Changes of interaction energy of rutile versus anatase submicron particles in DI water over time under UV irradiation.

As shown in Figure 4, the interaction energy curves illustrate a significant influence of prolonged UV irradiation on energy barriers for rutile and anatase, respectively. Based on Equations (3) and (4), the energy barriers of rutile and anatase were simulated as a function of irradiation time. Compared to the initial energy barrier of 333.5 k_BT and 118.2 k_BT, the maximum interaction energy decreased to only 46.1 k_BT and 33.6 k_BT for rutile and anatase, respectively, after 1 h of UV irradiation. Such a significant reduction of energy barriers indicates that UV irradiation facilitates the aggregation of rutile and anatase submicron particles. Furthermore, the faster aggregation rate of rutile particles could be a result of its lower energy barrier throughout UV exposure.

5. Conclusions

UV light–controlled aggregation of TiO_2 submicron particles in aqueous suspensions was investigated and it was shown that aggregation of both rutile and anatase particles can be facilitated by UV irradiation. Upon UV exposure, the measured mobility significantly decreased for both rutile and anatase particles, indicating a reduction of the Zeta potential. The reduction of the Zeta potential enhanced the attraction among TiO_2 particles, and therefore facilitated aggregation. In the experiments, rutile particles exhibited a much faster aggregation rate than anatase particles and rutile particles showed a lower mobility (a more neutral Zeta potential) than anatase particles under UV irradiation. This was concluded to be caused by the lower repulsive interaction which led to the observed faster aggregation rate of rutile particles. It is possible that the faster agglomeration rate of as-prepared rutile might come from its synthesis process. The obvious decrease of the barrier energy simulated through the DLVO model quantitatively confirmed the notable effects of UV light on rutile and anatase particle aggregation. This work contributes to further understanding of the fundamentals of light-controlled micro/nanoparticles in aqueous media and holds considerable promise for environmental remediation.

Acknowledgments: We appreciate the funding support from Old Dominion University and the equipment supplied from the Institute of Micro/Nanotechnology.

Author Contributions: Xiaoyu Zhang conceived and designed the experiments; Can Zhou directed the experimental investigation, conducted data analysis, and wrote the manuscript. Yashar Bashirzadeh and Timothy A. Bernadowski Jr. contributed to device fabrication and the experiments.

Conflicts of Interest: The authors declare no conflict of interest. The founding sponsors had no role in the design of the study; in the collection, analyses, or interpretation of data; in the writing of the manuscript, and in the decision to publish the results.

References

1. Pak, O.S.; Gao, W.; Wang, J.; Lauga, E. High-speed propulsion of flexible nanowire motors: Theory and experiments. *Soft Matter* **2011**, *7*, 8169–8181. [CrossRef]
2. Li, Y.; Mou, F.; Chen, C.; You, M.; Yin, Y.; Xu, L.; Guan, J. Light-controlled bubble propulsion of amorphous TiO_2/Au janus micromotors. *RSC Adv.* **2016**, *6*, 10697–10703. [CrossRef]
3. Wu, Z.; Si, T.; Gao, W.; Lin, X.; Wang, J.; He, Q. Superfast near-infrared light-driven polymer multilayer rockets. *Small* **2016**, *12*, 577–582. [CrossRef] [PubMed]
4. Dong, R.; Zhang, Q.; Gao, W.; Pei, A.; Ren, B. Highly efficient light-driven TiO_2–Au janus micromotors. *ACS Nano* **2015**, *10*, 839–844. [CrossRef] [PubMed]
5. Pavlick, R.A.; Sengupta, S.; McFadden, T.; Zhang, H.; Sen, A. A polymerization-powered motor. *Angew. Chem. Int. Ed.* **2011**, *50*, 9374–9377. [CrossRef] [PubMed]
6. Ibele, M.; Mallouk, T.E.; Sen, A. Schooling behavior of light-powered autonomous micromotors in water. *Angew. Chem. Int. Ed.* **2009**, *48*, 3308–3312. [CrossRef] [PubMed]
7. Li, J.; Singh, V.V.; Sattayasamitsathit, S.; Orozco, J.; Kaufmann, K.; Dong, R.; Gao, W.; Jurado-Sanchez, B.; Fedorak, Y.; Wang, J. Water-driven micromotors for rapid photocatalytic degradation of biological and chemical warfare agents. *ACS Nano* **2014**, *8*, 11118–11125. [CrossRef] [PubMed]
8. Ni, M.; Leung, M.K.; Leung, D.Y.; Sumathy, K. A review and recent developments in photocatalytic water-splitting using TiO_2 for hydrogen production. *Renew. Sustain. Energy Rev.* **2007**, *11*, 401–425. [CrossRef]

9. Fujishima, A. Electrochemical photolysis of water at a semiconductor electrode. *Nature* **1972**, *238*, 37–38. [CrossRef] [PubMed]
10. Hong, Y.; Diaz, M.; Córdova-Figueroa, U.M.; Sen, A. Light-driven titanium-dioxide-based reversible microfireworks and micromotor/micropump systems. *Adv. Funct. Mater.* **2010**, *20*, 1568–1576. [CrossRef]
11. Bennett, S.W.; Zhou, D.; Mielke, R.; Keller, A.A. Photoinduced disaggregation of TiO_2 nanoparticles enables transdermal penetration. *PLoS ONE* **2012**, *7*, e48719. [CrossRef] [PubMed]
12. Zhou, D.; Bennett, S.W.; Keller, A.A. Increased mobility of metal oxide nanoparticles due to photo and thermal induced disagglomeration. *PLoS ONE* **2012**, *7*, e37363. [CrossRef] [PubMed]
13. Sun, J.; Guo, L.-H.; Zhang, H.; Zhao, L. UV irradiation induced transformation of TiO_2 nanoparticles in water: Aggregation and photoreactivity. *Environ. Sci. Technol.* **2014**, *48*, 11962–11968. [CrossRef] [PubMed]
14. Bai, X.; Zhang, X.; Hua, Z.; Ma, W.; Dai, Z.; Huang, X.; Gu, H. Uniformly distributed anatase TiO_2 nanoparticles on graphene: Synthesis, characterization, and photocatalytic application. *J. Alloys Compd.* **2014**, *599*, 10–18. [CrossRef]
15. Hua, Z.; Zhang, J.; Bai, X.; Ye, Z.; Tang, Z.; Liang, L.; Liu, Y. Aggregation of TiO_2-graphene nanocomposites in aqueous environment: Influence of environmental factors and UV irradiation. *Sci. Total Environ.* **2016**, *539*, 196–205. [CrossRef] [PubMed]
16. Wang, P.; Qi, N.; Ao, Y.; Hou, J.; Wang, C.; Qian, J. Effect of UV irradiation on the aggregation of TiO_2 in an aquatic environment: Influence of humic acid and pH. *Environ. Pollut.* **2016**, *212*, 178–187. [CrossRef] [PubMed]
17. Mandzy, N.; Grulke, E.; Druffel, T. Breakage of TiO_2 agglomerates in electrostatically stabilized aqueous dispersions. *Powder Technol.* **2005**, *160*, 121–126. [CrossRef]
18. Berg, J.M.; Romoser, A.; Banerjee, N.; Zebda, R.; Sayes, C.M. The relationship between pH and Zeta potential of ~30 nm metal oxide nanoparticle suspensions relevant to in vitro toxicological evaluations. *Nanotoxicology* **2009**, *3*, 276–283. [CrossRef]
19. Kirby, B.J.; Hasselbrink, E.F. Zeta potential of microfluidic substrates: 2. Data for polymers. *Electrophoresis* **2004**, *25*, 203–213. [CrossRef] [PubMed]
20. Delgado, Á.V.; González-Caballero, F.; Hunter, R.; Koopal, L.; Lyklema, J. Measurement and interpretation of electrokinetic phenomena. *J. Colloid Interface Sci.* **2007**, *309*, 194–224. [CrossRef] [PubMed]
21. Ohshima, H. A simple expression for henry's function for the retardation effect in electrophoresis of spherical colloidal particles. *J. Colloid Interface Sci.* **1994**, *168*, 269–271. [CrossRef]
22. Zhang, J.; Zhou, P.; Liu, J.; Yu, J. New understanding of the difference of photocatalytic activity among anatase, rutile and brookite TiO_2. *Phys. Chem. Chem. Phys.* **2014**, *16*, 20382–20386. [CrossRef] [PubMed]
23. Sakai, N.; Fujishima, A.; Watanabe, T.; Hashimoto, K. Quantitative evaluation of the photoinduced hydrophilic conversion properties of TiO_2 thin film surfaces by the reciprocal of contact angle. *J. Phys. Chem. B* **2003**, *107*, 1028–1035. [CrossRef]
24. Wang, R.; Sakai, N.; Fujishima, A.; Watanabe, T.; Hashimoto, K. Studies of surface wettability conversion on TiO_2 single-crystal surfaces. *J. Phys. Chem. B* **1999**, *103*, 2188–2194. [CrossRef]
25. Ishibashi, K.-I.; Nosaka, Y.; Hashimoto, K.; Fujishima, A. Time-dependent behavior of active oxygen species formed on photoirradiated TiO_2 films in air. *J. Phys. Chem. B* **1998**, *102*, 2117–2120. [CrossRef]
26. Kosmulski, M. pH-dependent surface charging and points of zero charge. IV. Update and new approach. *J. Colloid Interface Sci.* **2009**, *337*, 439–448. [CrossRef] [PubMed]
27. Suttiponparnit, K.; Jiang, J.; Sahu, M.; Suvachittanont, S.; Charinpanitkul, T.; Biswas, P. Role of surface area, primary particle size, and crystal phase on titanium dioxide nanoparticle dispersion properties. *Nanoscale Res. Lett.* **2010**, *6*, 1–8. [CrossRef] [PubMed]
28. Barisik, M.; Atalay, S.; Beskok, A.; Qian, S. Size dependent surface charge properties of silica nanoparticles. *J. Phys. Chem. C* **2014**, *118*, 1836–1842. [CrossRef]

micromachines

MDPI

Article

Microfluidic Paper-Based Sample Concentration Using Ion Concentration Polarization with Smartphone Detection

Xue Li, Yanan Niu, Yunyi Chen, Di Wu, Long Yi and Xianbo Qiu *

Institute of Microfluidic Chip Development in Biomedical Engineering,
State Key Laboratory of Organic-Inorganic Composites, College of Information Science and Technology,
Beijing University of Chemical Technology, Beijing 100029, China; 2015210307@grad.buct.edu.cn (X.L.);
2015210306@grad.buct.edu.cn (Y.N.); 2015200729@mail.buct.edu.cn (Y.C.); wudi@mail.buct.edu.cn (D.W.);
yilong@mail.buct.edu.cn (L.Y.)
* Correspondence: xbqiu@mail.buct.edu.cn; Tel.: +86-10-6441-3467

Academic Editors: Xiangchun Xuan and Shizhi Qian
Received: 30 September 2016; Accepted: 1 November 2016; Published: 4 November 2016

Abstract: A simple method for microfluidic paper-based sample concentration using ion concentration polarization (ICP) with smartphone detection is developed. The concise and low-cost microfluidic paper-based ICP analytical device, which consists of a black backing layer, a nitrocellulose membrane, and two absorbent pads, is fabricated with the simple lamination method which is widely used for lateral flow strips. Sample concentration on the nitrocellulose membrane is monitored in real time by a smartphone whose camera is used to collect the fluorescence images from the ICP device. A custom image processing algorithm running on the smartphone is used to track the concentrated sample and obtain its fluorescence signal intensity for quantitative analysis. Two different methods for Nafion coating are evaluated and their performances are compared. The characteristics of the ICP analytical device especially with intentionally adjusted physical properties are fully evaluated to optimize its performance as well as to extend its potential applications. Experimental results show that significant concentration enhancement with fluorescence dye sample is obtained with the developed ICP device when a fast depletion of fluorescent dye is observed. The platform based on the simply laminated ICP device with smartphone detection is desired for point-of-care testing in settings with poor resources.

Keywords: ion concentration polarization (ICP); sample concentration; paper-based microfluidics; Nafion coating; smartphone; point-of-care test

1. Introduction

Ion concentration polarization (ICP) is an electrokinetic phenomenon caused by the transport of ions through ion-selective nanostructures [1]. As a technology for fast sample concentration with high flexibility, ICP has been used for water desalination, and separation and enrichment of charged bio-species with functionalized microchannels [2–4]. Because of ICP's effect, ion depletion occurs in the region of ion-selective nanostructures, which accordingly cause ion enrichment at the boundary of ion depletion. ICP can be adopted into an integrated analytical device for the detection of biomolecules by separating, and concentrating DNA or protein from the lysed cells [5].

As a simple, rapid, easy-to-use and low-cost diagnosis method, the lateral flow immunoassay plays an important role in screening or rapid testing [6,7]. The lateral flow immunoassay can be integrated into microfluidic systems to detect the presence of antigens and antibodies to various pathogens [8,9]. Once the sample is applied onto the sample pad of the lateral flow strip, it will be specifically captured by the immobilized protein on the test line area when it migrates along the strip

because of the capillary force. With the lateral flow on a nitrocellulose membrane, because of the capillary force, much simpler detection can be obtained compared to most other analytical methods [10]. Similar to the lateral flow strip test, microfluidic paper-based analytical devices (μPADs) rely on the capillary force to drive sample or reagent without active pumping [11,12]. With the characteristics of simplicity, versatility, low cost, ease of use, reagent storage, high throughput and disposability, μPADs have been regarded as ideal tools for point-of-care diagnostics in low-resource settings [13,14]. However, because of the natural limitation of the assays implemented on μPADs, their detection sensitivity still needs to be increased to improve both accuracy and specificity.

Recently, much effort has been made to increase the detection sensitivity of μPADs by adopting the ICP effect into paper-based microfluidic devices for sample concentration [15,16]. ICP normally occurs at the interface of microfluidic and ion-selective nanofluidic channels under an applied electric field [1], where a formed ion depletion region is able to repel the charged particles in the test sample continually toward a specific direction [17]. Various paper-based ICP devices are fabricated with different methods, for example wax printing, where wax is printed on paper with a wax printer and then heated to form paper-based channels where the applied sample is concentrated [18], and cutting, where each layer of the device including the channels is shaped in the desired dimensions and sizes with an electronic craft cutter or a computer-controlled blade [19]. In some cases, complicated lamination methods have to be adopted to fabricate the paper-based ICP devices [20], or paper-based ICP has to be performed with a trivial experimental setup [21], which is undesirable for point-of-care diagnosis whose essential features include simple and rapid detection, low cost and ease of operation.

Based on advanced embedded systems, smartphones provide a desired platform to implement point-of-care diagnosis with easy operation, cost-efficiency, convenience and portability [22,23]. With an integrated camera, various assays can be monitored in real time or at the end point by a smartphone when optical filters are incorporated if necessary [24,25]. The unique feature of auto-focus with a smartphone camera can significantly simplify the optical and mechanical design of the detection system. The standard function for camera control in the Java environment is beneficial to reduce the complexity of software development. Furthermore, the detection result can be conveniently transmitted by smartphone to other places, e.g., medical agencies for further analysis. As one of the potential solutions for point-of-care diagnostics, various smartphone-based microfluidic analytical devices are intensively being studied [26,27].

In this paper, we report a concise, simply fabricated, and easy-to-use microfluidic paper-based analytical device with an ICP effect for sample concentration. To obtain the ICP effect, two different methods are used to develop a Nafion-coated region on the sample channel, and their performances are evaluated and compared. To facilitate point-of-care diagnosis, the ICP process is monitored in real time by a smartphone camera and the collected fluorescent images are analyzed by a custom algorithm running on the smartphone for quantitative analysis. Paper-based ICP devices with intentionally adjusted physical properties are fabricated and evaluated to optimize their performance as well as to extend their application area. Experimental results with fluorescein isothiocyanate (FITC) show that significant concentration enhancement with the fluorescent dye sample on the developed microfluidic paper-based device is successfully achieved because of the ICP effect.

2. Materials and Methods

2.1. Design and Fabrication of Paper-Based ICP Device

The developed paper-based ICP device consists of a sample channel made from nitrocellulose membrane with a thickness of 0.14 mm where a region coated with cation-selective nanoporous Nafion is developed at one end, and two buffer pools made from paper-based absorbent pads, and three of them are laminated with one another and then fixed on a black backing layer (polyvinyl chloride (PVC)) with one sided tape (Figure 1A). In the reported literature [16], it has been demonstrated that nitrocellulose membrane is a desired substrate for electrokinetic operations, for example ICP. Because

nitrocellulose membrane is widely used in lateral flow immunoassay strips and μPADs, it will be much convenient for the ICP device made from nitrocellulose membrane to combine with those existed paper-based analytical devices to further improve their performance.

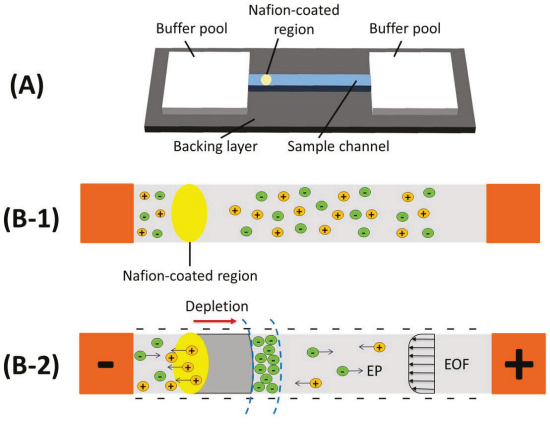

Figure 1. Design and operation of the paper-based ICP device. (**A**) Schematic of device with one sample channel, two buffer pools and one backing layer; (**B-1**) Schematic of non ICP state without an electrical field; (**B-2**) Schematic of ICP enrichment and depletion effects under applied voltage.

To operate the device, first enough DI water is added onto the two absorbent pads at both ends to establish two buffer pools. Once both absorbent pads are saturated with water, the middle nitrocellulose membrane will be prewetted by the DI water wicked from buffer pools because of the capillary force. And then, sample is added to the middle channel. As shown in Figure 1B-1, before a DC voltage is applied, there has no any ion enrichment. Nafion is an ion-selective material with negatively charged sulfonic groups [19]. Nafion containing nanopores on the nitrocellulose membrane substrate become ion-selective under the effects of an electrical field. In principle, the sulfonic acid groups in Nafion provide a net negative surface charge in the pores, which enables ion depletion by selectively transporting of cations through the Nafion-coated membrane during ICP [28,29]. Once ICP is induced because of DC electrical filed, cations are selectively gathered to form an ion enrichment zone around the boundary between the cathode and the Nafion-coated region (Figure 1B-2). Meanwhile, an ion depletion zone with electrical neutrality is being formed within the Nafion-coated region when anions are vacated. With the maintained DC electrical filed, the depletion zone propagates and drives anions toward the anode. Two major effects, the electrophoretic migration (EP) toward the anode and the electroosmotic flow (EOF) toward the cathode, both of which are determined by the distribution of both the applied electrical filed and the ionic concentration along the channel, dominate the net movement of anions in the channel. With lower ionic concentrations, higher EOF transport rates will be introduced and vice versa [30]. At one end of the channel close to the depletion zone, EP is higher than EOF, which drives anions to escape from the depletion zone and migrate in the anodic direction along the channel. At the other end of the channel close to the downstream of the depletion zone, EOF always drives the analytes to approach the depletion zone in the cathodic direction. Finally, the sample with negatively charged ions is focused at the depletion boundary by the two balanced opposing driving forces due to ICP effect.

Nanoporous Nafion is the key functional part in the paper-based analytical device to successfully induce ICP effect. To obtain desired nanoporous Nafion, it is important to find out a proper fabrication method to develop a Nafion-coated region on the ICP device. Therefore, as shown in Figure 2, two different methods for Nafion coating, which respectively corresponds to two types of paper-based

ICP devices (type I and II), are evaluated and compared. The Nafion-coated nitrocellulose membrane was then fixed on a black backing layer with one side tape and then covered by two paper-based absorbent pads at two ends. The laminated ICP devices were covered in Petri dishes at room temperature before use.

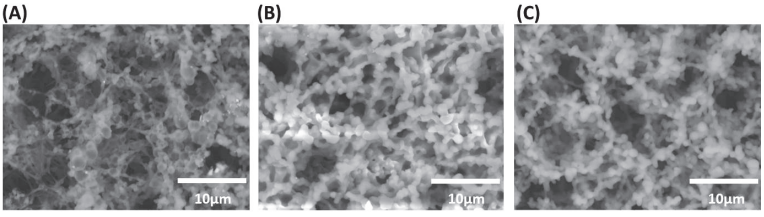

Figure 2. Scanning electron microscopy images of nitrocellulose membrane. (**A**) Without Nafion coating; (**B**) With Nafion coating (type I, without heating); (**C**) With Nafion coating (type II, with heating).

The nitrocellulose membrane (HF-180, GE Whatman) with mean pore diameters of 6–8 μm was cut by a manual craft cutter to form a straight channel. Nafion perfluorinated resin solution (20 wt % in lower aliphatic alcohols and water, Sigma-Aldrich) was pipetted into each device with a size of 0.5 μL. After that, two different methods were respectively adopted to treat the nitrocellulose membrane. For ICP device of type I (Figure 2B), the nitrocellulose membrane was directly immersed in deionized (DI) water for 30 min to hydrate the Nafion, and then it was allowed to dry at room temperature. For ICP device of type II (Figure 2C), the nitrocellulose membrane was heated in an oven at a temperature of 150 °C for 30 s in order to cure the Nafion structure. The nitrocellulose membrane was then immersed in 10^{-2} M tris buffer for 1 min in order to rinse the Nafion for a higher efficiency of concentration, and finally it was left to dry at room temperature. As shown in Figure 2, the porous structure of the pristine nitrocellulose membrane is different from that of ICP device of type I or II. The patterns of Nafion-coated region respectively with ICP devices of type I and II are different from each other.

2.2. Experimental Setup with Smartphone Detection

As shown in Figure 3, a portable device was developed to perform experiments on a paper-based ICP device with smartphone detection. Two platinum electrodes with a diameter of 1 mm were used to apply a DC voltage to the paper-based ICP device from two buffer pools of the channel. Two LEDs with a specific wavelength were used to shine the sample through their own optical filters from the top, and the fluorescent signal of the concentrated sample was detected by collecting fluorescence images from the ICP device with a preset interval by a smartphone camera through another optical filter. All the components were assembled in an enclosed instrument box (100 mm × 90 mm × 100 mm) for desired optical detection except a smartphone fixed from the outside to monitor the ICP process. Once a DC voltage is applied to the ICP device, the process of sample concentration with ICP effect can be monitored in real-time through the control to the camera with custom application software running on the smartphone. The working current of LEDs can be adjusted with the application software to prevent signal saturation. At the current stage, a standard power supply was used to provide a DC voltage from outside of the instrument. In the future, alternative strategies, e.g., a small circuit module for voltage amplification, or a couple of batteries in series, can be adopted to replace the standard DC power supply in order to build a fully portable, low-cost and easy-to-use microfluidic ICP system for point-of-care diagnosis.

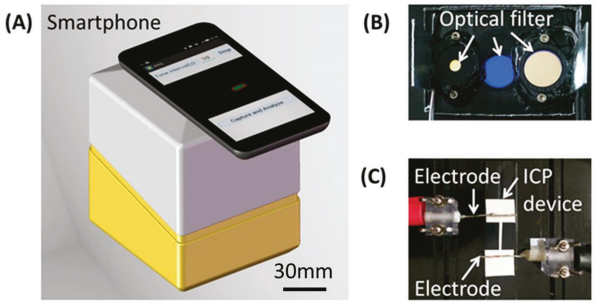

Figure 3. Experimental setup with smartphone detection. (**A**) Instrument box with a smartphone; (**B**) Optical module; (**C**) ICP device with applied electrodes.

2.3. Image Processing for Quantitative Analysis

A custom image processing algorithm was developed to track the concentrated sample in fluorescent images and then obtain the fluorescent signal intensity for quantitative analysis. As shown in Figure 4A,B, the original fluorescent image is first converted into a gray image.

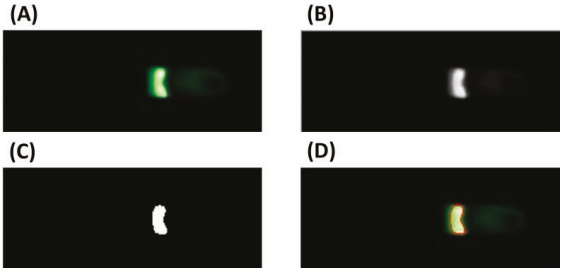

Figure 4. Image processing. (**A**) Original fluorescence image; (**B**) Converted gray image; (**C**) Converted binary image; (**D**) Marked fluorescence image.

The maximal gray value within the entire image is represented by max_*fluo*. In principle, the result of the sample concentration is relative to the gray value of the region with the concentrated sample which is normally larger than that of the background. A threshold value, *thres*, is defined to differentiate the region with the concentrated sample from the background,

$$thres = \max\_fluo - \frac{\max\_fluo}{a} \tag{1}$$

where $a \in [1.65,\ 1.95]$ is an empirical coefficient. Then, the gray value of each pixel in the gray image is redefined as follows, which further converts the original image into a binary image,

$$fluo\_value(x,y) = \begin{cases} 255, & fluo\_value\,(x,y) \geq thres \\ 0, & fluo\_value\,(x,y) < thres \end{cases} \tag{2}$$

The converted binary image is shown in Figure 4C. The boundary for the region with the concentrated sample is determined by analyzing the binary image with Canny operator [31]. As shown in Figure 4D, the boundary of the region with the concentrated sample is marked with a red circle in the fluorescence image. The average gray value of all pixels within the determined region is calculated to represent the fluorescent signal intensity of the concentrated sample.

3. Results and Discussion

3.1. ICP Devices with Different Fabrication Methods

As previously described, two types of paper-based ICP devices (type I and II), respectively, with two different methods for Nafion coating, were fabricated. For each ICP device, the middle channel made from Nafion-coated nitrocellulose membrane was cut into the dimensions of 2 mm × 16 mm. The two buffer pools were made from paper-based absorbent pads with the dimensions of 15 mm × 15 mm. The bottom layer was made from a black backing sheet with the dimensions of 20 mm × 50 mm. The width of the Nafion-coated region was around 2 mm, and the length was 2 mm. The distance from the Nafion-coated region to the closer buffer pool was around 2 mm. The real device is shown as an inset in Figure 5A or Figure 5B.

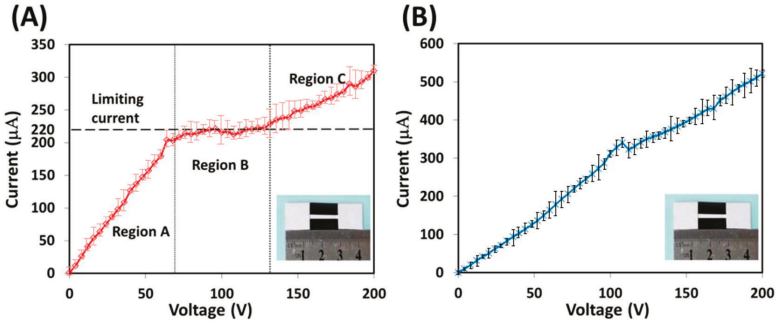

Figure 5. Current-voltage curves with two different types of ICP devices. (**A**) Type I; (**B**) Type II. The inset in A or B features a real ICP device.

To discover the ICP efficiency of the developed device, before experimenting with the fluorescent dye sample, its electrokinetic characteristics were evaluated. First, each 300 μL of 10^{-2} M tris buffer was added to one of the two absorbent pads to establish two buffer pools. Then, a DC voltage was applied to the ICP device through two platinum electrodes which respectively contacted with two prewetted absorbent pads. The current-voltage (I-V) response for the two types of ICP devices was measured as the applied voltage was increased from 0 to 200 V in 50 discrete steps.

As shown in Figure 5, there is a significant difference between the two I-V response curves, respectively, with ICP devices type I and II. For the type I ICP device, the I-V curve (Figure 5A) consists of three distinct regions (A, B and C). Region "A" is known as the ohmic region where the current and voltage exhibit a linear relationship, which means that the conductance of the device remains constant and there is no ICP effect. Region "B" is known as the limiting region where the current remains almost constant around a limiting value when the voltage increases, which means that an ion-depletion effect occurs and a significant increase in the device resistance is caused because of the lack of ionic charges. Region "C" is known as the overlimiting region where the current increases nonlinearly with an increasing voltage, which means that the depletion zone starts to expand and the previously balanced ICP effect is broken. Similar to experimental results from other literature [18,20], the I-V response curve in Figure 5A confirms that ICP is successfully induced in the developed type I device. However, as shown in Figure 5B, for the type II ICP device, there are no three clear regions with the I-V response curve as exhibited in the type I ICP device. The current always increases with an increasing voltage within the entire curve, except for a short maintaining stage, which indicates that there is an insignificant or almost no ICP effect with the type II device. The above experiment was repeated at least three times, and similar results were obtained.

In the next step, 10 μM of fluorescein isothiocyanate (FITC) was used as the fluorescent dye sample to evaluate the efficiency of the sample concentration with both types of ICP devices. To successfully

induce the ICP effect with the developed device, 140 V was chosen as the driven voltage based on the above I-V curve. The process of sample concentration with the ICP effect was monitored in real time by a smartphone camera. Figure 6A,B present parts of the fluorescent images of the concentrated sample at different times from 0 to 100 s, respectively, for ICP devices type I and II. The region with the concentrated sample, which is marked with a red enclosed curve, is isolated and tracked by the developed custom image processing algorithm. The "+" and "−" signs in Figure 6A,B represent, respectively, anode and cathode electrodes. Figure 6C presents the variation of both the fluorescent signal intensity of the concentrated sample and the corresponding concentration over different times for both types of devices. The fluorescent signal intensity of the concentrated sample was obtained through quantitative analysis on the fluorescent images. A quadratic polynomial function was used to figure out the concentration of the concentrated sample from its fluorescent signal intensity.

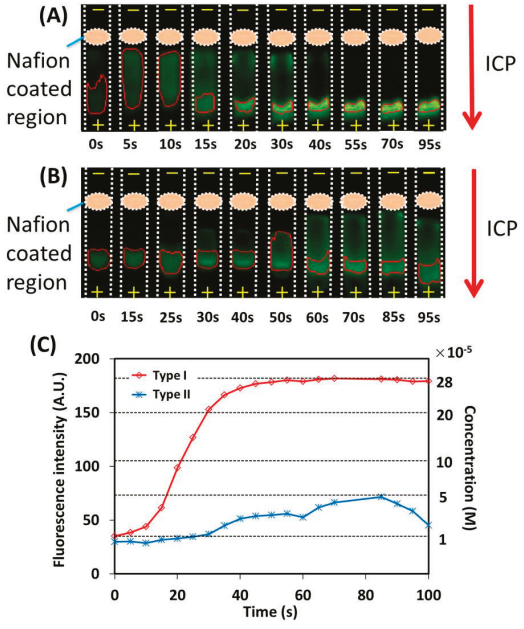

Figure 6. Experimental result with two types of ICP devices. (**A**) Fluorescence images captured at different times with ICP device type I; (**B**) Fluorescence images captured at different times with ICP device type II; (**C**) Variation of fluorescent signal intensity and corresponding sample concentration over time with two types of ICP devices.

As shown in Figure 6, for ICP device type I, the fluorescent signal intensity of the concentrated sample keeps increasing once the ICP effect has been induced, and finally a 28-fold maximal improvement in the sample concentration is obtained at 70 s. On the other hand, for ICP device type II, an insignificant sample concentration is observed and only a five-fold maximal improvement in the sample concentration is obtained. In terms of the increased fold in the sample concentration, it can be found that the efficiency of ICP device type I is significantly higher than that of type II. From the uniformity and porosity of the ion-selective nanostructures of the Nafion-coated region (scanning electron microscopy images in Figure 2), it can be inferred that improper heating to the Nafion-coated nitrocellulose membrane (ICP device type II) will most probably deteriorate the Nafion coating and hence decrease its ICP performance. The above experiment was repeated at least three

times, and similar results were obtained. In principle, even a higher-fold maximal improvement in sample concentration can be obtained when the dimensions and sizes of the ICP devices are modified.

3.2. ICP Device with Adjusted Dimensions

To further improve the efficiency of the sample concentration with the ICP effect, an effort has been made by adjusting the dimensions of the ICP device. Specifically, a paper-based ICP device (named type a), which consists of two buffer pools and a non-uniform sample channel including wide, transitional and narrow parts, was fabricated to evaluate the performance of the device with adjusted dimensions. In detail, for each ICP device, the sample channel consists of one wide part (width: 3 mm, length: 5 mm), one transitional part (width: 3 to 1.5 mm, length: 4 mm) and one narrow part (width: 1.5 mm, length: 7 mm). The rest of the dimensions of the ICP device are similar to those of the previously described device. The schematic of the ICP device is shown as an inset in Figure 7C. To induce an efficient ICP effect, the Nafion coating method without heating was adopted here. For comparison, a normal ICP device (named type b) with the dimensions of 3 mm$\times$ 16 mm was fabricated, the width of which was larger than that of the ICP device (type I) fabricated in Section 3.1. Further, 10 μM of fluorescein isothiocyanate (FITC) was used as the fluorescent dye sample and 140 V was applied to the ICP device to provide a DC electrical field. Figure 7A,B present parts of the fluorescent images of the concentrated sample at different times from 0 to 120 s, respectively, for the evaluated ICP device (type a) and the normal one (type b). The "+" and "−" signs in Figure 7A,B represent, respectively, anode and cathode electrodes. The region with the concentrated sample is isolated and tracked by the developed custom image processing algorithm for quantitative analysis. Figure 7C presents the variation of both the fluorescent signal intensity of the concentrated sample and the corresponding concentration over different times.

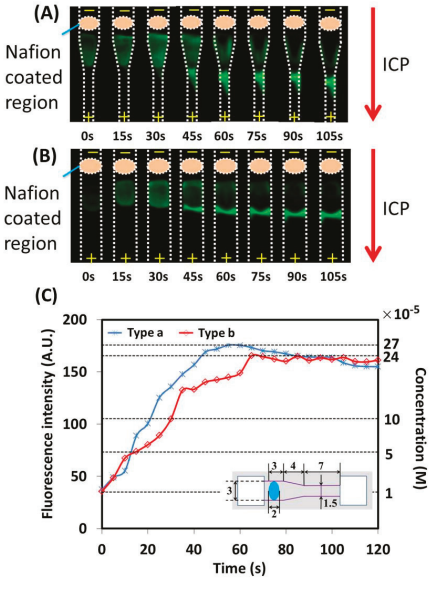

Figure 7. Experimental results with two types of ICP devices. (**A**) Fluorescence images captured at different times with ICP device type a; (**B**) Fluorescence images captured at different times with ICP device type b; (**C**) Variation of fluorescent signal intensity and corresponding sample concentration over time with two types of ICP devices. The insert in C features a schematic of ICP device type a.

As shown in Figure 7, for the ICP device (type a) with the adjusted dimensions, the fluorescent signal intensity of the concentrated sample increases once the ICP effect has been established, and finally a 27-fold maximal improvement in the sample concentration is obtained at 60 s. On the other hand, for the normal ICP device (type b), a 24-fold maximal improvement in the sample concentration is obtained at 65 s. For ICP device type a, the maximal fold of improvement in the sample concentration occurs when almost all of the sample reaches the narrow end of the transitional area of the non-uniform channel, and after that the increased fold slightly decreases. In terms of the increased fold in the sample concentration with the required time, the ICP device with adjusted dimensions shows higher efficiency than the normal device. The main reason for the improved efficiency is that the sample is physically concentrated when it moves from the wide channel to the narrow one. Because of different dimensions, the increased folds in the sample concentration with the normal ICP device, respectively, in Sections 3.1 and 3.2 are different from each other.

3.3. ICP Device with Two Jointed Nitrocellulose Membrane Parts

It is desired to extend the application area of the ICP device by incorporating the ICP effect into the existing analytical devices to obtain fast and efficient separation and concentration of different biomolecules. Therefore, to explore the possibility of combining the ICP device with a traditional lateral flow strip or other μPADs, an ICP device (named type 1) whose channel was made from two jointed nitrocellulose membrane parts was fabricated and evaluated. Basically, the dimensions of the developed ICP device are similar to those of the previously described device except that there is a small gap (~0.2 mm) between the two jointed nitrocellulose membrane parts. The dimensions of the sample channel are 3 × 16 mm. The real device is shown as an inset in Figure 8. For comparison, a normal ICP device (named type 2) was fabricated. Figure 8 presents the variation of both the fluorescent signal intensity of the concentrated sample and the corresponding concentration over different times.

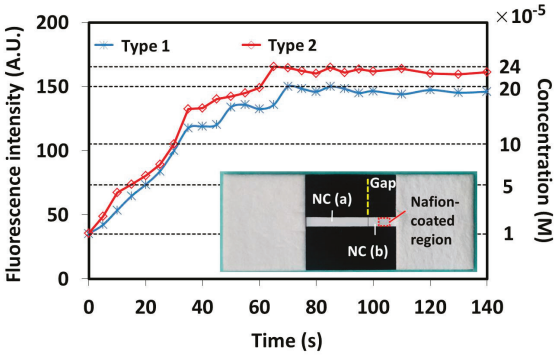

Figure 8. Variation of fluorescent signal intensity and corresponding sample concentration over time with two types of ICP devices. The inset features a real ICP device type 1.

As shown in Figure 8, for the ICP device (type 1) with two jointed nitrocellulose membrane parts, finally a 20-fold maximal improvement in the sample concentration is obtained at 70 s. It was found that there was a solution leakage around the gap between the two parts of the paper strips. The solution leakage can work as a bridge to establish the integral solution layer for the ICP effect. Alternatively, for the normal ICP device (type 2), a 24-fold maximal improvement in the sample concentration is obtained at 65 s. In terms of the increased fold in the sample concentration with the required time, the efficiency of the ICP device with two jointed nitrocellulose membrane parts shows slightly lower efficiency than the normal one. However, although it is not as good as the normal one, the performance with the jointed ICP device is within the acceptable range. Therefore, it is demonstrated that the ICP

effect will not be significantly deteriorated when the sample channel is made from two separated nitrocellulose membranes parts with a small gap in between. In the future, efforts can be made to develop an integrated analytical device based on the ICP effect.

4. Conclusions

This paper reports a microfluidic paper-based ICP device for sample concentration with smartphone detection. The microfluidic paper-based ICP device can be easily fabricated with a simple lamination method. To obtain the ICP effect, the nitrocellulose membrane, which is treated with a Nafion perfluorinated resin solution at one end, is used as the sample channel. Two buffer pools, which are made from paper-based absorbent pads, are used to prewet the sample channel through the capillary force to ensure that a proper electrical field will be established when a DC voltage is applied to the ICP device.

Smartphone detection is adopted for the real-time monitoring of the sample concentration with the ICP effect, which is beneficial to the potential application in point-of-care diagnosis. The fluorescent images of the concentrated sample are continuously collected at different times by a smartphone camera, and then processed by a custom algorithm for quantitative analysis. Beside the adjustment to the working current of LEDs, the smartphone also provides a friendly operational interface through custom application software developed with Java.

To successfully induce ICP, two different Nafion coating methods reported by the literature are evaluated and compared. With the experimental results, it has been demonstrated that improper heating to the Nafion-coated nitrocellulose membrane will deteriorate the Nafion coating and hence significantly decrease the ICP efficiency. To further improve the efficiency of the sample concentration due to the ICP effect, one type of ICP device with adjusted dimensions is fabricated and evaluated. It has been demonstrated that the efficiency of the sample concentration can be improved when the sample channel consists of multiple parts with different widths. To justify the feasibility of the integration of the ICP effect into the existing μPADs or traditional lateral flow strips, a combined ICP device consisting of two jointed nitrocellulose membrane parts with a small gap in between is fabricated and evaluated. Compared to the normal ICP device, a slightly lower efficiency of the sample concentration is obtained when the sample channel is made from two joint nitrocellulose membrane parts. In summary, a concise, simple and easy-to-operate ICP device with smartphone detection is developed for sample concentration, which is beneficial to improve the sensitivity of the paper-based analytical device at point-of-care diagnosis. With a small-size circuit for voltage amplification or a couple of batteries in a series to replace the bulky power supply, a portable microfluidic ICP-based system with smartphone detection can be developed for sample separation, concentration, or even diagnosis in settings with poor resources.

Acknowledgments: The work was supported by the National Natural Science Foundation of China (No. 81371711) and the Fundamental Research Funds for the Central Universities (ZZ1329, YS1404). Gong (Max M. Gong, a postdoctoral fellow, Microtechnology, Medicine, and Biology Lab, University of Wisconsin-Madison) provided insights into the device design, fabrication and experimentation.

Author Contributions: In this work, Long Yi and Xianbo Qiu conceived and designed the experiments; Di Wu constructed the smartphone detection system with guidance from Xianbo Qiu; Xue Li, Yanan Niu and Yunyi Chen performed the experiments and analyzed the data; Xue Li, Yanan Niu, and Yunyi Chen drafted the manuscript; Di Wu and Xianbo Qiu edited the manuscript.

Conflicts of Interest: The authors declare no conflict of interest.

References

1. Höltzel, A.; Tallarek, U. Ionic conductance of nanopores in microscale analysis systems: Where microfluidics meets nanofluidics. *J. Sep. Sci.* **2007**, *30*, 1398–1419. [CrossRef] [PubMed]
2. Kim, S.J.; Ko, S.H.; Kang, K.H.; Han, J. Direct seawater desalination by ion concentration polarization. *Nat. Nanotechnol.* **2010**, *5*, 297–301. [CrossRef] [PubMed]

3. Macdonald, B.D.; Gong, M.M.; Zhang, P.; Sinton, D. Out-of-plane ion concentration polarization for scalable water desalination. *Lab Chip* **2013**, *14*, 681–685. [CrossRef] [PubMed]
4. Scarff, B.; Escobedo, C.; Sinton, D. Radial sample preconcentration. *Lab Chip* **2011**, *11*, 1102–1109. [CrossRef] [PubMed]
5. Jeon, H.; Lim, G. Development of continuous cell lysis and separation device using repulsive force generated by ion concentration polarization. In Proceedings of the 18th International Conference on Miniaturized Systems for Chemistry and Life Sciences, San Antonio, TX, USA, 26–30 October 2014; pp. 2459–2461.
6. Corstjens, P.L.A.M.; Chen, Z.; Michel, Z.; Bau, H.H.; Abrams, W.R.; Malamud, D.; Sam, N.R.; Tanke, H.J. Rapid Assay Format for Multiplex Detection of Humoral Immune Responses to Infectious Disease Pathogens (HIV, HCV, and TB). *Ann. N. Y. Acad. Sci.* **2007**, *1098*, 437–445. [CrossRef] [PubMed]
7. Gu, Y.; Yang, Y.; Zhang, J.; Ge, S.; Tang, Z.; Qiu, X. Point-of-care test for C-reactive protein by a fluorescence-based lateral flow immunoassay. *Instrum. Sci. Technol.* **2014**, *42*, 635–645. [CrossRef]
8. Qiu, X.; Liu, C.; Mauk, M.G.; Hart, R.W.; Chen, D.; Qiu, J.; Kientz, T.; Fiene, J.; Bau, H.H. A portable analyzer for pouch-actuated, immunoassay cassettes. *Sens. Actuators B Chem.* **2011**, *160*, 1529–1535. [CrossRef] [PubMed]
9. Qiu, X.; Thompson, J.A.; Chen, Z.; Liu, C.; Chen, D.; Ramprasad, S.; Mauk, M.G.; Ongagna, S.; Barber, C.; Abrams, W.R.; et al. Finger-actuated, self-contained immunoassay cassettes. *Biomed. Microdevices* **2009**, *11*, 1175–1186. [CrossRef] [PubMed]
10. Liu, C.; Qiu, X.; Ongagna, S.; Chen, D.; Chen, Z.; Abrams, W.R.; Malamud, D.; Corstjens, P.L.A.M.; Bau, H.H. A timer-actuated immunoassay cassette for detecting molecular markers in oral fluids. *Lab Chip* **2009**, *9*, 768–776. [CrossRef] [PubMed]
11. López-Marzo, A.M.; Merkoçi, A. Paper-based sensors and assays: A success of the engineering design and the convergence of knowledge areas. *Lab Chip* **2016**, *16*, 3150–3176. [CrossRef] [PubMed]
12. Lankelma, J.; Nie, Z.; Carrilho, E.; Whitesides, G.M. Paper-Based Analytical Device for Electrochemical Flow-Injection Analysis of Glucose in Urine. *Anal. Chem.* **2012**, *84*, 4147–4152. [CrossRef] [PubMed]
13. Gerbers, R.; Foellscher, W.; Chen, H.; Anagnostopoulos, C.; Faghri, M. A new paper-based platform technology for point-of-care diagnostics. *Lab Chip* **2014**, *14*, 4042–4049. [CrossRef] [PubMed]
14. Hu, J.; Wang, S.; Wang, L.; Li, F.; Pingguan-Murphy, B.; Lu, T.; Xu, F. Advances in paper-based point-of-care diagnostics. *Biosens. Bioelectron.* **2014**, *54*, 585–597. [CrossRef] [PubMed]
15. Li, M.; Anand, R.K. Recent advancements in ion concentration polarization. *Analyst* **2016**, *141*, 3496–3510. [CrossRef] [PubMed]
16. Gong, M.M.; Nosrati, R.; Gabriel, M.C.S.; Zini, A.; Sinton, D. Direct DNA Analysis with Paper-Based Ion Concentration Polarization. *J. Am. Chem. Soc.* **2015**, *137*, 13913–13919. [CrossRef] [PubMed]
17. Pu, Q.; Yun, J.; Temkin, H.; Liu, S. Ion-Enrichment and Ion-Depletion Effect of Nanochannel Structures. *Nano Lett.* **2004**, *4*, 1099–1103. [CrossRef]
18. Hung, L.; Wang, H.; Yang, R. A portable sample concentrator on paper-based microfluidic devices. *Microfluid Nanofluid* **2016**, *20*. [CrossRef]
19. Yang, R.; Pu, H.; Wang, H. Ion concentration polarization on paper-based microfluidic devices and its application to preconcentrate dilute sample solutions. *Biomicrofluidics* **2015**, *9*, 1–11. [CrossRef] [PubMed]
20. Phan, D.T.; Shaegh, S.A.M.; Yang, C.; Nguyen, N. Sample concentration in a microfluidic paper-based analytical device using ion concentration polarization. *Sens. Actuators B* **2016**, *222*, 735–740. [CrossRef]
21. Yeh, S.; Chou, K.; Yang, R. Sample pre-concentration with high enrichment factors at a fixed location in paper-based microfluidic devices. *Lab Chip* **2016**, *16*, 925–931. [CrossRef] [PubMed]
22. Yang, K.; Peretz-Soroka, H.; Liu, Y.; Lin, F. Novel developments in mobile sensing based on the integration of microfluidic devices and smartphones. *Lab Chip* **2016**, *16*, 943–958. [CrossRef] [PubMed]
23. Zhang, D.; Liu, Q. Biosensors and bioelectronics on smartphone for portable biochemical detection. *Biosens. Bioelectron.* **2016**, *75*, 273–284. [CrossRef] [PubMed]
24. Zhang, C.; Cheng, G.; Edwards, P.; Zhou, M.; Zheng, S.; Liu, Z. G-Fresnel smartphone spectrometer. *Lab Chip* **2016**, *16*, 246–250. [CrossRef] [PubMed]
25. Zhu, H.; Yaglidere, O.; Su, T.; Tseng, D.; Ozcan, A. Cost-effective and compact wide-field fluorescent imaging on a cell-phone. *Lab Chip* **2011**, *11*, 315–322. [CrossRef] [PubMed]
26. Mancuso, M.; Cesarman, E.; Erickson, D. Detection of Kaposi's sarcoma associated herpesvirus nucleic acids using a smartphone accessory. *Lab Chip* **2014**, *14*, 3809–3816. [CrossRef] [PubMed]

27. Lu, Y.; Shi, W.; Qin, J.; Lin, B. Low cost, portable detection of gold nanoparticle-labeled microfluidic immunoassay with camera cell phone. *Electrophoresis* **2009**, *30*, 579–582. [CrossRef] [PubMed]
28. Gong, M.M.; Zhang, P.; Macdonald, B.D.; Sinton, D. Nanoporous Membranes Enable Concentration and Transport in Fully Wet Paper-Based Assays. *Anal. Chem.* **2014**, *86*, 8090–8097. [CrossRef] [PubMed]
29. Mauritz, K.A.; Moore, R.B. State of Understanding of Nafion. *Chem. Rev.* **2004**, *104*, 4535–4585. [CrossRef] [PubMed]
30. Thormann, W.; Zhang, C.; Caslavska, J.; Gebauer, P.; Mosher, R.A. Modeling of the impact of ionic strength on the electroosmotic flow in capillary electrophoresis with uniform and discontinuous buffer systems. *Anal. Chem.* **1998**, *70*, 549–562. [CrossRef] [PubMed]
31. Canny, J. A Computational Approach to Edge Detection. *IEEE Trans. Pattern Anal. Mach. Intell.* **1986**, *8*, 679–698. [CrossRef] [PubMed]

micromachines

MDPI

Article

A New Microfluidic Device for Classification of Microalgae Cells Based on Simultaneous Analysis of Chlorophyll Fluorescence, Side Light Scattering, Resistance Pulse Sensing

Junsheng Wang [1,2,*], Jinsong Zhao [1], Yanjuan Wang [1], Wei Wang [1], Yushu Gao [1], Runze Xu [1] and Wenshuang Zhao [1]

[1] College of Information and Science Technology, Dalian Maritime University, Dalian 116026, China; zhaojinsong9@gmail.com (J.Z.); wswl408@gmail.com (Y.W.); zwldmm@gmail.com (W.W.); ICMFLOC@dlmu.edu.cn (Y.G.); dlmuxwg@gmail.com (R.X.); zzlswl1@gmail.com (W.Z.)

[2] Collaborative Innovation Center for Vessel Pollution Monitoring and Control, Dalian Maritime University, Dalian 116026, China

* Correspondence: wangjsh@dlmu.edu.cn; Tel.: +86-411-8472-3190

Academic Editors: Xiangchun Xuan and Shizhi Qian
Received: 29 September 2016; Accepted: 28 October 2016; Published: 2 November 2016

Abstract: Fast on-site monitoring of foreign microalgae species carried by ship ballast water has drawn more and more attention. In this paper, we presented a new method and a compact device of classification of microalgae cells by simultaneous detection of three kinds of signals of single microalgae cells in a disposable microfluidic chip. The microfluidic classification device has advantages of fast detection, low cost, and portability. The species of a single microalgae cell can be identified by simultaneous detection of three signals of chlorophyll fluorescence (CF), side light scattering (SLS), and resistance pulse sensing (RPS) of the microalgae cell. These three signals represent the different characteristics of a microalgae cell. A compact device was designed to detect these three signals of a microalgae cell simultaneously. In order to demonstrate the performance of the developed system, the comparison experiments of the mixed samples of three different species of microalgae cells between the developed system and a commercial flow cytometer were conducted. The results show that three kinds of microalgae cells can be distinguished clearly by our developed system and the commercial flow cytometer and both results have good agreement.

Keywords: microalgae cells classification; ballast water; microfluidic chip

1. Introduction

Biological invasions brought by ship ballast water have caused serious effects to local ecological environments and human health [1–4]. Microalgae are the most common species exiting in ballast water and the main object for ship ballast water treatment and detection. Microalgae species identification is very important for ballast water treatment. Different species of microalgae cells may need different treatment methods or different doses of the same treatment method [5,6]. The survived microalgae in the treated ballast water also need to be further classified. Some harmful microalgae species need stricter treatments, while harmless ones do not need to be killed. Furthermore, according to the International Convention for the Control and Management of Ships' Ballast Water and Sediments, the detection of microalgae species for ballast water after being treated should not delay the normal navigation of ships. Therefore, fast on-site identification of microalgae species is necessary for ballast water detection.

The most traditional method for monitoring microalgae species is by using a microscope. Microalgae species are judged by the human eye and this method needs well-trained personnel, and is laborious and inaccurate (i.e., the identification results often depend on the operator's experience) [7,8]. Automatic monitoring methods mainly include optical imaging, absorption spectrum, and flow cytometry [9–15]. In the optical imaging method, microalgae cells are classified through image matching analysis and it is mainly applied for stationary objects, otherwise it will require high speed cameras. High-performance computer processing and real-time image processing algorithms are also key factors limiting the application of this method. In the absorption spectrum method, spectrophotometers are usually used to determine pigment compositions in microalgae cells, but they cannot count cells. Moreover, the commercial spectrophotometers are usually bulky and expensive. Flow cytometers can accurately identify microalgae species and count cells, but commercial flow cytometers involve complex operational procedures and are expensive and bulky. These factors limit their application in field and on-site detection.

The lab-on-a-chip (LOC) technique has many unique advantages for fast on-site detection, such as a small sample size, fast detection, low cost, and portability. It has been applied widely in biology, environmental science, chemistry, food, and medicine [16–25]. Some LOC-based microalgae identification methods and devices have been presented in the past few years [26–30]. The typical characteristics of these devices include using a microfluidic chip integrated with one or more optical fibers. There are two main reasons of integrating an optical fiber in a microfluidic chip. One reason is to improve excitation efficiency and emission light collection efficiency because the optical fiber can be put very close to the light source and cells. The other reason is to converge light to a small spot. For example, the method of forward scattering light (FSC), which is usually used to determine the cell's size, needs the light spot size close to the size of the cells by using optical fibers. However, this method of using optical fibers has also some disadvantages, such as high cost, complex fabrication, and poor replicability and stability. Compared with this method of optical fibers, the discrete optical layout can simplify the fabrication process of the microfluidic chips, reduce costs, improve replicability, and is more suitable for rapid on-site detection in ships.

Therefore, in this paper, we developed a new microalgae identification method and a compact system of using a disposable microfluidic chip and simultaneous detection of three kinds of signals of single microalgae cells: chlorophyll fluorescence (CF), side light scattering (SLS), and resistance pulse sensing (RPS). The microalgae cells flow one by one along the microchannel in a disposable microfluidic chip. When a single microalgae cell is passing through the detection spot, the CF, SLS, and RPS signals of the microalgae cell are detected simultaneously. Through the analysis of these three signals, the microalgae cell can be distinguished into the different species. The intensities of CF and SLS of single microalgae cells are detected with high sensitivity by the shift phase differential amplifier developed in this work. To demonstrate the performance of the presented method and the detection system, the comparison experiments of mixed samples of three different species of microalgae cells were conducted by using the developed system and a commercial flow cytometer.

2. Materials and Methods

2.1. Classification Principle of Microalgae Cells

The principle of classification of single microalgae cells in this paper is shown in Figure 1. When a single microalgae cell is passing through the detection spot, the microalgae cell is excited by the incident excitation light with ~480 nm wavelength along the negative y axis, three kinds of signals of CF, SLS, and RPS of the microalgae cell are detected simultaneously. The resulting CF of the microalgae cell with ~680 nm wavelength is detected from the positive z axis and SLS with ~ 480 nm wavelength is detected from the negative z axis. Meanwhile, the signal of RPS of the microalgae cell based on the Coulter principle is acquired from the difference of two sense arms of RPS+ and RPS−. These three signals of single microalgae cells correspond to three different characteristics of the

microalgae cell, respectively. CF is used to represent the activity of a microalgae cell; SLS can be used to characterize the intracellular contents and the size and surface roughness of the cell; and the size of a microalgae cell can be determined by RPS. These three characteristics of single microalgae cells are required to be detected in the international convention of ballast water treatment.

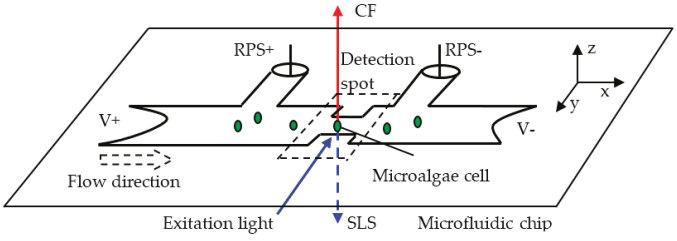

Figure 1. Illustration of the principle of classification of single microalgae cells based on the simultaneous detection of CF, SLS and RPS signals.

2.1.1. A Living Microalgae Cell Determination by CF Intensity

It is particularly important to judge if a microparticle is a living microalgae cell or not, for the microalgae cells species identification in ship's ballast water. Chlorophyll fluorescence (CF) comes from excess energy emission in the photosynthesis of plants and there exists a strong relationship between chlorophyll fluorescence and the photosynthesis electron transport chain. Chlorophyll fluorescence intensity has been proved to be positively correlated with chlorophyll contents in cells. More importantly, chlorophyll fluorescence can be used to evaluate the photosynthesis capacity and activity of plant cells [31–33]. Theoretically, the photosynthetic activity of microalgae cells can be represented by the net photosynthetic rate, which is proportional to the photosynthesis electron transport rate in Photosynthesis System II. This can be expressed by Equation (1):

$$P_n \propto k_I \times r_e \tag{1}$$

Here, P_n is the net photosynthetic rate, r_e is the photosynthesis electron transport rate in Photosynthesis System II, k_I is a coefficient related to the intercellular concentration of CO_2 and the CO_2 compensation point in the absence of mitochondria respiration. On the other hand, the intensity of chlorophyll fluorescence is proportional to the photosynthesis electron transport rate in Photosynthesis System II. Thus, we can obtain the following Equation (2):

$$I_{CF} \propto k_r \times r_e \propto \frac{k_r}{k_I} \times P_n \tag{2}$$

Here, I_{CF} is the intensity of chlorophyll fluorescence, k_r is a fixed scale factor related to energy conversion efficiency in the photosynthesis electron transport chain. k_I is usually a constant under the conditions of a given excitation light, temperature, and CO_2 concentration. Therefore, in this paper, the intensity of chlorophyll fluorescence is used to represent the activity of single microalgae cells and then determine whether a microparticle in ballast water is a living microalgae cell or not.

2.1.2. Contents Characteristics in a Microalgae Cell by SLS Intensity

When light is irradiated onto an object, light side scattering occurs, which is related to the intracellular contents, size, and surface roughness, and has a wide range of applications in biological, chemical, physical, optical, and other fields [34–38]. According to Mie scattering theory, when a cell

is irradiated by a beam of light with light intensity I_0 and wavelength λ, the light intensity I_θ in the direction of scattering angle θ can be expressed by the following Equation (3):

$$I(\theta) = I_0 \frac{\lambda^2}{8\pi^2 r^2} (i_1 + i_2) \tag{3}$$

Here, r is the distance between the particle or cell and detection spot, (i_1 + i_2) is an intensity function shown, as in Equation (4):

$$i_1 + i_2 = f\left(\frac{\pi d}{\lambda}, m, \theta\right) \tag{4}$$

This intensity function (i_1 + i_2) is related to the parameters including excitation wavelengh λ, scattering angel θ, the particle diameter d, and relative refractive index m. In this study, λ and θ are fixed and while the relative refractive index m depends on the intracellular contents and surface roughness, which cannot be expressed accurately by a mathematical function, the light intensity I_θ can only be determined by experiments.

2.1.3. Size Representation of a Microalgae Cell by RPS

As shown in Figure 1, when a microalgae cell enters the detection spot, the electrical resistance R of the area around the detection spot will change and according to Coulter principle [39,40], the change of electrical resistance ΔR is related to the parameters including the resistance of the buffer solution, the size of the microalgae cell d, the width D, and length L of the detection spot. When the structure of the microfluidic chip and the buffer solution are fixed, the value of ΔR is proportional to the size of the microalgae cell:

$$\Delta R \propto d \tag{5}$$

The change of ΔR will lead to the change of the voltage of the upstream $V_{\mathrm{RPS+}}$ and downstream $V_{\mathrm{RPS-}}$ of the detection spot, which can be expressed by the following Equations (6) and (7):

$$\Delta V_{\mathrm{RPS+}} = +\frac{R_1 \Delta R}{R_s^2 + R_s \Delta R} (V_- - V_+) \tag{6}$$

$$\Delta V_{\mathrm{RPS-}} = -\frac{R_3 \Delta R}{R_s^2 + R_s \Delta R} (V_- - V_+) \tag{7}$$

Here, $R_s = R_1 + R_2 + R_3$, where R_1, R_2, and R_3 are the upstream, detection spot, and downstream resistances in the microchannel, respectively.

Thus, we can obtain Equation (8) from Equations (6) and (7):

$$\Delta V_{\mathrm{RPS}} = \Delta V_{\mathrm{RPS+}} - \Delta V_{\mathrm{RPS+}} = \frac{(R_1 + R_3)\Delta R}{R_s^2 + R_s \Delta R} (V_- - V_+) \tag{8}$$

From Equation (8), it can be seen that ΔV_{RPS} is proportional to ΔR which, in turn, is proportional to the size of a microalgae cell d. Thus, the size of the microalgae cell can be determined by measuring the voltage difference between $V_{\mathrm{RPS+}}$ and $V_{\mathrm{RPS-}}$.

If two microalgae cells belong to the same category of microalgae, they will have similar chlorophyll and cell contents, as well as similar surface roughness and sizes. In this study, the species of microalgae cells will be identified by these characteristics detected by the self-developed compact system in our lab.

2.2. Simultaneous Detection System for Signals of CF, SLS, and RPS

As mentioned before, a microalgae cell can be classified by simultaneous detection of three different signals of CF, SLS, and RPS of the microalgae cell. The schematic diagram of the

detection system is shown in Figure 2a. The detection system is mainly comprised of a microfluidic chip, an excitation light source, photodetectors, signal amplifiers, data acquisition and processing, a microcontroller, and a data interface. All of these parts are integrated in a compact mechanical structure. The photos of the detection system are shown in Figure 2b. A microfluidic chip provides a sample platform for microalgae cells and the microalgae cells will flow along the designed microchannels in the microfluidic chip. An LED (LZ1-10B200, LED Engin, Inc., San Jose, CA, USA) was chosen as the excitation light source and the CF and SLS of the microalgae cell are generated simultaneously under the excitation of LED light when a microalgae cell is passing through the detection spot. The CF and SLS of the microalgae cell are detected by two photodiodes (S8745, Hamamatsu, Bridgewater, NJ, USA) along the positive z axis and the negative z axis, respectively. According to the excitation and emission spectra of CF of microalgae cells, an emission filter (ET680, Chroma, Bellows Falls, VT, USA) is placed between the microfluidic chip and the photodiode at the positive z axis direction. In order to block other stray light, an emission filter (ET470, Chroma, Bellows Falls, VT, USA) is mounted between the microfluidic chip and the photodiode at the negative z axis direction. A shift phase differential amplifier was designed to detect the pulse signals of CF and SLS from the photodiodes. Meanwhile, two microchannels are designed as RPS arms at both ends of the detection spot in the microfluidic chip. Through these two sensing arms, the RPS signal of the microalgae cell is processed further by the differential amplifier. An Acorn RISC Machine (ARM) development board with Linux OS (OK6410, Forlinx Embedded Technology, Inc., Baoding, Hebei, China) is used for data acquisition and processing. The RS232 and USB interfaces between ARM board and PC is set up for data communication. Labview software (National Instruments, Austin, TX, USA) on the PC is used for data saving and display.

2.3. Microfluidic Chip Design and Microfabrication

The structural diagram of the designed microfluidic chip is shown in Figure 3. This microfluidic chip has six reservoirs, including one sample reservoir, one waste reservoir, two sheath reservoirs, and two RPS reservoirs. The microalgae cell samples are put into the sample reservoir and phosphate buffer saline (PBS) buffer is placed into two sheath reservoirs for hydrodynamic focusing. The two laminar flow streams from the two sides will force the microalgae cells sample to move in a single line, and pass through the detection spot one by one along the main microchannel center line. The detection spot is at the sense gate where the signals of CF, SLS, and RPS of the microalgae cells are detected simultaneously. The width and length of the main microchannel from the sample reservoir to the waste reservoir junction is 200 μm and 3 cm, respectively. The width of the sheath microchannel and RPS sensing arms are both 100 μm, and the width of the sensing gate is 30 μm. All of the microchannels are 30 μm high and all reservoirs have a diameter of 4 mm and a depth of 2 mm.

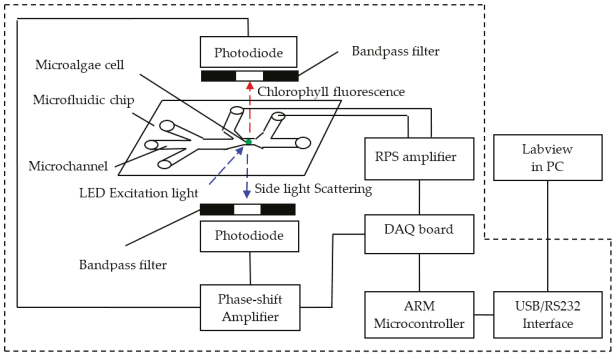

(**a**)

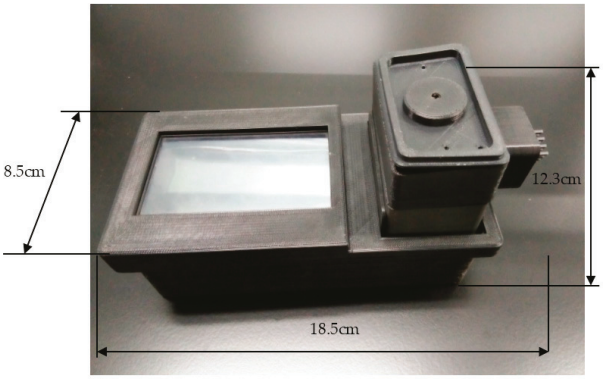

(**b**)

Figure 2. The schematic diagram and photos of the detection system of CF, SLS, and RPS signals of single microalgae cells: (**a**) the schematic diagram of the detection system; and (**b**) a photo of the detection system.

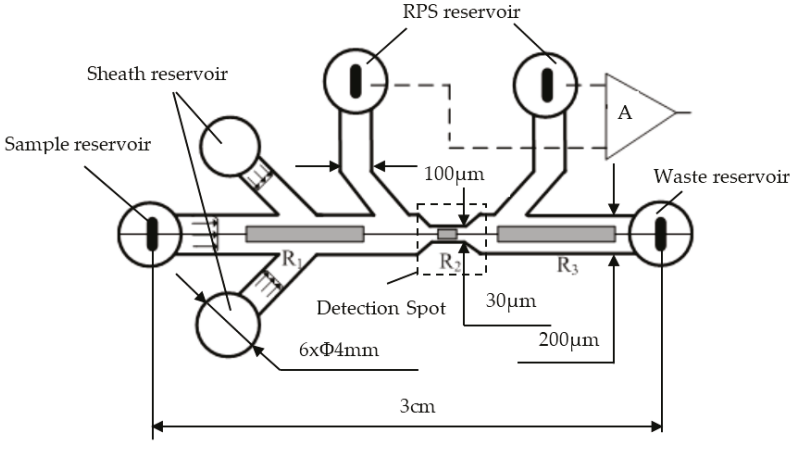

Figure 3. The diagram of the structure and dimensions of the microfluidic chip.

The microfluidic chip was fabricated by bonding a polydimethylsiloxane (PDMS) plate with a glass slide (24 mm × 50 mm × 0.15 mm, Citotest Labware Manufacturing Co., Ltd., Haimen, China) by the following standard soft-lithography protocol [41]: A layer of SU-8 photoresist (MicroChem Co., Newton, MA, USA) was spread on a bare silicon wafer (Lijing Co., Ltd., Quzhou, China) by a spin coater (G3P-8, Cookson Electronics Equipment, Indianapolis, IN, USA). Then a photomask containing the designed microchannel pattern was mounted on the silicon wafer and excited with an OAI 150 illuminator. The SU8 master was attained after post-baking and developing processes. Liquid PDMS and curing agent were mixed, degassed, and poured on the master, and then heated at 75 °C for 5 h in a vacuum oven (Isotempmodel 280A, Fisher Scientific, Pittsburgh, PA, USA) under normal pressure. Finally, the PDMS duplicate was taken from the master. Wells were formed by punching holes on the PDMS layer. The PDMS layer with the microchannel pattern was bound onto a glass slide after being treated for 60 s in a plasma cleaner (PDC-30G, Harrick Plasma, Ithaca, NY, USA).

2.4. Sample Preparation

2.4.1. Culture of Microalgae Cells

The microalgae species (*Chlorella vulgaris*, *Isochrysis galbana*, *Dunaliella salina*, *Pyramidomonas delicatula*, and *Tetraselmis chui*) were acquired from Liaoning Sea Fisheries Research Institute in Dalian, China. Each microalgae species was cultured individually in a conical flask of the enriched seawater medium [42], which was shaken one time every three hours. They grew in a CO_2 thermotank (MGC-300A, Yiheng Technical Co., Ltd., Dalian Maritime University (DMU), Dalian, China) under a photoperiod of 12 h. The temperature was kept at 23 °C and the illumination intensity was 3000–3500 d/m^2 in the thermotank.

2.4.2. Treatments and Standard Assays of Microalgae Cells

The microalgae cells were inactivated and maintained integrity by the water bath method and the operational process follows the standard protocol [43]. The activities of the microalgae cells were determined by using a commercial microscope (Ti-FLC-E, NIKON Corp., Tokyo, Japan). The standard assays of the classification of microalgae species were accomplished by a commercial flow cytometer (FACSCaliburTM Cytometer, BD Biosciences, San Jose, CA, USA). The operation of the commercial microscope and flow cytometer were conducted according to the standard operational instructions.

3. Results and Discussion

3.1. The Signals of CF, SLS, and RPS of the Single Microparticles

In order to demonstrate that the developed detection device can detect the signals of CF, SLS, and RPS of a single microalgae cell simultaneously, the microalgae cells of *Dunaliella salina* were chosen as samples to be tested by the developed device. The signals of CF, SLS, and RPS of individual living *Dunaliella salina*, *Pyramidomonas delicatula*, and *Isochrysis galbana* cells are shown in Figure 4A–C, respectively. As can be seen from Figure 4A,B, and C(a), the CF pulse of a microalgae cell generates when the microalgae cell is passing through the detection spot. Every pulse of CF represents a living microalgae cell and the quantities of the CF pulses are equal to the quantities of the living microalgae cells. The amplitude of the CF pulse is positively proportional to the activity of the microalgae cell. For the microalgae cells of the same species with similar activities, the amplitudes of the CF pulses are closed and fluctuate around an average value. At the same time, the SLS pulse of the microalgae cell also occurs when the microalgae cell enters the detection area, which is shown in Figure 4A,B, and C(b). Every SLS pulse is corresponding to a CF pulse and the amplitude of the SLS pulse is related to the surface roughness and intracellular contents of the microalgae cell. Meanwhile, the RPS pulse also occurs when the microalgae cell is moving through the sensing gate, which is shown in Figure 4A,B, and C(c). The RPS signal lags behind the other two signals of CF and SLS with a slight

delay. This is related to the position relationship between the photodetectors and the sensing gate in the microfluidic chip. If the sensing gate in the microfluidic chip is placed in front of the photodetectors, the RPS pulse will generate ahead of other two pulses, otherwise RPS pulse lags behind. Thus, it can be seen that the signals of CF, SLS, and RPS of a microalgae cell can be detected simultaneously by the developed device when the single microalgae cell is passing through the detection spot.

In addition to the living microalgae cells, there are many other impurities in ballast water, which are not the ones that are concerned in ballast water detection. To investigate if the detection device can distinguish between the living microalgae cells and other microparticles, dead *Dunaliella salina* cells and the polystyrene particles were used as samples to be also tested by the developed device. The results are shown in Figure 5a–c and Figure 6a–c, respectively. The process of the inactivation treatment of the microalgae cells has been stated before. From Figure 5a, it can be seen that when a dead microalgae cell passes through the detection spot, no CF pulse generates. This is because the photosynthetic electron transport chain was destroyed under the heat treatment and the microalgae cells lost the capacity of photosynthesis and, thus, no chlorophyll fluorescence emits from the microalgae cells. The pulses of SLS and RPS generate simultaneously, which are shown in Figure 5b,c, respectively. Compared with the signals of SLS and RPS of the living microalgae cells, the average signal-to-noise ratio of these two signals of dead microalgae cells declined slightly. The declines are possibly related to intracellular degradation. The signals of CF, SLS, and RPS of the polystyrene microsphere particles (~10 μm in diameter, Sigma-Aldrich, St. Louis, MO, USA) are shown in Figure 6a–c. It is obvious that there are no CF signals from the polystyrene particles. The signals of SLS and RPS of the polystyrene particles were detected simultaneously. The average amplitude of RPS pulses of the polystyrene particles are larger than that of the *Dunaliella salina* cells owing to the difference of the average size. More significantly, the average amplitude of SLS pulses of the polystyrene particles are much larger than that of the microalgae cells because a larger difference in the surface roughness and contents in the microparticles exists between the polystyrene particles and the *Dunaliella salina* cells. The above experiments show that the developed device can distinguish between the living microalgae cells and other impurity particles, such as the dead microalgae cells and the inanimate particles, by the signals of CF, SLS, and RPS.

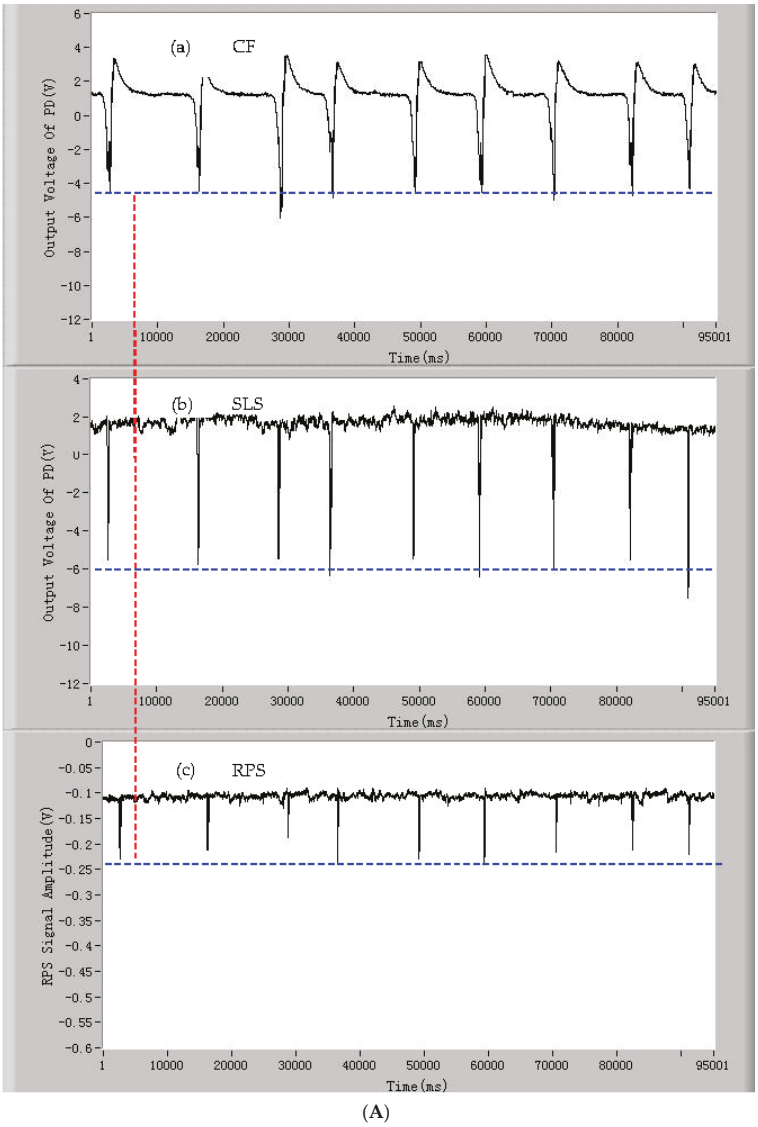

(**A**)

Figure 4. *Cont.*

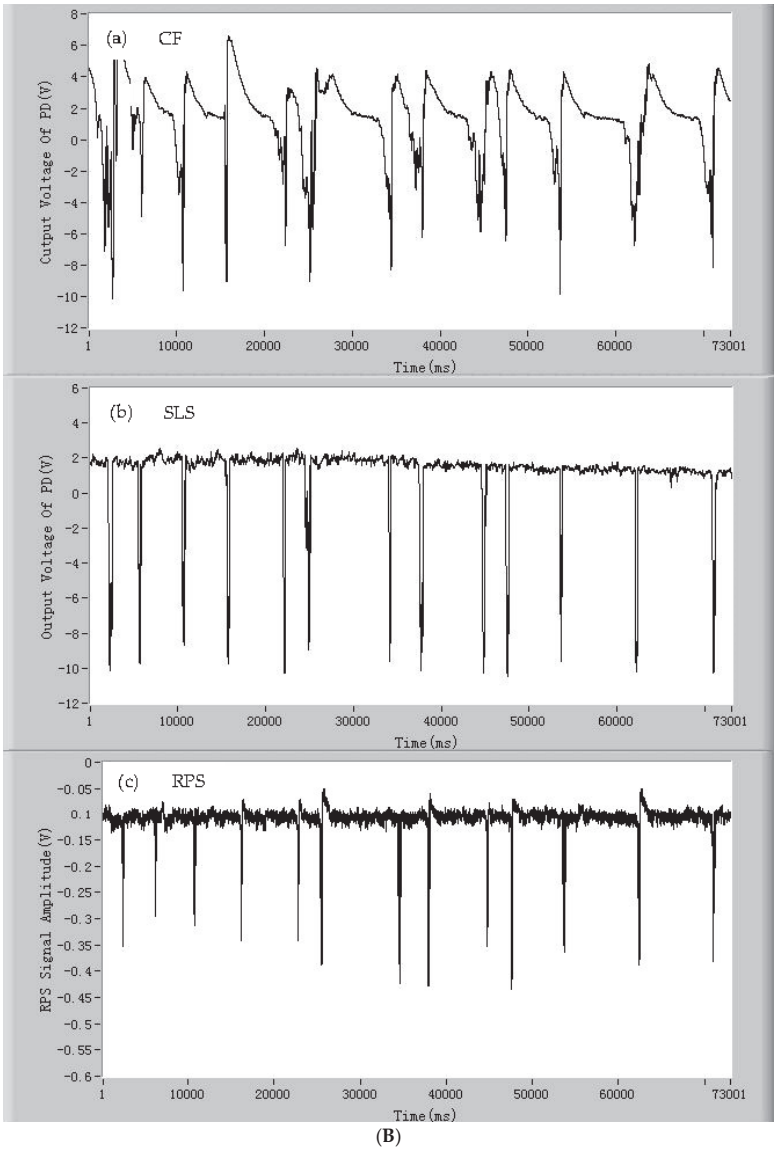

(**B**)

Figure 4. *Cont.*

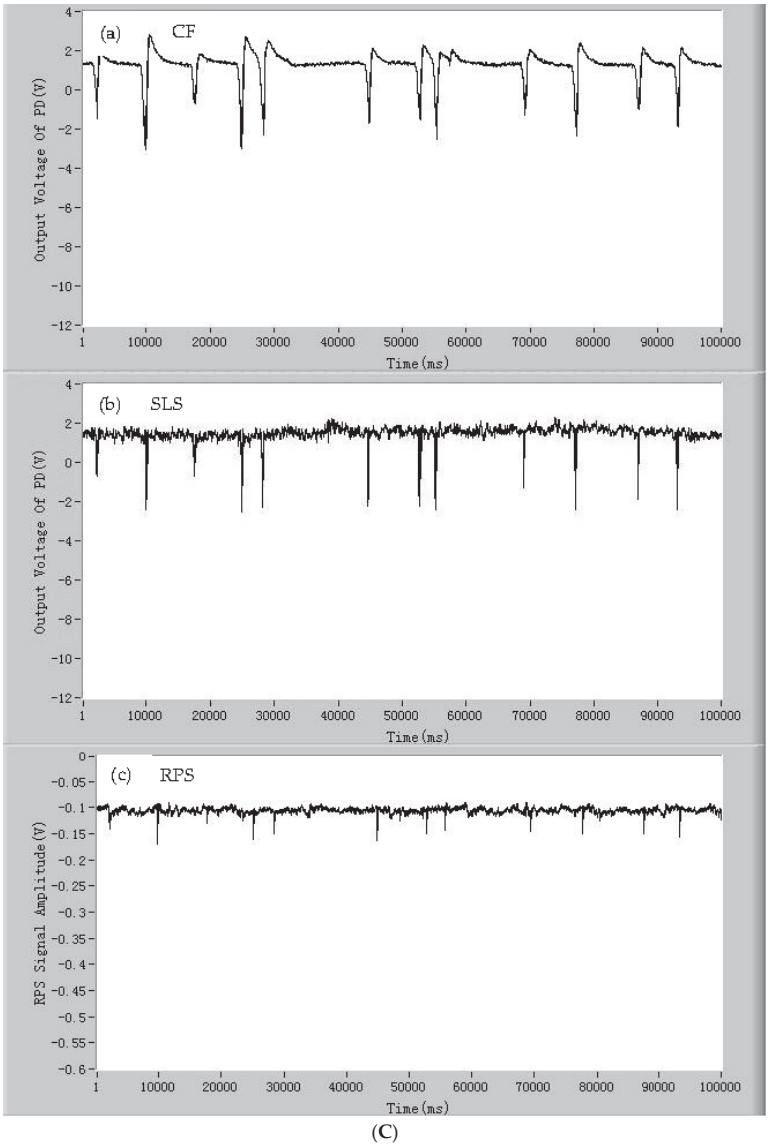

(**C**)

Figure 4. The signals of (**A**) individual living *Dunaliella salina* cells: (**a**) chlorophyll fluorescence (CF); (**b**) side light scattering (SLS); and (**c**) resistance pulse sensing (RPS). The signals of (**B**) individual living *Pyramidomonas delicatula* cells: (**a**) chlorophyll fluorescence (CF); (**b**) side light scattering (SLS); and (**c**) resistance pulse sensing (RPS). The signals of (**C**) individual living *Isochrysis galbana* cells: (**a**) chlorophyll fluorescence (CF); (**b**) side light scattering (SLS); and (**c**) resistance pulse sensing (RPS).

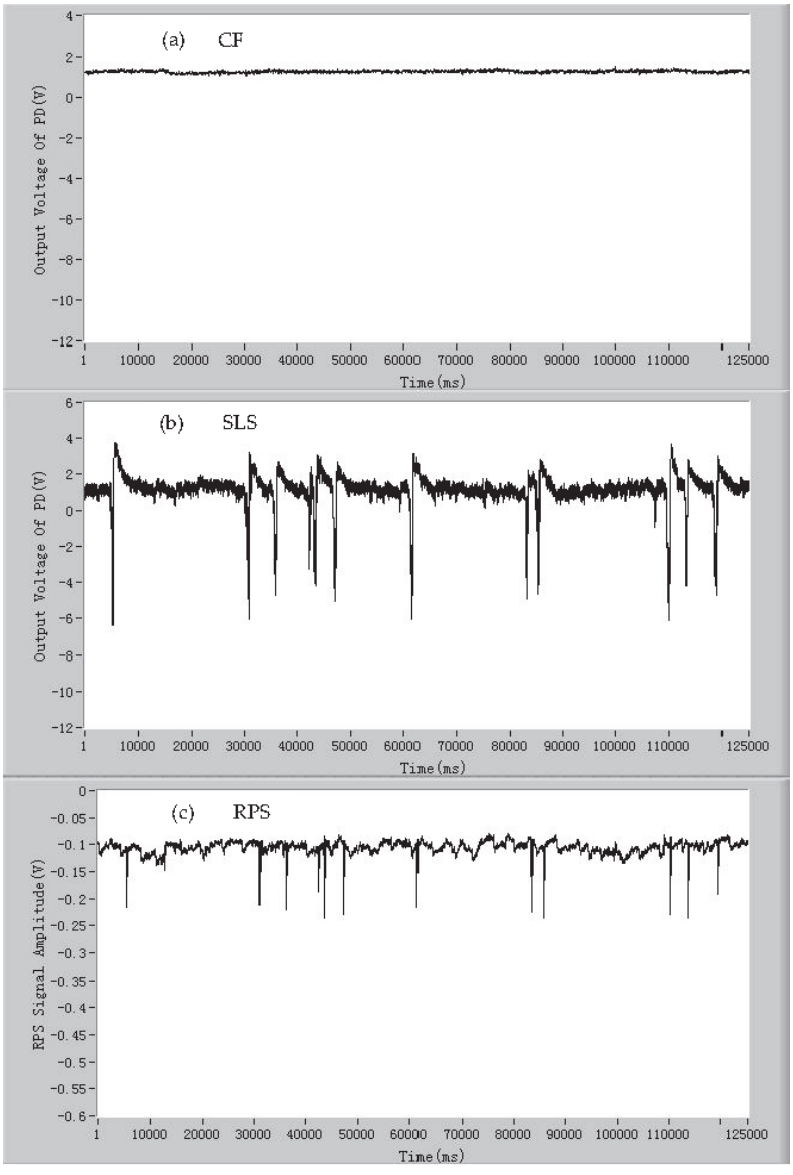

Figure 5. The signals of individual dead *Dunaliella salina* cells: (**a**) chlorophyll fluorescence (CF); (**b**) side light scattering (SLS); and (**c**) resistance pulse sensing (RPS).

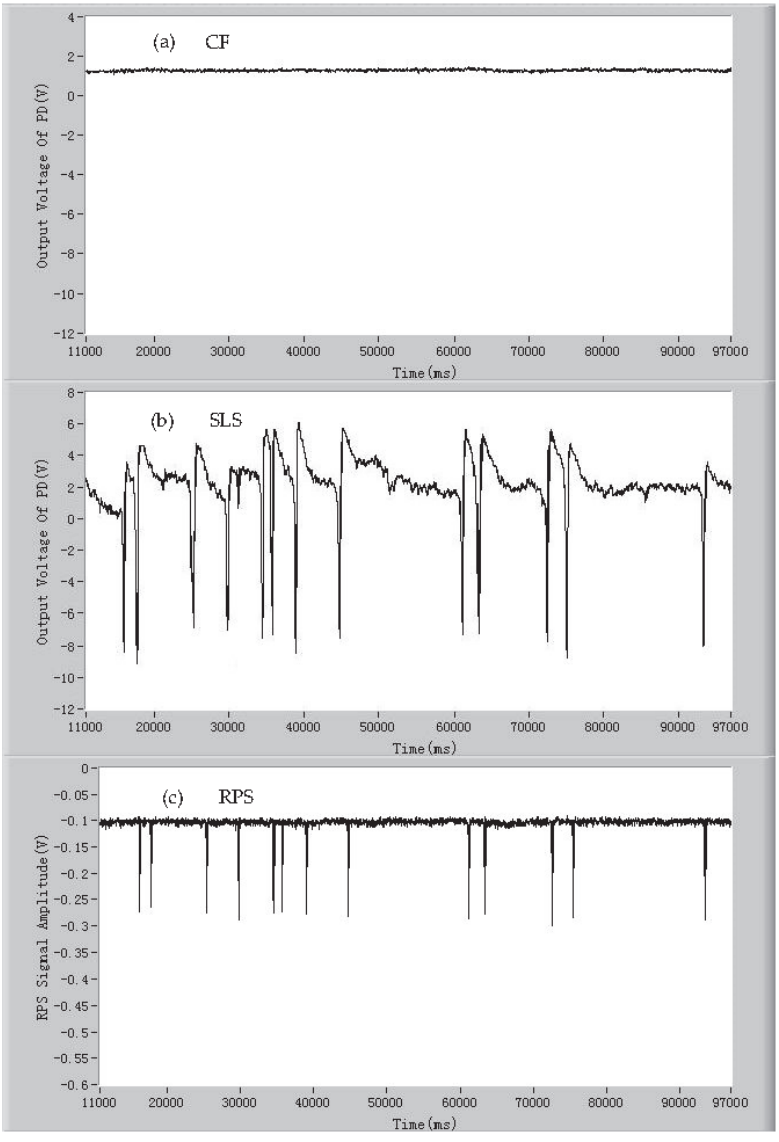

Figure 6. The signals of individual 10 μm polystyrene particles: (**a**) chlorophyll fluorescence (CF); (**b**) side light scattering (SLS); and (**c**) resistance pulse sensing (RPS).

3.2. The Classification of Species by Signals of CF, SLS, and RPS of the Mixed Microparticles

To investigate the performance of detection of the mixed microparticles by the developed device, three kinds of microalgae cells (*Isochrysis galbana*, *Dunaliella salina*, and *Tetraselmis chui*) were mixed as samples. In order to analyze the principle briefly and not lose generality, the signals of CF of the microalgae cells were taken as examples, and the CF signals of the mixed microalgae cells are shown in Figure 7. From the results, it can be seen that the average amplitudes of the CF pulses of three microalgae species cells are different, which are easy to be separated and marked by the dash line

with numbers ①, ②, and ③ in Figure 7. By the amplitudes of the CF pulses of the single microalgae cells, the microalgae cells can be divided into the different groups. The other two signals of SLS and RPS of the microalgae cells have also the similar characteristics; that is, the same or similar microalgae species cells have similar characteristics of SLS and RPS pulses.

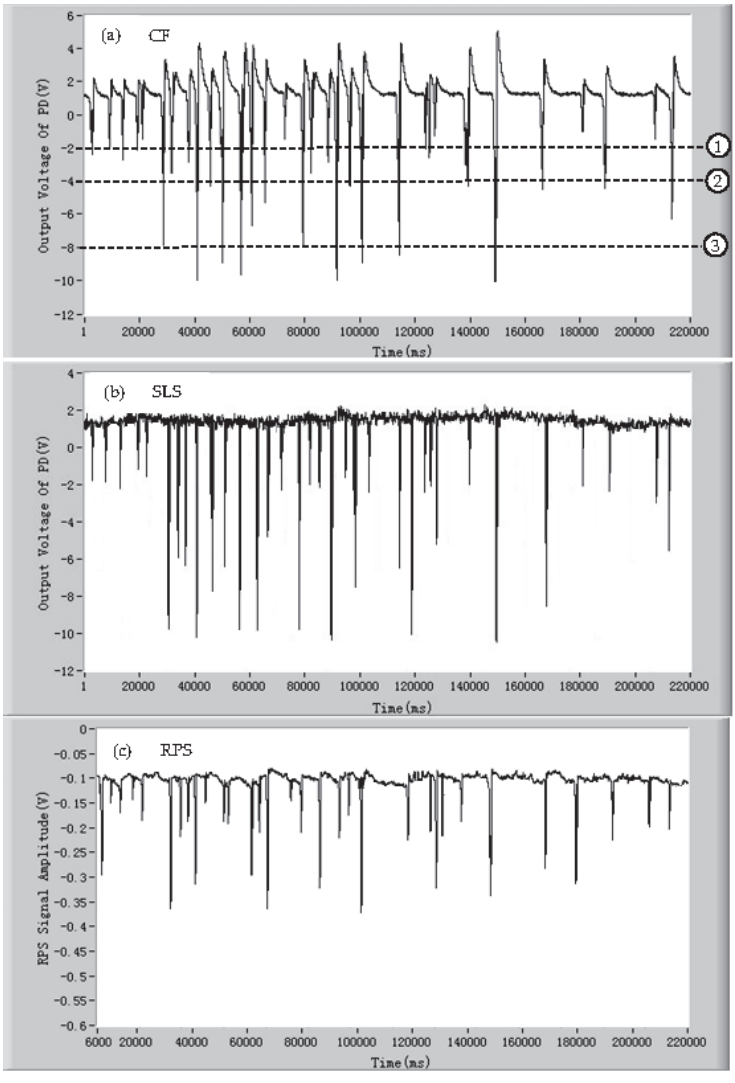

Figure 7. The signals of the CF of three mixed microalgae cells (*Isochrysis galbana*, *Dunaliella salina*, and *Tetraselmis chui*): (**a**) chlorophyll fluorescence (CF); (**b**) side light scattering (SLS); and (**c**) resistance pulse sensing (RPS).

3.3. Contrast Experiments between the Developed Device and the Commercial Flow Cytometer

Based on the above analysis, a microalgae cell can be classified by the amplitudes of CF, SLS, and RPS pulses of the microalgae cell. To demonstrate the performance of the classification of the microalgae cells of the developed device, three microalgae species (*Chlorella vulgaris*, *Dunaliella salina*,

and *Pyramidomonas delicatula*) were used as samples and contrast experiments between the commercial flow cytometer and the developed device were conducted, with the results shown in Figure 8. Two- and three-dimensional distributions of the microalgae species cells are given from the flow cytometer and the developed device, respectively. Three kinds of microalgae cells are divided clearly into three groups by the commercial flow cytometer and the developed device. The results show that there is a good agreement between the commercial flow cytometer and the developed device. Based on the principle of simultaneous detection of the CF, SLS, and RPS signals of single microalgae cells in a microfluidic chip, the developed compact device can identify the classification of the microalgae cells accurately. More importantly, the developed device is compact, portable, and low cost. In addition, three-dimensional characteristics of the microalgae cells may provide a greater fine classification of the microalgae cells.

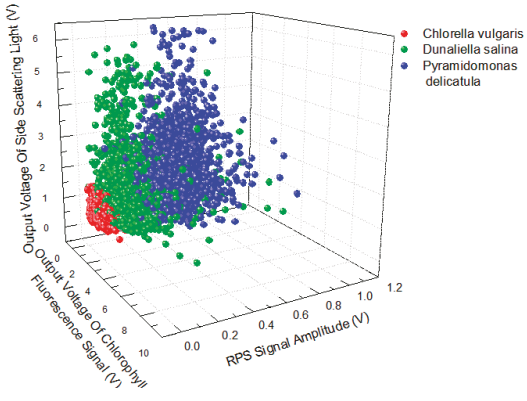

(**a**)

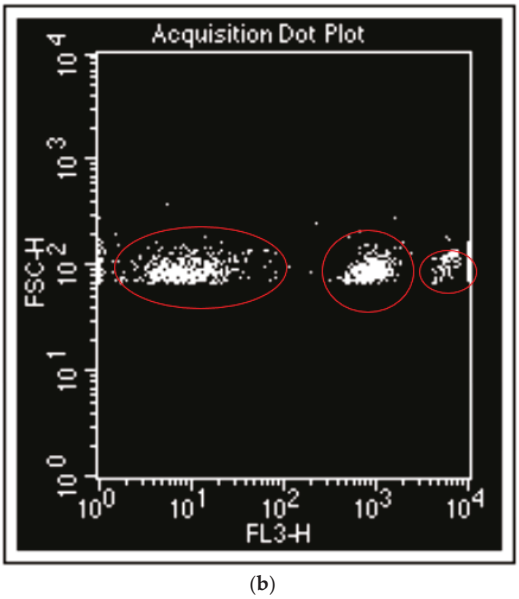

(**b**)

Figure 8. The comparison experiments of the classification of the microalgae cells between (**a**) the developed device and (**b**) the commercial flow cytometer.

3.4. Limit Analysis of Classification

The minimum among these three signals of CF, SLS, and RPS of the microalgae cells may constrain the limit of detection (LOD) of this device. Though the different microalgae species have different chlorophyll, intracellular contents, and surface roughness and sizes, in general, the amplitudes of the signals of CF, SLS, and RPS all decrease with the decrease in the size of the microalgae cells. The size of the microalgae cells can become a parameter to evaluate the LOD of the developed device. For the present developed device, the microalgae cells with a diameter of about 2–3 μm can be detected. At this time, the CF signal becomes the minimum of three signals, while the LOD of RPS can reach about several hundred nanometers and LOD of SLS is about 1–2 μm. Some feasible methods can also be taken to further improve the limit of detection, such as a smaller sensing gate, greater power of excitation light, more sensitive photodetectors, and so on.

4. Conclusions

A novel microfluidic device for the classification of microalgae cells was presented in this paper. The new features of the developed device include: (1) the physiological characteristics of microalgae cells corresponding to the signals of CF, SLS, and RPS were analyzed simultaneously to identify the classification of the microalgae cells, which include activity, surface roughness, intracellular contents, and size; (2) simultaneous detection of three signals of CF, SLS, and RPS of single microalgae cells on a disposable fiber-free microfluidic chip was accomplished; (3) the detection system was integrated in a compact device of about 18.5 cm × 8.5 cm × 12.3 cm and a weight of 720 g; and (4) the developed device has the advantages of accuracy, quickness, portability, and low cost, which are especially suitable for rapid on-site detection of ship ballast water.

Acknowledgments: This research is supported by National Natural Science Foundation of China (51309042), the Applied Basic Research Programs of Ministry of Transport of China (2014329225140), Liaoning Provincial Natural Science Foundation of China (2014025017) and the Fundamental Research Funds for the Central University (20110216003).

Author Contributions: Junsheng Wang conceived and designed the experiments and wrote the paper; Jinsong Zhao, Yanjuan Wang, Wei Wang, Yushu Gao, Runze Xu and Wenshuang Zhao performed the experiments. All the authors analyzed the data.

Conflicts of Interest: The authors declare no conflict of interest.

References

1. Niimi, A.J.; Reid, D.M. Low salinity residual ballast discharge and exotic species introductions to the North American great lakes. *Mar. Pollut. Bull.* **2013**, *10*, 1334–1340. [CrossRef]
2. Carney, K.J.; Delany, J.E.; Sawant, S.; Mesbahi, E. The effects of prolonged darkness on temperate and tropical marine phytoplankton and their implications for ballast water risk management. *Mar. Pollut. Bull.* **2011**, *62*, 1233–1244. [CrossRef] [PubMed]
3. Qi, Z.; Eames, L. Implication of ballast tank geometry and treatment technology on NIS removal. *Ocean Eng.* **2015**, *130*, 211–212. [CrossRef]
4. Tsolaki, E.; Diamadopoulos, E. Technologies for ballast water treatment: A review. *J. Chem. Technol. Biotechnol.* **2010**, *85*, 19–32. [CrossRef]
5. Sun, J.; Wang, J.; Pan, X.; Yuan, H. A new treatment strategy for inactivating algae in ballast water based on multi-trial injections of chlorine. *Int. J. Mol. Sci.* **2015**, *16*, 13158–13171. [CrossRef] [PubMed]
6. Christenson, L.; Sims, R. Production and harvesting of microalgae for wastewater treatment, biofuels, and bioproducts. *Biotechnol. Adv.* **2011**, *29*, 686–702. [CrossRef] [PubMed]
7. Levy, N.; Zhang, T.; Ha, J.; Sharifi, F.; Talin, A.A.; Kuk, Y.; Stroscio, J.A. Experimental evidence for *s*-wave pairing symmetry in superconducting $Cu_xBi_2Se_3$ single crystals using a scanning tunneling microscope. *Phys. Rev. Lett.* **2013**, *110*, 117001. [CrossRef] [PubMed]
8. Osten, P.; Margrie, T.W. Mapping brain circuitry with a light microscope. *Nat. Methods* **2013**, *10*, 515–523. [CrossRef] [PubMed]

9. Gobin, A.M.; Lee, M.H.; Halas, N.J.; James, W.D.; Drezek, R.A.; West, J.L. Near-infrared resonant nanoshells for combined optical imaging and photothermal cancer therapy. *Nano Lett.* **2007**, *7*, 1929–1934. [CrossRef] [PubMed]
10. Zhu, H.; Isikman, S.O.; Mudanyali, O.; Greenbaum, A.; Ozcan, A. Optical imaging techniques for point-of-care diagnostics. *Lab Chip* **2013**, *13*, 51–67. [CrossRef] [PubMed]
11. Clark, J.; Chang, J.F.; Spano, F.C.; Friend, R.H.; Silva, C. Determining exciton bandwidth and film microstructure in polythiophene films using linear absorption spectroscopy. *Appl. Phys. Lett.* **2009**, *94*, 163306. [CrossRef]
12. Wang, L.; McCleese, C.; Kovalsky, A.; Zhao, Y.; Burda, C. Femtosecond time-resolved transient absorption spectroscopy of $CH_3NH_3PBI_3$ perovskite films: Evidence for passivation effect of PbI_2. *J. Am. Chem. Soc.* **2014**, *136*, 12205–12208. [CrossRef] [PubMed]
13. Riccardi, C.; Nicoletti, I. Analysis of apoptosis by propidium iodide staining and flow cytometry. *Nat. Protoc.* **2006**, *1*, 1458–1461. [CrossRef] [PubMed]
14. Lacroix, R.; Robert, S.; Poncelet, P.; Kasthuri, R.S.; Key, N.S.; Dignat-George, F. Standardization of platelet-derived microparticle enumeration by flow cytometry with calibrated beads: Results of the International Society on Thrombosis and Haemostasis SSC Collaborative workshop. *J. Thromb. Haemost.* **2010**, *8*, 2571–2574. [CrossRef] [PubMed]
15. Vasanth, K.; Ilango, K.; MohanKumar, R.; Agrawal, A.; Dubey, G.P. Anticancer activity of *Moringa oleifera* mediated silver nanoparticles on human cervical carcinoma cells by apoptosis induction. *Colloid Surf. B Biointerfaces* **2014**, *117*, 354–359. [CrossRef] [PubMed]
16. Mirasoli, M.; Guardigli, M.; Michelini, E.; Roda, A. Recent advancements in chemical luminescence-based lab-on-chip and microfluidic platforms for bioanalysis. *J. Pharm. Biomed. Anal.* **2014**, *87*, 36–52. [CrossRef] [PubMed]
17. Wang, J.; Fan, Z.; Zhao, Y.; Song, Y.; Chu, H.; Song, W.; Song, Y.; Pan, X.; Sun, Y.; Li, D. A new hand-held microfluidic cytometer for evaluating irradiation damage by analysis of the damaged cells distribution. *Sci. Rep.* **2016**, *6*, 23165. [CrossRef] [PubMed]
18. Van Reenen, A.; de Jong, A.M.; den Toonder, J.M.; Prins, M.W. Integrated lab-on-chip biosensing systems based on magnetic particle actuation–A comprehensive review. *Lab Chip* **2014**, *14*, 1966–1986. [CrossRef] [PubMed]
19. Liu, C.C.; Wang, Y.N.; Fu, L.M.; Chieh, C. Micro-distillation system for formaldehyde concentration detection. *Chem. Eng. J.* **2016**, *304*, 419–425. [CrossRef]
20. Wang, J.; Song, W.; Song, Y.; Xu, D.; Zhang, M.; Pan, X.; Sun, Y.; Li, D. Quantitative evaluation of radiation dose by γ-H2AX on a microfluidic chip in a miniature fluorescence cytometer. *Radiat. Meas.* **2014**, *62*, 71–77. [CrossRef]
21. Oedit, A.; Vulto, P.; Ramautar, R.; Lindenburg, P.W.; Hankemeier, T. Lab-on-a-Chip hyphenation with mass spectrometry: Strategies for bioanalytical applications. *Curr. Opin. Biotechnol.* **2015**, *31*, 79–85. [CrossRef] [PubMed]
22. Hejazian, M.; Li, W.; Nguyen, N.T. Lab on a chip for continuous-flow magnetic cell separation. *Lab Chip* **2015**, *15*, 959–970. [CrossRef] [PubMed]
23. Neuži, P.; Giselbrecht, S.; Länge, K.; Huang, T.J.; Manz, A. Revisiting lab-on-a-chip technology for drug discovery. *Nat. Rev. Drug Discov.* **2012**, *11*, 620–632. [CrossRef] [PubMed]
24. Pérez-Mitta, G.; Tuninetti, J.S.; Knoll, W.; Trautmann, C.; Toimil-Molares, M.E.; Azzaroni, O. Polydopamine meets solid-state nanopores: A bioinspired integrative surface chemistry approach to tailor the functional properties of nanofluidic diodes. *J. Am. Chem. Soc.* **2015**, *137*, 6011–6017. [CrossRef] [PubMed]
25. Van Oordt, T.; Barb, Y.; Smetana, J.; Zengerle, R.; von Stetten, F. Miniature stick-packaging—An industrial technology for pre-storage and release of reagents in lab-on-a-chip systems. *Lab Chip* **2013**, *13*, 2888–2892. [CrossRef] [PubMed]
26. Schaap, A.; Rohrlack, T.; Bellouard, Y. Optical classification of algae species with a glass lab-on-a-chip. *Lab Chip* **2012**, *12*, 1527–1532. [CrossRef] [PubMed]
27. Lefevre, F.; Chalifour, A.; Yu, L.; Chodavarapu, V.; Juneau, P.; Izquierdo, R. Algal fluorescence sensor integrated into a microfluidic chip for water pollutant detection. *Lab Chip* **2012**, *12*, 787–793. [CrossRef] [PubMed]

28. Wang, J.; Song, Y.; Maw, M.M.; Song, Y.; Pan, X.; Sun, Y.; Li, D. Detection of size spectrum of microalgae cells in an integrated underwater microfluidic device. *J. Exp. Mar. Biol. Ecol.* **2015**, *473*, 129–137. [CrossRef]
29. Hønsvall, B.K.; Altin, D.; Robertson, L.J. Continuous harvesting of microalgae by new microfluidic technology for particle separation. *Bioresour. Technol.* **2016**, *200*, 360–365. [CrossRef] [PubMed]
30. Kim, H.S.; Weiss, T.L.; Thapa, H.R.; Devarenne, T.P.; Han, A. A microfluidic photobioreactor array demonstrating high-throughput screening for microalgal oil production. *Lab Chip* **2014**, *14*, 1415–1425. [CrossRef] [PubMed]
31. Wang, J.; Xing, D.; Zhang, L.; Jia, L. A new principle pHotosynthesis capacity biosensor based on quantitative measurement of delayed fluorescence in vivo. *Biosens. Bioelectron.* **2007**, *22*, 2861–2868. [CrossRef] [PubMed]
32. Stirbet, A. Chlorophyll a fluorescence induction: A personal perspective of the thermal phase, the J-I-P rise. *Photosynth. Res.* **2012**, *113*, 15–61. [CrossRef] [PubMed]
33. Mathur, S.; Jajoo, A.; Mehta, P.; Bharti, S. Analysis of elevated temperature-induced inhibition of photosystem II using chlorophyll a fluorescence induction kinetics in wheat leaves (*Triticum aestivum*). *Plant Biol.* **2011**, *13*, 1–6. [CrossRef] [PubMed]
34. Vercruysse, D.; Sonnefraud, Y.; Verellen, N.; Fuchs, F.B.; Di Martino, G.; Lagae, L.; Moshchalkov, V.V.; Maier, S.A.; Van Dorpe, P. Unidirectional side scattering of light by a single-element nanoantenna. *Nano Lett.* **2013**, *13*, 3843–3849. [CrossRef] [PubMed]
35. Fu, Y.H.; Kuznetsov, A.I.; Miroshnichenko, A.E.; Yu, Y.F.; Luk'yanchuk, B. Directional visible light scattering by silicon nanoparticles. *Nat. Commun.* **2013**, *4*, 1527–1550. [CrossRef] [PubMed]
36. Sikdar, D.; Cheng, W.; Premaratne, M. Optically resonant magneto-electric cubic nanoantennas for ultra-directional light scattering. *J. Appl. Phys.* **2015**, *117*, 083101. [CrossRef]
37. Schittny, R.; Kadic, M.; Bückmann, T.; Wegener, M. Invisibility cloaking in a diffusive light scattering medium. *Science* **2014**, *345*, 427–429. [CrossRef] [PubMed]
38. Hugall, J.T.; Baumberg, J.J. Demonstrating photoluminescence from Au is electronic inelastic light scattering of a plasmonic metal: The origin of SERS backgrounds. *Nano Lett.* **2015**, *15*, 2600–2604. [CrossRef] [PubMed]
39. Wu, X.; Chon, C.H.; Wang, Y.N.; Kang, Y.; Li, D. Simultaneous particle counting and detecting on a chip. *Lab Chip* **2008**, *8*, 1943–1949. [CrossRef] [PubMed]
40. Boyle, D.S.; Hawkins, K.R.; Steele, M.S.; Singhal, M.; Cheng, X. Emerging technologies for point-of-care CD4 T-lymphocyte counting. *Trends Biotechnol.* **2012**, *30*, 45–54. [CrossRef] [PubMed]
41. Biddiss, E.; Erickson, D.; Li, D. Heterogeneous surface charge enhanced micromixing for electrokinetic flows. *Anal. Chem.* **2004**, *76*, 3208–3213. [CrossRef] [PubMed]
42. Maw, M.M.; Wang, J.; Li, F.; Jiang, J.; Song, Y.; Pan, X. Novel Electrokinetic Microfluidic Detector for Evaluating Effectiveness of Microalgae Disinfection in Ship Ballast Water. *Int. J. Mol. Sci.* **2015**, *16*, 25560–25575. [CrossRef] [PubMed]
43. Wang, J.; Sun, J.; Song, Y.; Xu, Y.; Pan, X.; Sun, Y.; Li, D. A label-free microfluidic biosensor for activity detection of single microalgae cells based on chlorophyll fluorescence. *Sensors* **2013**, *13*, 16075–16089. [CrossRef] [PubMed]

micromachines

MDPI

Article

Tunable Particle Focusing in a Straight Channel with Symmetric Semicircle Obstacle Arrays Using Electrophoresis-Modified Inertial Effects

Dan Yuan [1], Chao Pan [1], Jun Zhang [1,2], Sheng Yan [1], Qianbin Zhao [1], Gursel Alici [1] and Weihua Li [1,*]

[1] School of Mechanical, Materials and Mechatronic Engineering, University of Wollongong, Wollongong, NSW 2522, Australia; dy983@uowmail.edu.au (D.Y.); cp128@uowmail.edu.au (C.P.); jz218@uowmail.edu.au (J.Z.); sy034@uowmail.edu.au (S.Y.); qz260@uowmail.edu.au (Q.Z.); gursel@uow.edu.au (G.A.)

[2] School of Mechanical Engineering, Nanjing University of Science and Technology, Nanjing 210094, China

* Correspondence: weihuali@uow.edu.au; Tel.: +61-2-4221-4577

Academic Editors: Xiangchun Xuan and Shizhi Qian

Received: 23 September 2016; Accepted: 19 October 2016; Published: 1 November 2016

Abstract: In this work, a novel microfluidic platform for tunable particle focusing in a straight channel with symmetric semicircle obstacle arrays using electrophoresis (EP)-modified inertial effects was presented. By exerting an EP force on the charged microparticles, a relative velocity gap between microspheres and fluid in a straight channel with symmetric semicircle obstacle arrays was implemented. The relative velocity and fluid shear will induce shear-slip lift force (Saffman lift force) perpendicular to the mainstream direction. Therefore, the focusing pattern can be altered using the electrophoresis-induced Saffman force. The effects of electric field direction, flow rate, electric field magnitude, and particle size were also studied. This demonstrates the possibility of adjusting the particle inertial focusing pattern in a straight channel with with symmetric semicircle obstacle arrays using electrophoresis. Manipulation of the lateral migration of focusing streaks increases controllability in applications such as blood cell filtration and the separation of cells by size.

Keywords: particle focusing; electrophoresis force; Saffman lift force

1. Introduction

Within the last decade, microfluidics has been considered as a technology that provides a miniaturization, integration, automation, and parallelization platform for the application of biomedicine and chemistry, called Lab-on-a-chip, or micro total analysis systems (μTAS) [1]. Compared with the traditional macro-scale platforms (e.g., petri dish, centrifuge, and flow cytometry, etc.), microfluidics has advantages, including fast processing, low cost, high sensitivity, and portability [2,3].

Generally, microfluidics manipulation technologies can be sorted as active and passive, according to the source of the manipulating force. Active techniques such as dielectrophoresis (DEP) [4], magnetophoresis [5], and acoustophoresis [6], etc. employ an external force field to achieve the function; however, passive technologies rely on hydrodynamic forces or channel geometry, such as pinched flow fractionation [7], deterministic lateral displacement [8], and inertial microfluidics [9], etc.

In recent years, inertia-based methods have become extremely popular due to their advantages of simplicity, passiveness, preciseness, continuity, and high-throughput [9–11]. Two common channel structures, spiral and serpentine microchannels, have been investigated intensively, and have been widely reported on [12–19]. Recently, some reports have used obstacle structures patterned along one or two sides of the straight microchannel to focus and separate microparticles [20–24]. Recently, the

observation that a particle can migrate toward the tube axis when it lags behind the fluid flow has been reported [25]. In a vertical upward Poiseuille flow in a tube, a particle heavier than the fluid lags behind the fluid, which creates a lift force that induces the particle's migration toward the tube center. This phenomenon was first demonstrated in macroscale flows in a tube [25], and in a rectangular channel [26]. After that, this phenomenon was reported in conjunction with microscale flows, which are intrinsically laminar flows with a Poiseuille parabolic velocity profile [27]. A lagging velocity of particles was induced by utilizing the negative electrophoretic mobility of the charged particles subject to Direct Current (DC) electric field in combination with pressure-driven flow. Therefore, axisymmetric particle focusing can be achieved.

In this work, a novel microfluidic platform for tunable particle focusing in a straight channel with symmetric semicircle obstacle arrays using electrophoresis (EP)-modified inertial effects is presented. Because almost all of the particles and cells will be exerted with net charges on the surface within an aqueous solution, an external direct current electric field can pull or push particles along the main flow stream due to the electrophoretic force, creating relative velocity between the microparticle and the surrounding fluid. The relative velocity and fluid shear will induce shear-slip lift force (Saffman lift force) perpendicular to the mainstream direction. Therefore, the inertial focusing pattern can be adjusted (either to the centre of the channel or to the channel walls) using the external electric field. The particle focusing and migration phenomenon was demonstrated and analysed in this paper by the electrophoresis-modified inertial method. The effects of electric field direction, flow rates, electric field magnitude, and particle sizes were also studied. This demonstrates the possibility of adjusting the particle inertial focusing pattern in a straight channel with symmetric semicircle obstacle arrays using electrophoresis, which may provide high controllability and versatile particle filtration and manipulation platforms for the practical application of biological sample treatment and clinical blood cell filtration.

2. Theoretical Background

2.1. Inertial Lift Force

In Newtonian fluids, the shear gradient lift force and wall lift force are the two dominant forces governing particle migration, and equilibrium positions are created by the balance of the two lift forces. The sum of the two inertial lift forces (called the net inertial lift force) can be expressed as [9,28]:

$$F_L = \frac{\rho_f U_m^2 a^4}{D_h^2} f_L(R_c, x_c) \tag{1}$$

$$R_c = \frac{\rho_f U_m D_h}{\mu_f} = \frac{2\rho_f Q}{\mu_f (w+h)} \tag{2}$$

where ρ_f, U_m, and μ_f are the fluid density, mean velocity, and dynamic viscosity, respectively; a is the spherical diameter of the particles; $D_h = 2wh/(w+h)$ is the hydraulic diameter of a rectangular channel, with w and h the width and height of the channel cross-section. Q is the flow rate. The lift coefficient of net inertial lift force $f_L(R_c, x_c)$ is a function of the position of the particles within the cross-section of channel x_c and the channel Reynolds number R_c [9].

2.2. Electrophoresis

In a spatially-uniform electric field, dispersed particles will move in the fluid in this electric field, and this motion is called electrophoresis [29,30]. According to the famous Helmholtz–Smoluchowski

result, the electrophoretic velocity $\vec{v}_{EP}$ (with respect to the fluid) is given as follows when Debye lengths are much smaller than particle size [31]:

$$\vec{v}_{EP} = \frac{\varepsilon\zeta}{\mu_f}\vec{E} \tag{3}$$

$\vec{v}_{EP}$ is independent of particle size and shape. The permittivity of the fluid is defined by ε. μ_f is dynamic viscosity, and ζ is the ζ-potential [31,32] of the electric double layer surrounding the particle. The electrophoretic mobility is defined by $u_{EP} = \frac{\varepsilon\zeta}{\mu_f}$, which is the proportionality factor between particle velocity and electric field $\vec{E}$. The electric field induces the electrophoretic motion; however, u_{EP} is only dependent on the particle charge (hidden in the ζ-potential [31]), and depends on properties of the electric double layer around the particle and the electrolyte.

2.3. Dielectrophoresis

In a non-uniform electric field, a net force (known as a DEP force) will exert on the particle. This is because the Coulomb forces on either side of the dipole moment can be different. A DEP motion is that where a particle moves towards or against the region of electric field maxima. The motion is directed by DEP force, which depends on the relative polarizabilities of the particle and the suspending medium [33].

The effective dipole moment of a spherical particle is [34,35]:

$$P = 4\pi\varepsilon_m r^3 Re\left[K(\omega)\right]E \tag{4}$$

where P is a vector, and the absolute permittivity of the suspending medium is defined by ε_m. r, $K(\omega)$, and Re indicate the particle radius, the Clausius–Mossotti (CM) factor, and the real part. The Clausius–Mossotti (CM) factor depends on the complex permittivity of the particle and the suspending medium, and also the frequency of the external electric field:

$$K(\omega) = \frac{\varepsilon_p^*(\omega) - \varepsilon_m^*(\omega)}{\varepsilon_p^*(\omega) + 2\varepsilon_m^*(\omega)} \tag{5}$$

Complex permittivity is defined by $\varepsilon^*(\omega) = \varepsilon - i\sigma/\omega$, where σ is the electrical conductivity ω is the frequency of the electric field. The particle and the suspending medium are described by subscripts p and m. In the presence of an electric field, the particles and suspending medium both exhibit dielectric and conductive properties, so the complex permittivities are presented here.

2.4. Saffman Force (Shear-Induced Lift Force)

Saffman force was recognized as arising from the interaction of the Stokeslet velocity field around the particle with the velocity gradient (shear rate). Using a matched asymptotic expansion method, Saffman [36] calculated the lateral lift force on a sphere in an unbounded simple shear flow, which has constant shear rate and zero shear gradients. The magnitude of this force is

$$F_S = \frac{K}{4}Va^2\left(\gamma v^{-1}\right)^{1/2} \tag{6}$$

where K is a numerical constant (K ~81.2), velocity gradient or shear rate is defined by γ, V is the relative velocity (velocity difference between fluid velocity at the streamline through the center of the particle and the particle), and v is kinematic viscosity.

When non-neutrally buoyant particles flow in a vertical fluid, or external force fields (electrical or magnetic) [11,27] induce particles to significantly lag or lead fluid flow, the Saffman force is more relevant, and net Stokeslet flow is more obvious. In this case, the Saffman force will direct to the

channel centreline when particles lag the flow and particles migrate to the channel centreline, or the Saffman force will direct to the channel walls when particles lead the flow, and particles migrate to channel walls.

3. Materials and Methods

3.1. Design and Fabrication of a Microfluidic Device

The microfluidic device was designed with one long straight microchannel with semicircular obstacle arrays, one inlet, one outlet, and two electrode chambers using AutoCAD. The channel consists of a 10 mm straight section with 20 periods of symmetric semicircle obstacles patterned on both sides of a microchannel with a constant distance of 500 μm. The depth of the channel is uniform at 40 μm. The width of the straight microchannel changes is 250 μm, and the dimeter of the semicircular obstacle is 200 μm. The distance of the two electrode chambers is 13 mm.

The device was fabricated using standard photolithography and soft lithographic techniques [37,38]. This fabrication included rapid prototyping on a silicon master, and polydimethylsiloxane (PDMS) replica molding and sealing through plasma oxidation.

3.2. Particle Preparation

Particle suspensions were prepared by diluting 5 μm internally green dyed fluorescent polystyrene microspheres (coefficient of variation (CV) < 5%, ThermoFisher Scientific, Waltham, MA, USA), and 13 μm internally red dyed fluorescent polystyrene microspheres (CV < 5%, Thermo Fisher Scientific) in deionized (DI) water containing 0.01% (v/v) Tween 20 (Sigma-Aldrich, San Antonio, TX, USA). Tween 20 was included in suspension to prevent particle aggregation. Before commencing each experiment, the particle solutions were re-suspended by vortex to provide uniform suspensions.

3.3. Experimental Setup

The microfluidic device was placed on an inverted microscope (CKX41, Olympus, Japan), illuminated by a mercury arc lamp. The particle suspension was infused into the microchannel with specific flow rate by a programmable syringe pump (Legato 100, Kd Scientific, Holliston, MA, USA). The electric field was generated by a DC-electric source (N5772A, Agilent Technologies, Santa Clara, CA, USA). The fluorescence images were observed and captured by a CCD camera (Rolera Bolt, Q-imaging, Albion, Australia) and then post-processed by Q-Capture Pro 7 software (Q-imaging). The exposure time for each frame was set at 100 ms. The experimental setup is shown in Figure 1.

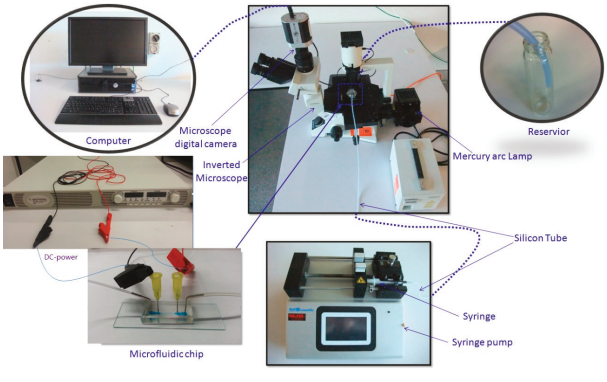

Figure 1. Experimental setup.

4. Results and Discussion

4.1. Schematic of Tunable Particle Focusing in the Straight Channel with Symmetric Semicircle Obstacle Arrays Using EP-Modified Inertial Effects

A non-uniform electric field can be generated within this channel when a DC power is imposed near the inlet and outlet of the channel. The particles experience a dielectrophoretic force (F_{DEP}) induced by the non-uniform electric field. Meanwhile, because the polystyrene particles are negatively charged in the electrolyte solution [27], they experience an electrophoretic force (F_{EP}) as well. The direction of the electrophoretic force is opposite to the direction of electric field. The electrophoretic force can decrease or increase the particle speed to induce particles to lag behind or lead the flow. The relative velocity and fluid shear can induce Saffman lift force perpendicular to the mainstream direction, which can drive particles to migrate toward the channel center or to the channel walls.

The schematic of tunable particle focusing in a straight channel with symmetric semicircle obstacle arrays using EP-modified inertial effects is shown in Figure 2. The direction of the electric field is reversed in Figure 2a,b. In Figure 2a, the anode is near the inlet, while the cathode is near the outlet, and the electric field direction is from inlet to outlet; in Figure 2b, the cathode is near the inlet, the anode is near the outlet, and the electric field direction is from outlet to inlet. Figure 2a,b show the principle of radially-inward (toward the channel center) and radially-outward (toward the channel wall) migration of particles by the electrophoresis-induced Saffman force, respectively. In this channel with the DC-electric field, particles are actually affected by dielectrophoretic, inertial, electrophoretic, and Saffman lift forces. However, the inertial lift force can be neglected when the flow rate is very low, and the dielectrophoretic force is too weak compared to electrophoretic and Saffman lift force. The schematic figure only demonstrates the additional forces (dielectrophoretic, electrophoretic, and Saffman lift forces) on the basis of inertial focusing. When the electrophoretic force direction is inverse to the flow direction of particles, the particles will lag behind the flowing fluid; therefore, the Saffman lift force directs to the center of the channel, and particles migrate to the channel centerline (Figure 2a). When the electrophoretic force direction is the same as the fluid flow direction exerted by the external pressure, the particles will lead the flowing fluid; therefore, the Saffman lift force directs to the channel sidewalls, and particles are modified to migrate toward channel walls (Figure 2b).

4.2. Effects of Electric Field Direction

Experiments were carried out by inserting an anode near the inlet, and a cathode near the outlet, while pumping fluid containing 5 μm particles into the channel. The electric field is from the inlet to outlet, and its direction was reversed by reversing the anode and cathode. Figure 3 shows the effects of electric field direction. The particle distribution under pure inertial flow conditions is used for comparison (Figure 3, Inertial). In Figure 3 (left, Inertial +500 V), the direction of electrophoretic force is inverse to the flow direction of the particles, and the particles lag behind the flowing fluid; therefore, the Saffman lift force directs toward the center of the channel, and particles migrate to channel centerline under the combination of dielectrophoretic force (F_{DEP}), electrophoretic force (F_{EP}), and Saffman force (F_S). Compared with the particle distribution under the pure inertial condition, the particle focusing width is much narrower under radially-inward Saffman force. When the direction of the electric field is from outlet to inlet, the direction of the electrophoretic force imposed on the negatively-charged particles is the same as the flow direction, and then the particles lead the flowing fluid; therefore, the Saffman lift force directs to the channel sidewalls, and particles migrate to channel walls under the combination of forces (Figure 3, Inertial −500 V). Compared with the particle distribution under the pure inertial conditions, the particles were pushed to the channel walls under radially-outward Saffman force. As can be seen from the corresponding fluorescent profiles as well, the particles' focusing width becomes narrower by radially-inward Saffman force, and particles are focused near channel walls under radially-outward Saffman force.

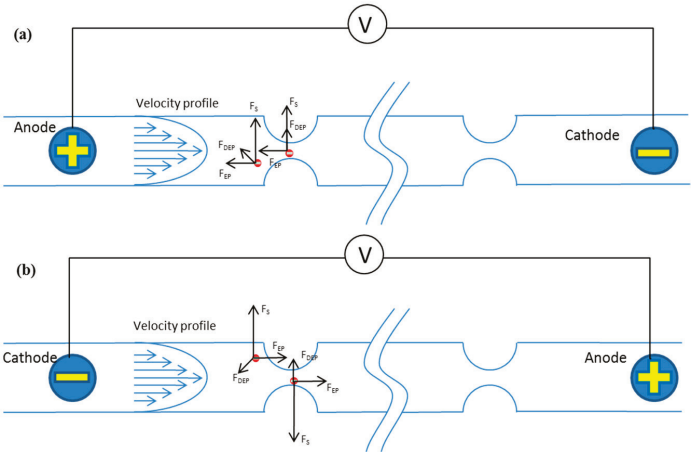

Figure 2. Schematic of tunable particle focusing in a straight channel with symmetric semicircle obstacle arrays using electrophoresis (EP)-modified inertial effects. (**a**) The principle of radially-inward (toward the channel center) migration of particles by the electrophoresis-induced Saffman force; (**b**) The principle of radially-outward (toward the channel wall) migration of particles by the electrophoresis-induced Saffman force.

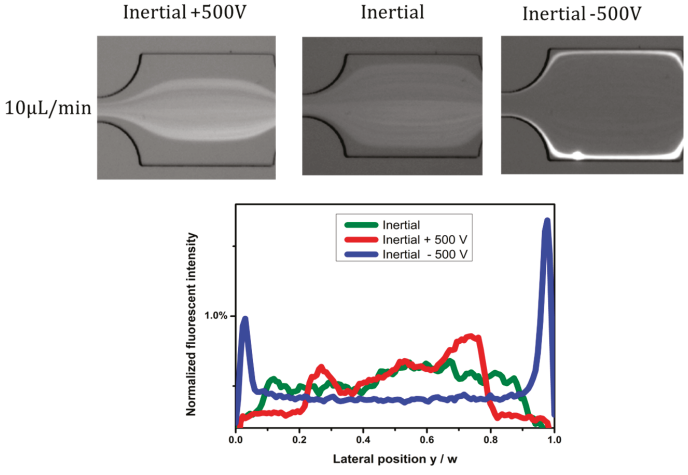

Figure 3. Effects of electric field direction.

4.3. Effects of Flow Rates

The effects of flow rates were investigated at fixed electric voltages of +500 V and −500 V, respectively. The flow rate range is from Q = 10 μL/min to Q = 100 μL/min. The particle distribution under pure inertial flow conditions is demonstrated for comparison (Figure 4, Inertial). In the inertial +500 V case, the Saffman force is radially-inward, and the particles' focusing width becomes narrower by Saffman force. When the flow rate is relatively low (from Q = 10 μL/min to Q = 30 μL/min), the inertial effects can be neglected. Therefore, the Saffman force can overcome the inertial lift force and push particles toward the center of the channel. However, as the flow rate increases (Q = 50 μL/min to Q = 100 μL/min), the inertial effect begins to become dominant, thus there is no significant difference

in the distribution of particles at pure Inertial and Inertial +500 V. In the Inertial −500 V case, the Saffman force is radially-outward, and the particles are pushed to the channel walls by Saffman force. When the flow rate is relatively low (from Q = 10 μL/min to Q = 80 μL/min), the inertial effects are very weak. Therefore, the Saffman force can overcome the inertial lift force and push particles toward the channel walls. However, as the flow rate increases further (Q = 100 μL/min), the inertial effect becomes dominant, and the Saffman force cannot overcome the inertial effects; thus, there is little difference in particle distribution at pure Inertial and Inertial −500 V. We also found that the effects of the radially-outward Saffman force occupy a much wider flow rate range than that of the radially-inward Saffman force. This is because the fluid flow and particle velocities near channel walls are much slower than that at the channel centre, and so a weak Saffman force can migrate particles toward sidewalls.

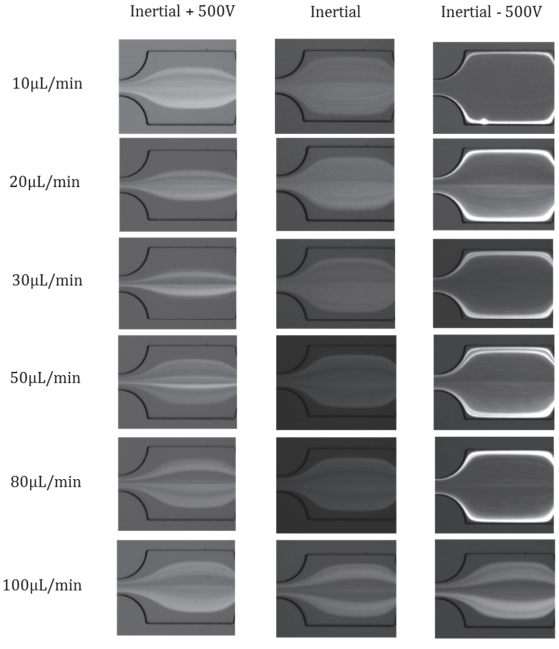

Figure 4. Effects of flow rates on particle distribution in Inertial +500 V, pure Inertial, and Inertial −500 V cases.

4.4. Effects of Electric Field Magnitude

The Saffman force can induce radially-inward or radially-outward particle migration, according to the direction of electric field; meanwhile, the magnitude of the electric field can also influence the particle distribution. The particle distributions are compared at different voltages (Inertial −300 V, Inertial −500 V) at each flow rate from 10 μL/min to 100 μL/min (Figure 5). When the voltage is 0 V, or under pure inertial condition, the particles are randomly distributed; once the voltages are imposed, the particles velocity leads the flowing fluid, therefore, the Saffman lift force directs to the channel sidewalls, and particles aggregate along the channel walls. The radially-outward particle migration is more obvious in Inertial −500 V compared with that in Inertial −300 V circumstance. However, when the flow rate increases to a certain value (30 μL/min), the inertial effect cannot be neglected; thus, the Saffman lift force in a relatively lower electric field cannot overcome the inertial effect (see Inertial −300 V), while the radially-outward particle migration is still obvious when Q = 80 μL/min in the Inertial −500 V case. At a flow rate of 100 μL/min, inertial effects overcome the Saffman force; thus,

particle distributions are almost the same in Inertial, Inertial −300 V, and Inertial −500 V circumstances. In summary, the Saffman force is more dominant in larger electric fields and slower flow rates.

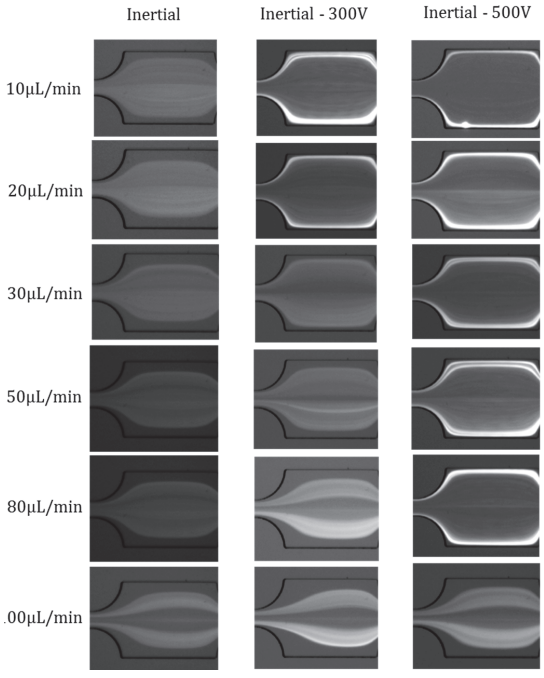

Figure 5. Effects of electric field magnitude on particle distribution (Inertial, Inertial −300 V, Inertial −500 V) from flow rate 10 μL/min to 100 μL/min. The electric field direction is from the outlet to the inlet.

4.5. Effects of Particle Size

In addition, we investigated the effects of particle size on particle distribution under the effects of Saffman force. The distribution of 5 μm and 13 μm particles in Inertial −500 V at flow rate 10 μL/min, 20 μL/min, and 50 μL/min is shown in Figure 6. Compared with 5 μm particle distribution, 13 μm particles are more randomly distributed at the channel central area, although two obvious focusing lines along the channel sidewalls can be observed. This is because, for particles with larger size, the inertial effect is more obvious, and particles are prone to be focused at the center of the channel (the inertial lift force is proportional to the fourth power of the particle size, while the Saffman force is proportional to the second power of the particle size). However, the saffman force cannot entirely overcome inertial lift force, and there is still a large amount of larger particles distributed across the whole channel. The inertial effect becomes more dominant at a higher flow rate; therefore, this phenomenon becomes more obvious as the flow rate increases (50 μL/min). Meanwhile, the inertial effects of smaller particles are much weaker than that of the larger particle; therefore, Saffman force can still pinch particles along two sidewalls when the flow rate is increased to 50 μL/min. In summary, the Saffman force is more dominant for particles with smaller sizes.

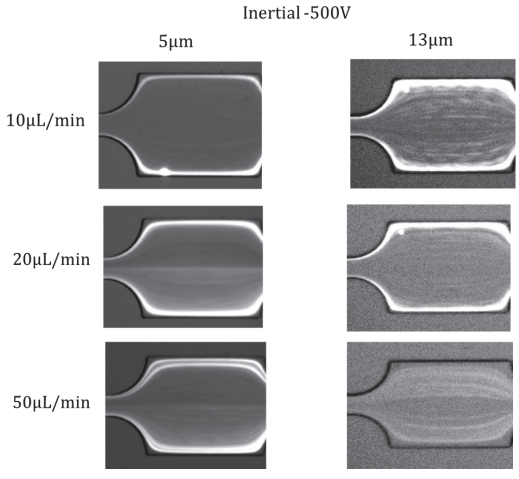

Figure 6. Distribution of 5 μm and 13 μm particles in Inertial −500 V at flow rate 10 μL/min, 20 μL/min, and 50 μL/min.

5. Conclusions

In summary, a novel microfluidic platform for tunable particle focusing in a straight channel with symmetric semicircle obstacle arrays using EP-modified inertial effects was presented. By exerting an EP force on the charged microparticles, the focusing pattern can be adjusted using the electrophoresis-induced Saffman force. Compared with particle distribution in pure inertial condition, particles' focusing width becomes narrower by radially-inward Saffman force, and particles are pushed to the channel sidewalls under radially-outward Saffman force. Based on this phenomenon, the effects of electric field direction, flow rate, electric field magnitude, and particle size were studied. This demonstrates the possibility of adjusting the particle inertial focusing pattern in a straight channel with symmetric semicircle obstacle arrays using electrophoresis, and this device has the potential to be used in biological or chemical applications, such as filtration, separation by size, or by the surface charge of bioparticles.

Acknowledgments: This work is supported by the University of Wollongong—China Scholarship Council joint scholarships.

Author Contributions: D.Y. wrote the paper; J.Z., C.P. and D.Y. conceived and designed the experiments; C.P. and D.Y. performed the experiments; S.Y. and Q.Z. helped analyze the data; G.A. and W.L. contributed experimental equipment, particles, and materials, analysis tools, and paper revisions.

Conflicts of Interest: The authors declare no conflict of interest.

References

1. Sackmann, E.K.; Fulton, A.L.; Beebe, D.J. The present and future role of microfluidics in biomedical research. *Nature* **2014**, *507*, 181–189. [CrossRef] [PubMed]
2. Bhagat, A.A.S.; Bow, H.; Hou, H.W.; Tan, S.J.; Han, J.; Lim, C.T. Microfluidics for cell separation. *Med. Biol. Eng. Comput.* **2010**, *48*, 999–1014. [CrossRef] [PubMed]
3. Zhang, J.; Li, W.; Li, M.; Alici, G.; Nguyen, N.-T. Particle inertial focusing and its mechanism in a serpentine microchannel. *Microfluid. Nanofluid.* **2014**, *17*, 305–316. [CrossRef]
4. Çetin, B.; Li, D. Dielectrophoresis in microfluidics technology. *Electrophoresis* **2011**, *32*, 2410–2427. [CrossRef] [PubMed]
5. Forbes, T.P.; Forry, S.P. Microfluidic magnetophoretic separations of immunomagnetically labeled rare mammalian cells. *Lab Chip* **2012**, *12*, 1471–1479. [CrossRef] [PubMed]

6. Wang, Z.; Zhe, J. Recent advances in particle and droplet manipulation for lab-on-a-chip devices based on surface acoustic waves. *Lab Chip* **2011**, *11*, 1280–1285. [CrossRef] [PubMed]
7. Yamada, M.; Nakashima, M.; Seki, M. Pinched flow fractionation: Continuous size separation of particles utilizing a laminar flow profile in a pinched microchannel. *Anal. Chem.* **2004**, *76*, 5465–5471. [CrossRef] [PubMed]
8. Huang, L.R.; Cox, E.C.; Austin, R.H.; Sturm, J.C. Continuous particle separation through deterministic lateral displacement. *Science* **2004**, *304*, 987–990. [CrossRef] [PubMed]
9. Di Carlo, D. Inertial microfluidics. *Lab Chip* **2009**, *9*, 3038–3046. [CrossRef] [PubMed]
10. Zhang, J.; Yan, S.; Yuan, D.; Alici, G.; Nguyen, N.-T.; Warkiani, M.E.; Li, W. Fundamentals and applications of inertial microfluidics: A review. *Lab Chip* **2016**, *16*, 10–34. [CrossRef] [PubMed]
11. Amini, H.; Lee, W.; Di Carlo, D. Inertial microfluidic physics. *Lab Chip* **2014**, *14*, 2739–2761. [CrossRef] [PubMed]
12. Bhagat, A.A.S.; Kuntaegowdanahalli, S.S.; Papautsky, I. Continuous particle separation in spiral microchannels using dean flows and differential migration. *Lab Chip* **2008**, *8*, 1906–1914. [CrossRef] [PubMed]
13. Kuntaegowdanahalli, S.S.; Bhagat, A.A.S.; Kumar, G.; Papautsky, I. Inertial microfluidics for continuous particle separation in spiral microchannels. *Lab Chip* **2009**, *9*, 2973–2980. [CrossRef] [PubMed]
14. Warkiani, M.E.; Guan, G.; Luan, K.B.; Lee, W.C.; Bhagat, A.A.S.; Chaudhuri, P.K.; Tan, D.S.-W.; Lim, W.T.; Lee, S.C.; Chen, P.C. Slanted spiral microfluidics for the ultra-fast, label-free isolation of circulating tumor cells. *Lab Chip* **2014**, *14*, 128–137. [CrossRef] [PubMed]
15. Wu, L.; Guan, G.; Hou, H.W.; Bhagat, A.A.S.; Han, J. Separation of leukocytes from blood using spiral channel with trapezoid cross-section. *Anal. Chem.* **2012**, *84*, 9324–9331. [CrossRef] [PubMed]
16. Kemna, E.W.; Schoeman, R.M.; Wolbers, F.; Vermes, I.; Weitz, D.A.; van den Berg, A. High-yield cell ordering and deterministic cell-in-droplet encapsulation using dean flow in a curved microchannel. *Lab Chip* **2012**, *12*, 2881–2887. [CrossRef] [PubMed]
17. Di Carlo, D.; Irimia, D.; Tompkins, R.G.; Toner, M. Continuous inertial focusing, ordering, and separation of particles in microchannels. *Proc. Natl. Acad. Sci. USA* **2007**, *104*, 18892–18897. [CrossRef] [PubMed]
18. Di Carlo, D.; Edd, J.F.; Irimia, D.; Tompkins, R.G.; Toner, M. Equilibrium separation and filtration of particles using differential inertial focusing. *Anal. Chem.* **2008**, *80*, 2204–2211. [CrossRef] [PubMed]
19. Zhang, J.; Yan, S.; Sluyter, R.; Li, W.; Alici, G.; Nguyen, N.-T. Inertial particle separation by differential equilibrium positions in a symmetrical serpentine micro-channel. *Sci. Rep.* **2014**, *4*, 4527. [CrossRef] [PubMed]
20. Lee, M.G.; Choi, S.; Park, J.-K. Three-dimensional hydrodynamic focusing with a single sheath flow in a single-layer microfluidic device. *Lab Chip* **2009**, *9*, 3155–3160. [CrossRef] [PubMed]
21. Lee, M.G.; Choi, S.; Kim, H.-J.; Lim, H.K.; Kim, J.-H.; Huh, N.; Park, J.-K. Inertial blood plasma separation in a contraction-expansion array microchannel. *Appl. Phys. Lett.* **2011**, *98*, 253702. [CrossRef]
22. Lee, M.G.; Shin, J.H.; Bae, C.Y.; Choi, S.; Park, J.-K. Label-free cancer cell separation from human whole blood using inertial microfluidics at low shear stress. *Anal. Chem.* **2013**, *85*, 6213–6218. [CrossRef] [PubMed]
23. Park, J.-S.; Song, S.-H.; Jung, H.-I. Continuous focusing of microparticles using inertial lift force and vorticity via multi-orifice microfluidic channels. *Lab Chip* **2009**, *9*, 939–948. [CrossRef] [PubMed]
24. Yuan, D.; Zhang, J.; Sluyter, R.; Zhao, Q.; Yan, S.; Alici, G.; Li, W. Continuous plasma extraction under viscoelastic fluid in a straight channel with asymmetrical expansion–contraction cavity arrays. *Lab Chip* **2016**, *16*, 3919–3928. [CrossRef] [PubMed]
25. Jeffrey, R.C.; Pearson, J. Particle motion in laminar vertical tube flow. *J. Fluid Mech.* **1965**, *22*, 721–735. [CrossRef]
26. Repetti, R.; Leonard, E. Segré-silberberg annulus formation: A possible explanation. *Nature* **1964**, *203*, 1346–1348. [CrossRef]
27. Kim, Y.W.; Yoo, J.Y. Axisymmetric flow focusing of particles in a single microchannel. *Lab Chip* **2009**, *9*, 1043–1045. [CrossRef] [PubMed]
28. Asmolov, E.S. The inertial lift on a spherical particle in a plane poiseuille flow at large channel reynolds number. *J. Fluid Mech.* **1999**, *381*, 63–87. [CrossRef]
29. Hunter, R.J. *Foundations of Colloid Science*; Oxford University Press: Oxford, UK, 2001.
30. Russel, W.B.; Saville, D.A.; Schowalter, W.R. *Colloidal Dispersions*; Cambridge University Press: Cambridge, UK, 1989.

31. Viovy, J.-L. Electrophoresis of DNA and other polyelectrolytes: Physical mechanisms. *Rev. Mod. Phys.* **2000**, *72*, 813. [CrossRef]
32. Bruus, H. *Theoretical Microfluidics*; Oxford University Press: New York, NY, USA, 2008.
33. Pohl, H. *The Behavior of Neutral Matter in Nonuniform Electric Fields*; Cambridge University Press: Cambridge, UK, 1978.
34. Jones, T.B.; Jones, T.B. *Electromechanics of Particles*; Cambridge University Press: Cambridge, UK, 2005.
35. Morgan, H.; Green, N. *AC Electrokinetics: Colloids and Nanoparticles*; Research Studies Press Ltd.: Hertfordshire, UK, 2003; p. 324.
36. Saffman, P.G. The lift on a small sphere in a slow shear flow. *J. Fluid Mech.* **1965**, *22*, 385–400. [CrossRef]
37. Sollier, E.; Murray, C.; Maoddi, P.; Di Carlo, D. Rapid prototyping polymers for microfluidic devices and high pressure injections. *Lab Chip* **2011**, *11*, 3752–3765. [CrossRef] [PubMed]
38. McDonald, J.C.; Whitesides, G.M. Poly(dimethylsiloxane) as a material for fabricating microfluidic devices. *Acc. Chem. Res.* **2002**, *35*, 491–499. [CrossRef] [PubMed]

micromachines

MDPI

Article

Deformability-Based Electrokinetic Particle Separation

Teng Zhou [1,2], Li-Hsien Yeh [3], Feng-Chen Li [4], Benjamin Mauroy [5] and Sang Woo Joo [2,*]

1 Mechanical and Electrical Engineering College, Hainan University, Haikou 570228, China; zhouteng@hainu.edu.cn
2 School of Mechanical Engineering, Yeungnam University, Gyongsan 712-719, Korea
3 Department of Chemical and Materials Engineering, National Yunlin University of Science and Technology, Yunlin 64002, Taiwan; lhyeh@yuntech.edu.tw
4 School of Energy Science and Engineering, Harbin Institute of Technology, Harbin 150001, China; litchi@hit.edu.cn
5 Laboratoire JA Dieudonné, UMR CNRS 7351, Université Côte d'Azur, Université de Nice Sophia Antipolis, Parc Valrose 06108 Nice Cedex 02, France; benjamin.mauroy@unice.fr
* Correspondence: swjoo@yu.ac.kr; Tel.: +82-53-810-2568

Academic Editors: Xiangchun Xuan and Shizhi Qian
Received: 14 July 2016; Accepted: 7 September 2016; Published: 20 September 2016

Abstract: Deformability is an effective property that can be used in the separation of colloidal particles and cells. In this study, a microfluidic device is proposed and tested numerically for the sorting of deformable particles of various degrees. The separation process is numerically investigated by a direct numerical simulation of the fluid–particle–electric field interactions with an arbitrary Lagrangian–Eulerian finite-element method. The separation performance is investigated with the shear modulus of particles, the strength of the applied electric field, and the design of the contracted microfluidic devices as the main parameters. The results show that the particles with different shear moduli take different shapes and trajectories when passing through a microchannel contraction, enabling the separation of particles based on their difference in deformability.

Keywords: arbitrary Lagrangian–Eulerian (ALE); dielectrophoresis; microfluidic; particle separation

1. Introduction

The separation of small particles is one of the most important steps in many chemical and biological analyses [1–6]. Over the past decade, many microfluidic devices for the separation of particles have been developed, including passive and active types [7–12]. Passive methods incorporate the internal force and the fluid mechanism, such as hydrophoretic filtration [13,14], hydrodynamic filtration (HDF) [15–17], lateral displacement (DLD) [18–20], and inertial forces [3,6,21–23], while active methods involve electrophoresis or dielectrophoresis (DEP) [4,24–30], magnetophoresis [2,31–33], optical methods [34,35], and acoustophoresis [36]. DEP is a phenomenon in which a force is exerted on a dielectric particle when it is subjected to a non-uniform electric field. DEP has great advantages: it is label-free, based on simple instruments, and correlated to high selectivity and sensitivity. In association with new and efficient microfluidic devices [27], DEP has been widely used to manipulate various micro/nano-scale bio-entities, such as cells [37], bacteria [38], and viruses [39,40].

A number of physical or topological properties of cells or particles, including size, shape, and deformability, can be used for separation. Some microfluidic separation devices that use the deformability of the motioned object have been proposed and validated. They are based either on inertia [41], obstacles [42] or on the DLD method [19]. In a straight microchannel, Hur et al. [41] found that deformability affects the particle equilibrium position, and were able to enrich cells

using inertial force, cells' deformability, and size acting as biomarkers. Zhu et al. [42] proposed a microfluidic device that can sort elastic capsules according to their deformability, using a channel with a semi-cylindrical obstacle and a diffuser. Using three-dimensional immersed-boundary finite-element lattice-Boltzmann simulations, Krueger et al. [19] demonstrated that DLD devices can be used to perform the deformability-based separation of red blood cells (RBC). Lin et al. [37] separated cancer cells from leukocytes based on size and deformability using a microfluidic ratchet mechanism. The aforementioned separation methods based on the particle deformability are passive methods [19,37,41,42], and rely either on both size and deformability or on significant differences in deformability.

Here we present a microfluidic device for the electric separation of particles based on their deformability, as shown in Figure 1. Separation is systematically investigated with numerical simulations. Fluid–structure interaction is simulated using finite elements and an arbitrary Lagrangian–Eulerian (ALE) method. The ALE method has been validated both experimentally and theoretically for rigid [5,12,13] and deformable [43,44] particles. The proposed microfluidic device is sensitive to the shear modulus of deformable particles, and is capable of separating particles with small differences in shear moduli. A parametric study is also conducted to optimize the performance of the proposed device.

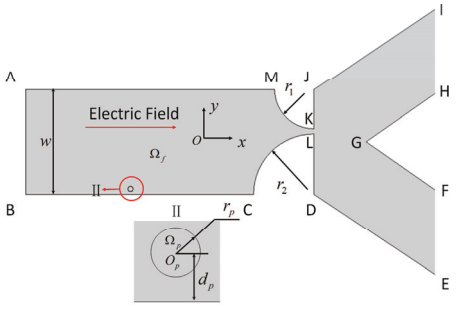

Figure 1. Electrokinetic motion of a deformable spherical particle of radius r_p in a microfluidic chip with a contraction throat. w: width of the main channel. Widths of the channels with outlet IH and FE are identical. r_1 and r_2 are the radii of the two quad-circles, respectively; d_p is the distance between the center of the spherical particle and the nearest channel wall.

The paper is organized as follows: Section 2 includes the theory for the deformable particle trajectory and separation mechanism. Section 3 presents the simulated results of the particle separation process and how the parametric studies—including the shear modulus, electric field intensity, and geometry parameters—affect the particle trajectory. Section 4 concludes the paper.

2. Formulation and Numerical Method

2.1. Mathematical Model

In this study, we consider a two-dimensional (2D) channel that consists of a uniform inlet section with a converging-expansion part, and two uniform outlet sections. This geometry is used to study electrokinetic particle translation, as shown in Figure 1. The contraction part of the converging-expansion channel is generated by two quad-circles with different radii. The two outlet sections are designed to sort particles with sufficiently different trajectories into two groups. A circular particle with radius r_p located at a distance d_p from the channel wall is shown in the magnified view below. An electric potential is applied externally from inlet AB to grounded outlets IH and FE to an incompressible Newtonian fluid domain Ω_f. The electric field E, generated in the domain, induces the electrokinetic motion of a hyperelastic particle Ω_p suspended in the fluid. Because the electric double layer (EDL) thicknesses adjacent to the charged particle and the channel wall are very thin

in comparison to the particle radius and the channel widths, the thin-EDL approximation is applied. The electrical potential ϕ in the domain Ω_f can be described by the Laplace equation,

$$\nabla^2\phi = 0 \text{ in } \Omega_f \tag{1}$$

The local electric field E can be calculated from the electric potential ϕ by

$$E = -\nabla\phi \text{ in } \Omega_f \tag{2}$$

Because a potential shift is applied across the microfluidic chip, the boundary conditions for ϕ on the entrance and exits of the microchannel are

$$\phi = \phi_0 \text{ on AB} \tag{3}$$

and

$$\phi = 0 \text{ on IH and EF} \tag{4}$$

Solid boundaries—including the channel wall (Γ_w) and particle surface (Γ_p)—are electrically insulating, yielding

$$n\cdot\nabla\phi = 0 \text{ on } \Gamma_w \text{ and } \Gamma_p \tag{5}$$

where n is the unit outward normal vector.

The Reynolds number in the microchannel is very small, so that the conservation of momentum and mass can be described by the Stokes and the continuity equations:

$$\rho_f \frac{\partial u}{\partial t} = \nabla\cdot[-p\mathrm{I} + \mu(\nabla u + \nabla u^{\mathrm{T}})] \text{ in } \Omega_f \tag{6}$$

and

$$\nabla\cdot u = 0 \text{ in } \Omega_f \tag{7}$$

where ρ_f and μ are the density and the viscosity of the fluid, respectively; u is the velocity vector; p is the hydrodynamic pressure; I is the unit tensor; and ∇u^T is the transpose of the velocity gradient ∇u. An open boundary condition is specified at the inlet and the outlets:

$$\nabla\cdot[-p\mathrm{I} + \mu(\nabla u + \nabla u^T)] = 0 \text{ on AB, IH and EF} \tag{8}$$

The Smoluchowski slip boundary condition for Newtonian electroosmotic flow (EOF) is applied on the charged channel wall:

$$u = u_w = \frac{\varepsilon_f \zeta_w}{\mu}(I - nn)\cdot\nabla\phi \text{ on } \Gamma_w \tag{9}$$

where u_w is the fluid velocity on the channel wall, and ε_f and ζ_w are, respectively, the fluid permittivity and the zeta potential of the channel wall.

The velocity u_p on the particle consists two parts: (i) the Smoluchowski slip velocity arising from the particle surface charge; and (ii) the velocity of the particle motion. The boundary condition on the particle surface is then

$$u = u_p = \frac{\varepsilon_f \zeta_w}{\mu}(I - nn)\cdot\nabla\phi + \frac{\partial S}{\partial t} \text{ on } \Gamma_p \tag{10}$$

where ζ_p is the zeta potential of the particle and S is the displacement of the deformable particle caused by the particle deformation and movement, governed by

$$\rho_p \frac{\partial^2 S}{\partial t^2} - \nabla\cdot\sigma(S) = 0 \text{ in } \Omega_p \tag{11}$$

Here ρ_p is the density of the deformable particle, and $\sigma(S)$ is the Cauchy stress in the solid phase, which is a function of the displacement of the particle. In the following simulations, the particle is considered as an incompressible neo-Hookean material, described by a strain energy density function [43].

The force on the particle–fluid interface consists of hydrodynamic and electrokinetic stresses:

$$\sigma_p \cdot n_p = \sigma_f \cdot n_f + \sigma_E \cdot n_f \tag{12}$$

$$\sigma_f = -pI + \mu(\nabla u + \nabla u^T) \tag{13}$$

$$\sigma_E = \varepsilon_f EE - \frac{1}{2}\varepsilon_f (E \cdot E) I \tag{14}$$

where σ_p, σ_f, and σ_E are, respectively, the total stress tensor on the particle surface, the hydrodynamic stress tensor, and the Maxwell stress tensor, respectively.

2.2. Numerical Method and Code Validation

The above system is solved numerically using the commercial finite element package COMSOL (Version 4.3a, COMSOL Group, Stockholm, Sweden) coupled with MATLAB (Version 8.2, MathWorks Inc., Natick, MA, USA), operated in a high-performance cluster. The coupled system of hydrodynamic, electrical field, and particle mechanics is solved simultaneously. As we are using the ALE method, the mesh is deformed in order to follow the motion of the particle, and the mesh quality decreases progressively when the particle progresses into the microfluidic device. When the mesh quality falls below 0.7 (out of a maximum 1.0) [1,6,13], the domain is re-meshed with the current particle position, the solution is mapped to the new mesh, and the computation is restarted. The previous step is repeated each time the mesh quality falls below 0.7.

To validate the present method, we compare its predictions with the analytical result of Keh and Anderson [45] for the electrophoresis of a rigid spherical particle of diameter d along the axis of an infinite long tube of diameter a. Under the conditions of thin EDL and negligible DEP force, the approximate analytical solution for the electrophoretic velocity of a spherical particle (U_p) is

$$U_p = \left[1 - 1.28987\left(\frac{d}{a}\right)^3 + 1.89632\left(\frac{d}{a}\right)^5 - 1.02780\left(\frac{d}{a}\right)^6\right]\left(1 - \frac{\zeta_w}{\zeta_p}\right) U_0 \tag{15}$$

where $U_0 = \varepsilon_f \zeta_p E_z/\mu$ is the Smoluchowski velocity, with E_z being the axial strength of the external electric field in the absence of particle. In the benchmark, E_z = 30 kV, ζ_w = 60 mV, ζ_p = 20 mV, $\varepsilon_f = 7.08 \times 10^{-10}$ F/m, ρ_f = 1000 kg/m^3, and μ = 0.001 Pa·s. To simulate a rigid particle, we used a very large value for G (G = 2000 Pa). As shown in Figure 2, the numerical predictions for U_p using our method (symbols) are in good agreement with the analytical solution of Keh and Anderson [45] (solid line).

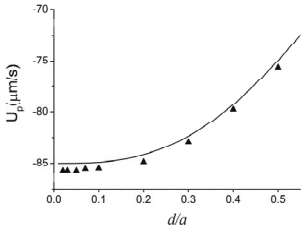

Figure 2. Velocity of a rigid sphere translating along the axis of a cylindrical tube as a function of the ratio between the diameter d of the sphere and diameter a of the channel. The solid line and triangle symbols represent the analytical solution of Keh and Anderson [45] and the numerical results from the present model, respectively.

3. Results and Discussion

In the cases reported here, the geometric parameters are set to w = 200 μm, r_p = 10 μm, and d_p = 10 μm, and the physical properties of the aqueous solution are ρ_f = 1000 kg/m^3, μ = 0.001 Pa·s, and $\varepsilon_f = 7.08 \times 10^{-10}$ F/m. The density and the permittivity of the neutrally buoyant deformable particle are assumed to be identical to those of the solution, ρ_p = 1000 kg/m^3 and $\varepsilon_p = 7.08 \times 10^{-10}$ F/m. The zeta potentials on the channel wall (ζ_w) and particle (ζ_p) are set to −60 mV and 20 mV, respectively; the particle is to move from left to right.

In this section, the separation process is presented, after which a parametric study is performed to investigate the effects of shear modulus, electric field intensity, and geometrical parameters (r_1 and r_2) on the particle separation process.

3.1. The Separation Process

The separation of dissimilar particles can be achieved by making their trajectories different. In this study, we chose to discriminate the particles using their shear modulus G as a marker. Particles with different shear moduli reach different deformations and shapes, even if their volumes are identical. Due to the difference in their shapes, the DEP force on the particles—which tends to push the particle away from the streamlines—is different, even if their location and surrounding electric field are identical. To illustrate that the DEP force on the particles depends on the particle shape, we calculated the DEP force in the spanwise direction for two different particles with the same volume: one with circular shape and one with elliptical shape. The distances from the centers of the particles to the wall were also set to be identical. In order to demonstrate the sole role of DEP forces on the two different particles, they are first fixed in space. Figure 3 shows that the force on the circular particle is larger than the force on the elliptical one. It is then expected that the circular particle will be pushed farther toward the center than the elliptical one. This also implies that the DEP focusing can be weakened by the particle deformation. In this way, particles with different shear moduli can be separated due to a difference in their deformations.

Figure 4 shows different trajectories for particles that exhibit only a difference in shear moduli. Shear moduli of 20, 40, 60, 80, 100, and 200 Pa are simulated, but only three cases are presented here for the sake of clarity. With different deformation and shape, the particles experience different hydrodynamic and Maxwell stresses, resulting in different particle trajectories for particles with different shear moduli.

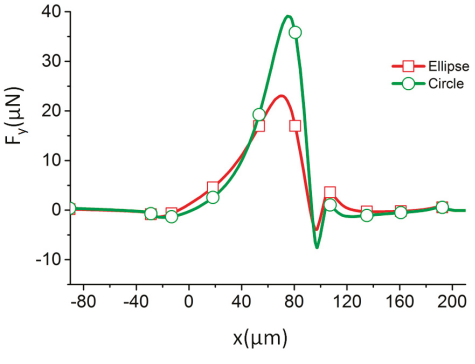

Figure 3. The spanwise component of dielectrophoretic (DEP) force along the channel for particles with two different shapes (identical volumes) with r_1 = 60 μm, r_2 = 120 μm. The radius of the circular particle is 5 μm, while the lengths of the major and minor axis of the ellipse are 6.25 and 4 μm, respectively.

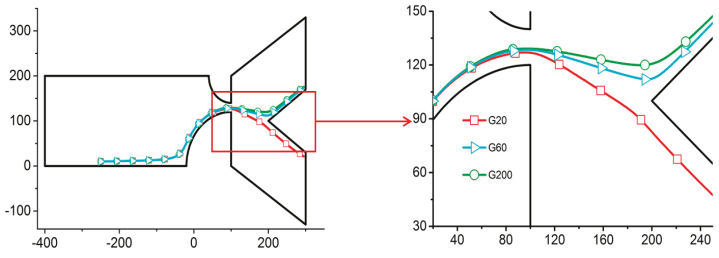

Figure 4. Trajectories of particles with different shear moduli G with r_1 = 60 μm, r_2 = 120 μm, and the strength of the axial electric field in the channel E = 30 V/m. An enlarged view of the contraction region is on the right. GN: shear modulus of the particle of N Pa. (axis in μm).

In Figure 5, two different particles with G = 20 and 200 Pa start from the same location. As the channel width decreases, the electric field intensity increases. At the beginning, the electric field is too weak to deform the particles, as between the first and third positions in Figure 5. The motion of the two particles is thus almost identical. The streamwise and spanwise components of the velocity vectors (shown in Figure 6) are also almost identical. As the particles progress through the channel, the electrical stress on the particle increases, inducing the particle with the lowest shear modulus to deform. In the fourth position in Figure 5, the electric field causes the particle with G = 20 Pa to deform, while it has little effect on the one with G = 200 Pa. Due to the difference in their shapes, the total forces on the two particles are different, as shown in Figure 3. Accordingly, the velocity components (shown in Figure 6) show conspicuous difference between particles with G = 20 Pa and G = 200 Pa. The spanwise components in particular show a negative value for G = 20 Pa, while that for G = 200 Pa has a positive value. The particles' trajectories are fully separated upon reaching the channel constriction, where the electric field is the strongest.

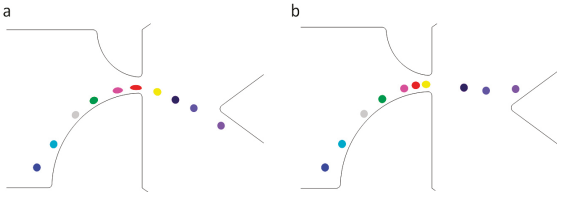

Figure 5. Time trace of a deformable particle passing through the contraction with the shear modulus (**a**) G = 20 Pa and (**b**) G = 200 Pa while r_1 = 60 μm, r_2 = 120 μm, and E = 30 V/m. The positions from left to right represent time lapse of 0, 25, 40, 46, 51, 53.5, 55, 60, and 80 ms.

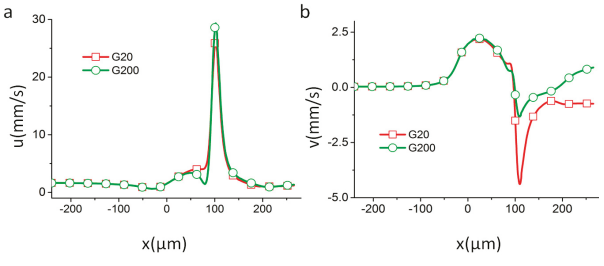

Figure 6. Velocity components of particles with different shear moduli in motion. (**a**) u, main flow direction; (**b**) v, orthogonal to main flow direction. Here r_1 = 60 μm, r_2 = 120 μm, and the electric field intensity in the channel is E = 30 V/m.

3.2. Effect of Shear Modulus

The effect of particle compliance is studied by varying the shear modulus G. Considering that many engineering materials have shear modulus in the MPa or GPa range, most cells are in the kPa range, and some artificial liposomes can be as small as on the order of unity in Pa, a wide range of G was used in the experiment. Here we only report the results for G = 20 to 200 Pa because for the electric potential used, it is sufficiently wide to exhibit representative particle behaviors ranging from compliant to rigid. Between 20 and 60 Pa, the electric field intensity is strong enough to cause the particle to deform. The trajectories are not very different up to the contraction. As the particles leave the contraction and reach the expansion channel, the differences become notable. Due to the elasticity, the particle tends to recover its original shape as the electrical stress fades away. This relaxation process is slow, however, and the differences in trajectories persist. For this reason, we can separate particles based on their shear moduli with difference between their trajectories in the tested configuration, as shown in Figure 4.

3.3. Effect of External Electric Field

The effect of the electric field intensity is studied by varying its amplitude in the straight channel by adjusting the electric potential between the inlet and outlet, before the contraction channel to 20, 30, and 40 V/m. In order to show the clear separation performance, the particles with shear moduli G = 20 and 200 Pa are used (Figure 7). The result shows that particles with the same shear modulus move nearer to the upper wall when the electric field intensity increases. In Figure 7, the trajectories of particles with G = 200 Pa are the first, second, and fifth lines from top to bottom, with electric field intensities E = 30, 20, and 10 V/m. The difference in the trajectories for different G increases when the electric field intensity increases. In order to amplify the difference, high electric field intensities are needed. In practice, however, using high electric field intensity might not be possible, depending on the nature of the particles (e.g., biological particles). The present result shows that E_x = 20 V/m is sufficient to separate the particles (Figure 7). The differences in the trajectories are, however, already very significant with E = 20 V/m, and such a reasonable electric field intensity should be sufficient for any actual applications [25–27].

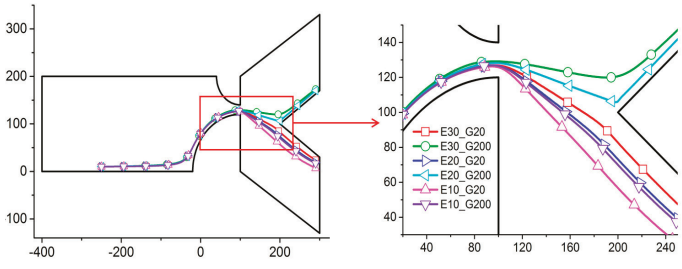

Figure 7. Trajectories of a particle for various combinations of the shear modulus G and strength of the axial electric field in the channel E_x with r_1 = 60 μm and r_2 = 120 μm. On the right is an enlargement of the contraction region. Ei_Gj stands for the electric field strength in the channel at i V/m and the shear modulus of the particle at j Pa. Axes are in μm.

3.4. Effect of Geometrical Parameters of the Contraction Region: r_1 and r_2

The geometrical parameters r_1 and r_2 can be used to control the particle trajectory (Figure 8). Due to the repelling force on the channel wall, the particle cannot stay very close to the channel wall in the contraction. The starting point of the particle is set to very close to the downward wall of the expansion channel. As the particle moves toward the contraction channel, the particle gradually moves away from the wall. There is thus a non-negligible distance between the particle and the channel wall.

The particle position will be adjusted by the channel wall, composed of two circles. Then, changing the size of r_1 and r_2 can be used to control the outlet as the particle leaves the channel.

The particles with different shear moduli still have different trajectories, even when the sizes of r_1 and r_2 are varied. In Figure 8a, the particles with shear moduli G = 20 and 200 Pa all exit from the downward outlet with r_1 = 90 μm and r_2 = 90 μm. The figure shows that the repelling force is not strong enough to push the particle up to the centerline of the channel. In order to separate the particles, the sizes of r_1 and r_2 should be adjusted in order to make the particle with 200 Pa shear modulus cross the centerline and to keep the particle with 20 Pa shear modulus below the centerline. After we reduced r_1 to 80 μm and increased r_2 to 100 μm, the particle with 200 Pa shear modulus crosses the centerline and exits through the upper outlet, while the particle with 20 Pa shear modulus exits through the downward outlet (Figure 8b). We then sweep the sizes of r_1 and r_2 in 10 μm increments. When r_1 = 40 μm and r_2 = 140 μm, the particles with shear moduli G = 20 and 200 Pa can still be separated in the tested configuration. However, the particles all leave the channel through the upper outlet when r_1 = 30 μm and r_2 = 150 μm. This method shows that we can count on a 40 μm tolerance for the design of r_1 and r_2.

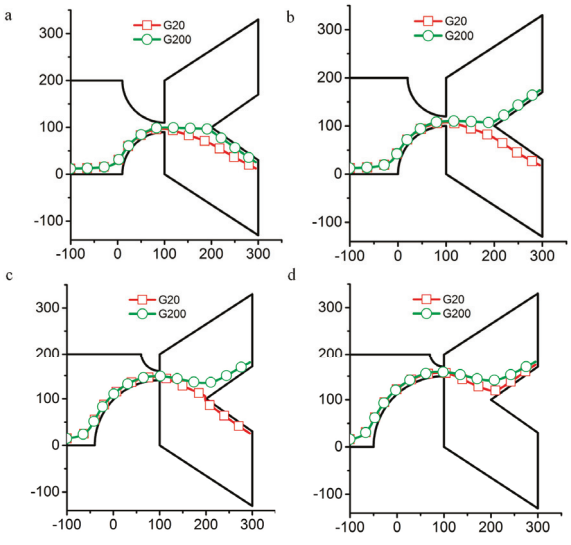

Figure 8. Trajectories of particles with two different shear moduli G for various values of r_1 and r_2 when the axial electric field in the channel is E = 30 V/m. (**a**) r_1 = 90 μm and r_2 = 90 μm; (**b**) r_1 = 80 μm and r_2 = 100 μm; (**c**) r_1 = 40 μm and r_2 = 140 μm; (**d**) r_1 = 30 μm and r_2 = 150 μm. Axes are in μm.

4. Conclusions

An electrokinetic microfluidic device for particle separation is designed and analyzed using an ALE-based finite elements computation. Separation is controlled with the particles' shear modulus, which affects the particles' deformation, in turn affecting the particles' trajectories. The present study suggests that if the microfluidic device is properly designed, shear modulus is an effective separation marker for deformable particles. Furthermore, the proposed design exhibits a reasonable tolerance, which might ease any fabrication process. Additionally, we showed that low electric field intensities can be used without reducing separation efficiency, which allows the safeguarding of fragile particles, such as biological cells. Finally, we showed that geometrical parameters of the contraction channel provide flexibility in the design of the device proposed.

Acknowledgments: This work is funded by the Yeungnam University Research Grant.

Author Contributions: T.Z. and B.M. conceived and designed the experiments; T.Z. performed the experiments; T.Z. and F.L. analyzed the data; S.W.J. contributed reagents/materials/analysis tools; T.Z., L.Y., B.M. and S.W.J. wrote the paper.

Conflicts of Interest: The authors declare no conflicts of interest.

References

1. Ai, Y.; Sanders, C.K.; Marrone, B.L. Separation of escherichia coli bacteria from peripheral blood mononuclear cells using standing surface acoustic waves. *Anal. Chem.* **2013**, *85*, 9126–9134. [CrossRef] [PubMed]
2. Verbruggen, B.; Toth, T.; Cornaglia, M.; Puers, R.; Gijs, M.A.M.; Lammertyn, J. Separation of magnetic microparticles in segmented flow using asymmetric splitting regimes. *Microfluid. Nanofluid.* **2015**, *18*, 91–102. [CrossRef]
3. Amini, H.; Lee, W.; di Carlo, D. Inertial microfluidic physics. *Lab Chip* **2014**, *14*, 2739–2761. [CrossRef] [PubMed]
4. Dubose, J.; Lu, X.; Patel, S.; Qian, S.; Woo Joo, S.; Xuan, X. Microfluidic electrical sorting of particles based on shape in a spiral microchannel. *Biomicrofluidics* **2014**, *8*, 014101. [CrossRef] [PubMed]
5. Ai, Y.; Park, S.; Zhu, J.; Xuan, X.; Beskok, A.; Qian, S. DC electrokinetic particle transport in an L-shaped microchannel. *Langmuir ACS J. Surf. Colloids* **2010**, *26*, 2937–2944. [CrossRef] [PubMed]
6. Lu, X.; Xuan, X. Inertia-enhanced pinched flow fractionation. *Anal. Chem.* **2015**, *87*, 4560–4565. [CrossRef] [PubMed]
7. Xuan, X.C.; Zhu, J.J.; Church, C. Particle focusing in microfluidic devices. *Microfluid. Nanofluid.* **2010**, *9*, 1–16. [CrossRef]
8. Pamme, N. Continuous flow separations in microfluidic devices. *Lab Chip* **2007**, *7*, 1644–1659. [CrossRef] [PubMed]
9. Lenshof, A.; Laurell, T. Continuous separation of cells and particles in microfluidic systems. *Chem. Soc. Rev.* **2010**, *39*, 1203–1217. [CrossRef] [PubMed]
10. Sajeesh, P.; Sen, A.K. Particle separation and sorting in microfluidic devices: A review. *Microfluid. Nanofluid.* **2014**, *17*, 1–52. [CrossRef]
11. Yu, Z.T.F.; Yong, K.M.A.; Fu, J. Microfluidic blood cell sorting: Now and beyond. *Small* **2014**, *10*, 1687–1703. [CrossRef] [PubMed]
12. Ai, Y.; Zeng, Z.; Qian, S. Direct numerical simulation of AC dielectrophoretic particle-particle interactive motions. *J. Colloid Interf. Sci.* **2014**, *417*, 72–79. [CrossRef] [PubMed]
13. Zhou, T.; Liu, Z.; Wu, Y.; Deng, Y.; Liu, Y.; Liu, G. Hydrodynamic particle focusing design using fluid-particle interaction. *Biomicrofluidics* **2013**, *7*, 054104. [CrossRef] [PubMed]
14. Choi, S.; Song, S.; Choi, C.; Park, J.-K. Hydrophoretic sorting of micrometer and submicrometer particles using anisotropic microfluidic obstacles. *Anal. Chem.* **2009**, *81*, 50–55. [CrossRef] [PubMed]
15. Aoki, R.; Yamada, M.; Yasuda, M.; Seki, M. In-channel focusing of flowing microparticles utilizing hydrodynamic filtration. *Microfluid. Nanofluid.* **2009**, *6*, 571–576. [CrossRef]
16. Sugaya, S.; Yamada, M.; Seki, M. Observation of nonspherical particle behaviors for continuous shape-based separation using hydrodynamic filtration. *Biomicrofluidics* **2011**, *5*, 24103. [CrossRef] [PubMed]
17. Masuda, T.; Niimi, M.; Nakanishi, H.; Yamanishi, Y.; Arai, F. Cancer cell separator using size-dependent filtration in microfluidic chip. *Sens. Actuators B Chem.* **2013**, *185*, 245–251. [CrossRef]
18. Liu, Z.; Huang, F.; Du, J.; Shu, W.; Feng, H.; Xu, X.; Chen, Y. Rapid isolation of cancer cells using microfluidic deterministic lateral displacement structure. *Biomicrofluidics* **2013**, *7*, 011801. [CrossRef] [PubMed]
19. Krueger, T.; Holmes, D.; Coveney, P. Deformability-based red blood cell separation in deterministic lateral displacement devices-a simulation study. *Biomicrofluidics* **2014**, *8*, 054114. [CrossRef] [PubMed]
20. Mcgrath, J.; Jimenez, M.; Bridle, H. Lab on a chip deterministic lateral displacement for particle separation: A review. *Lab Chip* **2014**, *14*, 4139–4158. [CrossRef] [PubMed]
21. Zhou, J.; Papautsky, I. Fundamentals of inertial focusing in microchannels. *Lab Chip* **2013**, *13*, 1121–1132. [CrossRef] [PubMed]
22. Masaeli, M.; Sollier, E.; Amini, H.; Mao, W.; Camacho, K.; Doshi, N.; Mitragotri, S.; Alexeev, A.; di Carlo, D. Continuous inertial focusing and separation of particles by shape. *Phys. Rev. X* **2012**, *2*, 031017. [CrossRef]

23. Ramachandraiah, H.; Ardabili, S.; Faridi, A.M.; Gantelius, J.; Kowalewski, J.M.; Martensson, G.; Russom, A. Dean flow-coupled inertial focusing in curved channels. *Biomicrofluidics* **2014**, *8*, 034117. [CrossRef] [PubMed]
24. Song, Y.; Peng, R.; Wang, J.; Pan, X.; Sun, Y.; Li, D. Automatic particle detection and sorting in an electrokinetic microfluidic chip. *Electrophoresis* **2013**, *34*, 684–690. [CrossRef] [PubMed]
25. Pethig, R. Review article-dielectrophoresis: Status of the theory, technology, and applications. *Biomicrofluidics* **2010**, *4*, 022811. [CrossRef] [PubMed]
26. Li, M.; Li, W.H.; Zhang, J.; Alici, G.; Wen, W. A review of microfabrication techniques and dielectrophoretic microdevices for particle manipulation and separation. *J. Phys. D Appl. Phys.* **2014**, *47*, 063001. [CrossRef]
27. Jubery, T.Z.; Srivastava, S.K.; Dutta, P. Dielectrophoretic separation of bioparticles in microdevices: A review. *Electrophoresis* **2014**, *35*, 691–713. [CrossRef] [PubMed]
28. Lu, X.; Hsu, J.-P.; Xuan, X. Exploiting the wall-induced non-inertial lift in electrokinetic flow for a continuous particle separation by size. *Langmuir* **2014**, *31*, 620–627. [CrossRef] [PubMed]
29. Lu, X.; Patel, S.; Zhang, M.; Woo Joo, S.; Qian, S.; Ogale, A.; Xuan, X. An unexpected particle oscillation for electrophoresis in viscoelastic fluids through a microchannel constriction. *Biomicrofluidics* **2014**, *8*, 021802. [CrossRef] [PubMed]
30. Patel, S.; Qian, S.; Xuan, X. Reservoir-based dielectrophoresis for microfluidic particle separation by charge. *Electrophoresis* **2013**, *34*, 961–968. [CrossRef] [PubMed]
31. Yung, C.W.; Fiering, J.; Mueller, A.J.; Ingber, D.E. Micromagnetic-microfluidic blood cleansing device. *Lab Chip* **2009**, *9*, 1171–1177. [CrossRef] [PubMed]
32. Cheng, R.; Zhu, T.; Mao, L. Three-dimensional and analytical modeling of microfluidic particle transport in magnetic fluids. *Microfluid. Nanofluid.* **2014**, *16*, 1143–1154. [CrossRef]
33. Wilbanks, J.J.; Kiessling, G.; Zeng, J.; Zhang, C.; Tzeng, T.-R.; Xuan, X. Exploiting magnetic asymmetry to concentrate diamagnetic particles in ferrofluid microflows. *J. Appl. Phys.* **2014**, *115*, 044907. [CrossRef]
34. Leake, K.D.; Phillips, B.S.; Yuzvinsky, T.D.; Hawkins, A.R.; Schmidt, H. Optical particle sorting on an optofluidic chip. *Opt. Express* **2013**, *21*, 32605–32610. [CrossRef] [PubMed]
35. Lee, S.Y.; Walsh, G.F.; Dal Negro, L. Microfluidics integration of aperiodic plasmonic arrays for spatial-spectral optical detection. *Opt. Express* **2013**, *21*, 4945–4957. [CrossRef] [PubMed]
36. Guo, J.; Kang, Y.; Ai, Y. Radiation dominated acoustophoresis driven by surface acoustic waves. *J. Colloid Interf. Sci.* **2015**, *455*, 203–211. [CrossRef] [PubMed]
37. Lin, B.K.; McFaul, S.M.; Jin, C.; Black, P.C.; Ma, H. Highly selective biomechanical separation of cancer cells from leukocytes using microfluidic ratchets and hydrodynamic concentrator. *Biomicrofluidics* **2013**, *7*, 034114. [CrossRef] [PubMed]
38. Puchberger-Enengl, D.; Podszun, S.; Heinz, H.; Hermann, C.; Vulto, P.; Urban, G.A. Microfluidic concentration of bacteria by on-chip electrophoresis. *Biomicrofluidics* **2011**, *5*, 044111. [CrossRef] [PubMed]
39. Pagaduan, J.V.; Sahore, V.; Woolley, A.T. Applications of microfluidics and microchip electrophoresis for potential clinical biomarker analysis. *Anal. Bioanal. Chem.* **2015**, *407*, 6911–6922. [CrossRef] [PubMed]
40. Ai, Y.; Qian, S. Electrokinetic particle translocation through a nanopore. *Phys. Chem. Chem. Phys.* **2011**, *13*, 4060–4071. [CrossRef] [PubMed]
41. Hur, S.C.; Henderson-MacLennan, N.K.; McCabe, E.R.B.; di Carlo, D. Deformability-based cell classification and enrichment using inertial microfluidics. *Lab Chip* **2011**, *11*, 912–920. [CrossRef] [PubMed]
42. Zhu, L.; Rorai, C.; Dhrubaditya, M.; Brandt, L. A microfluidic device to sort capsules by deformability: A numerical study. *Soft Matter* **2014**, *10*, 7705–7711. [CrossRef] [PubMed]
43. Ai, Y.; Mauroy, B.; Sharma, A.; Qian, S. Electrokinetic motion of a deformable particle: Dielectrophoretic effect. *Electrophoresis* **2011**, *32*, 2282–2291. [CrossRef] [PubMed]
44. Ai, Y.; Qian, S.; Liu, S.; Joo, S.W. Dielectrophoretic choking phenomenon in a converging-diverging microchannel. *Biomicrofluidics* **2010**, *4*, 13201. [CrossRef] [PubMed]
45. Keh, H.; Anderson, J. Boundary effects on electrophoretic motion of colloidal spheres. *J. Fluid Mech.* **1985**, *153*, 417–439. [CrossRef]

micromachines

MDPI

Article

Enhanced Throughput for Electrokinetic Manipulation of Particles and Cells in a Stacked Microfluidic Device

Lin Zhu [1], Saurin H. Patel [2], Mark Johnson [2], Akshay Kale [2], Yash Raval [3], Tzuen-Rong Tzeng [3] and Xiangchun Xuan [2,*]

1 School of Engineering, Anhui Agricultural University, Hefei 230036, China; zl009@mail.ustc.edu.cn
2 Department of Mechanical Engineering, Clemson University, Clemson, SC 29634-0921, USA; saurinp@g.clemson.edu (S.H.P.); mhjohns@g.clemson.edu (M.J.); akale@g.clemson.edu (A.K.)
3 Department of Biological Sciences, Clemson University, Clemson, SC 29634-0314, USA; yraval@g.clemson.edu (Y.R.); TZUENRT@clemson.edu (T.-R.T.)
* Correspondence: xcxuan@clemson.edu; Tel.: +1-864-656-5630

Academic Editors: Shizhi Qian and Wen Jung Li
Received: 27 July 2016; Accepted: 29 August 2016; Published: 1 September 2016

Abstract: Electrokinetic manipulation refers to the control of particle and cell motions using an electric field. It is an efficient technique for microfluidic applications with the ease of operation and integration. It, however, suffers from an intrinsic drawback of low throughput due to the linear dependence of the typically very low fluid permittivity. We demonstrate in this work a significantly enhanced throughput for electrokinetic manipulation of particles and cells by the use of multiple parallel microchannels in a two-layer stacked microfluidic device. The fabrication of this device is simple without the need of a precise alignment of the two layers. The number of layers and the number of microchannels in each layer can thus be further increased for a potentially high throughput electrokinetic particle and cell manipulations.

Keywords: dielectrophoresis; reservoir; particle separation; particle concentration; parallel operation

1. Introduction

Electric field-driven flow is the transport method of choice in microfluidic devices over traditional pressure-driven flow due to its more favorite scaling with microchannel dimensions and easier operation with no mechanical connections [1–5]. It moves liquids by electroosmosis and charged samples (e.g., molecules, viruses, particles, cells, etc.) by electrophoresis [6,7]. The combination of these two motions gives the so-called electrokinetic motion, which possesses an essentially plug-like velocity profile in typical microchannels and thus can be precisely controlled [8–10]. However, electrokinetic manipulation of particles and cells suffers from an intrinsic drawback of low throughput due to its linear dependence of the fluid permittivity and particle/wall zeta potentials that usually have very small values [11,12]. While the increase of electric field can partially mitigate this problem, the throughput of electrokinetic manipulation is still limited because large electric fields can cause severe adverse effects such as Joule heating [13,14] and electrical damages [15,16] on both the sample and the microfluidic device itself.

We demonstrate in this work that the throughput of electrokinetic manipulation of particles and cells can be significantly increased by a parallel operation in multiple microchannels of a two-layer stacked microfluidic device. A similar idea of using multiple parallel channels has been recently developed to increase the signal-to-noise ratio in electric current monitoring for electroosmotic flow measurement under low ionic strengths [17]. It has also been demonstrated for achieving a high

throughput in many other applications [18–24]. We utilize our recently developed reservoir-based dielectrophoresis (rDEP) technique [25,26] to implement a continuous concentration and separation of particles and cells inside the central reservoir of the stacked microfluidic device. A numerical model is also developed to simulate the electrokinetic particle and cell manipulations.

2. Experiment

2.1. Microfluidic Device Fabrication

Figure 1a shows a picture of the microfluidic device fabricated for our experiments. This device consists of two stacked layers of polydimethylsiloxane (PDMS) slabs on top of a glass slide. Each PDMS layer has four straight rectangular microchannels that are arranged in the radial direction of the central inlet reservoir (for the supply of particles and cells), and each has an independent outlet reservoir. The microchannels in each layer of PDMS were fabricated using the standard soft lithography technique as described elsewhere [25]. They are each 500-μm-wide and 5-mm-long overall with a tapered 50-μm-wide, 500-μm-long constriction at the central reservoir-microchannel junction. This design is made to locally enhance the electric field and its gradients such that the electric voltage for particle and cell manipulations via rDEP can be reduced. All microchannels are of rectangular shape with a uniform 40-μm depth. The first layer of PDMS, i.e., Layer B in Figure 1a, was bonded to the glass slide after plasma treating (PDC-32G, Harrick Scientific, Ithaca, NY, USA), where no alignment was needed. The second layer of PDMS, i.e., Layer A in Figure 1a, was then plasma-bonded to the top of the first layer after the equal-sized reservoirs in each layer were aligned using only the naked eye. No precise alignment of the two layers is needed in this step because the electrokinetic manipulation of particles and cells at every central reservoir-microchannel junction takes place on its own and has no cross-talk with that at any other junctions.

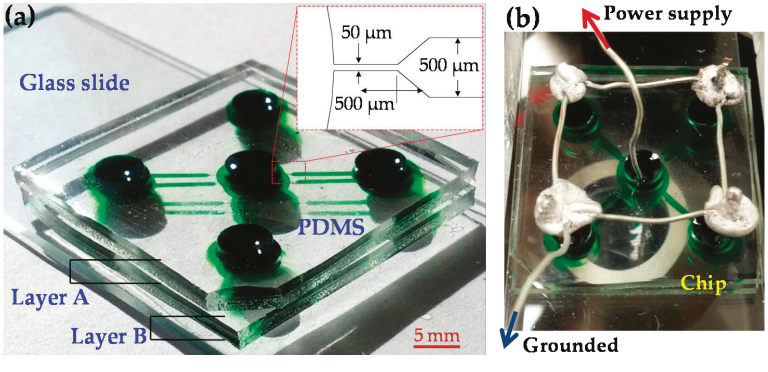

Figure 1. (**a**) Picture of the stacked PDMS/glass microfluidic device (reservoirs and microchannels are filled with green food dye for clarity) used in experiments, which consists of two PDMS layers with four 5-mm-long straight rectangular microchannels each; (**b**) Electrical connections for the stacked microfluidic device.

2.2. Particle and Cell Solutions Preparation

Spherical polystyrene particles of 5 μm in diameter (Sigma-Aldrich, St. Louis, MO, USA) were used to demonstrate the electrokinetic trapping and concentration at the central reservoir-microchannel junctions via rDEP. They were re-suspended into 1 mM phosphate buffer to a final concentration of around 10^6 particles per milliliter. The electric conductivity of the buffer solution was measured to be 210 μS/cm. In the electrokinetic separation experiment, 3-μm-diameter spherical polystyrene particles (Sigma-Aldrich) were mixed into the 5-μm particle solution at a similar final concentration.

Tween 20 (Fisher Scientific, Waltham, MA, USA) was added to both particle suspensions at 0.1% v/v for suppressing the aggregation of particles and their adhesions to channel walls.

Yeast cells (*Saccharomyces cerevisiae* ATCC 9763) were procured from American Type Culture Center (Manassas, VA, USA), and cultivated in yeast-mold (YM) agar plates/yeast-mold broth at 30 °C. Briefly, a single colony of fresh yeast grown on a YM agar plate was used for inoculating YM broth (15 mL) in a sterile tube. The cells were grown at 30 °C under shaking conditions (250 rpm) for 24 h, and then centrifuged at 5000× g for 5 min before being re-suspended into 1× sterile phosphate buffer saline (PBS) for storage in a refrigerator. Prior to tests, yeast cells were washed/centrifuged with PBS at least 3 times and finally re-suspended in 1 mM phosphate buffer to a concentration of around 10^6 cells per milliliter. They were mostly round with a measured diameter ranging from 4 to 8 μm. Tween 20 was also added to the cell suspension at 0.1% v/v to help dispersing cells, which did not cause visible lysis of the suspended yeast cells.

2.3. Particle/Cell Control and Visualization

The electrokinetic transport and manipulation of particles and cells in the stacked microfluidic device was attained by imposing DC-biased AC electric fields across all microchannels. The DC-biased AC voltages were imposed upon the platinum electrode (Fisher Scientific, Hampton, NH, USA) in the central inlet reservoir and supplied by a function generator (33220 A, Agilent Technologies, Santa Clara, CA, USA) in conjunction with a high-voltage amplifier (609E-6, Trek, Medina, NY, USA). The platinum electrodes in all four outlet reservoirs (see Figure 1) were grounded as viewed from Figure 1b. The experiment was run at 20 °C. The AC voltages had a sine waveform with a fixed frequency of 1 kHz. The motions of particles and cells were monitored through an inverted microscope (Nikon Eclipse TE2000U, Nikon Instruments, Lewisville, TX, USA) and recorded with a CCD camera (Nikon DS-Qi1Mc, Nikon Instruments Inc., Lewisville, TX, USA) at a frame rate of 15 per second. The focal point of the microscope objective lens was moved around horizontally and adjusted vertically to visualize the particle and cell behaviors at every central reservoir-microchannel junction in each PDMS layer. The obtained digital images were processed in the Nikon imaging software (NIS-Elements AR 3.22, Nikon Instruments Inc.). The particle and cell streak images were each obtained by superimposing a sequence of snapshot images.

3. Theory

3.1. Electrokinetic Particle and Cell Manipulation via rDEP

The theory of rDEP has been detailed in our earlier study [27]. Briefly, due to the size difference between a reservoir and a microchannel, electric field gradients are inherently formed at each junction between the central inlet reservoir and the four microchannels in each PDMS layer as shown in Figure 2. A dielectrophoretic force is thus induced, which acts upon the incoming particles or cells and directs them back towards the central reservoir under DC and low-frequency (<100 kHz) AC electric field fields [16,28]. The resulting motion negative dielectrophoretic, U_{DEP}, for spherical particles or cells of diameter d is written as [26,27]

$$U_{DEP} = -\frac{\varepsilon d^2}{24\eta}\nabla E^2, \tag{1}$$

where ε is the permittivity of the suspending medium, η is the dynamic viscosity of the suspending medium, and E is the electric field. Note that the Clausius–Mossotti (CM) factor has been assumed to be approximately -0.5 in Equation (1). This is because polystyrene particles and biological cells, which appear insulating in DC and low-frequency AC electric fields [16,28], have a much smaller electric conductivity than the suspending buffer solution in our experiments [29]. As illustrated by the particle velocity analysis in Figure 2, the streamwise component of the negative U_{DEP}, i.e., U_{DEP_s}, is against the electrokinetic motion of the particle, U_{EK}. Since U_{EK} is a linear function of the DC field component only, the increase in electric field, especially the AC component, will be able to make U_{DEP_s}

greater than U_{EK}, yielding an electrokinetic trapping and concentration of particles and cells inside the reservoir [25–27]. Moreover, as U_{DEP} is a second-order function of particle diameter while U_{EK} has only a weak dependence, larger particles can be trapped more easily than smaller ones, enabling a selective concentration and separation of particles and cells at the reservoir-microchannel junction [27]. In addition, the cross-stream component of U_{DEP}, i.e., U_{DEP_n}, deflects particle and cells towards the channel centerline and produces a focusing effect [26,27]. We utilize U_{DEP_s} to demonstrate in a stacked microfluidic device the electrokinetic concentration and separation of particles and cells at a significantly enhanced throughput in this work.

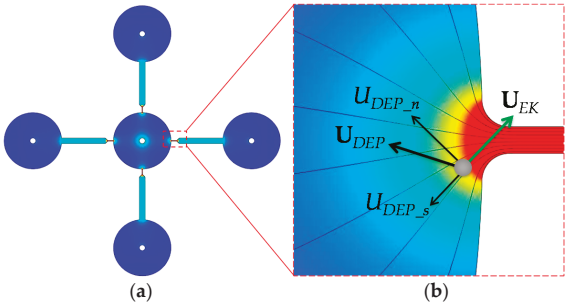

Figure 2. (**a**) Electric field contour in the four parallel microchannels of one PDMS layer of the stacked microfluidic device (see Figure 1). (**b**) Velocity analysis for a particle or cell at the central inlet reservoir-microchannel junction, where the electrokinetic motion, U_{EK}, transports the particle or cell into the microchannel while the negative dielectrophoretic motion, U_{DEP}, directs it towards the reservoir (by the streamwise component, U_{DEP_s}) and the centerline of the microchannel (by the cross-stream component, U_{DEP_n}). The thin lines represent the electric field lines or equivalently the fluid streamlines in the absence of the particle [30]. The darker background color indicates a larger electric field magnitude. The small circle at the center of the reservoir on the left plot indicates an iso-potential electrode surface.

3.2. Numerical Simulation

To predict the electrokinetic manipulation of particles and cells in the parallel-operating microchannels of the stacked microfluidic device, we developed a 2D numerical model in COMSOL (Burlington, MA, USA) that covered all the reservoirs and microchannels in one layer of PDMS (see Figure 1). The Particle Tracing function was used to compute the trajectories of particles or cells that were released from different positions in the central inlet reservoir. The particle or cell velocity, U_p, is the vector addition of U_{EK} (due to the DC field component) and U_{DEP} (due to both the DC and AC field components),

$$U_p = \mu_{EK} E_{DC} + \lambda_c \mu_{DEP} \left(1 + \alpha^2\right) \nabla E_{DC}^2, \tag{2}$$

where μ_{EK} is the electrokinetic particle mobility, $\boldsymbol{E}_{DC}$ is the DC field component, λ_c is the correction factor for particle size effects on DEP [31,32], $\mu_{DEP} = -\varepsilon d^2/24\eta$ is the dielectrophoretic particle mobility, and α is the AC to DC electric field ratio that is equal to the applied AC to DC voltage ratio. In the simulation, μ_{EK} was determined by tracking the motions of individual particles or cells in the main-body of the microchannel under a small DC field where both the DEP and Joule heating effects are negligible [25–27]. We found $\mu_{EK} = 3.3 \times 10^{-8}$ m^2/(V·s) for 5-μm and 3-μm polystyrene particles, and $\mu_{EK} = 2.0 \times 10^{-8}$ m^2/(V·s) for live yeast cells. It is important to note that the electroosmotic fluid flow pattern in the parallel microchannels is similar to the electric field distribution [30], whose influence on the particle and cell motions has been accounted for by μ_{EK} in Equation (2) as a vector addition of electroosmotic mobility and electrophoretic mobility [4,10,12]. The influence from the wall frictional force has been considered by both μ_{EK} and μ_{DEP} in Equation (2). In addition, as the

electroosmotic flow (and hence the electrokinetic particle motion) has a plug-like velocity profile, the cross-section of the microchannels has an insignificant influence on the particle and cell motions.

The DC electric field in Equation (2) was solved from Laplace equation with insulating and iso-potential boundary conditions on the walls and electrodes (see the small circle at the center of each reservoir in Figure 2), respectively [27]. The model equation was discretized using the finite element method and solved in an unstructured triangular mesh with a second-order accuracy. This numerical method has been validated in previous studies [10]. For the second term of U_p on the right hand side of Equation (2), the dielectrophoretic mobility was calculated from the definition of μ_{DEP} with $\varepsilon = 6.9 \times 10^{-10}$ C/(V·m) and $\eta = 0.001$ kg/(m·s). The correction factors were set to 0.6 and 0.8 for 5-μm and 3-μm particles, and 0.5 for yeast cells, which are consistent with the values used in our earlier studies [33,34] and found to match the experimental results well. Note that, although the yeast cells in our experiment have a size ranging from 4 to 8 μm, they were assumed spherical with an average diameter of 6 μm in the model. This treatment has been demonstrated to reasonably predict the experimental observation [10,25,33,34] because the electric field, which is identical in the experiment and simulation, is large enough to ensure that even the smallest cells can be sufficiently manipulated.

4. Results and Discussion

4.1. Electrokinetic Parallel Concentration of 5-μm Polystyrene Particles

Figure 3 shows the electrokinetic trapping and concentration of 5-μm polystyrene particles inside the central inlet reservoir of the stacked microfluidic device under a 50-V DC-biased 500-V AC voltage. The two snapshot particle images in Figure 3a,b were taken from the PDMS layers A and B (see Figure 1), respectively, while the superimposed image in Figure 3c was from a different reservoir-microchannel junction in Layer A. Consistent with our earlier studies in a single-microchannel device [26,27], the trapped particles were observed to first form chains and then clusters before the entrance of every microchannel in the stacked microfluidic device while at a 700% higher throughput. With the further increase of the number of parallel-operating microchannels, this wholly in-reservoir operation can potentially be used for a high-throughput pre-concentration and filtration of various types of particles and cells. Figure 3d shows the numerically predicted particle trajectories, which agree with the superimposed particle image in Figure 3c well.

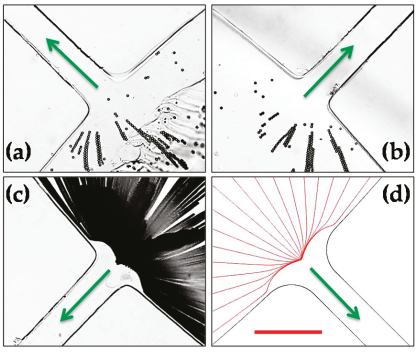

Figure 3. Electrokinetic trapping and concentration of 5-μm-diameter polystyrene particles inside the central inlet reservoir of the stacked microfluidic device under the application of a 50-V DC-biased 500-V AC voltage: (**a**) snapshot image in Layer A (see Figure 1); (**b**) snapshot image in Layer B; (**c**) superimposed image at a different reservoir-microchannel junction of Layer A; and (**d**) numerically predicted trajectories at any reservoir-microchannel junction. The arrows indicate the fluid and particles moving directions from the central inlet reservoir into the parallel microchannels. The scale bar represents 100 μm and applies to all images.

4.2. Electrokinetic Parallel Separation of 5-μm and 3-μm Polystyrene Particles

Figure 4 shows the electrokinetic separation of 5-μm and 3-μm polystyrene particles at the central reservoir-microchannel junctions of the stacked microfluidic device. Under the application of a 50-V DC-biased 500-V AC voltage, 5-μm particles become trapped and concentrated inside the central reservoir, which is consistent with the observation in Figure 3. In contrast, 3-μm particles can travel into the microchannels in the form of an apparently narrowed stream. This is because the streamwise dielectrophoretic motion, U_{DEP_s}, of the smaller particles induced at the junctions is not strong enough to overcome the particle size-independent electrokinetic motion, U_{EK}. Meanwhile, however, the cross-stream dielectrophoretic motion, U_{DEP_n}, takes effect to deflect the smaller particles towards the centerline of every microchannel. With this observed electrokinetic focusing, concentration and separation behaviors of the particle mixture at every central reservoir-microchannel junction of the stacked microfluidic device are again consistent with those in a single-microchannel device in our earlier study [26,27]. Moreover, these experimental observations are all reasonably predicted by the numerical model.

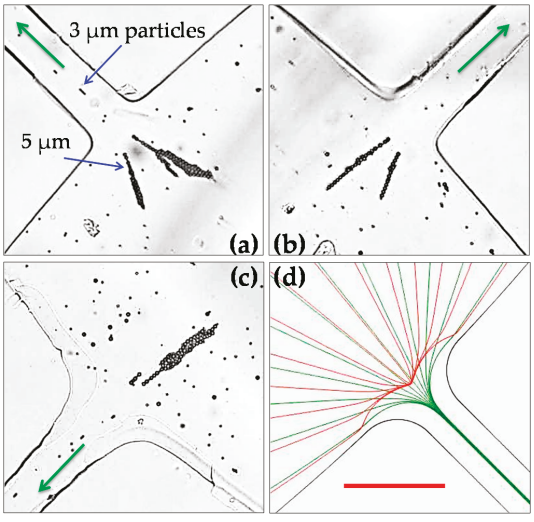

Figure 4. Electrokinetic concentration and separation of 5-μm-diameter polystyrene particles from 3-μm polystyrene particles at different central reservoir-microchannel junctions of the stacked microfluidic device under a 50-V DC-biased 500-V AC voltage: (**a**) snapshot image in Layer A (see Figure 1); (**b**) snapshot image in Layer B; (**c**) snapshot image at a different reservoir-microchannel junction of Layer A; and (**d**) numerically predicted trajectories at any reservoir-microchannel junction. The arrows indicate the fluid and particle moving directions during the separation. The scale bar represents 100 μm and applies to all images.

4.3. Electrokinetic Parallel Concentration of Yeast Cells

Figure 5 demonstrates the application of the stacked microfluidic device to electrokinetic concentration of yeast cells inside the central inlet reservoir. To reduce the potential electrical damages to cells as well as the negative Joule heating effects on the cells, we used a smaller DC bias voltage of 25 V to drive the cell suspension. We found that an AC voltage of 200 V is sufficient to achieve the trapping and concentration of yeast cells at the reservoir-microchannel junction by rDEP. No apparent increase in the electric current was monitored, indicating insignificant Joule heating effects during this experiment [13,14]. Moreover, the concentrated yeast cells were extracted from the central inlet reservoir using a digital pipette and tested with methylene blue. More than 90% of the cells were

found still live after enduring the electrokinetic trapping process. In addition, it is interesting to note that the trapped yeast cells tend to first form smaller irregular clusters and then larger clusters, which is different from the observed trapping pattern for polystyrene particles in Figure 3. This may be due to the irregular shape of yeast cells that can significantly complicate the cell–cell interactions in the electric field [29]. Our numerical model traces only single particles or cells, and hence is unable to predict the trapping pattern for both polystyrene particles in Figure 3 and yeast cells in Figure 5.

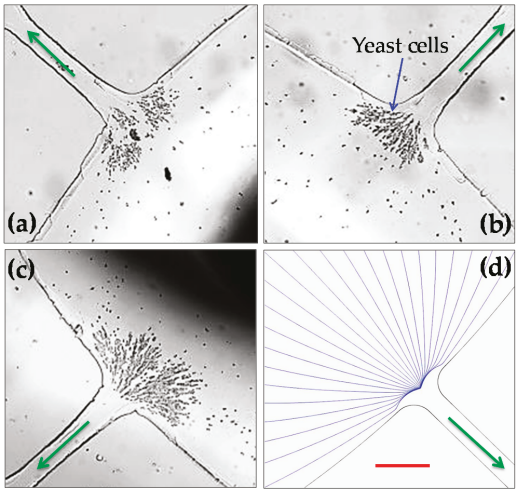

Figure 5. Electrokinetic concentration of live yeast cells at different central reservoir-microchannel junctions of the stacked microfluidic device under a 25-V DC-biased 250-V AC voltage: (**a**) snapshot image in Layer A (see Figure 1); (**b**) snapshot image in Layer B; (**c**) snapshot image at a different reservoir-microchannel junction of Layer A; and (**d**) numerically predicted trajectories at any reservoir-microchannel junction. The arrows indicate the fluid and cell moving directions. The scale bar represents 100 μm and applies to all images.

5. Conclusions

We have fabricated a two-layer stacked microfluidic device with four parallel microchannels in each layer using the custom-modified soft lithography method. Our recently developed rDEP technique has been used to demonstrate a significantly enhanced throughput for electrokinetic manipulation of particles and cells in this device, as compared with that in a single-microchannel device. As the electrokinetic manipulations take place wholly within the central inlet reservoir of this stacked device, the extraction of the concentrated and separated particles and cells is simplified. The process of the device fabrication is straightforward without the need to precisely align the two layers. The number of layers and the number of microchannels in each layer of this device can thus be further increased for a potentially high throughput. However, one potential problem with densely packed microchannels for electrokinetic manipulations is the increase in volumetric Joule heating effects [13,14], which is a problem that becomes more severe if the electrical conductivity of the suspending medium must not be low in order to keep the nature of bio-samples [15,16].

Acknowledgments: This work is supported in part by NSF under grant CBET-0853873 (Xiangchun Xuan), by Clemson University through the University Research Grant (Xiangchun Xuan and Tzuen-Rong Tzeng), Honors Undergraduate Research Program (Xiangchun Xuan) and Creative Inquiry Program (Xiangchun Xuan). The support from the National Natural Science Foundation of China (Grant No. 51575003) and the Key Project of Anhui Education Committee (Grant No. KJ2015A031) is also gratefully acknowledged (Lin Zhu).

Author Contributions: Lin Zhu, Tzuen-Rong Tzeng, and Xiangchun Xuan conceived and designed the project; Saurin H. Patel and Mark Johnson performed the experiment and prepared the experimental images; Saurin H. Patel and Akshay Kale conducted the simulation and prepared the numerical plots; Yash Raval and Tzuen-Rong Tzeng contributed bio-related reagents/materials and analysis; Lin Zhu, Saurin H. Patel, and Xiangchun Xuan wrote the paper; all authors commented on the paper.

Conflicts of Interest: The authors declare no conflict of interest.

References

1. Bruin, G.J.M. Recent developments in electrokinetically driven analysis on microfabricated devices. *Electrophoresis* **2000**, *21*, 3931–3951. [PubMed]
2. Wong, P.K.; Wang, T.; Deval, J.H.; Ho, C.M. Electrokinetics in micro devices for biotechnology applications. *IEEE/ASME Trans. Mechatron.* **2004**, *9*, 366–376.
3. Chang, H.C.; Yeo, L.Y. *Electrokinetically Driven Microfluidics and Nanofluidics*; Cambridge University Press: New York, NY, USA, 2010.
4. Li, D. *Electrokinetics in Microfluidics*; Elsevier Academic Press: Burlington, MA, USA, 2004.
5. Masliyah, J.H.; Bhattacharjee, S. *Electrokinetic and Colloid Transport Phenomena*; Wiley-Interscience: Hoboken, NJ, USA, 2006.
6. Hunter, R.J. *Zeta Potential in Colloid Science*; Academic Press: New York, NY, USA, 1981.
7. Lyklemma, J. *Fundamentals of Interface and Colloid Science*; Academic Press: New York, NY, USA, 1991.
8. Whitesides, G.M.; Stroock, A.D. Flexible methods for microfluidics. *Phys. Today* **2001**, *54*, 42–48.
9. Kang, Y.; Li, D. Electrokinetic motion of particles and cells in microchannels. *Microfluid. Nanofluid.* **2009**, *6*, 431–460.
10. Qian, S.; Ai, Y. *Electrokinetic Particle Transport in Micro-/Nanofluidics: Direct Numerical Simulation Analysis*; CRC Press: Cleveland, OH, USA, 2012.
11. Probstein, R.F. *Physicochemical Hydrodynamics*, 2nd ed.; John Willey and Sons: New York, NY, USA, 1994.
12. Kirby, B.J. *Micro and Nanoscale Fluid Mechanics: Transport in Microfluidic Devices*; Cambridge University Press: New York, NY, USA, 2010.
13. Xuan, X. Joule heating in electrokinetic flow. *Electrophoresis* **2008**, *29*, 33–43. [PubMed]
14. Cetin, B.; Li, D.Q. Effect of Joule heating on electrokinetic transport. *Electrophoresis* **2008**, *29*, 994–1005. [PubMed]
15. Lee, R.C. Cell injury by electric forces. *Ann. N. Y. Acad. Sci.* **2005**, *1066*, 85–91. [PubMed]
16. Voldman, J. Electrical forces for microscale cell manipulation. *Annu. Rev. Biomed. Eng.* **2006**, *8*, 425–454. [PubMed]
17. Saucedo-Espinosa, M.A.; Lapizco-Encinas, B.H. Refinement of current monitoring methodology for electroosmotic flow assessment under low ionic strength conditions. *Biomicrofluidics* **2016**, *10*, 033104. [PubMed]
18. Yung, C.W.; Fiering, J.; Mueller, A.J.; Ingber, D.E. Micromagnetic–microfluidic blood cleansing device. *Lab Chip* **2009**, *9*, 1171–1177. [PubMed]
19. Choi, S.; Ku, T.; Song, S.; Choi, C.; Park, J.K. Hydrophoretic high-throughput selection of platelets in physiologicalshear-stress range. *Lab Chip* **2011**, *11*, 413–418. [PubMed]
20. Hur, S.C.; Mach, A.J.; Di Carlo, D. High-throughput size-based rare cell enrichment using microscale vortices. *Biomicrofluidics* **2011**, *5*, 022206.
21. Hyun, K.A.; Kwon, K.; Han, H.; Kim, S.; Jung, H. Microfluidic flow fractionation device for label-free isolation of circulating tumor cells (CTCs) from breast cancer patients. *Biosens. Bioelectron.* **2013**, *40*, 206–212. [PubMed]
22. Kim, S.; Kim, J.; Kim, D.; Han, S.; Weitz, D. Enhanced-throughput production of polymersomes using a parallelized capillary microfluidic device. *Microfluid. Nanofluid.* **2013**, *14*, 509–514.
23. Zhang, J.; Yan, S.; Li, W.; Alicia, G.; Nguyen, N.T. High throughput extraction of plasma using a secondary flow-aided inertial microfluidic device. *RSC Adv.* **2014**, *4*, 33149–33159.
24. Yu, Z.T.F.; Guan, H.; Cheung, M.K.; McHugh, W.M.; Cornell, T.T.; Shanley, T.P.; Kurabayashi, K.; Fu, J. Rapid, automated, parallel quantitative immunoassays using highly integrated microfluidics and AlphaLISA. *Sci. Rep.* **2015**, 11339. [CrossRef]

25. Patel, S.; Showers, D.; Vedantam, P.; Tzeng, T.; Qian, S.; Xuan, X. Microfluidic separation of live and dead yeast cells using reservoir-based dielectrophoresis (rDEP). *Biomicrofluidics* **2012**, *6*, 034102.
26. Patel, S.; Qian, S.; Xuan, X. Reservoir-based dielectrophoresis (rDEP) for microfluidic particle separation by charge. *Electrophoresis* **2013**, *34*, 961–968. [PubMed]
27. Zhu, J.; Hu, G.; Xuan, X. Electrokinetic particle entry into microchannels. *Electrophoresis* **2012**, *33*, 916–922. [PubMed]
28. Ermolina, I.; Morgan, H. The electrokinetic properties of latex particles: Comparison of electrophoresis and dielectrophoresis. *J. Colloid Interface Sci.* **2005**, *285*, 419–428. [PubMed]
29. Morgan, H.; Green, N.G. *AC Electrokinetics: Colloids and Nanoparticles*; Research Studies Press: Hertfordshire, UK, 2002.
30. Cummings, E.B.; Griffiths, S.K.; Nilson, R.H.; Paul, P.H. Conditions for similitude between the fluid velocity and electric field in electroosmotic flow. *Anal. Chem.* **2000**, *72*, 2526–2532. [PubMed]
31. Zhu, J.; Xuan, X. Dielectrophoretic focusing of particles in a microchannel constriction using DC-biased AC electric fields. *Electrophoresis* **2009**, *30*, 2668–2675. [PubMed]
32. Kang, K.; Kang, Y.; Xuan, X.; Li, D. Continuous separation of microparticles by size with DC-dielectrophoresis. *Electrophoresis* **2006**, *27*, 694–702. [PubMed]
33. Zhu, J.; Canter, R.C.; Keten, G.; Vedantam, P.; Tzeng, T.; Xuan, X. Continuous flow separation of particles and cells in a serpentine microchannel via curvature-induced dielectrophoresis. *Microfluid. Nanofluid.* **2011**, *11*, 743–752.
34. Church, C.; Zhu, J.; Wang, G.; Tzeng, T.J.; Xuan, X. Electrokinetic focusing and filtration of cells in a serpentine microchannel. *Biomicrofluidics* **2009**, *3*, 044109.

micromachines

MDPI

Article

Fabrication of High-Aspect-Ratio 3D Hydrogel Microstructures Using Optically Induced Electrokinetics

Yi Li [1], Sam H. S. Lai [1], Na Liu [2], Guanglie Zhang [3], Lianqing Liu [2], Gwo-Bin Lee [4] and Wen Jung Li [1,2,3,*]

1 Department of Mechanical and Biomedical Engineering, City University of Hong Kong, Kowloon, Hong Kong, China; yili58-c@my.cityu.edu.hk (Y.L.); samlai5-c@my.cityu.edu.hk (S.H.S.L.)
2 State Key Laboratory of Robotics, Shenyang Institute of Automation, Chinese Academy of Sciences (CAS), Shenyang 110016, China; liuna@sia.cn (N.L.); lqliu@sia.cn (L.L.)
3 Shenzhen Academy of Robotics, Shenzhen 518000, China; glzhang@szarobots.com
4 Department of Power Mechanical Engineering, National Tsinghua University, Hsinchu 300, Taiwan; gwobin@pme.nthu.edu.tw
* Correspondence: wenjli@cityu.edu.hk; Tel.: +852-9172-4105

Academic Editor: Sami Franssila
Received: 2 December 2015; Accepted: 11 March 2016; Published: 12 April 2016

Abstract: We present a rapid hydrogel polymerization and prototyping microfabrication technique using an optically induced electrokinetics (OEK) chip, which is based on a non-UV hydrogel curing principle. Using this technique, micro-scale high-aspect-ratio three-dimensional polymer features with different geometric sizes can be fabricated within 1–10 min by projecting pre-defined visible light image patterns onto the OEK chip. This method eliminates the need for traditional photolithography masks used for patterning and fabricating polymer microstructures and simplifies the fabrication processes. This technique uses cross-link hydrogels, such as *poly(ethylene glycol) (PEG)-diacrylate* (PEGDA), as fabrication materials. We demonstrated that hydrogel micropillar arrays rapidly fabricated using this technique can be used as molds to create micron-scale cavities in PDMS (*polydimethylsiloxane*) substrates. Furthermore, hollow, circular tubes with controllable wall thicknesses and high-aspect ratios can also be fabricated. These results show the potential of this technique to become a rapid prototyping technology for producing microfluidic devices. In addition, we show that rapid prototyping of three-dimensional suspended polymer structures is possible without any sacrificial etching process.

Keywords: optically induced electrokinetics; polymer microfabrication; hydrogel microstructures; 3D polymer structures

1. Introduction

The demand for micro-/nano-scale MEMS components and devices has been rapidly increasing in electronics, optics, medicine, bioengineering, automotive and optical communication-related research and products [1,2]. Some specific applications include organ implants, rapid diagnostic devices, wearable health-monitoring devices, micro-scale gyroscopes and micro-lenses. Moreover, microfluidic chip components such as micro heaters, micro-scale pumps, valves and mixing devices also require MEMS fabrication technology. Recently, there has been increasing research interest in developing micro-/nano-scale 3D (three-dimensional) fabrication technologies such as photolithography, colloidal epitaxy with masking, and direct writing [3]. The micro-/nano-scale lithography technologies include X-ray lithography, extreme ultraviolet lithography, nanoimprint lithography, scanning probe lithography, and thermochemical nanolithography [4,5]. Using these

technologies, 3D micro-/nano-scale MEMS structures have been fabricated, including 3D polymer scaffolds and complex 3D polymer vascular networks [6]. Among these technologies mentioned above, direct writing offers flexibility in materials selection, capability for rapid prototyping, and micro-/nano-scale precision with low operation and maintenance costs; hence, it is becoming one of the most promising approaches for 3D micro-/nano-scale fabrication. Even though this technique shows promise in rapid prototyping fabrication applications, the path scanning process inherent in this technique still imposes a x-y plane fabrication speed limitation of ~5 mm/s with a limited lateral resolution of 150 μm for a nozzle-based scanning method [7]. We should note that the OEK-based technique reported in this paper has already demonstrated patterns with lateral resolution of ~5 μm. Moreover, the opto-electrokinetics-based micromanipulation techniques have been reported since 2000. For example, researchers have shown that the particles form colloidal crystals could be assembled using optically tunable patterns to control electrokinetics forces [8,9]. However, the manipulation force was so weak that the whole experiment process took ~2 h [8]. This technique was improved by Chiou *et al.*, who realized massively manipulated single cells and micro-particles in OEK chips [10]. We should note here that our system is similar to the system originally reported by Chiou *et al.* in [10] Other researchers also have demonstrated using opto-electrokinetics techniques that introduce changes in the organic thin film local area surface hydrophilicity, and hence enabled the manipulation of small particles [11].

In this paper, we present our recent work in using a light pattern induced electrokinetics field to fabricate 3D polymer microstructures in a microfluidic environment. In our previous research [12], basic micron-scale *poly(ethylene glycol) (PEG)-diacrylate* (PEGDA) hydrogel features approximately 3 μm in height were fabricated using an optically-induced electrokinetics (OEK)-based platform. The principle of the OEK can be described as follows. When an AC bias voltage is applied across the top ITO glass and the bottom OEK chip, which is made from an ITO glass coated with an a-Si:H layer, a small electric potential drops across the liquid layer and an uniform electric field is produced in the liquid layer. When a projected light pattern is illuminated onto the photosensitive a-Si:H thin film, the conductivity of the a-Si:H thin film will increase from 10^{-11} to 10^{-5} S/m. This local conductivity change on the a-Si:H thin film will cause a localized non-uniform distribution of the electric field, and hence the projected light pattern acts as a virtual localized electrode. The particles in between the two glasses will experience OEK force and move towards or away from the virtual localized electrode [12]. We have further investigated the OEK-based polymerization technology and show in this paper that a single-step fabrication process can be used to rapidly prototype polymer microfluidic components and create 3D suspended polymer microstructures. We should note here that PEGDA is a commonly used biomaterial and could be polymerized with free radicals to form long-chain molecular networks with adjustable mechanical properties when exposed to an ultraviolet light source as shown by others in the past [13]. In this paper, we demonstrate the PEGDA polymerization process when it is exposed to a non-uniform AC electrical field and a non-ultraviolet light source in an OEK chip. This technique can be used to rapidly fabricate micron-scale PEGDA structures within a typical 60–120 s. We also demonstrate the fabrication process of microtubes and 3D microstructures with undercut features using the aforementioned technique. Different from the existing photolithography technique, this method uses hydrogel materials like PEGDA as pre-polymer. DI water was used as the developing solution during the hydrogel mold fabrication process. Thus, this fabrication process is an inexpensive, simple, fast and environmentally friendly micro-/nano-scale features patterning technique. In addition to the micro-/nano-scale rapid prototyping capability, this technology could potentially be used for micro-particle trapping and manipulation, which is also reported in this paper.

2. Materials and Methods

2.1. OEK System

The OEK integrated research platform used for the experiments is shown in Figure 1. The system includes two main modules: the OEK chip module and the peripheral supporting module. The OEK chip module includes three parts, as shown in the inset of Figure 1: (1) a glass slide (3 cm × 3 cm) cover coated with an indium tin oxide (ITO) thin film, which serves as the top electrode; (2) a microfluidic chamber made with PDMS (*polydimethylsiloxane*) thin film in which the PEGDA solution is contained; (3) an OEK glass substrate (3 cm × 3 cm), which has a thin layer of a-Si:H film on top of glass coated with ITO. The gap between ITO glass and OEK chip is 50 μm; ITO and OEK chip thickness are 2 mm respectively. The peripheral supporting module includes a microscope, a computer-controlled projector, and a signal generator.

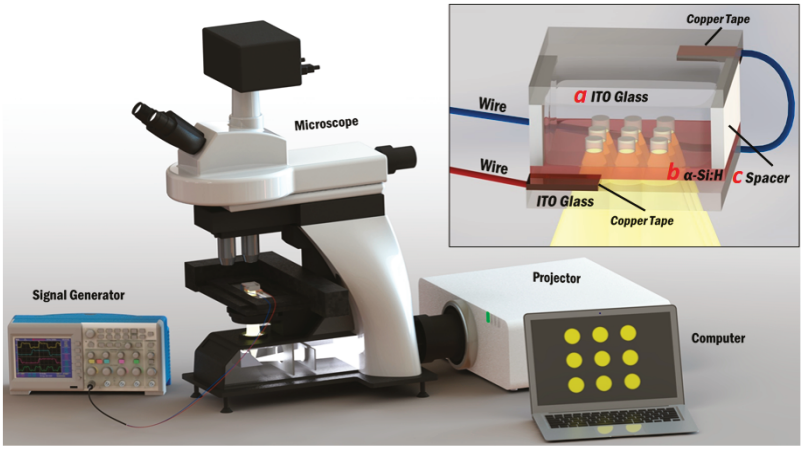

Figure 1. Illustration of the experimental system and the OEK chip (shown in inset). The experimental system consists of a computer, a signal generator, a display projector, and a microscope; the inset figure shows structural details of the different OEK chip layers. (a) ITO glass thickness is 2 mm; (b) a-Si:H layer thickness is 200 nm; (c) spacer height is 50 μm.

The basic process of assembling the three components of the OEK chip module is described below. The first step is to clean the top ITO glass and bottom OEK glass substrates by immersing them in 95% v/v ethanol (Sigma-Aldrich Co. LLC., St. Louis, MO, USA) and sonicating them for 30 min at a frequency of 59 kHz (KS-8893, Ningbo Haishu Kesheng Ultrasonic Equipment Co., Ltd., Ningbo, China). Then, they are blown dry with nitrogen gas. Subsequently, the top ITO glass and OEK glass substrates are assembled with a spin-coated and patterned PDMS spacer layer (50 μm thick), placed between the two glass substrates to form a microfluidic "OEK chamber" into which the PEGDA pre-polymer solution can be injected. The OEK chip module is loaded on a two-dimensional high precision translation stage, as shown in Figure 1. An AC electrical signal generated by a signal generator (Agilent 33522A, Agilent Technologies, Inc., Santa Clara, CA, USA) with an amplifier (TG4001, TTI, Huntingdon, Cambridgeshire, UK) is applied between the top ITO glass and bottom OEK glass electrodes. Then, a series of programmable light patterns, generated by a commercially available computer software (Microsoft PowerPoint 2010, Microsoft Co., Redmond, WA, USA), are projected from an LCD projector (PT-EW630, Panasonic Co., Osaka, Japan) onto the OEK glass a-Si:H substrate through a custom-designed light condenser module (Eclipse Ti-E, Nikon Instruments Inc., Melville, NY, USA).

2.2. OEK-Induced Polymerization

Similar to the fabrication of photoresist-based structures, traditional PEGDA microstructure fabrication processes were based on photolithographic technique, meaning that an ultraviolet light source is essential to curing the solution of PEGDA mixed with photoinitiator. A lithographic mask is also necessary to define the predesigned microstructure patterns. By contrast, the photon-induced electrokinetics method presented in this paper could fabricate PEGDA microstructures without the use of ultraviolet light and masks. The mechanism of polymerizing the PEGDA hydrogel has been demonstrated in our previous work. That is, the electrons generated from the a-Si:H layer of the OEK chip by the photoelectric effect will combine with the hydrogen ions in a hydrogel solution and continue to reduce to hydrogen radicals. These hydrogen radicals will trigger the PEGDA polymerization chain reaction [14].

2.3. Micro-Scale Feature Characterization

To determine the relationship between micro-feature geometry and exposure time experimentally, we fabricated micropillar arrays using the OEK-induced polymerization system. Figure 2a shows an optical image of a micropillar array and demonstrates the relationship between the diameters of patterned hydrogel pillars as a function of exposure time. We chose four different exposure times (10, 30, 60, 90 s) and measured the diameters of the PEGDA micropillars in the 4 × 3 array using an optical microscopy image, as shown in the inset of Figure 2a. From the optical images shown in the Figure 2a inset, the diameters of the PEGDA pillars grow as the exposure time increases. Initially, the hydrogel micropillar diameter was relatively small, less than the 10-μm diameter projected image spot size. As the exposure time increased, the diameter increased; however, the diameter size became stable after ~90 s.

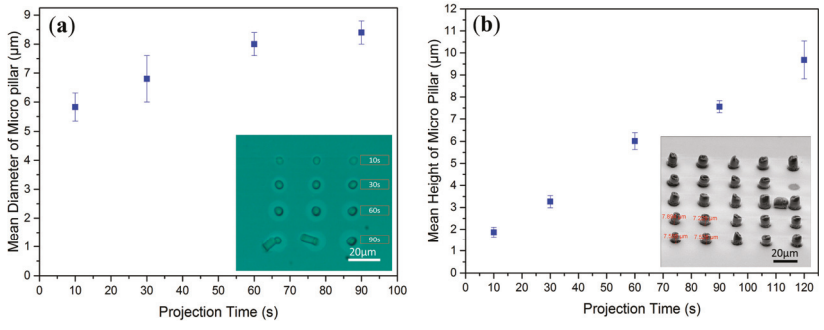

Figure 2. The relationship between physical size of hydrogel micro pillar structure and exposure time. (**a**) The dependence of hydrogel micropillar diameter on exposure time (3 pillars were measured for each data point). Inset: Optical image of a 4 × 3 pillar array showing that the micropillar aspect ratio increased as a function of exposure time. (**b**) Plot of the relationship between hydrogel micropillar height and light pattern exposure time. Each data point contains height measurements from 4 microstructures. Inset: eSEM image of a 5 × 5 micro pillar array. The light pattern projection time required to obtain the structures shown here was 90 s.

Figure 2b shows the relationship between micropillar height and light pattern projection time. The hydrogel micropillar heights were measured using environmental scanning electron microscope (eSEM) images, as shown in the Figure 2b inset. Figure 2b shows a plot of the relationship between hydrogel micropillar height and light pattern projection time. The error bars in Figure 2a,b represent the standard deviation of the fabrication mean diameter and fabrication mean height of the micropillars, respectively. The measurement of the physical size of the micropillar is based on a commercial image processing software, so the error bars show the fabrication error for every sample group.

3. Results and Discussion

3.1. Effect of Solution Conductivity

PEGDA polymerization on an OEK chip is controlled by the potential drop across the a-Si:H/hydrogel solution interface. There is a minimum potential, which can activate the polymerization process. Based on the equivalent circuit of the OEK chip [14], the interface potential will decrease with the increase of the AC frequency, but it will increase with the increase of AC voltage and solution conductivity. Therefore, at a given combination of conditions of AC voltage and solution conductivity, there is a maximum frequency below which all the AC electric field can activate the polymerization process. Figure 3 gives the mean experimental maximum frequency under different V_{pp} and solution conductivities. For example, for an applied voltage of 35 V_{pp} (the equivalent electric field value is 0.7 $V_{pp}/\mu m$) and a solution conductivity of 1.48×10^{-3} S/m, all AC frequencies less than ~7 kHz are suitable to activate the PEGDA polymerization process. However, when the voltage decreases to 20 V_{pp} (the equivalent electric field value is 0.4 $V_{pp}/\mu m$), the maximum frequency is ~3 kHz. The error bars in Figure 3 represent the standard deviation of the mean maximum frequency required for PEGDA polymerization. The PEGDA polymerization depends on the mean maximum frequency (the mean maximum frequency can be defined as the mean value of maximum frequency from the three experiments, which is shown as one data point in Figure 3), applied voltage, and conductivity of the PEGDA solution. For a single data curve, as the applied voltage is increased, the PEGDA polymerization mean maximum frequency also increased. If we fix the voltage, as the PEGDA solution conductivity increased, the PEGDA polymerization mean maximum frequency also increased. The curve clearly shows these relationships.

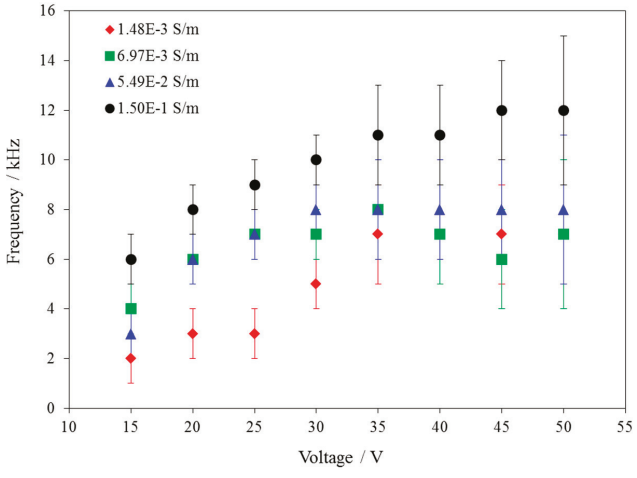

Figure 3. The required mean maximum frequency and voltage for hydrogel polymerization using PEGDA solutions with different polymer solution electrical conductivities. This plot indicates that as the electrical conductivity of the solution increases or the applied voltage increases, the frequency required for hydrogel polymerization also increases.

3.2. Mold Fabrication

These hydrogel micropillar arrays can also be used as molds for PDMS casting, with potential applications in microfluidics. This molding process is shown in Figure 4a. A PDMS (Sylgard 184, Dow Corning S.A., Seneffe, Belgium) elastomer solution was prepared by mixing prepolymer with a cross-linking agent at a weight ratio of 10:1. Air bubbles in the PDMS mixture were removed by

placing the mixture under vacuum for 1 h. Then, the PDMS mixture was poured onto the fabricated hydrogel mold and cured in an oven at 65 °C for 2 h. After curing, the PDMS replica was peeled from the mold. Figure 4b shows an optical image of the micropillar array, and Figure 4c shows an eSEM image of the micro-cavity array corresponding to the micropillar mold.

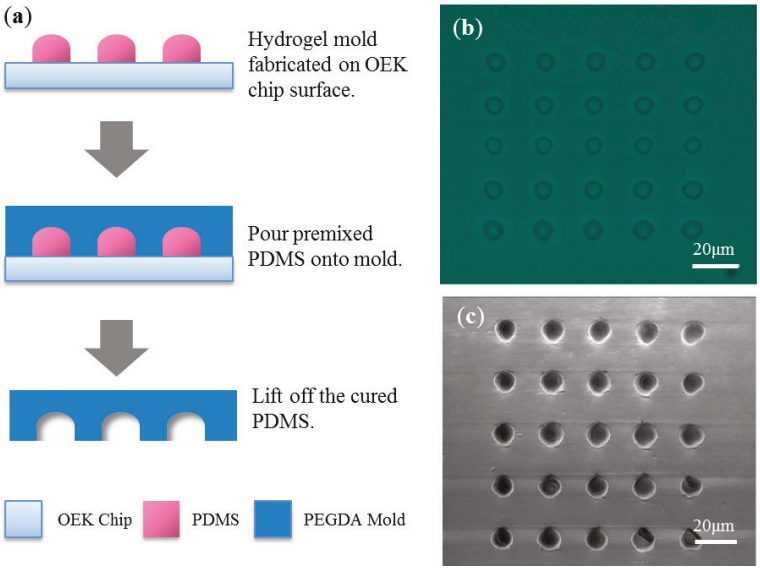

Figure 4. Illustration of the PDMS microcavity array fabrication process using a PEGDA mold fabricated by the OEK-based process. (**a**) Process flow schematic of the PDMS microcavity array fabrication. (**b**) Optical microscope image of a 5 × 5 PEGDA hydrogel micropillar array. Each micropillar was approximately 10 μm in diameter and approximately 5 μm in height. Optical pattern projection time is 60 s, apply voltage is AC 10 V_{pp}, (the equivalent electric field value is 0.2 V_{pp}/μm), frequency is 10 kHz. (**c**) eSEM image of the micron-scale cavities molded from the PEGDA hydrogel micropillar array. Each microcavity was approximately 10 μm in diameter and approximately 5 μm in depth.

The first advantage of the mold fabrication method depicted in Figure 4 is that the method is very simple compared with other existing molding processes. The photolithography-based mold creation process comprises substrate cleaning, spin coating, pre-baking, UV exposure, post-baking and resist developing. These steps usually require tens of minutes for completion, in addition to requiring the use of photolithographic masks. However, the hydrogel mold fabrication process described here can be completed in a few minutes and requires no lithographic masks. Moreover, this hydrogel mold fabrication process is an inexpensive method. In general, photolithography processes require UV exposure systems, spin-coating machines, and hot plates. By contrast, the hydrogel fabrication method described in this paper only requires a small visible light source. Photolithography processes are typically completed on silicon wafers using expensive photoresists, such as SU-8, KMPR, and AZ; each type of photoresist requires the use of a suitable developing solution. By contrast, the slide substrate and hydrogel used in the OEK-based method described here are inexpensive materials, and DI (deionized) water can be used as the "developing solution" during the hydrogel mold fabrication process, *i.e.* any unexposed hydrogel can be washed away by DI water. Thus, this fabrication process is an inexpensive, simple, fast and environmentally friendly patterning process.

However, one challenge of this novel process that needs to be overcome is the adhesion between the fabricated hydrogel structures and the substrate. To be used as a mold for subsequent casting

procedures, firm adhesion of the hydrogel to the substrate is required. It was found that the water used to remove the unexposed hydrogel solution during the development step caused the polymerized hydrogel material to swell. However, the substrates, which were made of other materials such as glass, silicon and metal did not swell. These volume expansions mismatched in two different materials resulted in stress increased at the contact surface. Hence, the adhesion force between the hydrogel structures and the substrate was not sufficient to allow the hydrogel micropillars to serve as molds for creating micro-cavities in a PDMS substrate. We solved this problem by adding a thin hydrogel layer on top of the OEK chip surface after inducing the OEK-based polymerization process. A circle light pattern with a diameter bigger than diagonal length of micropillar array will project to the OEK chip. The exposure time is 1 s with same electrical parameters as micropillar fabrication. Then, a thin layer of polymerized PEGDA will attach itself to the micropillar array. This method will help to fix the microfeatures on top of a-Si:H.

3.3. Micro-Scale Tube Fabrication

In addition to applying the OEK-induced hydrogel polymerization principle to fabricate hydrogel micropillars for molding microfluidic cavities, this method can also be applied to other 3D microstructures, as shown in Figure 5. We show that the OEK-induced hydrogel polymerization technique can be used to fabricate hydrogel tubes of different sizes. Such micro-tubes could be the basic building blocks to a complex vascular network. The generation of a complex 3D vascular network could then be used to engineer highly vascularized tissues and organs for regenerative medicine [15] and pharmacological screenings [16]. In general, the process described here could be used to fabricate functionalized microstructures with different sizes and aspect ratios on top of the same substrate.

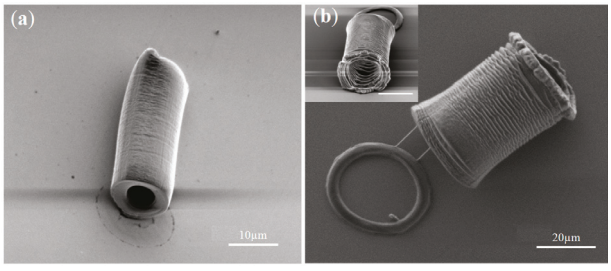

Figure 5. eSEM images of hydrogel microtubes. (**a**) A PEGDA hydrogel tube with a length of approximately 20 μm, an outer diameter of approximately 10 μm, and an inner diameter of approximately 5 μm. Optical pattern projection time is 200 s with applied voltage AC 10 V_{pp}, the equivalent electric field value is 0.2 V_{pp}/μm, and frequency is 10 kHz. (**b**) A PEGDA hydrogel tube with a length of approximately 35 μm, an outer diameter of approximately 25 μm, and an inner diameter of approximately 20 μm. Optical pattern projection time is 320 s, apply voltage is AC 10 V_{pp}, the equivalent electric field value is 0.2 V_{pp}/μm, and frequency is 10 kHz. The inset image is a tilted view of the PEGDA hydrogel tube, scale bar: 20 μm.

3.4. Polystyrene Bead Trapping by a Hydrogel Tube

For applications in biomedicine, traditional cellular studies are conducted using large quantities of cells; consequently, the resulting measurements only indicate statistical cellular data. This approach may misinterpret the true physiological state of cells because it ignores the differences between individual cells. In the past few decades, single-cell analysis has become more important in biomedical research, and many cell entrapment or manipulation techniques have been explored. Existing methods physically isolate cells *in vitro* and maintain them in normal cellular physiological conditions. Moreover, many encapsulation methods have been developed in recent years. These techniques are generally

classified as either micro-encapsulation or macro-encapsulation [17]. The OEK-induced polymerization principle has potential for applications in cell trapping and encapsulation because of the capsule permeability, mechanical properties, and biocompatibility of hydrogels. Hydrogels have already been used as cell culture scaffolds, and our group reported such work in 2014 [18]. The serial optical images shown in Figure 6a–d show the process of a 5 μm polystyrene bead becoming trapped in a hydrogel tube using the OEK-based polymerization technique. First, a green ring pattern was projected to the OEK chip to trigger the hydrogel polymerization process, which enabled the hydrogel tube to grow and trap the bead. After that, the hydrogel tube continued to elongate and trapped the bead to move away from its original location. The experiment conditions were as follows: voltage was 20 V_{pp} (the equivalent electric field value is 0.4 $V_{pp}/\mu m$) and the frequency was 10 kHz. The experimental results show that, by using this technique, we can trap and manipulate micro-particles in a liquid solution, potentially paving the way for a technology capable of trapping and manipulating live cells in real time with high spatial resolution. These small hydrogel vesicles could be used to encapsulate particles of different physical sizes, such as proteins, nanoparticles, and cells.

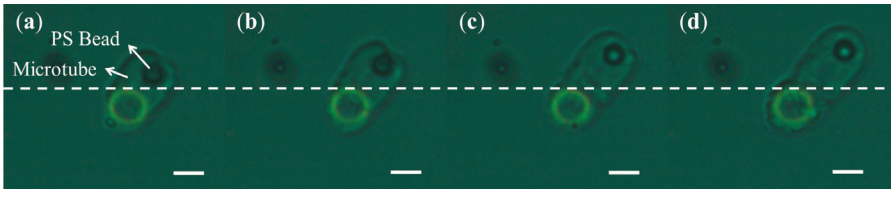

Figure 6. Optical images of a PS (*polystyrene*) bead trapped and manipulated by a hydrogel microtube structure. (**a**–**d**) Time-lapse images recorded the process of a PS bead been trapped by a hydrogel microtube (scale bar: 5 μm): (**a**–**c**) 5s interval; (**d**) after 180 s exposure time. Green ring is the projected light pattern. White dash line indicates the initial position of PS bead.

3.5. 3D Undercut Features

We demonstrate in this section that the OEK-induced polymerization principle can also be used for 3D micron-scale rapid prototyping, including the fabrication of suspended 3D structures. Suspended, or "undercut" structures can be easily constructed by controlling the image patterns and projection time on the surface of an OEK chip. Figure 7a,b shows the schematic of 3D "micro-bridge" structures fabricated using the OEK-based process. First, a rectangular light pattern of 20 μm × 10 μm in size was projected onto the OEK layer for 10 s to form the "bridge floor." Then, two small rectangular light patterns of 10 μm × 5 μm in size, with a 10 μm gap between them, were projected onto the OEK chip surface just beneath the bottom of short side of "bridge floor" for 122.5 s to form the "pillars of the bridge". As the pillars grow upward, the former "bridge floor" could be lifted off by these two pillars. The applied voltage was 20 V_{pp} (the equivalent electric field values was 0.4 $V_{pp}/\mu m$) with a frequency of 10 kHz for both of these two steps. Figure 7c shows an eSEM image of two hydrogel "bridge" structures fabricated using the OEK-induced polymerization process described above. We note here that the "wave structures" observed in the sidewall of the pillars appeared only after SEM images were taken of the structures, *i.e.* we did not observe these "wave" structures on the pillars under the microscope after the fabrication process. We speculate that these "waves" or "ripples" in the structures are due to the loss of water content inside the hydrogel structures when SEM chamber pumps out air during the vacuuming process. That is, the water content near the surface of the structures evaporate and cause the collapse of the structure, thereby creating "wave-like" feature on the structures.

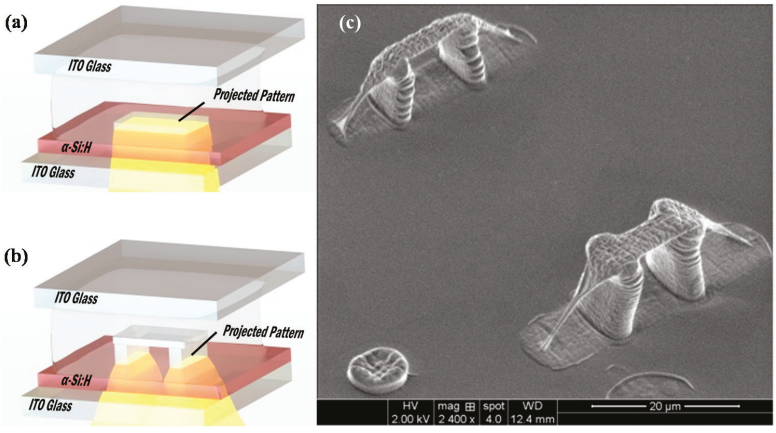

Figure 7. Fabrication process of the 3D suspended micro-scale structure and eSEM image. (**a**,**b**) Schematic of the 3D suspended "microbridge" microstructure fabrication process, the light pattern exposure time in step (**a**) is 10s and in step; (**b**) is 122.5 s; (**c**) eSEM image of PEGDA hydrogel 3D suspended "micro-bridge" structures. The bridge floor thickness is about 2 μm; the height of bridge pillar is about 10 μm.

4. Conclusions

We report in this paper a non-UV and non-photoinitiator 3D micron-scale rapid prototyping technique by using an optically induced electrokinetics (OEK) based polymerization process. This new technique allows the fabrication of 3D high-aspect-ratio and suspended hydrogel polymer structures not possible using OEK-based techniques reported in the past. This technique enables the fabrication of micron-scale hydrogel structures of different sizes, shapes, and aspect ratios using a single-step projection process without requiring any microlithographic masks. Furthermore, the rapid OEK-induced polymerization process presented in this paper also enables the "direct writing" of micron-scale hydrogel features within a few seconds to a few minutes, depending on the desired aspect ratio of the microstructures. This OEK-based micro-scale fabrication method achieves a highly parallel fabrication speed by utilizing localized projection light patterns that can be dynamically reconfigured. Using this novel method, hydrogel micropillar arrays rapidly prototyped were used as molds to create micron-scale cavities in PDMS substrates. This method was also used to create hollow, circular tubes with a high-aspect ratio and controllable wall thickness within the time span of a few minutes. Three-dimensional suspended polymer structures were also fabricated, without any sacrificial etching process. In contrast to traditional microlithographic processes, this process does not require relatively expensive and toxic chemicals, such as acetone, methanol or resist-developer; once the microstructures are formed using the OEK-based process, they only need to be rinsed with DI water and dried with nitrogen gas. Hence, in the future, the OEK-based technique could become a very environmentally friendly rapid prototyping technology for the fabrication of polymer microstructures.

Acknowledgments: The authors gratefully acknowledge support from the Hong Kong Research Grants Council (Project no: CityU 116912), the Chinese Academy of Sciences–Croucher Funding Scheme for Joint Laboratories (Project no: 9500011), and The Science Technology and Innovation Committee of Shenzhen Municipality grants (JCYJ20140813161522550 and JCYJ20150828104330541).

Author Contributions: In this work, Yi Li and Wen Jung Li conceived and designed the experiments; Sam H. S. Lai constructed the ODEP system with guidance from Guanglie Zhang and Wen Jung Li; Yi Li performed the experiments and analyzed the data; Na Liu and Lianqing Liu gave suggestions for the experimental processes. Yi Li drafted the manuscript; Guanglie Zhang, Wen Jung Li and Lianqing Liu edited the manuscript.

Conflicts of Interest: The authors declare no conflicts of interest.

References

1. Alting, L.; Kimura, F.; Hansen, H.N.; Bissacco, G. Micro Engineering. *CIRP Ann. Manuf. Technol.* **2003**, *52*, 635–657. [CrossRef]
2. Ehmann, K.F.; Bourell, D.; Culpepper, M.L.; Hodgson, T.J.; Kurfess, T.R.; Madou, M.; Rajurkar, K. *International Assessment of Research and Development in Micromanufacturing*; World Technology Evaluation Center: Baltimore, MD, USA, 2005.
3. Alfons, V.B.; Rene, R.; Pierre, W. Template-directed colloidal crystallization. *Nature* **1997**, *385*, 321–323.
4. Wacaser, B.A.; Maughan, M.J.; Mowat, I.A.; Niederhauser, T.L.; Linford, M.R.; Davis, R.C. Chemomechanical surface patterning and functionalization of silicon surfaces using an atomic force microscope. *Appl. Phys. Lett.* **2003**, *82*, 808–810. [CrossRef]
5. Wang, D.; Kodali, V.K.; Underwood, W.D., II; Jarvholm, J.E.; Okada, T.; Jones, S.C.; Okada, T.; Jones, S.C.; Rumi, M.; Dai, Z.; *et al.* Thermochemical nanolithography of multifunctional nanotemplates for assembling nano-objects. *Adv. Funct. Mater.* **2009**, *19*, 3696–3702. [CrossRef]
6. Gerlier, L.; Lamotte, M.; Wille, M.; Kreuz, P.C.; Vanlauwe, J.; Dubois, D.; Meurgey, F.M. The cost utility of autologous chondrocytes implantation using ChondroCelect(R) in symptomatic knee cartilage lesions in Belgium. *Pharm. Econ.* **2010**, *28*, 1129–1146. [CrossRef] [PubMed]
7. Lewis, J.A. Direct ink writing of 3D functional materials. *Adv. Funct. Mater.* **2006**, *16*, 2193–2204. [CrossRef]
8. Hayward, R.C.; Saville, D.A.; Aksay, I.A. Electrophoretic assembly of colloidal crystals with optically tunable micropatterns. *Nature* **2000**, *404*, 56–59. [PubMed]
9. Williams, S.J.; Aloke, K.; Steven, T.W. Electrokinetic patterning of colloidal particles with optical landscapes. *Lab Chip* **2008**, *8*, 1879–1882. [CrossRef] [PubMed]
10. Chiou, P.Y.; Aaron, T.O.; Ming, C.W. Massively parallel manipulation of single cells and microparticles using optical images. *Nature* **2005**, *436*, 370–372. [CrossRef] [PubMed]
11. Kumar, A.; Chuang, H.S.; Steven, T.W. Dynamic manipulation by light and electric fields: Micrometer particles to microliter droplets. *Langmuir* **2010**, *26*, 7656–7660. [CrossRef] [PubMed]
12. Wang, S.; Liang, W.F.; Dong, Z.L.; Lee, G.B.; Li, W.J. Fabrication of micrometer- and nanometer-scale polymer structures by visible light induced dielectrophoresis (DEP) force. *Micromachines* **2010**, *2*, 431–442. [CrossRef]
13. Dang, T.D.; Kim, Y.H.; Choi, J.H.; Kim, G.M. A novel simple preparation method of a hydrogel mold for pdms micro-fluidic device fabrication. *J. Micromech. Microeng.* **2012**, *22*, 15–17. [CrossRef]
14. Liu, N.; Li, P.; Liu, L.; Yu, H.; Wang, Y.; Lee, G.B.; Li, W.J. 3-D non-UV digital printing of hydrogel microstructures by optically controlled digital electropolymerization. *J. Microelectromech. Syst.* **2015**, *9*, 2128–2135. [CrossRef]
15. Levenberg, S.; Rouwkema, J.; Macdonald, M.; Garfein, E.S.; Kohane, D.S.; Darland, D.C.; Marini, R.; van Blitterswijk, C.A.; Mulligan, R.C.; D'Amore, P.A.; *et al.* Engineering vascularized skeletal muscle tissue. *Nat. Biotech.* **2005**, *23*, 879–884. [CrossRef] [PubMed]
16. Griffith, L.G.; Swartz, M.A. Capturing complex 3D tissue physiology *in vitro*. *Nat. Rev. Mol. Cell Biol.* **2006**, *7*, 211–224. [CrossRef] [PubMed]
17. Uludag, H.; De Vos, P.; Tresco, P.A. Technology of mammalian cell encapsulation. *Adv. Drug Deliv. Rev.* **2000**, *42*, 29–64. [CrossRef]
18. Liu, N.; Liang, W.; Liu, L.; Wang, Y.; Mai, J.D.; Lee, G.B.; Li, W.J. Extracellular-controlled breast cancer cell formation and growth using non-UV patterned hydrogels via optically-induced electrokinetics. *Lab Chip* **2014**, *14*, 1367–1376. [CrossRef] [PubMed]

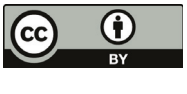

MDPI AG
St. Alban-Anlage 66
4052 Basel, Switzerland
Tel. +41 61 683 77 34
Fax +41 61 302 89 18
http://www.mdpi.com

Micromachines Editorial Office
E-mail: micromachines@mdpi.com
http://www.mdpi.com/journal/micromachines

MDPI AG
St. Alban-Anlage 66
4052 Basel
Switzerland

Tel: +41 61 683 77 34
Fax: +41 61 302 89 18

www.mdpi.com

ISBN 978-3-03842-453-6